Campbell, Fraser Alexander (2021) *Design and optimised production of an integrated nanopillar platform.* PhD thesis.

http://theses.gla.ac.uk/82018/

Design and optimised production of an integrated nanopillar platform

Fraser Alexander Campbell

Submitted in fulfilment of the requirements for the degree of

Doctor of Philosophy

June 2020

School of Engineering

College of Science and Engineering

University of Glasgow

Abstract

There has been a recent trend in the study of cell response to nanotopographical cues and substrate mechanical properties, represented best by the interaction between a cell and an array of sub-millimetre scale polymeric pillars. This has led to an increased understanding of the driving forces behind cell behaviours like differentiation, proliferation and migration, and has been greatly facilitated by replication techniques that reduce the time and cost of device fabrication. Low throughput and the lack of a standardised format can make integration into widely used biological investigative techniques difficult. This thesis aims to overcome these issues by combining high throughput replication by injection moulding with a format familiar to most biologists; the well-plate.

Firstly, the fabrication process of large area, high aspect ratio nanopillar arrays is optimised to improve production yield. A quality analysis process for setting part tolerances is developed to define batch production. The various mechanisms that contribute to high quality replication accuracy are identified and linked to mechanical and thermal stresses. This is used as a predictive tool for intelligent device design for three pillar devices. These devices are integrated into in-house fabricated 24-well plates using ultrasonic welding, and the yield of successful devices is measured.

As a cell moves across a pillar it bends it, thus in order to fully understand the mechanics at play the model used for pillar bending must be accurate. To this end, an investigation was carried out to determine the limitations of using the Euler-Bernoulli spring constant to define pillar deflection under a load. Hard limits are set on the aspect ratio of a pillar, as well as the overall side-wall angle and how these two couple. Lastly, a new amendment to the Euler-Bernoulli equation is derived to account for non-linear pillar sidewalls. As replication accuracy is dominant in determining pillar bending mechanics and part tolerances, a fabrication process is designed to create pillars that promote replication accuracy using an inductively coupled plasma to control individual pillar dimensions. This results in high speed etching, nanometre scale resolution and control of pillar profile angle within 0.5°.

Presented here is a process allowing for the smooth transition from design of individual high aspect ratio nanostructures to fully fabricated arrays. These arrays have been used in a subsequent biology experiment to great success, with one array accurately representing the stiffness bone microenvironment and each individual array stimulating a unique cell response. By using an integrated nanopillar array like this, the design process can be steered towards positive hits in larger scale experiments, allowing for fast processing of results and rapid design changes.

Table of Contents:

List of Figures:

List of Tables

Table of abbreviations:

AFM	atomic force microscopy
ANOVA	analysis of variance
AR	aspect ratio
BIG	Biomedical Interfaces at Glasgow
CINA	Cell Interface with Nanostructure Arrays
d_B	base diameter
d_M	mid-diameter
d_T	tip-diameter
EBL	electron beam lithograohy
ER	etch rate
FEA	finite element analysis
GDMB	gradient at diameter (mid-base)
GDMT	gradient at diameter (mid-tip)
hMSC	human mesenchymal stem cells

ICP	inductively coupled plasma
IPA	Isopropyl alcohol (isopropanol)
k_{BZ}	Bezier spring constant
k_{CLY}	cylindrical spring constant
k_{CON}	conical spring constant
k_{SOL}	modelled spring constant
LAV	local area variance
MER	mask erosion rate
MFP	mean free path
MSC	mesenchymal stem cells
NIL	nano-imprint lithography
NMP	N-Methyl-2-pyrrolidone
PC	polycarbonate
PDMS	polymethylsiloxane
PECVD	plasma-enhanced chemical vapour deposition
PMMA	polymethyl methacrylate
PPE	polyphenyl ether
PS	polystyrene
RF	radio frequency
RIE	reactive ion etching
RO	reverse osmosis
SEM	scanning electron microscopy
SWA	sidewall angle
UHAR	ultra high aspect ratio
UV	ultraviolet
QA	quality analysis

Output

Publications (1)

Huethorst E, Cutiongco MF, Campbell FA, et al. *Customizable, engineered substrates for rapid screening of cellular cues.* Biofabrication (2020); 12: 025009-025009. DOI: 10.1088/1758-5090/ab5d3f

Acknowledgements

There are always many people to thank at the end of a PhD programme, particularly one as long as mine. So I'll start by thanking the most important contributor to my work; coffee. Without you, none of this would have been possible.

The people who have impacted my life and work these past five-ish years can broadly be split into two categories, academic and social, with some amount of crossover. I'll start with the people who need to be formally credited for their contributions to my thesis. Thanks to Professor Gadegaard for starting me down this path, he and the BIG group have helped me take a vague idea about what I wanted to do with this project and shape it into an actual thesis. Thanks also to Professor Robert McMeeking of UC Santa Barbara for tips and tricks on deriving equations – the use of the Maclaurin series expansion saved me a lot of headaches, and thanks to the EPSRC for funding (all probably more influential than the coffee).

From the group, I'd like to name check Emma for letting me cannibalise her Matlab code and force it to analyse pillar dimensions instead of cell morphology. That saved me hours of work and only cost me hundreds of pounds in coffee payment. Marie and Eline for making use of my pillars! Your amazing cell work has given me a publication and the beautiful fluorescence images that I've made good use of in this thesis. Tim Horton's for life! Eternal gratitude be to Johnny for coming back to the group and rescuing my PhD. Props to Rachel, my thin foil moulding buddy. I hope I never see the word discrete again. Thanks again to Johnny and Marie, who helped take a nearly four hundred page document and reduce it to the digestible text you see before you. This thesis has had more final forms than a Dragon Ball Z villain.

Thanks to all the staff at the JWNC, without who none of this fabrication work would be possible. I'd like to in particular thank Michael and Dougie for their patience and enthusiasm for my dry etch experiments! Thanks to the KNT folk, your hive mind of nanofab has been an eternal boon and I can't express how much easier it's made my thesis. Particularly Corrie whose encyclopaedic knowledge of dry etch was better than the entirety of the literature, and Oliver for his technique of metal deposition.

Finally, I'd like to thank my family and friends who have had my back this entire time. My parents, (particularly Dad for proof reading!), Gran, Emily, Francesca and the entire gang. Your love and support have carried me over the line, and I can't express how grateful I am for that. If there's one thing I can take forward from this experience it will be this:

There is no secret ingredient.

Author's Declaration

I declare that all work presented in this thesis was carried out by me, unless otherwise acknowledged or referred to.

Fraser Alexander Campbell

June 2020

1.0 Introduction

Nanotechnology pervades every aspect of modern life, and continues to do so at an increasing pace. From smartphones to smart cities, the rapid collision of technology and day to day living offers unprecedented opportunity to interrogate the world around us and further the quality of living of everyone. Novel medical techniques in regenerative medicine[2], plasmonics based cancer treatments[3, 4], integrated smart technology with sports equipment[5], and intelligently designed water filtration systems[6] are just a few of the uses of nanoscale science to better the lives of everyone on the planet.

The field of biology has benefited greatly from a rapid increase in available nanofabrication techniques, and with those the ability to investigate cell behaviour at much smaller length scales.

1.1 Cell interactions with nanotopography

Research of individual cell behaviour at sub-micrometre length scales has become a staple of cell investigations in the literature with two main avenues of investigation – topographical and mechanical changes to the microenvironment[7-11]. Nanotechnology is well suited to influencing the arrangement of nanoscale topographies, with investigations into the effect of the geometry of nanoscale features on hMSC lineage selection[12], the use of chemical micropatterning to regulate stem cell differentiation and adhesion[13], the use of nanotopographical features to probe endocytosis in live cells[14], and the use of sub-micrometre scale gratings to promote alignment of cells[15].

Initial mechanical approaches utilise the adaptability of gel based substrates to regulate cell response[16, 17]. Notably is recent research into the relationship between rigidity sensing and cancer metastasis[18-21]. This is particularly efficient at directing stem cell lineages, with a large number of studies trying to control cell behaviour using the cell mechanical environment[1, 16, 17, 22-28]. **(Figure 1.1)** illustrates the findings regarding stem cell differentiation and matrix stiffness. By varying the stiffness of the gel substrates the naïve mesenchymal stem cells (MSCs) were seeded on, the individual cells were found to differentiate along different lineages, exhibiting neurogenesis, myogenesis and osteogenesis at distinctly different substrate stiffness.

It should be noted here that E, the Young's modulus, measures the substrate stiffness, the response to axial compression/tension, and G, the shear modulus, measures the rigidity, the response to a shear stress. **Table 1.1** outlines the results of a review of the literature, including the substrate material used, the quoted Young's modulus, and the given tolerance.

Author	Substrate	E(kPa)	Tolerance(kPa)	Tolerance (%)
Charrier[29]	PAA Gel	18	1.44	8%
Ye[30]	PEG Gel	130	10	8%
		3170	413	13%
Gilbert[31]	PEG Gel	40	5	13%
		15	2	13%
Nam[32]	Electro Spun Nanofibers	7100	3000	42%
		30600	4100	13%
Pagliari[33]	PCL film	1530	160	10%
		910	80	9%
		49670	2560	5%
		133230	8670	7%
Huth[34]	PAA Gel	175	7	4%
		165	5	3%
		125	4	3%
Tse[35]	Acrylamide Gel	0.2	0.03	15%
		0.71	0.24	34%
		3.24	0.58	18%
		1.8	0.44	24%
		8.44	0.82	10%
		2.61	0.82	31%
		19.66	1.19	6%
Cavo[36]	Alginate Gels	150	50	33%
		300	50	17%
		2500	1500	60%
Average	-	-	-	*17%*

Table 1.1 – Table of mechanically categorised gels from the literature for cell-based experiments and their quoted tolerances.

Of note in the table is the large variance not only in the tolerance given for the quoted Young’s moduli, but also the range of stiffnesses covered, from 200kPa to 1.3GPa, all using different substrate materials, and different fabrication methods. The average tolerance from the literature is 17%, the median being 13%. The tolerances are important, particularly for all conclusions made about cell-substrate interactions in comparison to in-vivo tissue values.

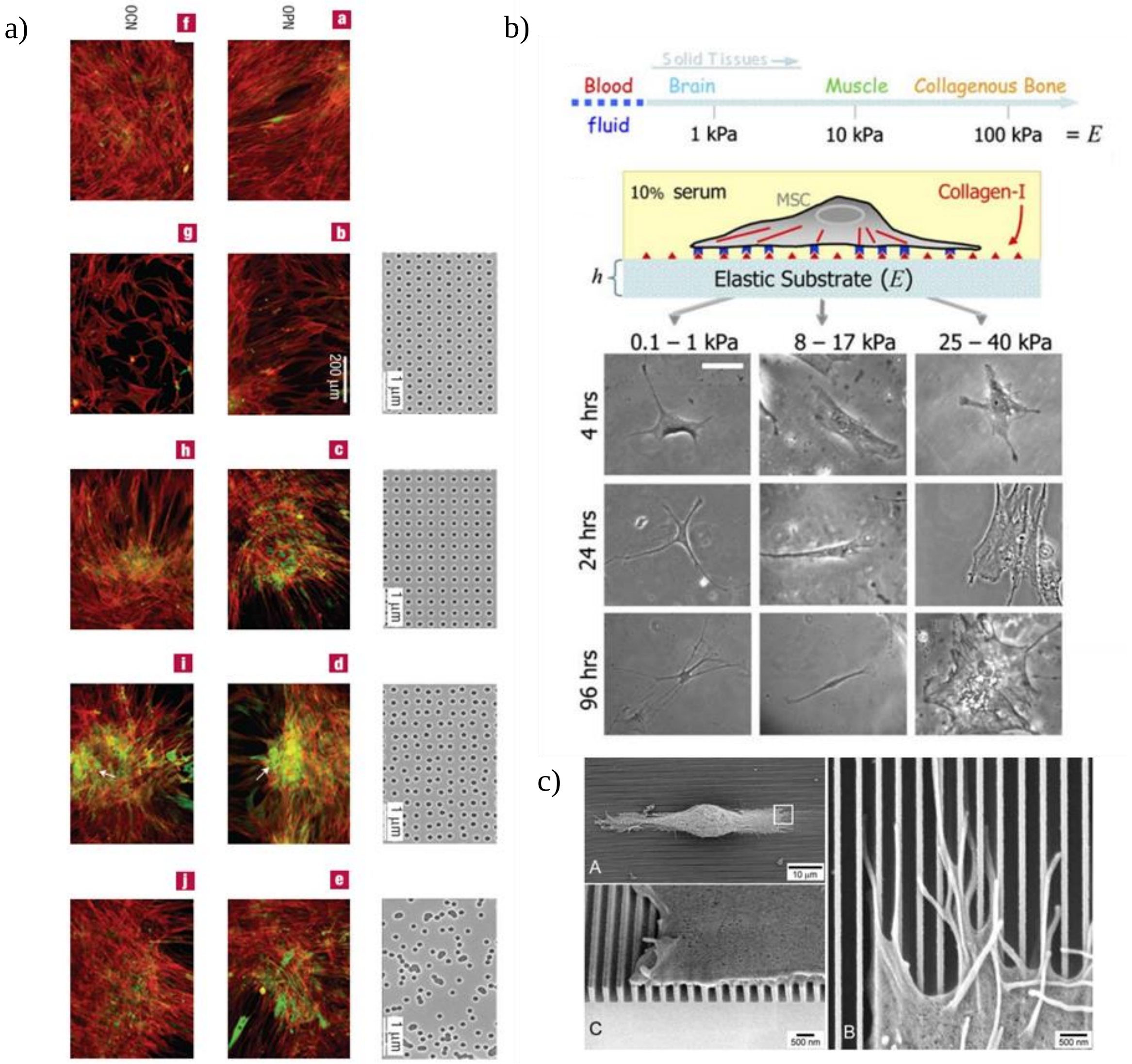

Figure 1.1 - Examples from the literature of cell interactions with nanotopographies. Panels a) exhibiting the effect of varying geometry on osteogenesis of MSCs (figure adapted from Dalby et al)[12] and c) of human corneal epithelial cells aligning to nanoscale gratings[15], whilst b) demonstrates the effect that substrate stiffness (E, the Young's modulus) has on lineage selection of naïve MSCs, directing them towards neuro, myo and osteogenesis at 0.1-1, 8-17 and 25+ kPa respectively[1]. Images replicated with permission from the copyright holder.

A scale of tissue stiffness is presented in (**Figure 1.1-b)**, ranging from brain tissue at 1kPa to collagenous bone, 100kPa. By mimicking ranges of in vivo stiffness using the gels, MSCs were reported to differentiate along lineages consistent with the relevant mechanical environment. In this way, stem cell fate can be controlled by manipulation of their mechanical environment only. Combining topographical and mechanical approaches to controlling cell behaviour, allow for the production of designed cell micro-environments with custom, tuneable mechanical and topographical properties by fabrication of an array of sub-millimetre scale pillars.

1.2 Pillar arrays as mechanical stimulus

Pillar arrays allow for both the integration and the decoupling of topography and surface mechanics. A pillar array has two design parameters that can be varied, individual pillar dimensions and array geometry. The individual pillars can be altered in diameter and height, and the geometry of the pillars arrayed in terms of pitch (pillar to pillar spacing) and pattern, for example; **(Figure 1.1-a)** demonstrates arrays of nanofeatures with square, hexagonal and disordered geometries that each elicit a unique response. The height and diameter are the dominant factors in determining the pillar bending mechanics. **(Equation 1.1)** is the Euler-Bernoulli expression of a cylindrical cantilever beam deflecting under a force:

$$\mathrm{k} = \frac{3\pi \mathrm{E}}{64}\frac{\mathrm{d}^4}{h^3}$$ **Equation 1.1**

where k is the spring constant of the beam – i.e. the ratio of deflection to applied force. E is the Young's modulus of the bulk material, d is the diameter and h is the height of the pillar. This equation can be applied by assuming that the pillar has a fixed base and is an ideal cylinder. By creating multiple generations of substrates each facet of the pillar array can be changed whilst allowing direct comparisons to be drawn between them. This allows for the probing of cell responses to these stimuli in a systematic fashion. For example, the literature reports that PDMS or other elastomeric based micropillars can be used as individual mechanical sensors to measure the traction forces of cells[37], to dictate cell morphology and focal adhesion formation[38], and to investigate effect that changing substrate mechanics has on cell migration[39], and that of pillar scale (micron and sub-micron scale) on cellular response[40].

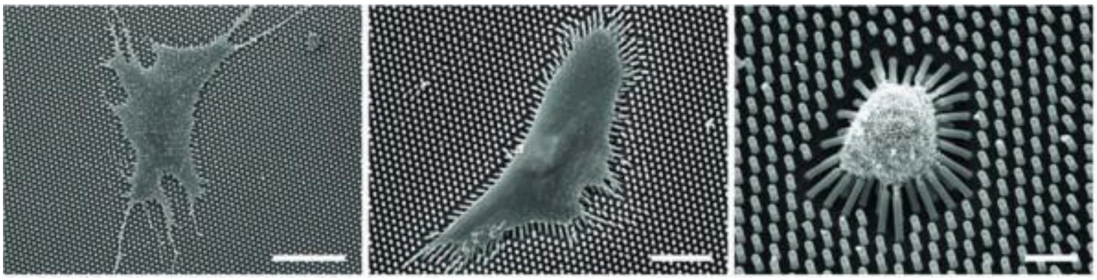

Figure 1.2 - SEM of hMSCs seeded on PDMS micropillar arrays of varying heights. The cells bind to and deform the pillars to varying degrees. As the aspect ratio increases (left to right, 0.53, 3.2 and 7 to 1 respectively) the cell bends the pillar more, greatly influencing their morphology. Scale bar Figure taken from reference[38]. Scale bars 50, 30 and 10μm respectively. Images replicated with permission from the copyright holder.

These PDMS and elastomeric pillars are fabricated using a process called soft lithography[41]. A UV or thermally curable elastomer is poured into a negative relief mould of the desired pattern, subjected to pressure and a temperature bake or ultraviolet (UV) exposure, and then demoulded. The mould is fabricated using micro and nanofabrication techniques to achieve the high aspect ratio, sub-millimetre feature sizes. With the ability to replicate features that require lengthy nanofabrication comes an increase in throughput. A mould can take weeks to fabricate, whilst tens of elastomer replicates can be made in a day.

This process lends itself well to smaller scale studies that focus particularly on the analysis of single-cell responses. This replication process also takes hours, and nanofabricated moulds are expensive to produce. Add to this that the resulting pillar arrays can be prone to capillary collapse[42, 43], and an avenue for rapid throughput fabrication held great appeal. Upscaling the availability of these substrates would allow for the incorporation of wider scale studies, making more rapid tuning of nanofeatures and prototyping of pillar arrays a viable addition to the process.

1.3 Fabrication by injection moulding.

Injection moulding of thermoplastic polymers offers a viable alternative to the soft lithography process. A high throughput industrial process for fabrication of plastic parts, it has been documented as having the capability of producing thermoplastic devices, termed parts or replicates, with nanometre scale resolution replicating accurately collagen fibres[44-47], and is used in industry to fabricate blu-ray discs with regularity in nanoscale patterns[48]. Note: a part typically refers to either a generation of moulded products or the generalised product, whilst replicates denote products made from the same mould.

The high throughput nature of the technology lies in the separation of mould and polymer melt **(Figure 1.3)** which allows for the maintenance of a molten thermoplastic and a temperature controlled mould. The thermoplastic is heated past its glass transition temperature, $\mathbf{T_g}$, where it softens and begins to behave as a viscous fluid, allowing it to fill the mould. This process is automated, and so can produce moulded products in minute timescales, in contrast to the tens per day of soft lithography. The main limiting factors in throughput are sample size and the injected polymer cooling time required. Injection moulding also has two other benefits – two of the most readily available and widely used thermoplastics, polystyrene and polycarbonate, are bio-inert and biocompatible.

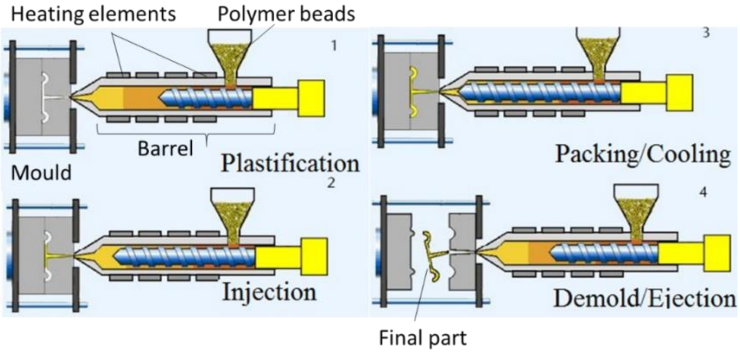

Figure 1.3 - 2D representation of the inside of an injection moulding machine. Indicating the separation of tool and barrel, and the distinction between barrel cavity and screw. The moulded part is identified, as well as moving and stationary platens and the ejection stage. Polymer beads are fed into the hopper and heated along the screw before being injected into the mould. A stage termed packing/holding adds pressure to fully fill the mould, before a period of cooling. Finally, the moving platen retreats and the part is either ejected with pins or removed by a robotic arm. Figure adapted from[49]. Image licensed under creative commons.

However, immediately a problem can be found in this approach. PDMS has a Young's modulus with stiffness typically of 2.5MPa, therefore using **(Equation 1.1)** pillars with low aspect-ratio, micro-scale feature sizes can easily replicate pillars with 1-10pN/nm spring constants flexible enough to be considered as 'soft' by a cell. Thermoplastics have Young's moduli in the range of GPa, 1000x stiffer. Therefore, the scale of the pillars must be reduced, and their aspect ratio increased in order to be viable for these kinds of cell-based experiments.

This approach has been used to create ultra high aspect ratio (UHAR) pillar arrays using hybrid polymer inlays in place of standard metal tooling**[50]** for injection moulding of polycarbonate**[51]**. 100nm diameter, 1000 – 2000nm height pillar arrays have been fabricated, as well as a continuous height gradient that caused spontaneous segmentation of mixed cells**[52]**. A hybrid inlay allows for a more restrained cooling cycle and, therefore, parts with nanoscale features that are less susceptible to thermal and mechanical part stress during production. Not only does it increase the throughput of production, the increase in number of replicates from a pillar mould drastically lowers the overall cost of the process.

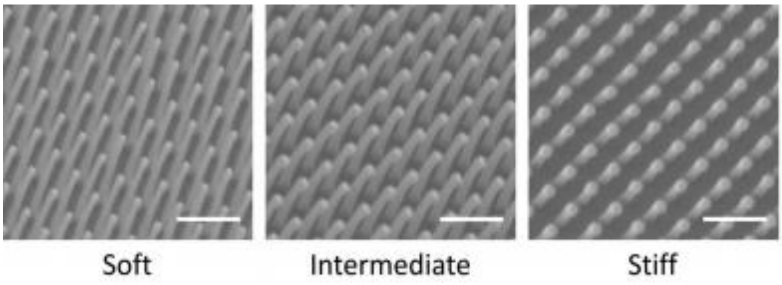

Figure 1.4 - SEM of injection moulded UHAR nanopillar arrays of different array mechanics. Demonstrating arrays with effective Young's moduli of 34.6, 242 and 2800kPa respectively. Image taken from[53]. Scale bar 1µm. Image licensed under creative commons.

This method of fabricating high aspect ratio pillar arrays, however, induces a deformation of the features from the original mould design. This has been exploited to create regular high aspect ratio arrays that exceed 10:1 aspect ratio, however what remains to be seen is the exact effect this will have on the pillar spring constants, and whether or not this stretching phenomena is a regular and manageable occurrence.

An added benefit of moving to nanoscale pillar features, is the formation of tightly packed arrays. These denser arrays have a higher chance of forming an apparently continuous surface for a cell to proliferate on, as the pillars formed are on a scale smaller than that of single-cell focal adhesions. Categorising these arrays as continuous will allow for comparison to experiments like that of Engler et al, where the Young's modulus of the environment can be mimicked. To do this, the array of pillars must be expressed in terms of a shear or Young's modulus also.

Rasmussen et al. **[53]** used this approach to mathematically derive an equivalent shear and Young's modulus for three pillar arrays of varying pillar spring constants, represented by a Young's moduli of 34.6, 242 and 2800kPa. They did this by assuming that an array of pillars acts, to a cell moving tangentially across them, as a group of discrete shear moduli. The sum of these shear moduli then equate to an overall, equivalent shear modulus. Taking an array of pillars and multiplying the spring constant **(Equation 1.1)** by a fill factor that is dependent on diameter and pitch:

$$f = \frac{\pi r^2}{p^2}$$ **Equation 1.2**

Where f is the fill factor, r is the pillar radius, and p is the array pitch, and combining it with the Poisson's ratio between a Young's modulus and a shear modulus for a bulk substrate:

$$G = \frac{E}{2(1+\nu)}$$ **Equation 1.3**

where ν is the Poisson's ratio. Combining equations **Equation 1.1**, **Equation 1.2**, **Equation 1.3,** yields a representative shear modulus for a pillar array:

$$\bar{G} = \frac{3}{16}\left(\frac{d}{l}\right)^2 fE$$ **Equation 1.4**

Where $\bar{G}$ is the effective shear modulus of the array of pillars, thus allowing for ease of comparison between a bulk substrate and a pillar array counterpart. In this manner, an array of injection moulded nanopillars with highly tuneable dimensions can be fabricated to test against a set of gel-based experiments. An additional benefit of injection moulding is that it allows for a much finer resolution of tip diameter and pitch. This opens up up a regime of study at a much smaller scale than any soft-lithography based technology can achieve.

It is worth considering the potential interactions of such small scale pillars and the cell membrane. As has been noted in the literature, bacteria have a tendency to either adhere to the gaps between pillars and proliferate**[54]**, or rupture due to their high aspect ratio and narrow profile**[55]**. A method of predicting the likelihood of a cell settling on a pillar array is developed in the literature, termed the Cell Interface with Nanostructure Arrays (CINA) model**[56]**, and provides a threshold of aspect ratio to array pitch above which cells are unlikely to proliferate on an array.

There do exist other methods of fabrication that reach this resolution in pillar array formation. For example, 3D printing using direct laser writing can create cylindrical, ordered pillar arrays, on similar scale to those of injection moulding**[57]**. However, as with soft lithography, the process is limited in its throughput, and therefore for the purposes of high volume studies, injection moulding remains the most efficient method of production.

1.4 High throughput biology analysis and nanopillar technology

The throughput of experiments define the potential scope of an experiment. Cell based investigations like those given in **Section 1.1** and **Section 1.2** have for the most part been somewhat limited in scope by the technology employed to generate substrates. Those that are created to test multiple nanotopographies lack reliable isolation of patterns of interest**[58, 59]**, and tend to be incompatible with standardised biology experiments, such as immunofluorescence microscopy or gene expression assays**[60, 61]**.

High content analysis for biology is defined by automation of both microscopy and quantitative image analysis. It is also complimented by biology techniques which require isolated substrates in order to ensure veracity of results. To this end, most of these techniques rely on multiwell plates, typically 96, to isolate individual test samples whilst allowing batch processing to prevent cross-talk between different cell substrates.

Whilst this has been done by combining hydrogels and a well-plate format[62, 63], there is yet to exist one that combines a fully customisable nanotopography/pillar array with a multiwell array – allowing for the expansion of pillar based analyses into the larger scope investigations in biology and machine learning.

The impetus for this lies in the vast application of a high throughput pillar based technology to biology. In excess of the myriad uses for studying and unpicking the relationship between cells and substrate mechanics, geometry, topography and available surface area, there are numerous cases in the literature that exhibit other interesting avenues of exploration.

Nanopillars have been shown to have the capacity for neuron pinning noninvasively, allowing the observation of the same neuron over an extended time period[64]. The nuclear and perinuclear mechanics of adherent cells have been investigated on nanopillar arrays with varying pitch and geometry[65, 66], and the behaviour of cancer cells on such samples promises avenues for capture and manipulation of circulating tumour cells[67]. Another use for nanopillar arrays has been in the guided growth of cardiomyocites[68]. These are just some of the pillar-based technologies that would benefit from the upscaling in volume of nanopillar arrays into a format that allows for this type of thorough investigation.

1.5 Summary and Aims

By combining high aspect ratio injection moulded nanopillars with a 96 well-plate format, it is hoped that a new, high throughput technology can be made available with nanometre scale control of surface topographies. This will allow:

- rapid prototyping of surface mechanics for different cell-based experimentation
- upscaling in quantity of production
- integration with existing analysis methods that require a high number of available substrates for experimentation.

Injection moulding is uniquely suited to the mass-production of combined multiwell pillar arrays, and the findings of this thesis will demonstrate the expansion of these processing techniques in scale – both in area coverage of the nanofeatures, and in volume of production.

The thesis will also demonstrate the flexibility of this process to encompass a wide range of nanofeatures, from very high aspect ratio nanopillars to some weird and wonderful accidental pillar formations, demonstrating the potential for the technology to be applied to a number of different fields outside that of biology.

As the injection moulding process makes use of the deformation of nanofeatures to larger aspect ratios, it will be important to investigate this stretching phenomena. The thesis will attempt to categorise the root causes of pillar stretching during injection moulding, and its effect on nanopillar spring constant calculations, as this will undoubtedly influence the calculation of array moduli. Lastly, it is important to push the boundaries of this fabrication approach to higher aspect ratios, whilst maintaining control over the nanofeatures created.

The aims of this thesis are:

1) Replicate high aspect ratio pillars through injection moulding over a sufficiently large area to fill a standardised 96-plate well, and fabricate multiple different array geometries for use in cell experimentation. By outlining the mechanisms of stretching, the variability of pillar deformation across a surface and across production, fabrication tolerance can be set.

2) Upscale the fabrication to microscope slide sized parts, with multiple pillar designs integrated into a single device.

3) Combine the slide sized parts with in-house fabricated multiwell plates in a production format, keeping within the high throughput nature of the technology used.

4) Investigate the effect stretching has on pillar profile and the effect this will have on the use of Euler-Bernoulli beam theory, outlining any useful relationships between pillar profile and bending mechanics therein.

5) Develop the nanofabrication process to increase the aspect ratio of nanopillars, and in light of the identified mechanisms of stretching, explore avenues of nanofabrication that can increase the precision of fabrication to suit.

In summary, what is presented is the integration of an existing method of high throughput fabrication of nanopillar arrays[50] with a standardised experimental device format. Unlike those presented in the literature[62], this will include high aspect-ratio features with much smaller dimension sizes, and the potential to expand both of these facets of the pillar arrays. The bending mechanics are interrogated, and a new amendment to the Euler-Bernoulli spring constant is derived, as well as the limitations of its application. Lastly, ICP etching is used to rapidly fabricate quartz pillars with nanometre scale precision in tip diameter, and sidewall angle – both important features in injection moulding replication.

1.6 Structure of this thesis.

This chapter has so far outlined the evolution of nanotechnology as a means of manipulating cell behaviour, some of the key findings and contributions to this area, the logical next step in the evolution of this process and the aims of this thesis.

What will follow are the methods used in attempting to fulfil these aims, and three experimentally focused chapters that break the text into the key areas of investigation. These are:

Chapter 2 – Methods. This chapter outlines the methods used in the various experimental chapters, highlighting novel contributions to any approaches taken from literature or previous work in-group.

Chapter 3 - Development of multiwell integrated UHAR arrays. This chapter details results of upscaling the surface area of pillar coverage, and the establishing of thermal modelling as a predictive tool for stretching behaviour and quality replication, as well as the identification of a critical facet in non-uniform stretching response of delicate nanofeatures. This chapter will also address the fabrication of microscope slide sized parts with multiple pillar array designs, the issues and solutions encountered, and the integration with well plate technology.

Chapter 4 – Analysis of pillar sidewall morphology: an amended spring constant. Chapter 4 describes the results of an examination of Euler-Bernoulli beam theory as it applies to pillar arrays. This includes probing the boundaries of what is acceptable in the approximation of a pillar to an idealised cylinder, and the derivation of an appropriate amendment to the Euler-Bernoulli cantilever case for pillars with non-linear sidewalls.

Chapter 5 – ICP deep silica etch optimisation: towards better replication accuracy. Development of an Inductively Coupled Plasma (ICP) reactive ion etching process for nm-scale control of rapid deep silica etching, to improve injection moulding replication accuracy and quality, and present a viable avenue for controlled fabrication of higher aspect ratio nanopillar devices.

Chapter 6 – Conclusions. A summary of the work presented in the text, highlighting the key findings and contributions to the relevant fields.

Chapter 7 – Appendices. Additional information for each chapter where required that was not included in the main text for brevity.

2.0 Methods

This project builds on previous work on the fabrication of high aspect ratio nanofeatures using injection moulding[50, 51] of ultra high aspect ratio (UHAR) pillar arrays. To achieve this, nanofabrication techniques are combined with standard injection moulding procedure to replicate nanofeatures in thermoplastic polymers, namely polycarbonate and polystyrene in 25mm x 25mm x 1mm square parts, the UHAR squares, and 30mm x 80mm x 1mm microscope slide sized parts, the UHAR slides.

The fabrication process can be distilled into three distinct parts, outlined in figure **number**:

1. Quartz imprint stamp fabrication – **Figure 2.1 a)**. An array of high aspect ratio nanopillars are fabricated in quartz silica with the intended pillar dimensions for experimentation. This process is outlined in section **2.1**, and developed in chapter **5.0.**

2. SU-8 / Cirlex® hybrid inlay fabrication – **Figure 2.1 b)**. The quartz pillars are imprinted in SU-8 bonded to Cirlex® polyimide to form a negative of the array, creating a mould for injection moulding. This process is outlined in section **2.5**.

3. Injection moulding of polycarbonate replica parts – **Figure 2.1 c)**. Lastly, injection moulding is used to mass produce replicas of the quartz pillar array in polycarbonate. This final step is the main focus of chapter **3.0**.

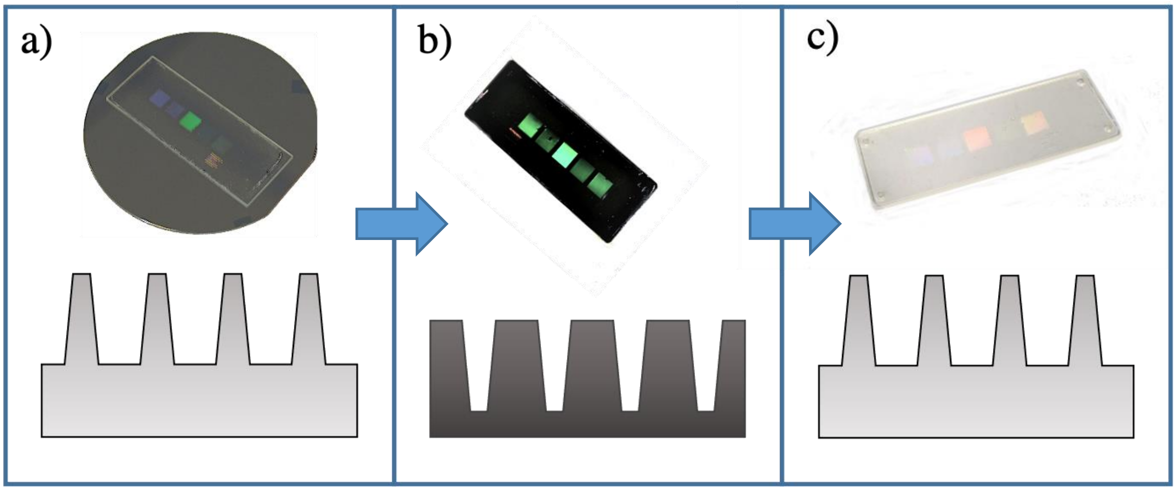

Figure 2.1 – Process of fabricating injection moulded replicates. a) quartz nanopillar arrays on a slide part and rendering of pillars, b) SU-8/Cirlex® hybrid array and rendering of imprinted pits, and c) injection moulded polycarbonate nanopillar arrays, and rendering of pillars. This outlines the process of taking quartz pillars and replicating them in polycarbonate.

In this way, precision high aspect ratio pillars can be fabricated in quartz using well documented nanofabrication techniques that are of interest to cell-based investigations.

2.1 Quartz stamp fabrication

The imprint stamps from which the nanopillars are replicated are fabricated from quartz using a combination of; electron beam lithography (EBL), metal deposition and lift-off, and RIE plasma etching **(Figure 2.2)**

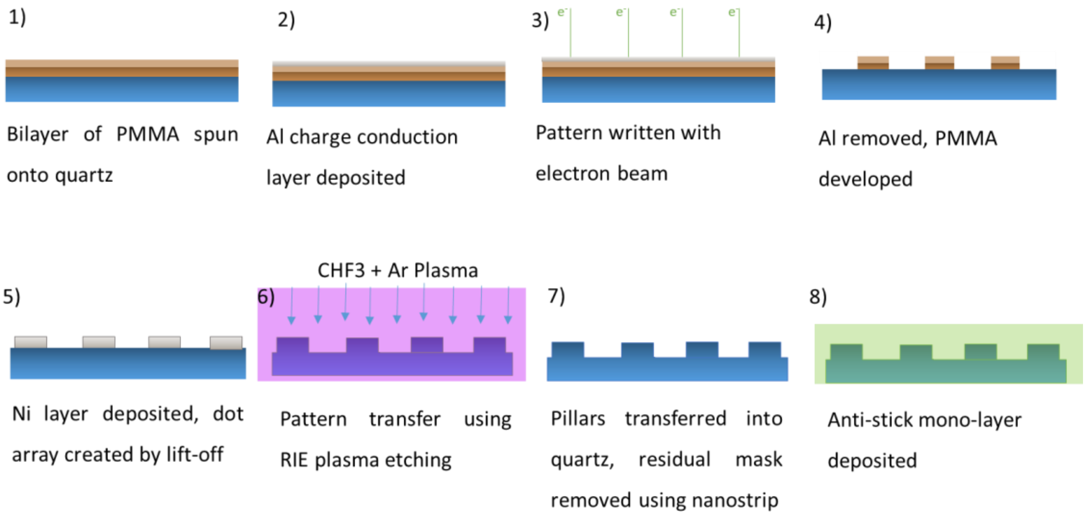

Figure 2.2 - Process of fabricating quartz imprint stamps. Fabrication process of quartz imprint stamp using standard nanofabrication techniques for high aspect ratio nanopillar arrays[51, 69].

A 25 x 25 x 1 mm quartz substrate was cleaned by sequentially immersing for 5 minutes in OptiClear^{TM} solvent and RO water to remove residual wax, then sequentially in acetone, methanol and isopropanol (IPA) in an ultrasonic bath to ensure a defect free surface. The cleaned substrate was then dehydrated for 1 hour in a 180°C oven.

A bilayer of polymethyl methacrylate (PMMA, AllResist AR-P.632-50k and AR-P.679-950k) is spun to sub-µm thickness **(Figure 2.2)** – step 1

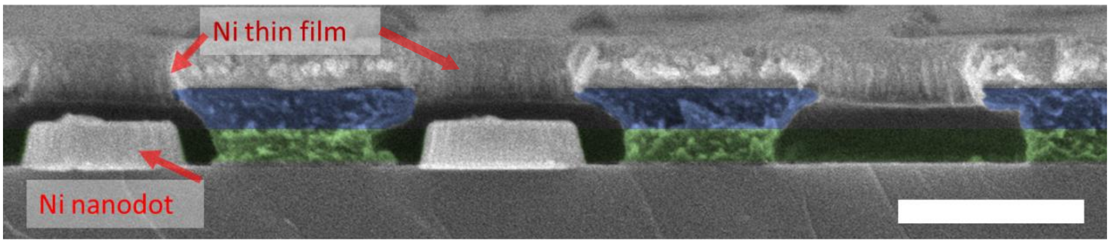

Figure 2.3 - cleaved SEM of an array of Ni nanodots with bilayer formation. Post Ni deposition but before lift-off, showing the overhang created by bilayer formation that makes it possible to create the isolated features. The two PMMA layers are indicated by the blue (high molecular weight) and green colours (low molecular weight). The Ni and quartz are highlighted by the change in contrast, the metal showing brighter in the image, as indicated by the red arrows. Note the sharp formation at the far left feature. Scale bar 100nm.

The PMMA bilayer consisting of different molecular weights is imperative to the successful creation of nanodot features. As outlined in **(**Figure 2.3) PMMA facilitates the generation of isolated features whilst preventing the metal film from becoming continuous. This is possible because of the rate at which the two layers develop.

The bottom layer, consisting of low molecular weight PMMA, develops faster causing the overhang seen in **(**Figure 2.3) Onto this, a 10nm film of Al is deposited as a charge conduction layer for the EBL thin film metal deposition tool (Plassys) – **step 2.**

An electron beam writer tool (Vistec VB6 UHR EWF) is used to generate arrays of nanodots using a multi-pixeling method **–** **step 3**, detailed in 2.8.1Circularity analysis using ImageJ. The Al is removed in a solution of Microposit CD-26 developer containing tetramethylammonium hydroxide for 2min, followed by thorough rinsing in RO water.

The sample is then developed in a **2.5 : 1** solution of IPA : methyl isobutyl ketone at 23°C for 1min, followed by a 30s IPA rinse and drying with N_2. To remove any residual PMMA from the bottom of the nanopit, the sample was plasma treated using a barrel-asher (PlasmaFab RF barrel, 30s, 80W O_2) **- step 4.**

The metal etch mask is created by depositing 30 – 100nm thick layer of Ni using the Plassys tool.For lift-off of the developed resist, the substrate is placed into a solution of n-methhyl-2-pyrrolidone (NMP)-based solvent (Microposit^{TM} remover 1165) at 50°C overnight. The NMP dissolves the resist, removes the attached Ni layer and leaves behind the nanodot array. The substrate is rinsed in RO water, and then plasma treated (150W O_2 plasma) for 5 min to remove residual PMMA **- step 5**.

Plasma etching was carried out using an Oxford RIE 80+ etching tool **– step 6**. (Etch rate of 33nm/min, mask selectivity Quartz:Ni, 30:1). **Section 2.4** and **chapter 5.0** have more details on the process. After etching, the residual metal mask is removed at 80°C using a composition of sulphuric acid and hydrogen peroxide with a stabilising agent (Nanostrip), and water. The sample is then thoroughly rinsed in RO water **- step 7**.

Finally, the quartz substrate is treated with an anti-stick coating to create a stamp. A trichloro(1H,1H,2H,2H-perfluorooctyl)silane monolayer is vapour deposited onto the substrate. To test for hydrophobicity, the stamp will have a completely dry surface after immersion in water.

2.2 Metrology – SEM conditions

Throughout the thesis, images taken by scanning electron microscopy (SEM) are used as the primary means of measuring nanopillar dimensions. Two scanning electron microscopes are used, the Nova^{TM} NanoSEM 630 from FEI, and the Hitatchi SU8240. Unless otherwise stated, images are taken on the FEI with working distance (distance of sample from aperture) of 5mm, tilt of 30^0, beam energy of 10kV in secondary electron (SE) mode. In order to prevent charging effects, a 3-5nm layer of sputtered AuPd was used to coat the quartz and polycarbonate substrates.

When it was necessary to allow the substrate features to be used in subsequent fabrication steps, the FEI was used with the Helix detector attached, and used to take rough measurements of the nanopillar dimensions without gold-palladium coating **(Figure 2.4)**. This is a lower resolution mode, however offers the benefits of not necessitating additional process steps to add/remove AuPd.

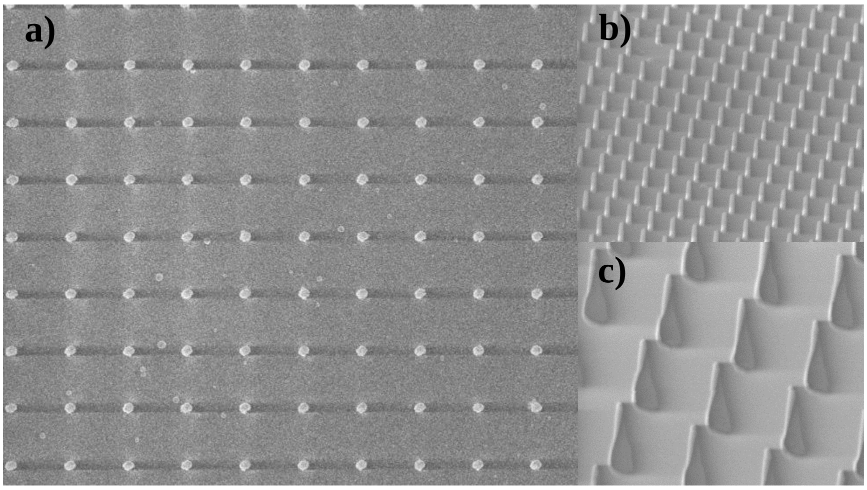

Figure 2.4 - SEM of nanodots and etched nanopillars taken using the Helix detector on the FEI. Note the slightly blurry quality caused by the charging effects present. Due to this fact, pixel-based analysis like those described in later sections are inaccurate, and therefore these measurements can be used as guidelines only. Scale bar 1μm.

By carefully choosing an appropriate magnification on the SEM, nm/pixel resolution can be maximised whilst illuminating clearly the boundary between feature and background. This, inevitably, invokes an error in the measurement, typically equivalent to 1 pixel, which will be commented on in the various results sections in this work. The minimum this pixel value can be is defined by the resolution of the microscope, which at 10kV is 1.1nm. This is exacerbated by the contrast ratio, which was automatically tuned for each set of images to minimise the number of nm represented by a pixel. This was necessary due to the use of a sputter coating, which varied in thickness between 3 and 5nm.

2.3 Electron beam lithography – multipixel methods

Traditional EBL techniques define a shape, beam size and beam current amplitude. For non-quadrilateral objects, this is problematic. Defining a circle in terms of a number of circular exposures leads to a staggered, almost serrated object. Making a continuous shape using a high resolution beam size for millions of features increases the process time extraordinarily. To create features that are smooth and circular in a short amount of time, the multipixel method was used. First developed and implemented by the Biomedical Interfaces at Glasgow (BIG) lab group at the University of Glasgow, the technique was modified to incorporate novel shapes to aid in the formation of smaller dots **(Figure 2.5**).

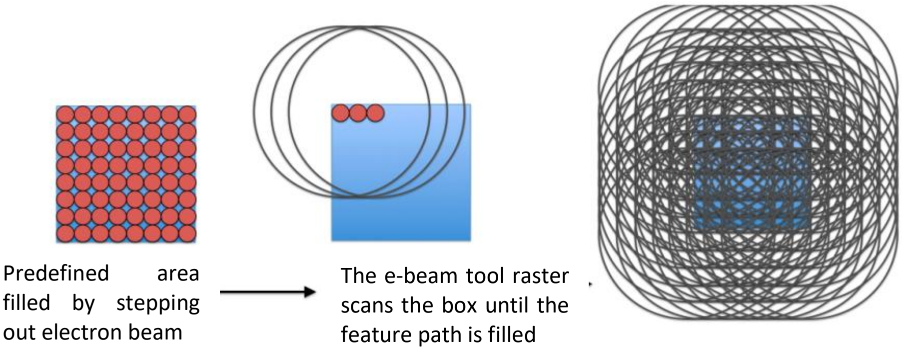

Figure 2.5 - Illustration of the principle of the multipixel method. By designating a shape with a minimal beam step size, multiple ‘pixels’ are generated. The same area is flooded with a large beam of electrons, creating radial scattering effect that causes a much larger feature to appear during development.

The multipixel method begins with a small principal shape (initially a box) to concentrate a large amount of energy in a small area. Because of the large saturation/charging effect, particularly on a quartz substrate, the principal shape can grow to many times its designed size. In addition, the radial nature of electron scattering causes developed features to steadily become more circular with increasing over-exposure of a region. **(Figure 2.5)** demonstrates the principle of the multipixel method.

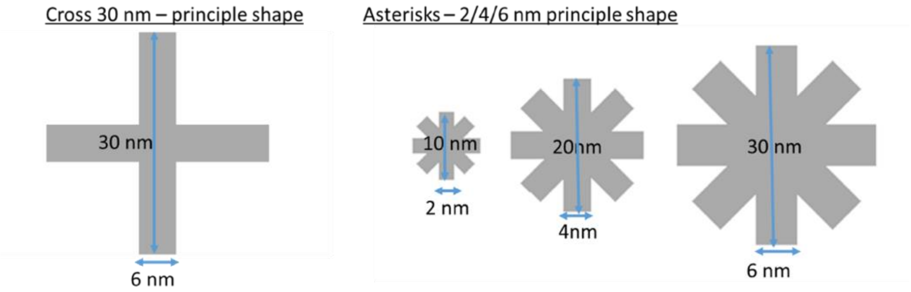

Figure 2.6 - Multipixel principal shapes. principal shapes developed to improve resolution and circularity of nanodots created. The more complex the shape, the more concentrated the highest dose is.

More complex principal shapes, like asterisks, allow for smaller dots to be fabricated by concentrating the electron exposure in the middle of the object. Then, extra exposure at the ends of the arms to bulk out the circularity of the feature. **(Figure 2.6)** illustrates the key principle shapes developed using the multi-pixel method. Optimisation of the principal shape, exact dose, beam current and size, and beam step size required to write nanodots of differing diameter and circularity was performed **(Appendix A).**

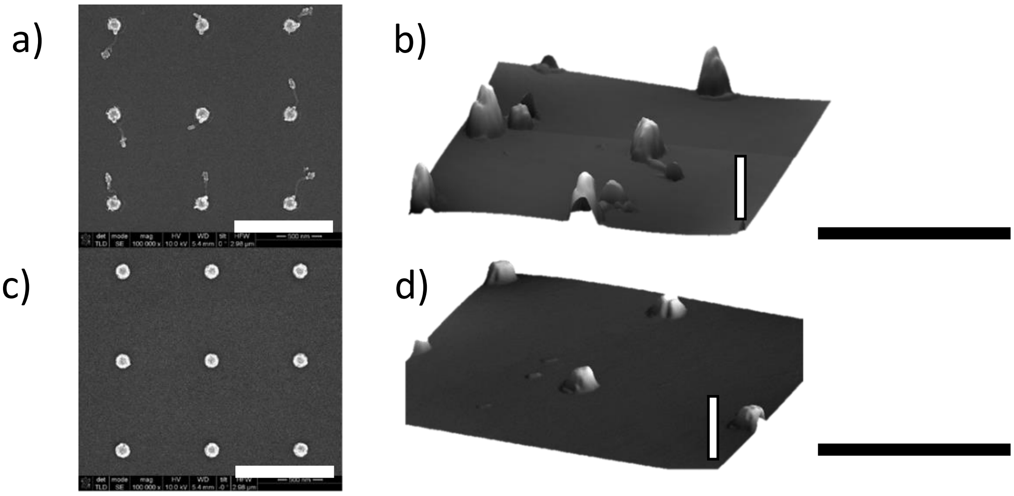

Figure 2.7 - Before and after plasma processing of nanodots. a) and c) SEM of tagging issue of Ni nanodots before and after an extra plasma ashing step was introduced, along with the move to an asterisk-like principal shape. b) and d) AFM scan renderings in 3D, to the same scale, of the same samples. Horizontal scale bar 300nm, vertical scale bar 200nm.

A common issue that appears when fabricating a metal etch mask is tagging, where circular features have irregular circumferences**.** Using square principal shapes for nanodots smaller than 120nm diameter exaggerated this issue. It arises because of two reasons: insufficient development / residual PMMA left on the nanodots, and an inadequate liftoff process **(Figure 2.7- a).** Changing solvent to NMP, undeveloped PMMA is thoroughly disolved. Any residual PMMA tags left on the dots after this can be removed by exposure to a high power O_2 plasma.

The use of a more concentrated dose in the centre of the nanofeature may also contribute to the tagging observed, with non-uniform edges being created by the different exposure pattern. However, this is refuted by the additional dose data displayed in **(Appendix A** which demonstrates the higher resolution and better circularity when using crosses and asterisks. As the dots are deliberately over-developed, any irregular edges will be smoothed. **(Figure 2.7)** illustrates quite clearly the improvements made to the individual nanodots because of these changes. By changing the principal shape and introducing a thorough plasma cleaning step, the large tags attached to the features are removed improving feature morphology. Ni tags adhered to residual PMMA from either of the aforementioned mechanisms is removed with it, thus increasing circularity.

2.4 Reactive Ion Etching

Reactive Ion Etching (RIE), is a method for pattern transfer and 3D feature creation in micro and nanofabrication. It utilises a chemically reactive plasma of radicals, electrons and ions to react and remove layers of a substrate on a molecular basis – selectively removing one material from exposed areas not covered by a masking material.

Precision at this stage determines the diameter, height and pitch of nanopillar arrays. As such, it is vital to control the RIE process as it influences the accuracy of the injection moulding process, the success or failure to imprint or injection mould nanopillars, and the degree to which the pillars stretch upon demoulding.

In this section RIE will be detailed as used with the RIE 80+ instrument from Oxford, whereas the new dry-etch process developed using inductively coupled plasma (ICP) etching will be outlined in **Chapter 5**.

(Figure 2.8) illustrates the RIE process using a CHF_3/Ar gas mixture as the main plasma components. An oscillating, radio frequency (RF) electromagnetic field is applied to ionise CHF_3 gas molecules and generate electrons and radicals that compose the plasma. The chemically reactive CHF_3 gas is often complimented by an inert gas (in this case argon) in order to control the rate of reaction, introduce a level of sputtering to aid anisotropy, and maintain a stable plasma through control of the plasma density.

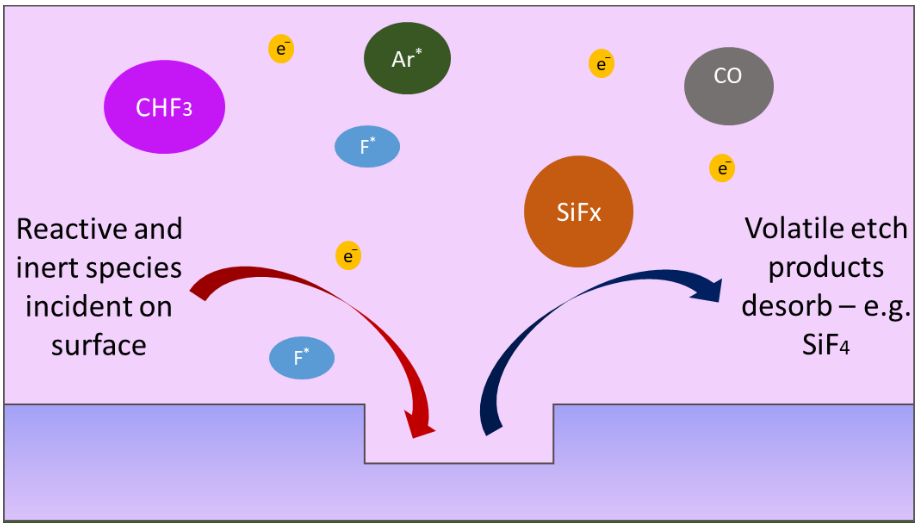

Figure 2.8 - Simplified diagram depicting the basics of the reactive ion etching. An ionised gas creates ions and radicals that interact chemically with an exposed surface in order to create volatile material. Etch masks are used to protect areas from etching and define substrate features.

Dry etching is superior to its counterpart, wet chemical etching, in that the control factors of the process allow for the optimisation of anisotropic processes of directional etching. It is in this way that free standing nanopillars can be created.

2.5 Fabrication of hybrid polymer inlays

Once the quartz substrate has been created, a negative relief can be made through thermal embossing and UV photolithography. **(Figure 2.9)** outlines this process, adapted from previous work**[50, 51]**.

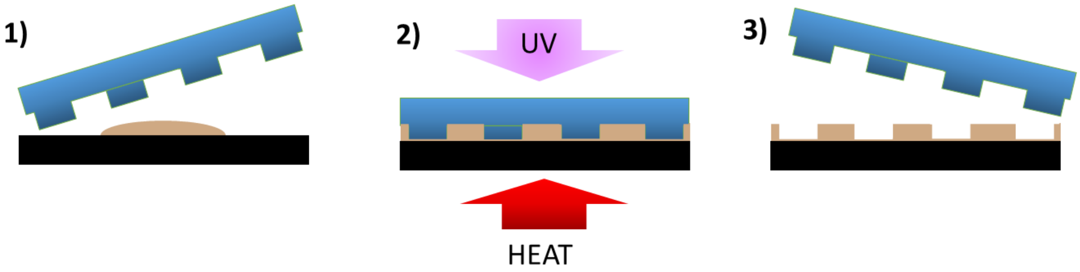

Figure 2.9 - Diagram of the creation of hybrid polymer inlays. indicating the three stages – stamping, exposure and separation. All of this is done under temperature to ensure proper cross linking of the SU-8 polymer, evaporation of the solvent and ease of demoulding to maintain stamp integrity and minimise shrinkage induced by thermal stress. Quartz substrate (blue), SU-8 (brown) and CIRLEX (black).

A precision CNC machined polyimide (CIRLEX®) was chosen as a support material due to its thermal resistance. Firstly, the machined polyimide substrate is cleaned in OptiClear solution to remove any dirt and oil from the surface. After rinsing in RO water, polyimide was exposed to an O_2 plasma, 150W for 5min, to increase surface roughness and to promote bonding to SU-8 3050.

A drop of the SU-8 3050 3 to 5mm in diameter is deposited onto polyimide (roughly 0.5ml). SU-8 was pre-baked for a minimum of 1hr at 95°C to evaporate solvent and remove microbubbles. The quartz stamp is then lowered at an angle to the SU-8 to reduce defects caused by trapped air. The SU-8 droplet is allowed to spread over the stamp at 95°C for 5min, with small pressure being applied at the edges of the stamp to remove bubbles and allowed to stand for a further 5min. The SU-8 is then illuminated with UV light (365nm, 3W) for 3min, after which the substrates are left to stand for 15min at 95°C to ensure full curing of the SU-8. This step was added to the methodology to preserve the imprinted features before quartz stamp demoulding. The quartz stamp is then cleaned in acetone in an ultrasonic bath, and the polyimide/SU-8 inlay is developed in EC-solvent and rinsed in IPA in 5min cycles. The imprinted SU-8 is reinforced with an additional baking for 1hr in 180°C.

Finally, the inlay must be coated with an anti-stick monolayer – **(Figure 2.2**, **step 8)**. In keeping with previous work, PECVD of silicon nitride was used to deposit a 10nm coating onto the polymer inlay to provide a surface for the monolayer to adhere to.

2.6 Injection moulding of thermoplastics

The machine used for mass replication of the quartz UHAR pillar stamps was a fully hydraulic injection moulding tool (Engel Victory 28, **Figure 2.10**). The injection moulding process ensures consistency between moulded parts and high fidelity manufacture of nanoscale features. The relative size of the machine, as well as its ability to have interchangeable mould cavities, allow it to produce parts of a range of sizes.

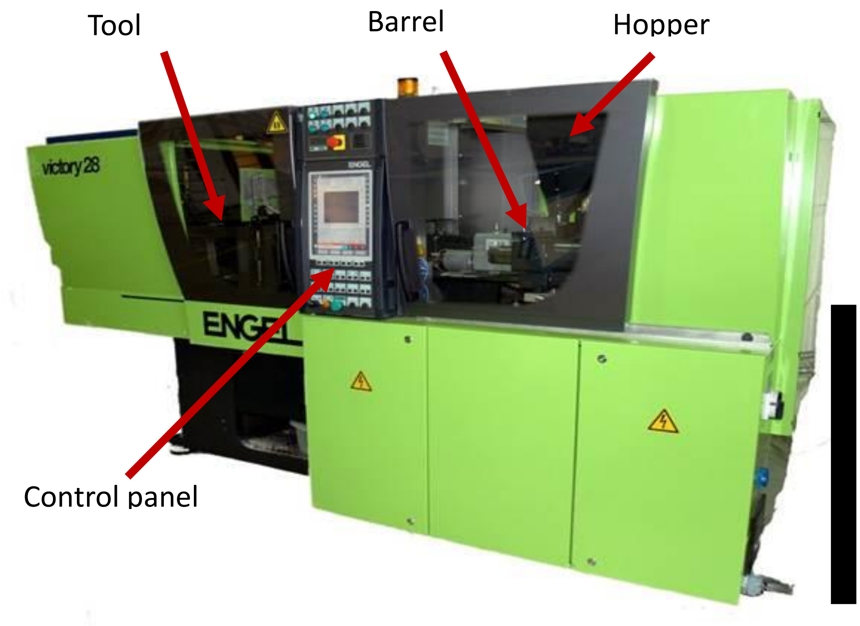

Figure 2.10 - Engel Victory injection moulding machine. Image of the Engel Victory injection moulding machine used in the fabrication of UHAR squares and slides. Scale bar 1m.

Two recipes were used for injection moulding of UHAR array parts, one for 25mm x 25mm x 1mm square polycarbonate parts, and another for the 75mm x 25mm microscope slide size parts. These are outlined in **Table 2.1**.

Part recipe	*Melt (°C)*	*Tool (°C)*	*Injection speed (cm^3s^{-1})*	*Holding pressure (bar)*	*Packing time (s)*	*Cooling time (s)*	*Retraction method*
Square	280	80	50	1000	6s	20s	continuous
Slide	280	80	50	1000-1500	8s	25s	staggered

Table 2.1 - Injection moulding recipes for the UHAR square and UHAR slide parts - used for the fabrication of polycarbonate devices. The individual parameters are: the temperature at which the polymer is held in the nozzle (melt temperature), the temperature at which the mould inlay is held (tool temperature), the speed at which molten polymer is injected into the mould (injection speed), the pressure at which the polymer is held in the mould for a period of time to allow proper filling (holding pressure/packing time respectively), and the time allowed for part cooling. The retraction method denotes the approach to separation of part and mould using the moving platen of the tool. continuous denotes one smooth movement, whilst staggered has an initial pause for 5 seconds before a slower retraction to prevent any additional stress occurring in the moulded part.

2.7 Ultrasonic Welding

The need for integration of the fabricated polycarbonate pillar arrays to a 24-well plate requires a process that will not hamper the overall throughput of device fabrication. It therefore needs speed, efficiency and most importantly cannot introduce additional material that could be harmful to cell culture. Ultrasonic welding is well suited to this need. This process of welding can be used to bond two thermoplastic materials together by causing the melting of a pre-designed joint using ultrasonic energy focused into a material.

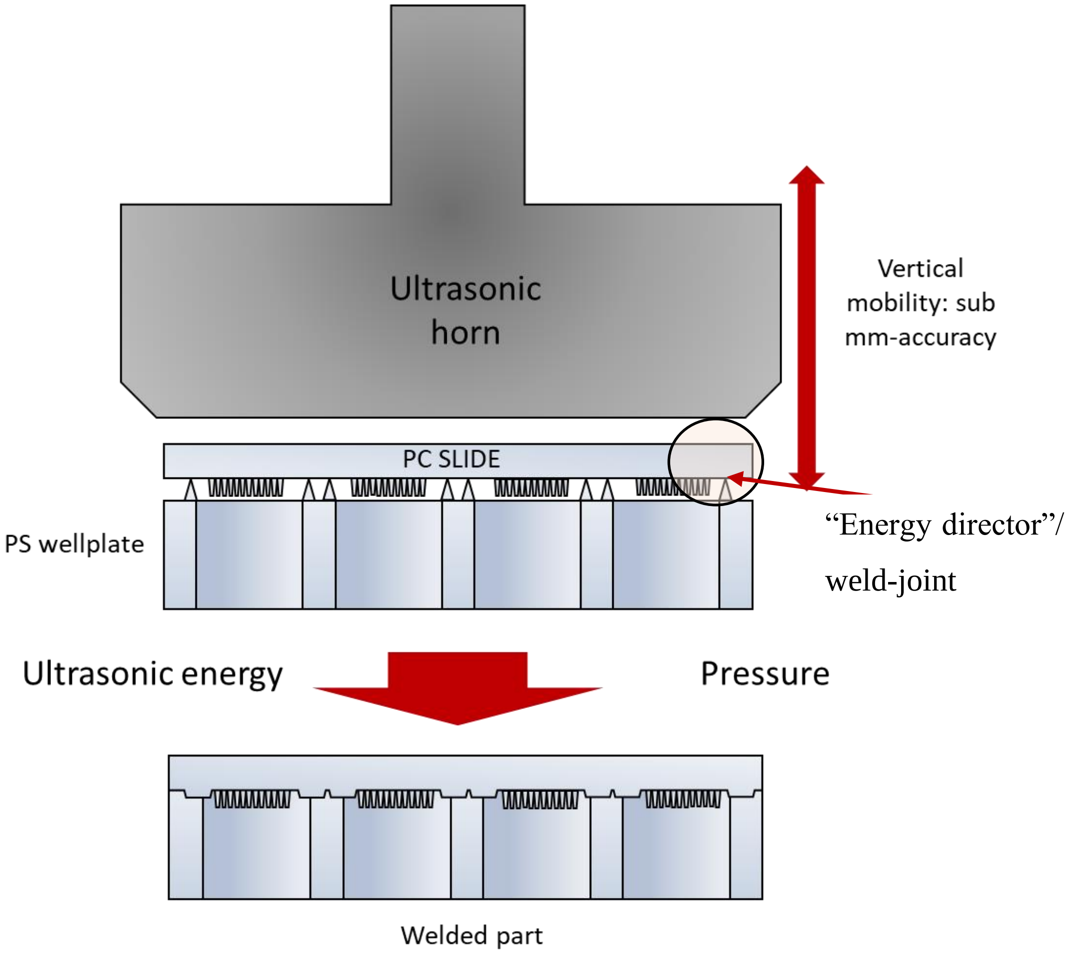

Figure 2.11 - Ultrasonic welding of thermoplastics to create isolated UHAR arrays in a multiwell format. A basic depiction of the ultrasonic welding process, where two parts to be joined are placed in contact. The ultrasonic horn then applies pressure and delivers energy to the substrate to cause welding by collapsing protruding features of the well-plate and melting them into the slide.

A Rinco Ultrasonics Standard 3000 ultrasonic welding machine was used to bond UHAR samples onto in-house fabricated 24-well plates[70]. **(Figure 2.11)** outlines the basic operation of the machine, as well as a diagram of the weld seam. Whilst this process is not automated, as with injection moulding, it is highly efficient and can produce up to 10 welded parts per minute.

Table 2.2 below outlines the basic parameters used for this process in travel differential mode, whereby the machine is set to apply energy until the contacted slide has moved a specified distance, indicating the presence of a weld.

Parameter	Setting
Throttle	5.0
Amplitude	80%
Gain	21μm
Trigger	1.0
Welding travel	250μm
Hold time	1500ms

Table 2.2 – Settings for ultrasonically welding UHAR pillar array injection moulded parts to 24-well multiwell plates.

2.8 Analysis of pillars using software

The qualitative assessment of fabricated parts is essential for process optimisation, batch identification, tolerance predictions and, the proper assessment of the mechanical properties of fabricated nanopillar arrays. In this section the main methods of analysis will be detailed. Namely:

- image-based analysis of the circularity of features to identify dose values for EBL and success rates of nanopillar replication
- image-based analysis combined with modelling to identify the profile of stretched pillars and fit Bézier polynomials for use in spring constant calculations
- Finite Element Analysis (FEA) to identify the areas of high-quality replication of nanofeatures, and to validate the calculation of the spring constant of nanopillars with non-linear cross sections.

It quickly became apparent that automation of this process using software such as ImageJ and scripts on Matlab was necessary in order to deal with the sheer volume of pillars to be imaged. Over the course of this thesis, millions of nanopillars were measured for their circularity, five diameters and height, therefore for optimum batch categorisation Matlab scripts were employed: **section 2.8.2.**

2.8.1 Circularity analysis using ImageJ

Analysis of top-down SEM of nanopillars can yield information on the success of fabrication at the metal mask fabrication and injection moulding stages.

$$circularity = 4\pi \frac{area}{perimeter^2}$$

Equation 2.1

An ideal surface, i.e. one that is not deformed by shrinkage and warpage from residual injection moulding stresses, will provide a flat surface for imaging. Injection moulded pillars, therefore, will be perpendicular to said surface, appearing circular from the top. As a pillar leans more towards collapse, i.e. being totally parallel to the surface, the circularity will move from 1, and ideal circle, and approach 0, a straight line.

The ImageJ software can be used to detect the boundaries of objects, such as pillars, due to the contrast between the pillar and the background. Characteristics of individual pillars, such as the circularity, can be measured from identified objects automatically. These can then be collated into average measurements with a standard deviation assigned to each image. This process is outlined in **(Figure 2.12)**.

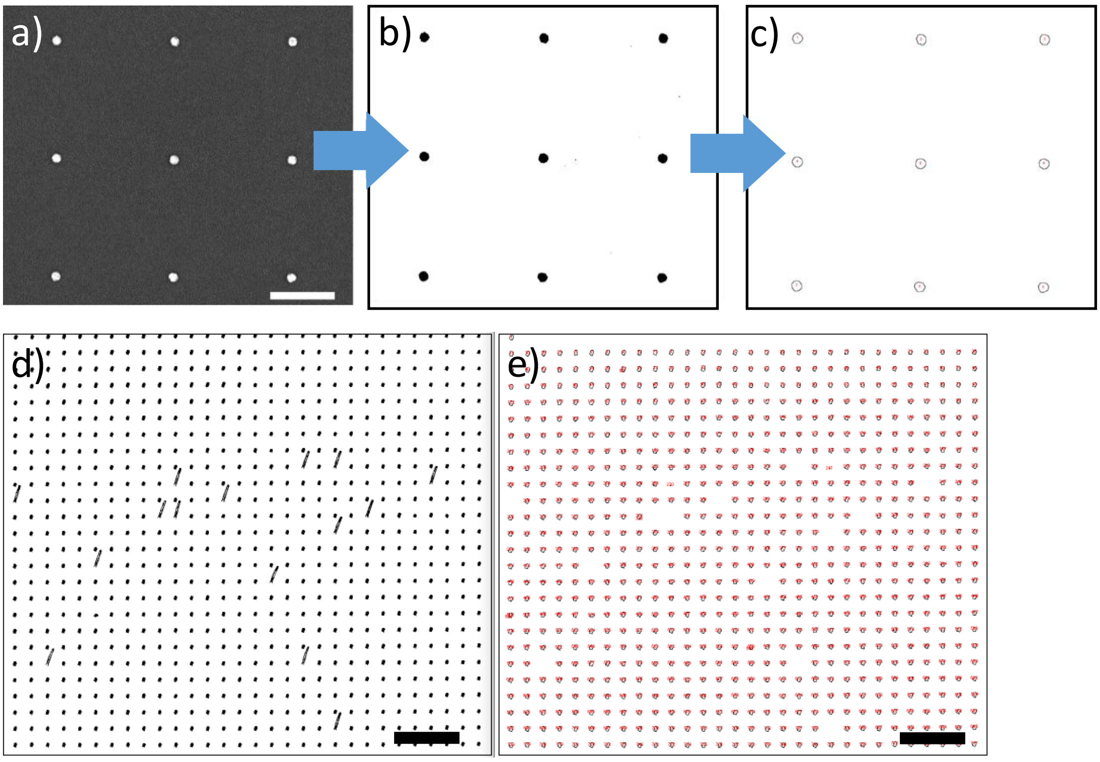

Figure 2.12 - Circularity analysis of nanofeatures – defining successful fabrication. a) -c) process of taking SEM of Ni nanodots, thresholding them and then identifying objects to be analysed in ImageJ - scale bar 300nm. d) and e), images of free-standing and collapsed pillars identified in a single image using ImageJ, by setting a circularity threshold, only standing pillars will be counted as measurable objects. Scale bar 2µm.

2.8.2 Measuring pillar dimensions using Matlab

Nanopillar mechanics are dependent heavily on their sidewall morphology (discussed in detail in **chapter 5**). It was, therefore, necessary to automate the measurement of pillar dimensions along their height. A Matlab script was written to convert SEM micrographs into binary images and extrapolate dimensions in an automated manner. **(Figure 2.13)** illustrates the process of automated profile extraction. Height data, an approximate diameter and height [d(h)] relationship, and five diameters spaced equally along the pillar height. It then takes median pillar measurements in the image to negate outliers and outputs these as the average pillar values for the image. By this method, the dimensions of nanopillars in an array can be approximated, including a standard error with a minimum of measurement error of 1 pixel which can, depending on magnification, equate to 5% of the feature being measured.

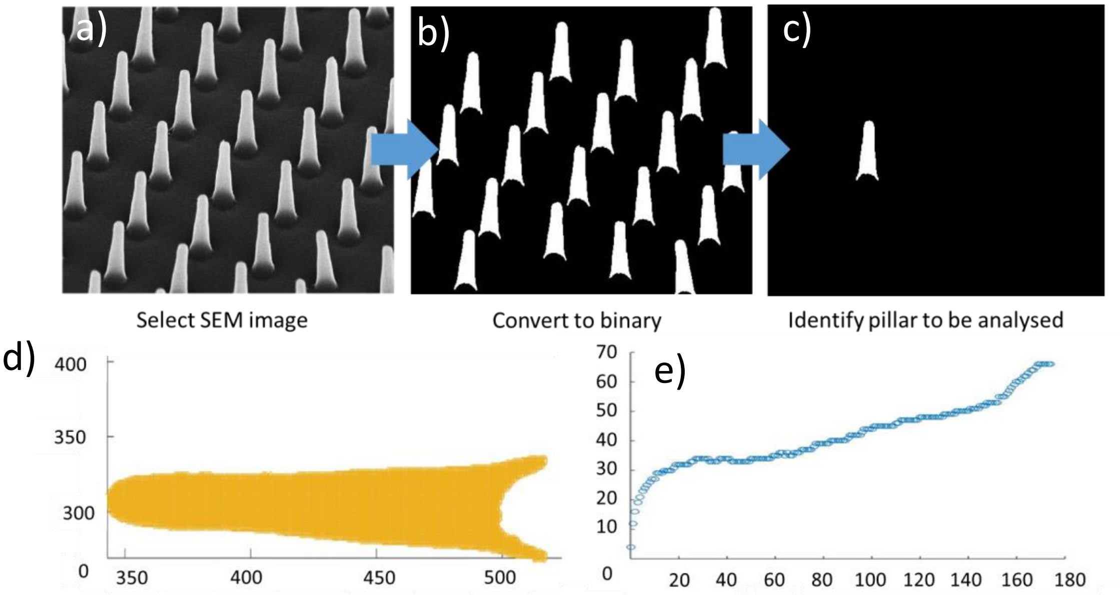

Select SEM image

Convert to binary

Identify pillar to be analysed

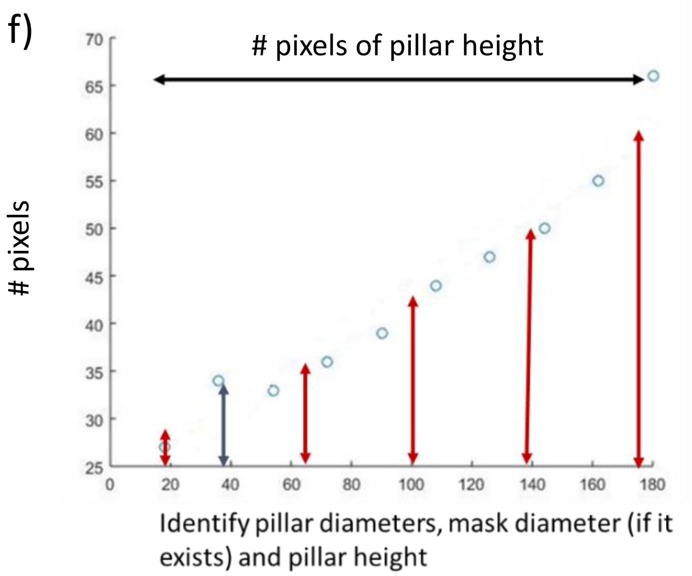

Identify pillar diameters, mask diameter (if it exists) and pillar height

Figure 2.13 - Process of automated single pillar dimension analysis. a), the initial SEM of PC pillars, through b) converting to binary, c) object identification and vertical pillar reorientation d) conversion to a pixel map. This is then converted into a measurement of pixels across at each height e), removing the need for a flattening step of the base, from which the final measurements are taken f) – five diameters (red), the mask diameter if it exists (blue) and the pillar height.

Note, as the pillars are imaged at an angle of 30° to the normal, **(Figure 2.13–a),** the final height is a multiple of the recorded height divided by the sine of the angle of measurement. Standardising the magnification allows for saving of individual scripts to improve efficiency.

2.8.3 Applying a Bézier curve

The nature of the d(h) relationship that the Matlab script identifies is important to determine the appropriate equation to be used in calculating the pillar spring constant. For linear and approximately linear sidewalls, a linear relationship can be used:

$$d(h) = (a*h) + d_T$$ **Equation 2.2**

where h is the height at which the measurement is taken, d_T is the tip diameter, and a is some constant. However, for non-linear d(h) relationships, a polynomic relationship must be approximated. For ease of calculation of the spring constant from a general formula, this was chosen to be represented as a Bézier polynomial of order n=2. To achieve this, the tip and base diameters are used to generate a range of Bézier curves using:

$$d(\xi) = (1-\xi)^2 P_0 + 2\xi(1-\xi)P_1 + \xi^2 P_2$$ **Equation 2.3**

Where P_0, P_1 and P_2 are three points defining the curve, and ($\xi = h - x$), x being some distance along the height of the curve. By varying P_1, different curves can be tested for their closeness to the d(h) relationship. The script then fits a curve that most closely represents the distribution of d(h) as measured by the initial program. This is used to determine the P_1 value, and therefore the curve describes the pillar profile (**Figure 2.14**). These two Matlab scripts allow for the swift analysis of thousands of pillars, generating an average pillar profile for each image. These can then be reanalysed using the second script again to generate a profile based on the average pillar for a group of images.

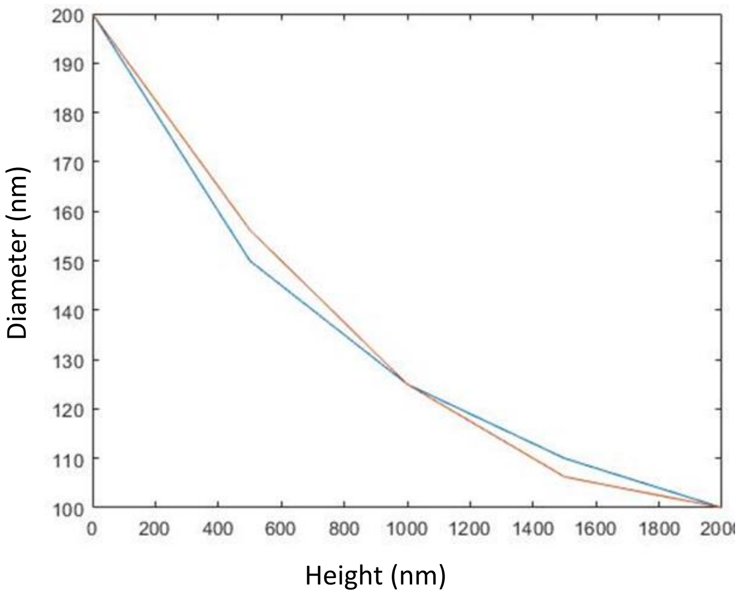

Figure 2.14 - Bézier approximation of the d(h) distribution of a pillar profile. Note – the approximation diverges in two key shoulder areas, however tests indicate that this deviation is negligible when used as a formula for spring constant calculation.

2.9 Finite element analysis

Finite element analysis is a numerical method used extensively and applied here, to predict the distribution of thermal stress caused by injection moulding and investigate the bending mechanics of cantilever-like beams. This technique allows a much larger and more complex problem to be broken down into a series of smaller, easily solvable simultaneous algebraic equations. Using COMSOL FEA software, a geometric entity is broken down into a mesh of finite geometric elements connected by nodes. These nodes make up these sets of simultaneous equations, and can be substituted and solved at speed to replace a set of partial differential equations. For example, those that describe how a rigid body responds to the application of stress, or how heat is transferred across a material boundary over time.

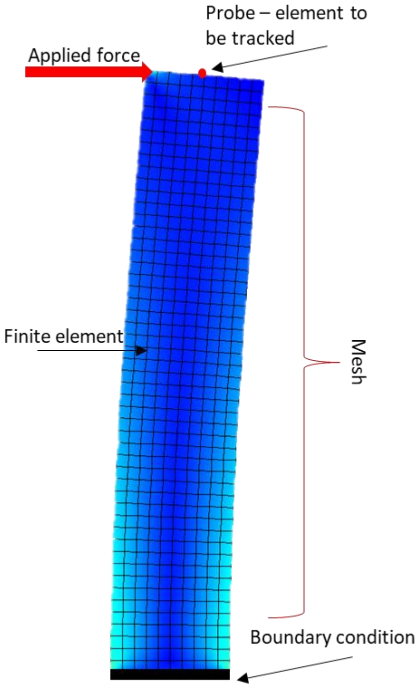

Figure 2.15 - Illustration of a finite element model from COMSOL. Identifying the area of applied force, individual finite element, location of probe, illustration of fixed base boundary condition, and stress distribution through the pillar, in this case highlighted by the changing blue colouring through the object.

Boundary conditions are then added to the model, such as material parameters or factors that limit the response of the model. The software can then determine how each node will respond relative to other nodes, and therefore the change induced in each element. (**Figure 2.15)** illustrates the meshing of a cantilever, and its deformation over an applied load. The boundary conditions limit any rotation or movement at the base of the cantilever, and by affixing probes in the model the relevant change, here displacement, can be monitored for different applied loads, material properties and boundary conditions. This approach is used as there is no empirical measuring approach for nanofeatures this small, and is well established in the literature**[38, 71]**.

3.0 Development of multiwell integrated UHAR arrays

There exists a unique opportunity to expand the scope of possible biological studies using substrates with mechanical properties set by pillar arrays. By combining existing fabrication methods with a standardised biological sample format, the well-plate, pillar arrays are made available to high content biology techniques. The use of injection moulding scales up the production of ultra-high aspect ratio (UHAR) nanopillar arrays. Combined with multiwell plates fabricated in-house, study of biological effects of UHAR nanopillars can be easily multiplexed using standard biological equipment. The resulting multiwell integrated device has been used in the publication of this process, and the resulting effects on MC3T3 pre-osteoblast cells[70].

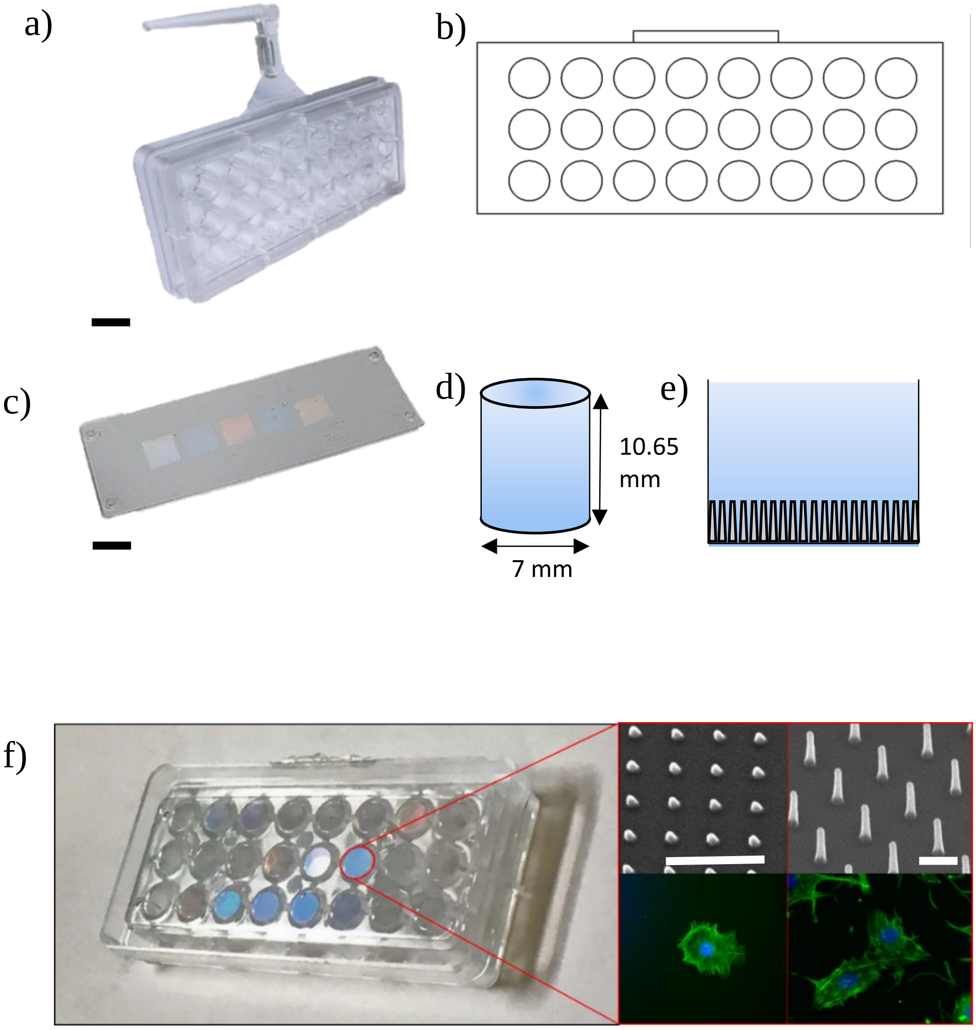

Figure 3.1 - Diagram of the components of multiwell integrated UHAR arrays. Images and diagrams of the multiwell plate and slide-polycarbonate part fabricated for this chapter. a) a photograph of the multiwell plate fabricated in house, scale bar 1cm b) a diagram of the layout of the 8x 3 wells c) photograph of the injection moulded multi-mechanical slide sample, scale bar 1cm d) and e) illustrations of the individual well and the containing nanopillar array respectively. f) Diagram of the final welded part, with examples of topographies used and fluorescence images of live cells seeded, adapted from[70], scale bars 1μm. Images licensed under creative commons.

In order to maximise the potential of this technology, UHAR pillar arrays must meet the following criteria:

1. The accuracy with which injection moulded pillars replicate their quartz master counterparts (termed replication accuracy) should be equivalent across a single. This is to ensure validity of any inferences made from experiments.

2. UHAR pillar arrays must have a measurable, and preferably predictable, part-to-part dimension tolerance in order for batch processing to be viable. Diameter, height, profile and percentage of pillars successfully fabricated in an array (replication success rate). This is doubly important when fabricating devices with multiple UHAR pillar array designs, to ensure uniformity.

3. UHAR devices must have the ability to be designed with arrays of different UHAR pillar designs. This is achieved following processes outlined in the **(Methods 2.1)**, either by changing the design of e-beam lithography and/or RIE recipes.

This chapter fulfils aims 1-4 of the thesis by demonstrating the following results:

- Fabrication of pillar arrays with surface area of > 100mm^2 coverage, increased from previously fabricated substrates of 4mm^2. The replication accuracy and replication success rate for a pillar array is linked to thermal stress along the part by the ejection mechanism present in the tool, and by general degradation of the mould inlay.

- FEA is used to identify areas of high thermal stress. By linking this to insights gained from changing replication accuracy across samples, it can be used to predict areas of quality nanopillar fabrication. This allows for more intelligent designing of mould inlays, and testing of new inlay materials, thermoplastics or tool designs.

- Finally, fabricated multi-mechanical UHAR pillar array devices are integrated with the multiwell plate using ultrasonic welding, with minimal damage to the UHAR nanopillars.

3.1 Upscaling UHAR array area

It is important to establish the maximum possible area of contiguous replication to ensure that the first criteria for UHAR, that replication accuracy is maintained across any given array, is met. This subsection details the investigation into the upscaling of the pillar area, and the measurements of part quality across injection moulding cycles. Measurements of replication quality are split into two categories – replication success and replication accuracy. Success in this case is defined as a freestanding replicated nanopillar, whereas accuracy is a measure of its dimensions compared to its quartz counterpart.

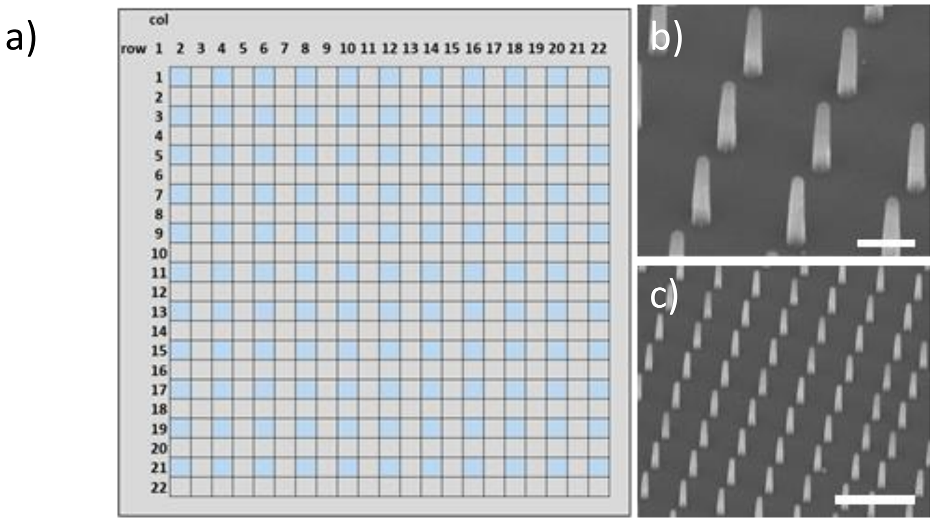

Figure 3.2 - layout of the 11 x 11 UHAR pillar array: 1mm2 UHAR pillar arrays used in the analysis of replication success across the 22mm x 22mm part arranged in a matrix to save time in fabrication and analysis, with SEM images of the quartz stamp pillars. Scale bars b) 0.5 and c) 2µm.

3.1.1 Replication success of UHAR pillar arrays over large areas

By using an 11 x 11 array of 1mm^2 pillars, 110nm diameter, 1.4µm height, 1µm pitch, the replication success across parts from the same batch of injection moulded samples is obtained by using the circularity analysis (**Methods 2.8.1**). These are discretised into 1mm x 1mm areas in 11 rows, and 11 columns, which give a clear and visual representation of the evolution of replication success over time **(Figure 3.2).** For brevity, all results are collapsed into the 11 x 11 array.

Here, I define two replication thresholds: adequacy and quality. Adequate replication is achieved when over 68% of nanopillar features are fabricated. Meanwhile, a limit of 78% of replication success indicates a quality area of replication **(Figure 3.3).** These limits were defined by the point at which the gross mechanical properties of the array begin to deteriorate from failed pillar replication, and are outlined in **Appendix B.1**).

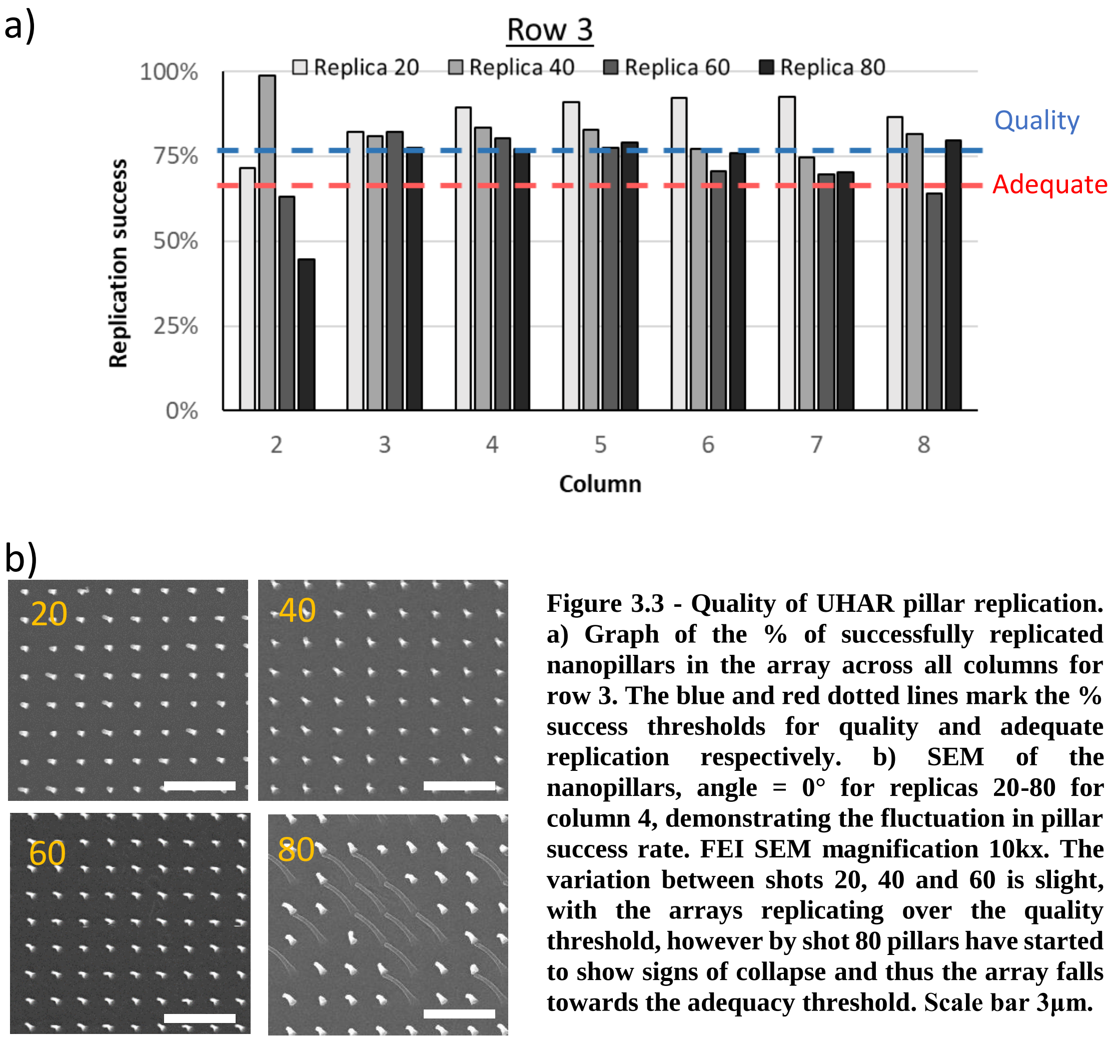

Figure 3.3 - Quality of UHAR pillar replication. a) Graph of the % of successfully replicated nanopillars in the array across all columns for row 3. The blue and red dotted lines mark the % success thresholds for quality and adequate replication respectively. b) SEM of the nanopillars, angle = 0° for replicas 20-80 for column 4, demonstrating the fluctuation in pillar success rate. FEI SEM magnification 10kx. The variation between shots 20, 40 and 60 is slight, with the arrays replicating over the quality threshold, however by shot 80 pillars have started to show signs of collapse and thus the array falls towards the adequacy threshold. Scale bar 3µm.

All array analysis is orientated in the same direction as this image, with row 1 closest to the sprue **(Figure 3.2-a),** and row 11 farthest, and indicates the vertical and lateral directions of the array. A colour heatmap to indicate replication success shows broad areas of successful pillar replication **(Figure 3.4-a).** The colour heatmaps show a bias of high replication success towards the sprue. This directionality (**Figure 3.4-a)** defines lateral and vertical directions) in the replication success and accuracy is repeated across several metrics, indicating that it is vertically orientated towards the sprue. The success rate is also laterally influenced, with pillar replication dropping off towards the edges of the part.

By superimposing the thresholds for replication adequacy and quality, I obtained the areas of replication success **(Figure 3.4-c and d).** Obtaining the intersection of these two areas provides the area of overlapping, high quality replication **(Figure 3.4-e and f).** An area is considered contiguous if it contains twice the number of successful arrays as unsuccessful ones. The analysis of replication accuracy across the pillar arrays is concentrated on this specific area.

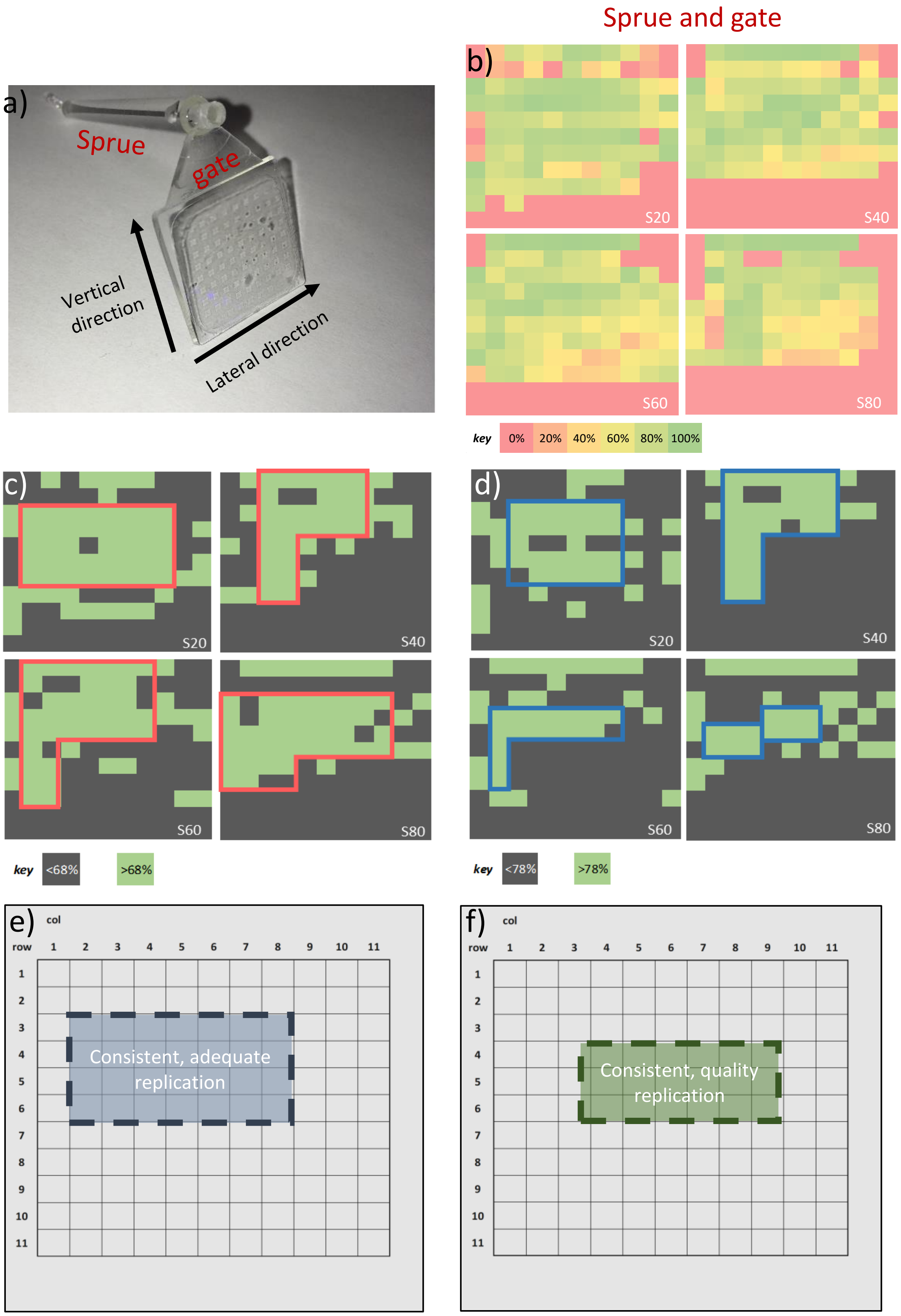

Figure 3.4 - Graphical representations of replication success across multiple samples. a) heatmaps of replicas 20-80 of the 11 x 11 array, with red demonstrating 0% of features are successfully replicated, moving towards dark green, 100% of features replicated successfully. b) is a photograph of the 11 x 11 array, illustrating the sprue end (red), around which image analysis is orientated. c) and d) are colour maps that denote areas above and below the thresholds for replication adequacy (red) and quality (blue) respectively. e) and f) The consistent areas of adequate and quality moulding are outlined in blue and green respectively.

3.1.2 Replication accuracy of UHAR arrays over quality replication area

With the areas of highest pillar replication success established, the effect of continued moulding on replication accuracy must be determined. It is important to investigate if this happens consistently across the substrate and across pillar dimensions **(Figure 3.5).**

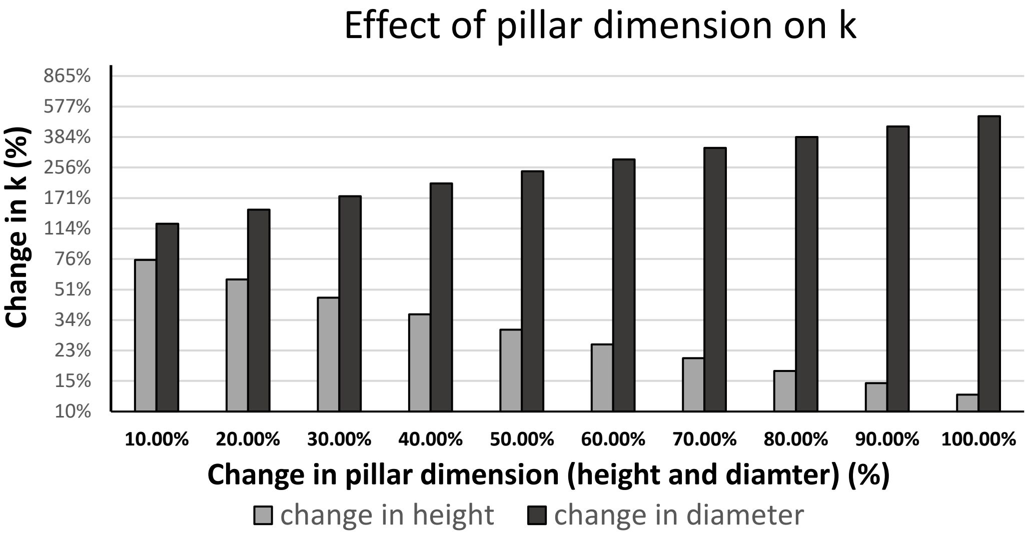

Figure 3.5 - Spring constant vs change in pillar dimension. Graph of the effect of changing diameter and height on the spring constant calculated from the Euler-Bernoulli equation for a 2µm tall, 100nm wide pillar. Changing pillar dimensions alter individual pillar spring constants, which we want to be continuous across the replicated array for a consistent mechanical surface.

From this figure, it becomes apparent that minute changes in diameter have an enormous effect on the bending mechanics of the pillar, **(Equation 1.1)**, and changes in the height of the pillar contribute to the change in relative spring constant. This means that for the first UHAR criteria to be met, the part-to-part tolerance in replication accuracy must be on the order of nanometres for pillar diameters, and in the 10’s or 100’s of nm for the pillar heights.

(Figure 3.5) illustrates the change in pillar morphology in discretised areas over 100 replications, and evidences the changes in replication equivalence over time as more moulded parts are fabricated from the same inlay. The diameter and height of these nanopillars, including those from the other columns that constitute the area of quality replication, were measured and the average spring constant used to determine the equivalent Young’s moduli of the discretised UHAR arrays. From **(Figure 3.6)**, it can be seen that the pillars maintain their profile, diameter and height to a greater degree across the production cycle the closer they are situated towards the sprue.

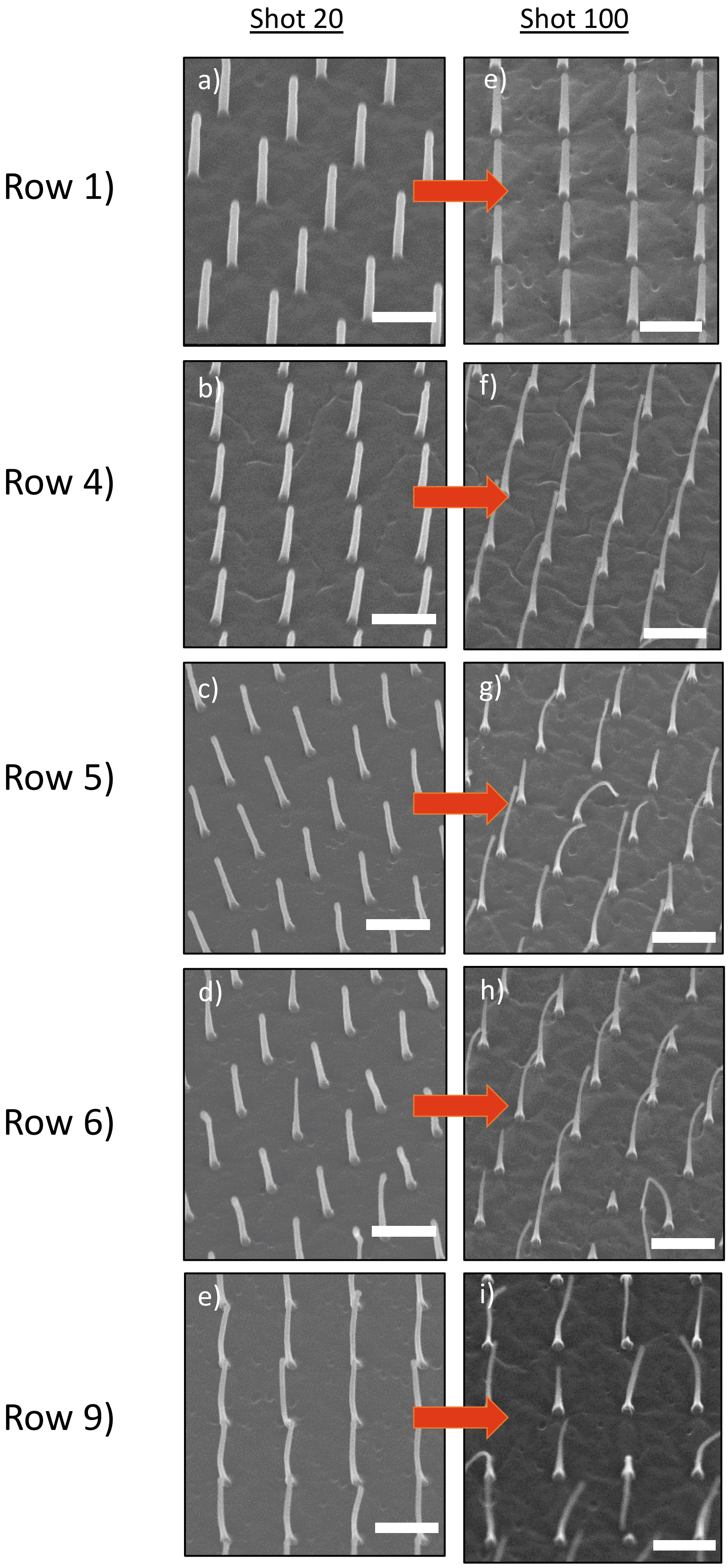

Figure 3.6 - Changes in pillar morphology over 100 moulded replicas. SEM of UHAR pillars from column 6, for rows 1, 4, 5, 6, and 9, a – i. Replica 20 (a-e), replica 100 (f-i). It can be seen that the nanopillars from replica 20 have a more stretched, thin morphology. R4-6 constitute the area of quality replication outlined in Figure 3.4. Scale bar 1µm.

Demonstrated in **(Figure 3.7)** are graphs of Ē vs replica # for each of the images shown. The consistent decrease in Ē affirms this stretching phenomena – as the pillars increase in height and decrease in diameter, the spring constant, and therefore effective Young's moduli, decrease. This effect was not replicated horizontally across the substrate, with columns in the same row maintaining a similar level of stretching. This lends weight to the hypothesis that the main cause of pillar stretching is vertically orientated towards the sprue. Therefore, there must be a mechanical force that is sprue-orientated that is driving this change across the sample - the tool ejection mechanism. Whilst this may not be of great concern to lower aspect ratio feature replication, it is imperative that in all future tool and part designs for UHAR devices account for this.

The tooling used has a single-pin ejection system, which may cause a non-uniform distribution of demoulding force across the part. This force would account for the increased deterioration in accuracy with increasing replications. Criteria 1 of this chapter stipulates that replication accuracy must be conserved across a continuous area, making this issue important to resolve. As the tool design for UHAR squares cannot be changed, it is helpful to determine the part-to-part batch groupings of these devices.

An argument could be made for the stretching phenomena to simply be the result of a degradation of the polymer mould, resulting in part filling over time and a thinning of the pillars. This was investigated in previous work**[51]**, and again in the course of this thesis, and this was found to occur at much greater replication numbers than are presented here. Measurements of the change in pillar height were taken for several samples that show a definitive change in pillar length relative to the sprue, indicating stretching as the primary phenomena. For rows closer to the sprue height increased by factor 1.2, whereas at the opposite end of the part, they almost double. This is backed up by the fact that changing the orientation of an inlay gives the same results, and that part filling is expected to be degenerative, causing entire pillar sites to become unusable.

When setting tolerance ranges between moulded parts of the same replication cycle, replication accuracy is more conveniently defined as pillars that are mechanically equivalent according to the Euler-Bernoulli beam theory and derived equivalent Young's moduli, Ē (referred to as replication equivalence). As the aim of these devices is for use in biological investigations that require a continuous mechanical surface, thresholds are set following those identified in the literature by Engler et al for neurogenic, myogenic and osteogenic lineage selection of naïve MSCs. Superimposing these onto the calculated Ē for the pillar arrays on the sample yields **(Figure 3.7)**

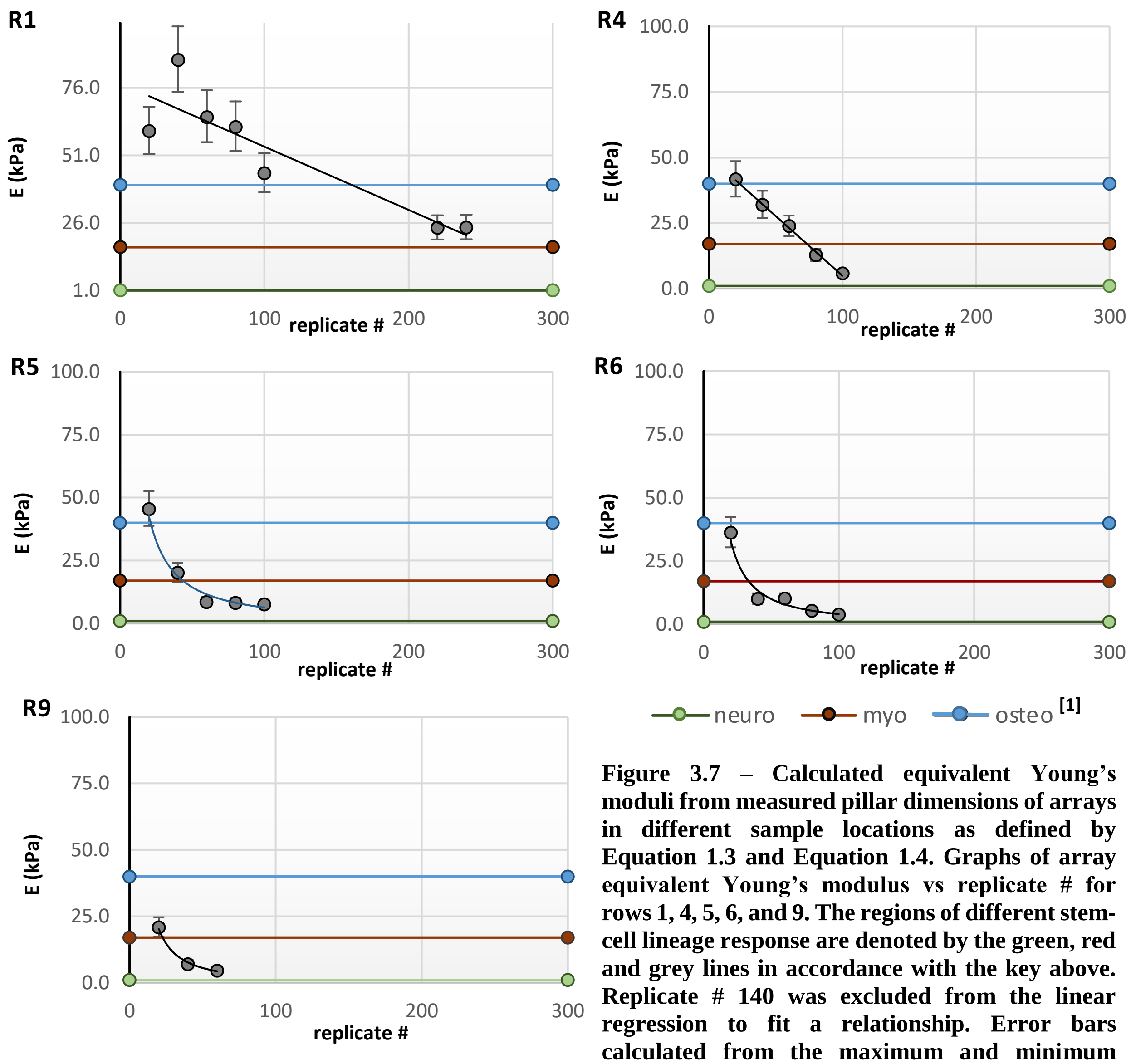

Figure 3.7 – Calculated equivalent Young's moduli from measured pillar dimensions of arrays in different sample locations as defined by Equation 1.3 and Equation 1.4. Graphs of array equivalent Young's modulus vs replicate # for rows 1, 4, 5, 6, and 9. The regions of different stem-cell lineage response are denoted by the green, red and grey lines in accordance with the key above. Replicate # 140 was excluded from the linear regression to fit a relationship. Error bars calculated from the maximum and minimum calculated spring constants inclusive of measurement errors.

These relationships also make clear the point at which pillars fail to replica for each row in this column, with replica #100 being the cut-off point for this. Evaluating this in terms of part-to-part tolerance, it would appear that replicas 1 – 40 offer a generation of nanopillar arrays with one series of mechanical properties. Replicas 40 – 100 form a split in the sample, with one section offering a more consistent area of osteogenic arrays, and one section fabricating an area that should stimulate a myogenic response.

These linear regression relationships allow for the array Ē to be calculated from initial measurements of pillar dimensions only, depending on their geographical location on the UHAR square sample. This cuts the time for quality analysis significantly. Combining these results with the quality replication areas identified allows for the creation of a predictive model of the Young's modulus from initial measurements of the pillar dimensions, combined with their position relative to the sample edge, and the sprue.

The area of quality replication is identified and the type of substrate mechanics most likely to fabricate well in this area for a UHAR square device can be illustrated for replicas 20-100 (**Figure 3.8**).

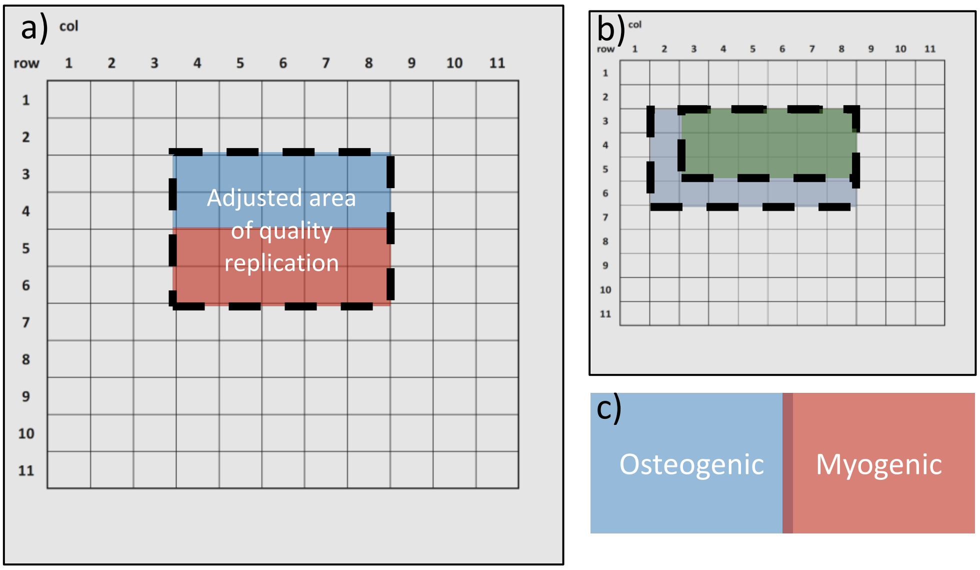

Figure 3.8 - Adjusted area of quality replication based on replication accuracy. a) adjusted area of quality replication for high rates of replication success and accuracy, depicting areas of osteogenic and myogenic pillar arrays as defined by substrate stiffness (1-17 kPa for myogenic, 18-40kPa for osteogenic) between replicas 40 and 100, with b) demonstrating the areas of adequate and quality replication success. c) colour table representing osteogenic and myogenic regions.

This revised area of quality replication has a surface coverage of 80mm^2 and, depending on the aim of the replication, pillar features will have mechanical properties that can be considered mechanically equivalent. In this case, that equates to 10-15kPa. This in itself poses as a multiplexed device of a single large area array, similar to those created by plasma polymerisation in the literature[52].

Applying thresholds of desired array parameters, such as topography or equivalent Young's moduli, devices with specific end-uses can be fabricated. For example, if a larger gradient of equivalent stiffness is desired, this can be achieved by introducing a gradient in diameter in a vertical or horizontal direction. Applying these findings, two sample series were created with a continuous array over the area of quality replication. One at 0.5µm pitch to scale up the previously designed nanopillars that were useful to literature, and one at 1µm pitch to create a softer array by having less surface coverage of pillars in the same area.

By setting Ē thresholds for osteogenic and myogenic responses, those with pitch and pillar dimensions that have been demonstrated to be obtainable over a large number of replicas, the replica arrays can be illustrated in terms of the expected stem cell response. These are the myogenic threshold ($1kPa < \bar{E}_{array} < 17kPa$), and the osteogenic threshold ($\bar{E}_{array} > 18kPa$).

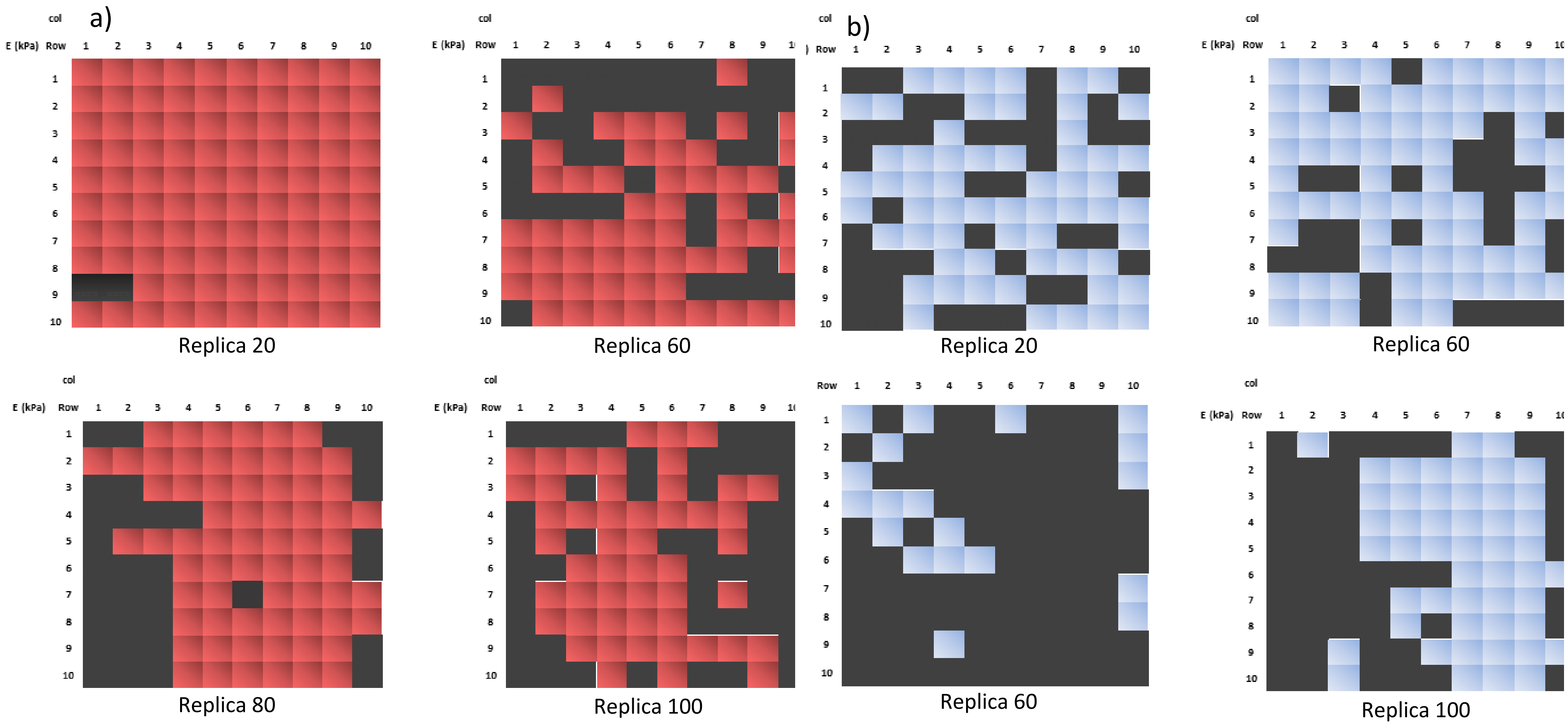

Replica 20

Replica 60

Replica 20

Replica 60

Replica 80

Replica 100

Replica 60

Replica 100

Figure 3.9 - Maps of continuous array samples, demonstrating myogenic and osteogenic responses based on array pitch. Red indicates the array sits within the myogenic threshold, blue osteogenic. a) are arrays fabricated at 1µm pitch b) 0.5µm.

Whilst replication quality begins to drop off over successive replicas, the areas that fall outside the desired osteogenic/myogenic thresholds still host nanopillars that are within +/-5 kPa of their target. This proves that injection moulding can fabricate a continuous area of nanopillars with mechanics < 20kPa. This is an overall reduction of the Young's modulus of polycarbonate by a factor of at least 115000x, the first pillar array of this kind that is comparable to such a soft hydrogel, with approximately 3.92×10^8 nanopillars sharing spring constants that are within tolerance.

In order to adapt this method for a variety of end-uses, these tolerance ranges must be adjusted to suit any novel nanofeature designs, for example elliptical pillars or pillars with varied pitch values. These will be high aspect ratio and face similar difficulties in fabricating large areas as have been outlined in this thesis, as the entire fabrication process is highly sensitive to changes in the nanofeature design. The presented areas of quality replication will allow for intelligent device planning, saving time and effort in any quality analysis. This is particularly true for the fabrication of largr diameter pillar arrays, which are useful for pillar-tracking to determine the forces a cell is exerting on its environment.

This subsection has outlined the steps taken to establishing large area arrays with continuous nanopillar replication accuracy, success and equivalence. An 11x11 array of small area pillars was used to establish a contiguous working area with high quality replication. The profile of these pillars was used to link the stretching of nanopillars to their location on the sample. This changes the pillar spring constants significantly, depending on the quartz pillar design. The non-uniform stretching across the sample was attributed to the single-point ejection mechanism of the injection moulding tooling.

Finally, large area UHAR pillar arrays were fabricated within the working area that yield continuous mechanical properties over 100 replication cycles. The area of quality replication was established, and in this area of quality replication UHAR pillar arrays were fabricated for myogenic and osteogenic stiffness.

3.2 Modelling thermal stress in injection moulded parts to predict quality UHAR pillar replication

The previous section demonstrated that replication success changes laterally with respect to the sprue across the moulded sample. This is independent of the change in replication accuracy demonstrated to be a result of a non-uniform ejection force. Custom designed tooling is ideal for proper ejection force distribution but cost prohibitive and time consuming. Injection moulding is used for its high throughput, reducing the overall cost of nanofabrication.

This subsection uses COMSOL FEA to determine the distribution of thermal stress through the moulded part during cooling in order to fulfil the second UHAR criteria: the ability to predict part-to-part tolerances as part of the process design for scaling the UHAR square process into microscope slide sized parts.

As the inlay is made of insulating polyimide, and the housing frame is made of thermally conducting steel, there will be a sharp change in material properties at the boundary between inlay, frame and thermoplastic polycarbonate. This will cause a high thermal gradient across the part, causing shrinkage and warpage due to residual stresses in the moulded part.

Whilst these can be reduced with proper injection moulding optimisation, there still exists a minimum level of part deformation obtainable due to the hybrid nature of the inlay. Categorising the temperature gradient across the part as it cools will indicate areas of thermal stress that cause part deformation.

This allows the thermal stress and the replication success to be quantifiably linked, which is useful for two reasons.

- It streamlines the design process and creates a tool for intelligent nanofabrication design that by identifying the areas that result in inconsistent replication.

- It allows for the materials used in the fabrication and moulding process to be changed in the model. This will allow the prediction of replication quality of nanofeatures when using alternative thermoplastics, or alternative inlay materials. By modelling different temperature conditions, the most likely optimal process can be determined, establishing a firm baseline for further experimentation and optimisation.

3.2.1 Thermal modelling of UHAR square parts

Firstly, UHAR squares with known replication success distributions are modelled using FEA. The models used moulding conditions of 80°C tool temperature and 280°C melt temperature. For ease of modelling the melt temperature was taken to be the initial temperature of the polycarbonate part, and the tooling and mould inlay are already in thermal equilibrium at 80°C, resulting in the following thermal distributions during part cooling **(Figure 3.10)**. The modelled polycarbonate part sits within a stainless-steel block, with the boundaries of the block held at a constant 80°C. The model has two meshing thresholds, with a maximum mesh at the edges of 0.01mm, and the maximum mesh towards the centre of the part at 0.1mm. The mechanical forces during cooling are inferred from the temperature distribution. As the tooling is custom made to the exact dimensions of the SU-8 inlay, the inlay interface is assumed not to slip.

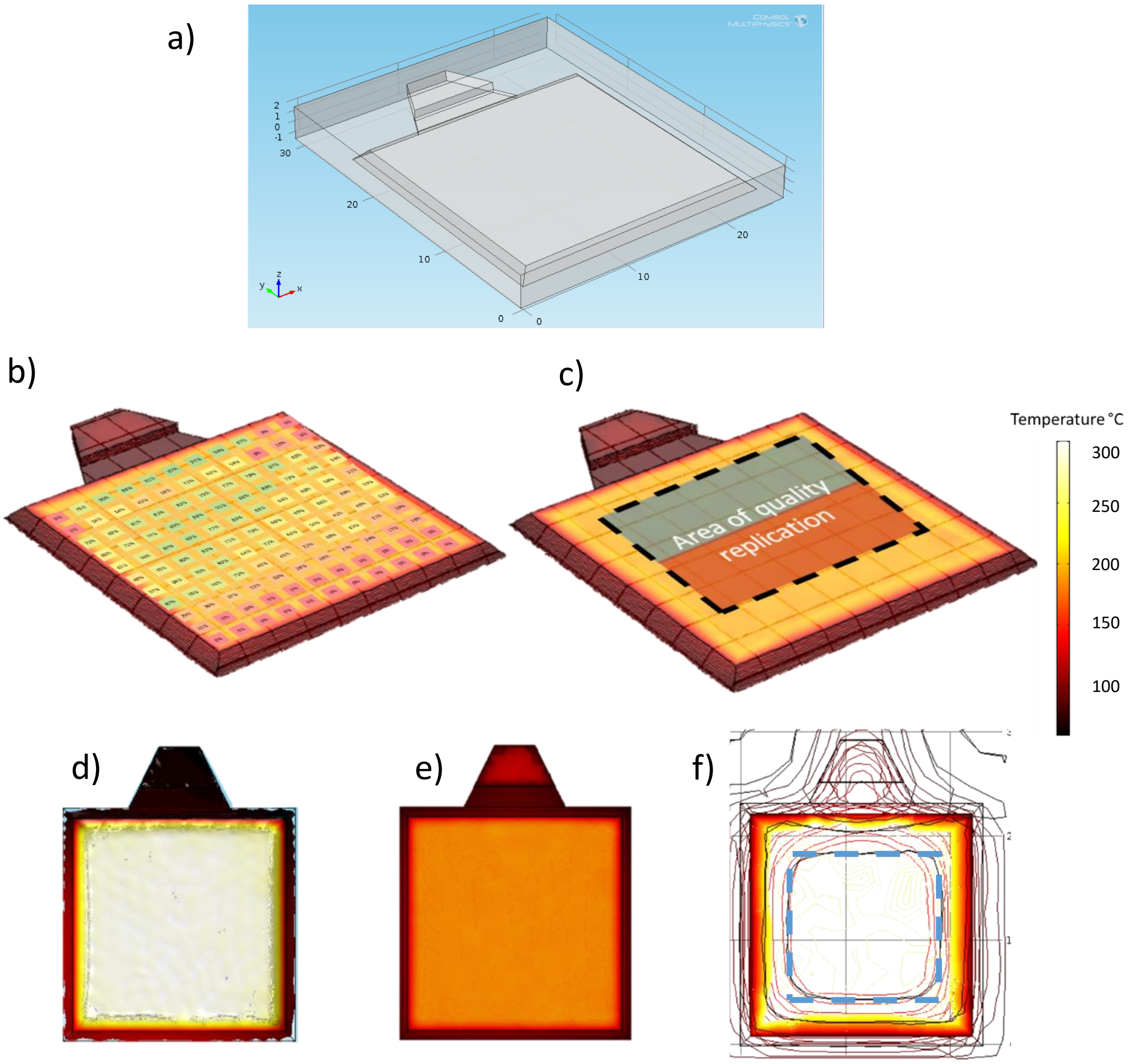

Figure 3.10 - Thermal stress distribution across a moulded part, visualised by temperature gradients. a) 3-D rendering of the model used. The temperature distribution after 1 second of cooling across the sample is presented overlaid with b) the average replication success rate map, c) the area of quality replication. d) Isothermal contour volume map demonstrating the areas of highest thermal stress, e) temperature distribution after 8 seconds, still demonstrating a thermal gradient across the sample, and f) 2-D isothermal contour map at 1 second, with the bounding box denoting clearly an area of least thermal stress.

Observing a slice from the 3-D model, there exists an area of regular temperature gradient in the centre of the sample **(Figure 3.10-e)** shifted upwards due to the presence of the injection site, as indicated by the blue box. Overlaying the quality replication area, these two maps match well and provide a more concrete picture of the effect of thermal stress across the part. The overall replication success rates also fit neatly into the isothermal contour map. When combined with insights gained from looking at temperature gradients through the middle of the sample from 2-D models **(Appendix B.2)** it also becomes apparent that the rate of cooling changes drastically through the middle of the sample resulting in a centre-orientated shrinkage that accelerates from the back face of the sample.

SEM and optical profilometry of a cleaved sample shows a bowing effect in both longitudinal and lateral cuts through the middle of the sample **(Figure 3.11)**.

This bowing effect is an exaggeration of the already induced warpage due to thermal stress, and will contribute strongly to the loss of replication success at the sample edges.

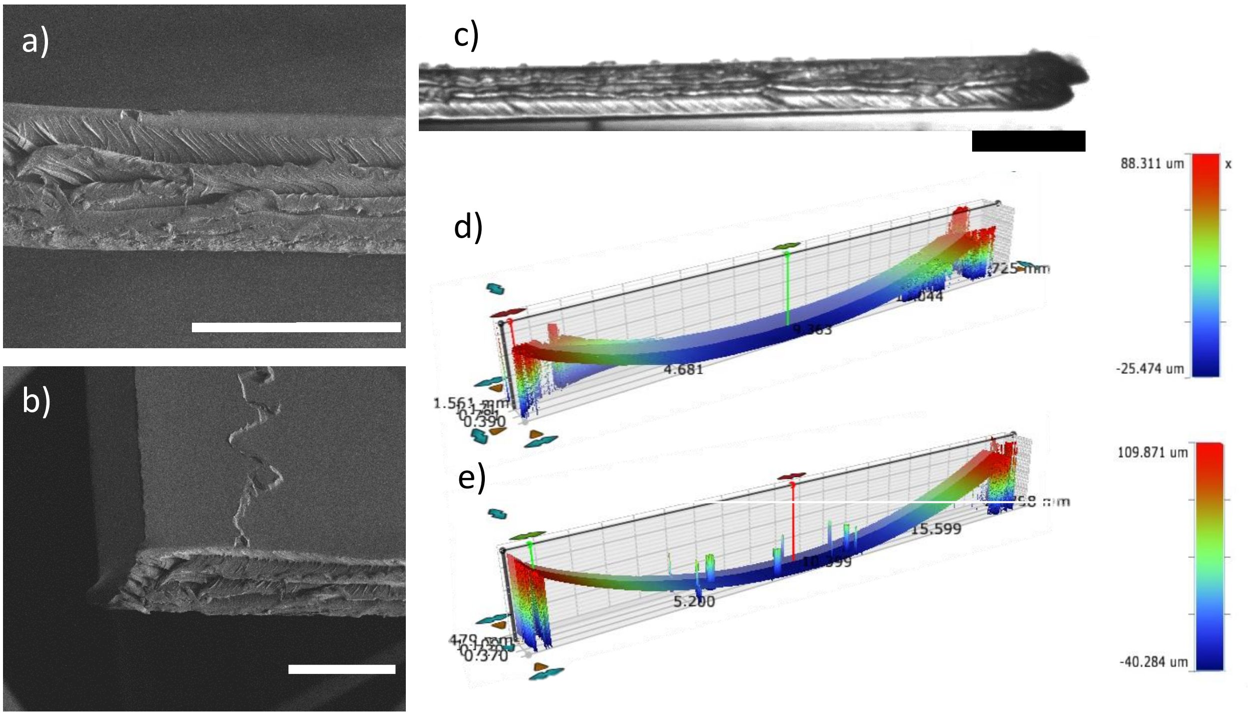

Figure 3.11 - Images of the warping of polycarbonate moulded parts due to residual stress from thermal gradients during cooling. Images depicting the warpage induced in moulded parts. a) and b) are SEM of cleaved samples demonstrating the change in part thickness across the middle of the sample, shown in larger scope by photograph c), with d) and e), optical profilometry renderings of lateral slices near the sprue and in the middle of the sample respectively, 3 and 12 mm from the sample edge. Scale bar 1mm.

The most important result from the optical profilometry was the change in bowing across the sample from the sprue-end to the middle. There is an increase is from 80µm from edge to centre for **(Figure 3.11–d)** and 160µm for **(Figure 3.11-e)**. The longitudinal slices of the same sample show no obvious signs of large warpage, which lends weight to the argument that two independent, sprue-orientated axis stresses exist on the sample that amplify the latent edge-effect caused by hybrid tooling. One from the change in cooling rate that arises because of the influence of the sprue, and one from the uneven distribution of demoulding forces.

What is also interesting is the existence of an apparent strata within the sample, most evident in **(Figure 3.11-c)**. These strata indicate the areas of high residual stress in the part. This area of rapid cooling matches the 2-D models very closely, indicating that the FEA model conditions, despite not accounting for mechanical forces of expansion and contraction, or additional stresses or changes in crystalline structure that may incur due to the change between glasss and molten states in the polycarbonate material, are accurate in their prediction of residual stresses in fabricated parts.

This modelling approach can be used to outline areas of minimal thermal stress that should have the best conditions to facilitate quality replication of high aspect ratio nanofeatures. These predictive quality replication areas account for all expected influences on the UHAR nanofeatures so long as the ejection force evenly distributed across the moulded part.

3.2.2 Thermal modelling of UHAR slide parts

As the ultimate aim of this chapter is to develop integrated multi-well UHAR slide devices, the next logical step is to run this experiment in reverse using the microscope slide sized parts. It is important to check the replication success and accuracy over a production cycle of a hundred parts or so of these designs, then finally fabricate high aspect ratio nanopillar arrays with surface areas and arrangement that will allow for an integration with this 24-well plate.

The initial takeaways from the temperature distribution maps **(Figure 3.12)** is the similarity to the edge effect of the small-tool parts. The shift from a square to a rectangular array begins to affect the distribution of thermal stress within the part, causing an increase in the density of isothermal contours in the corners of the sample which induces increased bowing at these edges. This makes the welding of the plates to the well-plate tricky in these areas.

(Figure 3.12-d) outlines the estimated area of quality replication overlaid onto the thermal stress map, again assuming linear/consistent ejection forces. The distance measurements were taken from 2-D models of the part in combination with the overall 3-D measurements.

This leaves an area for quality replication of roughly 18mm x 64mm in the centre of the sample. Taking into account the arrangement and surface area of the multiwell array, this leaves between six and eight patterns localised to the centre of the part.

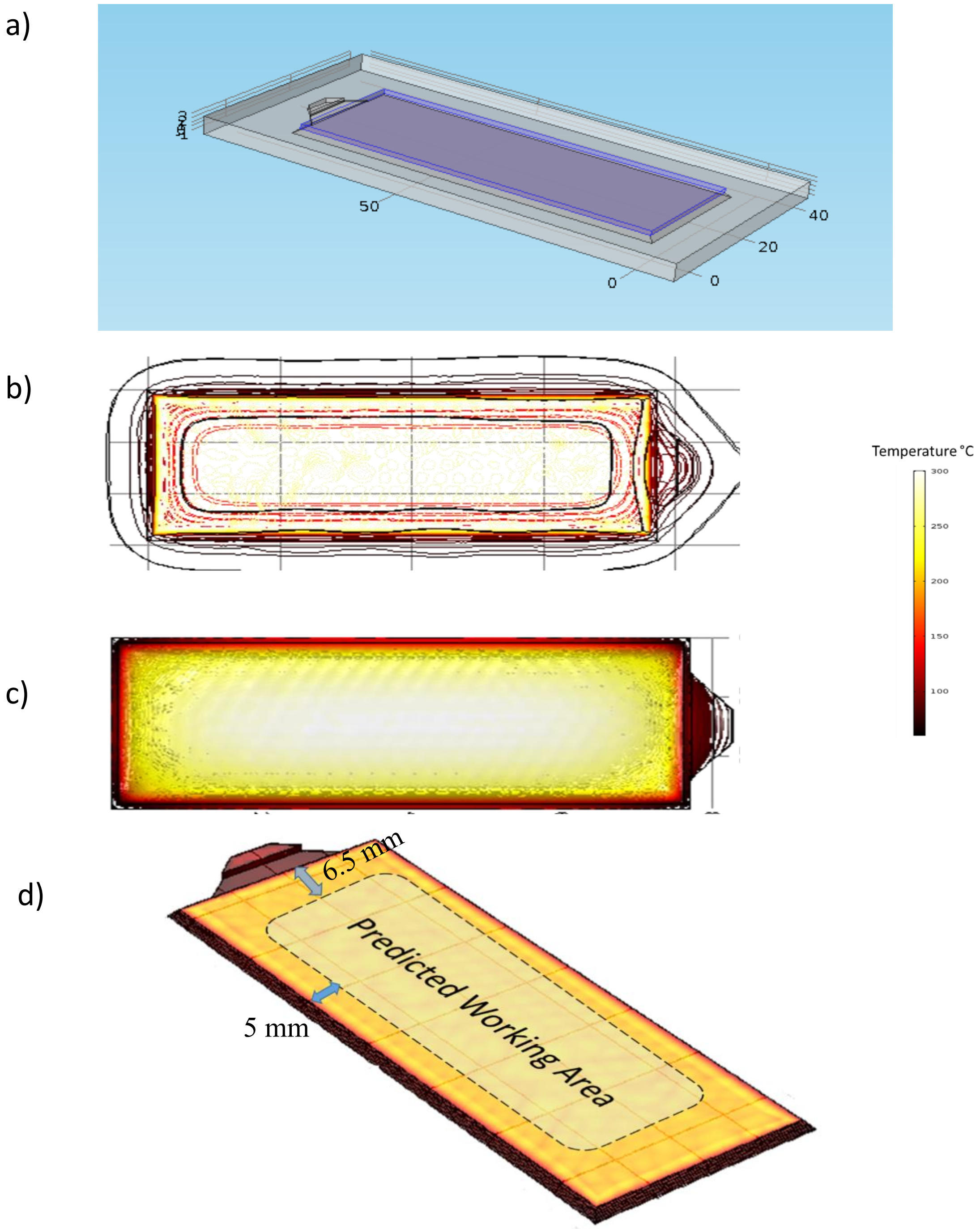

Figure 3.12 - Results of thermal FEA modelling to predict the working area for quality replication in microscope slide sized parts. a) is a rendering of the 3-D model used , b) is an isothermal contour plot and c) a collated isothermal contour volume map demonstrating the distribution of temperature through the part as it cools. d) is an overlay of the estimated working area for quality replication onto a thermal map of the sample after 0.5s of cooling.

In order to test FEA model predictions, two large area (56.5mm^2) pillar arrays were fabricated inside the working area. One of the UHAR square patterns, and another that aimed to reach even higher aspect ratios by etching 2µm tall, 1µm pitch highly tapered conical pillars (**Figure 3.13**).

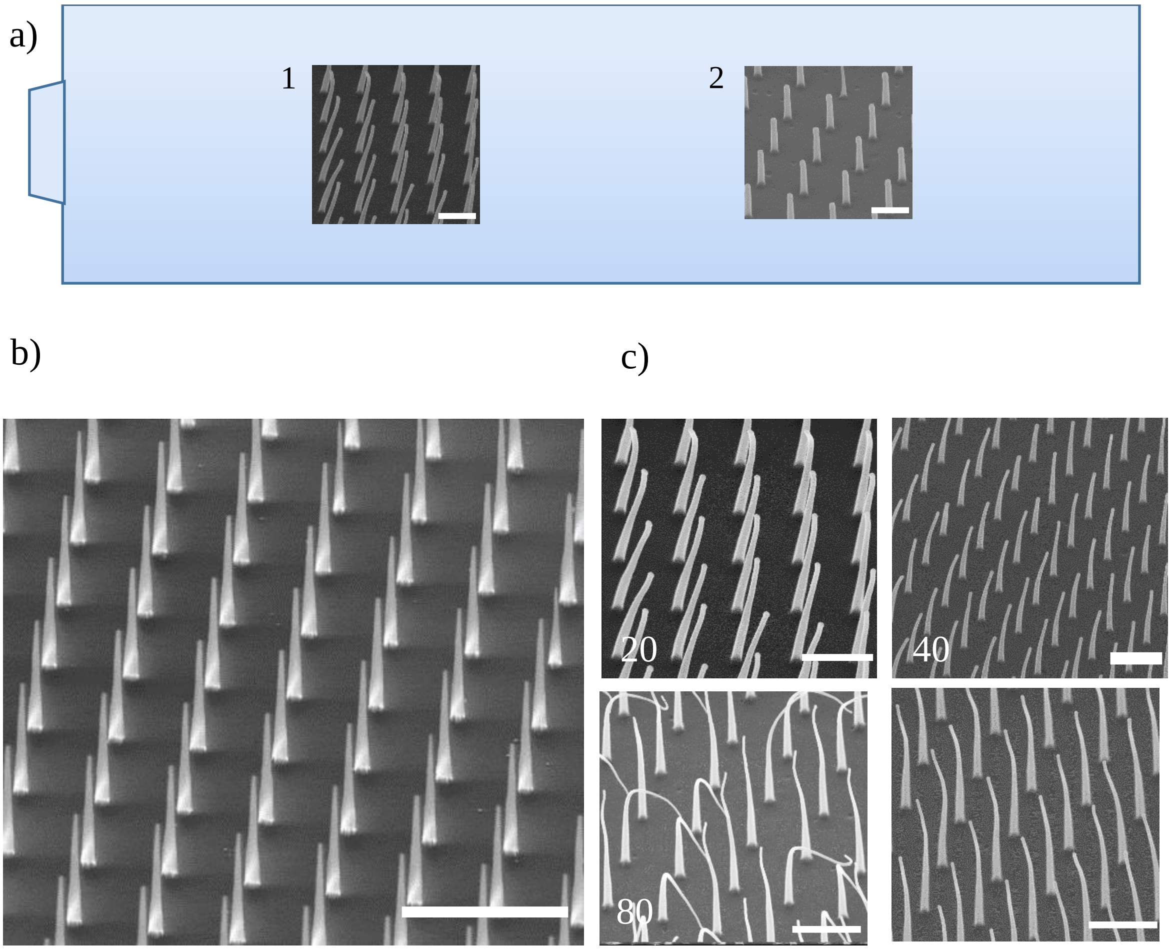

Figure 3.13 - Trial of slide working area with higher aspect ratio nanopillars. a) diagram / rendering of the placement of the pillar-arrays on the slide-sample, relative to the sprue indicated on the left-hand side of the sample, scale bar 1µm. b) SEM of the quartz master after mask-removal c) SEM of representative nanopillars fabricated over 80 replicas, for the taller pillar patterns (pattern 1) scale bars 2µm and 1µm respectively

The replication accuracy of UHAR slides shows less deterioration over replication cycles compared to the UHAR square parts. Comparing the pillars from **(Figure 3.13-b and c)**, the pillar replication accuracy only begins to degrade at around shot 60, with pillars otherwise being subject to only a moderate amount of stretching, reaching a height of 2.6µm. It is believed that this is a direct result of the conical profile of the quartz master stamps.

This indicates that the nanopits, despite narrowing pit diameters with increasing inlay depth, are coated by the anti-stick layer. It would also appear that the conical profile has also improved demoulding characteristics, despite the fragile individual pillars in both quartz master and polycarbonate replica. Whether this is due to the mechanics of the demoulding or the increase in surface area for monolayer to form onto in the pit remains requires further examination.

This introduces a new important feature for replication success from the point of view of the master stamp fabrication. In literature examples, diameter and height, therefore aspect ratio, were the only important factors measured to play a part in replication accuracy.

The sidewall angle between base-diameter and tip-diameter is proven to be another dimension with which to improve replication accuracy. What is also important here is that the tooling purchased for the fabrication of microscope slide sized parts has a four-pin ejection system that will distribute the demoulding force more evenly across the part surface, and this is why there is no degradation in the shorter pillar array replication accuracy as is seen in the UHAR square parts.

Whilst the slide tool parts do not appear to be any more resistant to the degree of relative part warpage in the moulding process, the nanofeatures replicate better in these conditions along the axis of least thermal stress (**Appendix B.3).**

This subsection has illustrated the generation of a COMSOL model and method of analysis that quantifies thermal stress along a moulded part and collaborates that with a study into the changing replication success, accuracy and equivalence across an entire moulded part. This model can be used to predict areas of lowest thermal stress in a moulded part that helps define a working area with high nanopillar replication quality, and be used to test novel tool designs, materials and thermoplastics.

3.3 Multiplex sample designs – fabricating multi-mechanical samples

Section 3.2.2 identified a 28 mm x 64 mm area for quality replication. This leaves a lot of unused space in the moulded part – those not completely within the quality replication area. The question arises, therefore, of how best to utilise this space.

The existence of more robust pillars with conical profiles leaves an avenue for the exploration of this, with the fabrication of more robust features around the periphery of the sample being one option. The next step, then, is to use these insights to make UHAR slides with multiple patterns of different mechanical properties for use in biological investigations.

Three UHAR arrays were successfully fabricated using the models of quality replication and tolerance estimation to assay cell response on different mechanical properties.

3.3.1 Multi-Pitch pillars on UHAR squares to test cell response to geometrical cues

The UHAR square parts are ideal for rapid prototyping, process optimisation, and cell response optimisation. Easily replicated and faster to fabricate, the turnaround for updating design parameters and fabricating a new quartz stamp is as short as a week. To this end, a multi-pitch substrate was fabricated with 12 x 8mm^2 pillar arrays at pitches ranging from 500nm to 1500nm **(Figure 3.14).**

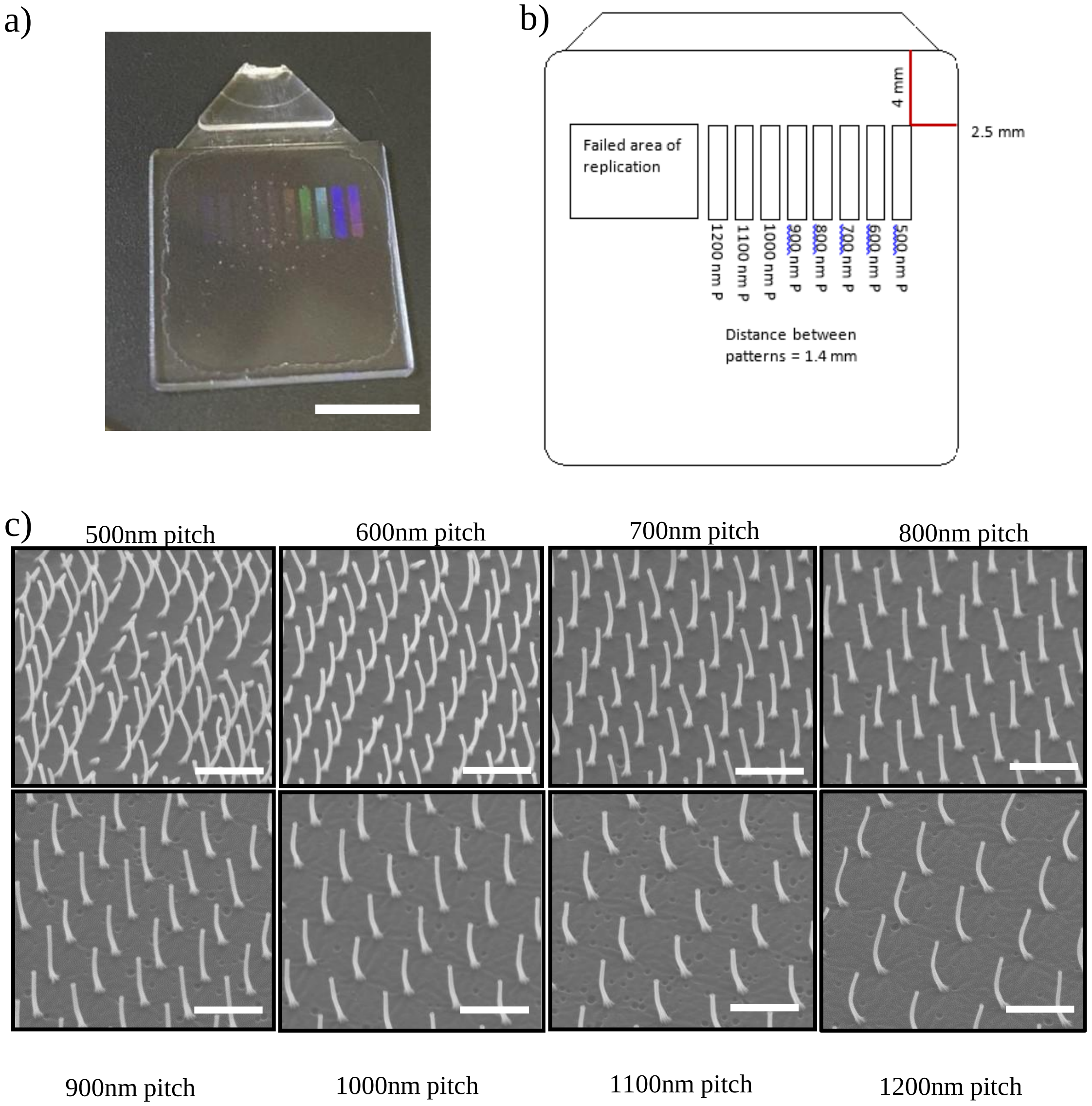

Figure 3.14 - Multi-pitch square substrate for testing cell response to varying pillar pitch. A diagram of the multi-pitch square array, with a summary of nanopillars fabricated and layout of the sample. Pillars above 1.2µm pitch failed to replicate, this was most likely due to an inlay fault in the fabrication process causing mass pillar breakage, however the sample is proof of principle that such a substrate can be made. Scale bar a) 10mm, c) 1µm.

The aim of the multi-pitch UHAR square was to allow for seeding of different cell types on multiple nanopillar arrays and to observe the effect that the change in spacing had on adhesion, proliferation and migration of the cells.

Whilst the literature discusses a mathematical approach to determining cell settling on nanopillar arrays[56], having a stock of small samples presenting multiple pillar types can be used for rapid experimentation. Arrays like these can be used to select optimum pillar dimensions for long-term and functional biological assays. It is expected using this formula that closer pitch arrays will promote adhesion, and the likelihood of cell adhesion across these pitches should be the same for each array. These multi-pitch array devices would be an invaluable extension to existing methods of determining cell settling potential[56], allowing the establishment of an additional term that estimates the % likelihood of settling based on a larger dataset of empirical evidence.

3.3.2 Multi-mechanical UHAR slides by varying height: robust features

The next generation of samples are the first of the slide tool multi-height UHAR slides. These have nanopillars fabricated along the sides of the part, in addition to those in the identified working area. These pillars were fabricated using a trial stepwise etch process, and although that process produced some unexpected results, it led to biomimetic moth-eye structures with bactericidal properties. Whilst these pillars are far too stiff to form a soft substrate array, the changing geometry and height of the pillars enables traction force-based measurements[20, 21, 66]. This is also the first instance of multiple pillars fabricated simultaneously in a multiwell format, meaning that bactericidal studies of previously low throughput fabrication nanoscale features can be merged with high content biology analyses.

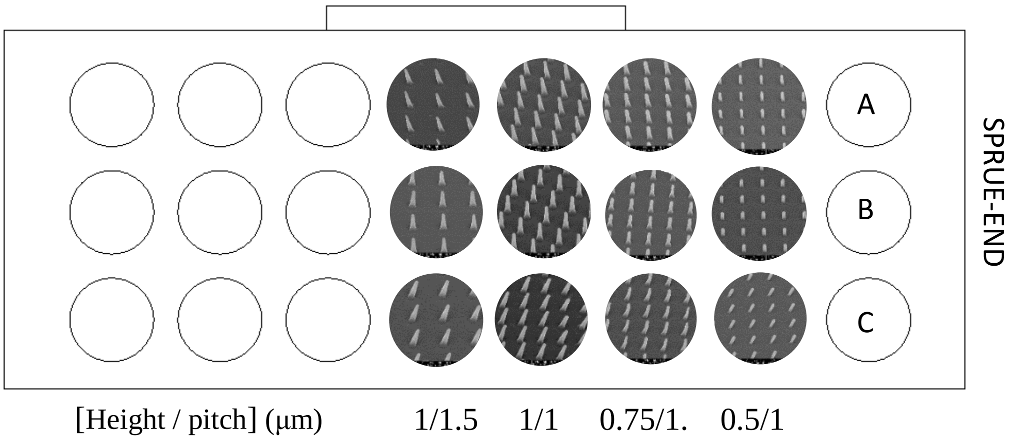

Figure 3.15 - Multi-mechanical slide with robust pillars of different heights. Sketch of the design for the height varied UHAR slides with respect to orientation in multiwell format, with row and column numbers designated, and sprue location highlighted. Four distinct patterns were fabricated, at three separate heights and two different pitches, the combination of which is indicated at the bottom of the figure in µm.

(**Figure 3.16)** illustrates the sample-to-sample variations of the different pillar heights, which show remarkable replication accuracy, and demonstrate equally impressive part-to-part replication equivalence.

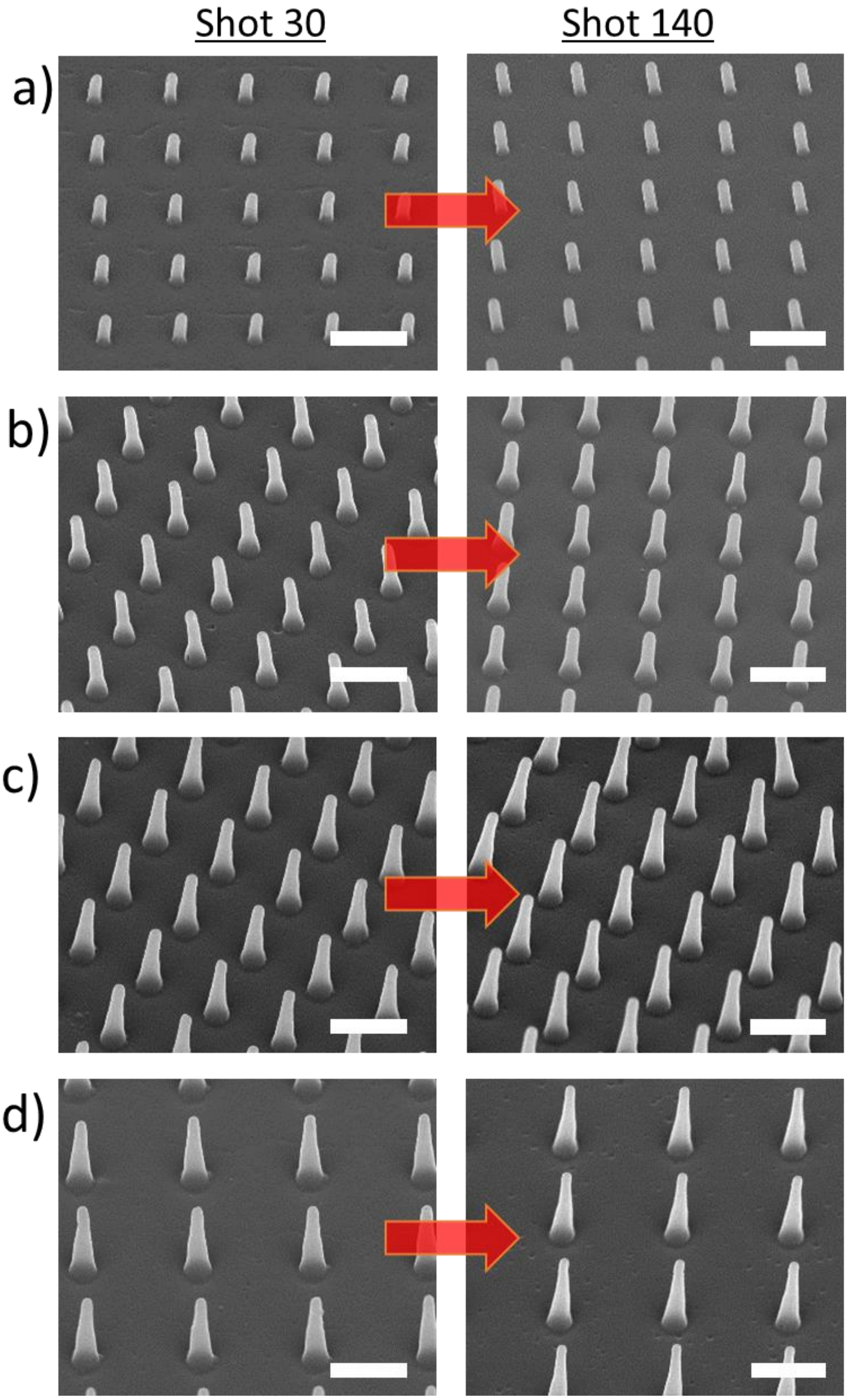

Figure 3.16 - Part-to-part variation of the multi-height UHAR slide pillars. SEM of replicas 30 (left column) and 140 (right column) of the central column patterns. a) 500nm tall, b) 750 nm tall, c) 1000nm tall, 1µm pitch pillars, and d) 1000nm tall, 1.5µm pitch pillars. Whilst there are some noticeable changes in the pillar morphology, the overall part-to-part variance across the 110 replicas is less than 10% in both height and tip diameter (mean of 60nm and 7nm respectively). Scale bar 1µm.

The replication accuracy, predictably, changes at the edges of the sample **(Appendix B.3)** The pillars there have a tendency to be stretched along the direction of thermal stress. As the demoulding forces are relatively constant along the part, this is a result of the temperature gradient as predicted by the FEA modelling**. (Figure 3.17)** is an example of the changing spring constant over four replicas for the 1µm tall, 1µm pitch arrays, and indicates two things: the difference in average spring constant of each pattern, and the overall replication equivalence over time.

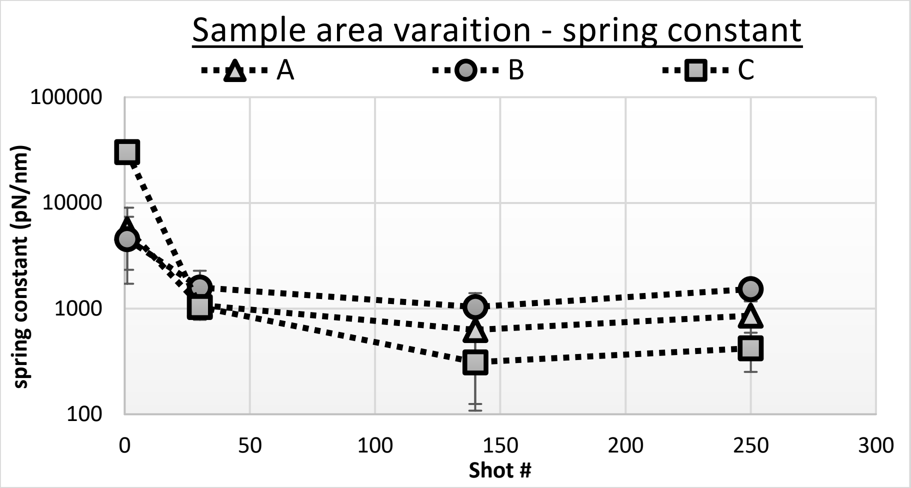

Figure 3.17 - Spring constant variation over 250 replicas of multi-height UHAR slide samples. Graph of spring constant vs shot number for 1µm tall, 1µm pitch nanopillars over replicas 1-250 for rows A, B and C denoted by triangular, circular and square data points respectively. Error bars indicate the maximum and minimum spring constants calculated by using the standard deviations of height, tip diameter and base diameter.

The graph reveals one particularly interesting trend. It could be argued that higher replication accuracy equates to stiffer mechanical bodies due to the mechanical integrity of these lower aspect ratio, or more conical, pillars. If this is the case, the injection moulding process will need to have a controlled stretching regime to attain “softer” features at higher replication cycles. As has been evidenced by the UHAR square nanopillar arrays, higher degrees of stretching cause the yield of samples from a single inlay to fail. It may therefore be a facet of this technology that soft substrates must be relatively lower in yield, producing useable samples in the tens rather than the hundreds.

The multi-height nanostructures are far too stiff to be of much use in stimulating a variety of cell responses from their mechanical properties alone. With equivalent Young’s moduli in the range of > 550 kPa, these are well outside the limits of polyacrylamide hydrogels in the experiments by Engler et. al[1, 28, 72]. The multiple height UHAR slides would be more suited to experiments that require stiff substrates but controlled topography, and a distance from the flat surface.

Experiments such as those trying to limit the formation of biofilms by bacteria, or the production of anti-reflective devices [73, 74], to investigate cell settling on pillar surfaces without the surface mechanics interfering with results[56], or even experiments to test the limits of cell-substrate force interactions on different length scales[38] would benefit from this type of pillar device, as the diameter and height of these stable nanostructures can be tuned with ease.

The promising feature of these devices is that these more robustly shaped features replicated well at the sides of the sample, making use of the otherwise dead space. Pillars above the aspect ratio of 5:1 begin to replicate at an angle to the surface. If it is determined that these structures have detrimental effects on cell settling and adverse effects on behaviours such as proliferation, then only edge features of aspect ratios lower than 5:1 can be used.

3.3.3 Multi-mechanical UHAR slides: a true range of array moduli

As the stepwise etch process resulted in highly conical pillars, another approach to fabricate softer pillars required changing the diameter of the metal mask. The initial aim was to decouple mechanical from topographical properties by fabricating pillars with different mechanical properties but constant diameter, however, this was not possible with the current etching technology (further addressed in **chapte**r **5** of this thesis). To solve this, patterns were etched in a single process, and the tip diameter of the pillars was varied from 50 -As these pillars are expected to be more susceptible to stretching, the patterns were fabricated in the central row of the slide in accordance with the quality area defined in the FEA model **(Figure 3.12)**.

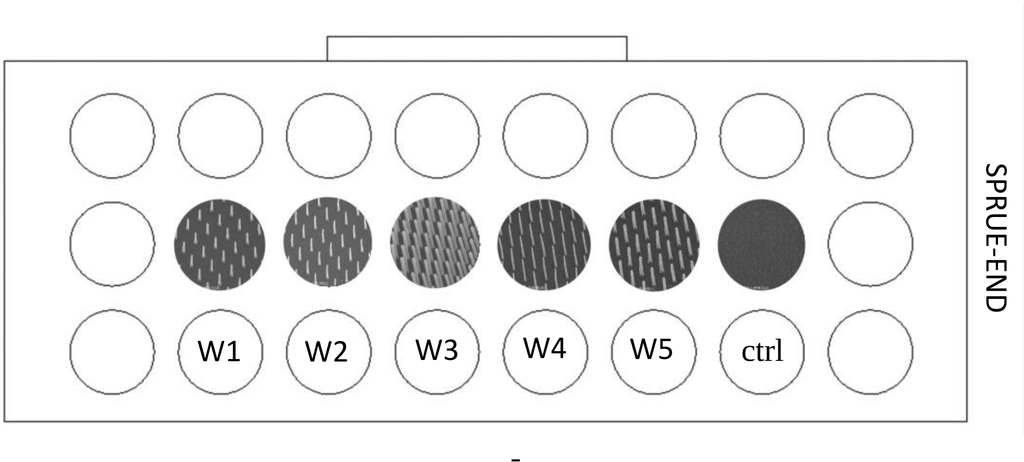

Figure 3.18 - Multi-mechanical slide with range of $\bar{E}$ – myogenic to osteogenic. Sketch of the design for the multi-mechanical UHAR slide samples with respect to orientation in multiwell format, with slide sprue location indicated. W1-W5 indicate the well numbering system used.

The fabricated UHAR arrays have dimensions and mechanical properties as outlined in **Table 3.1**.

Well	d_t (nm)	height (µm)	pitch (µm)	k (pN/nm)	$\bar{E}$ (kPa)	Tolerance +/- (kPa)
1	115	1.95	1	47.8	234	30
2	70	1.6	1	10.6	43	3
3	100	1.9	0.5	11.4	251	20
4	70	2.35	1	3.9	25	2
5	90	1.35	1	51.7	189	3
Control	-	-	-	-	$2.3\text{x}10^6$	-

Table 3.1 - Dimensions and properties of multi-mechanical UHAR slides. Tolerance is created using maximum standard deviation from dimension measurements (diameter, height) of pillars in each well, then converted into equivalent Young's modulus.

Over 160 parts were fabricated, a number that encompasses the range in which the small tool pillars of similar dimensions replicated well, and encroaches into the range of the multi-height UHAR slides. Four parts were taken from the replication cycles, and replicas 30, 60, 90 and 110 were analysed to determine pillar replication success. It is also important to establish the continuity of mechanical properties of the individual pillar array going back to the first criteria for UHAR nanopillars. Each array in replica #60 was analysed for fluctuations that occur across the height (h) and tip diameter (d_T), the two dominant factors in Euler-Bernoulli based estimation of spring constant.

(Figure 3.19) and **(Figure 3.20)** are area graphs of the fluctuations across the average value in each discretised section of these two dimensions of the individual pillars of the arrays (termed localised area variations, or LAV). **(Figure 3.20)** indicates a larger fluctuation in pillar heights in wells 1 and 2, concentrated at the edges of the pillar arrays. It can be expected that this will contribute to a larger variation in the overall mechanics within each well.

However as these pillars are quite high in spring constant, the overall tolerance range for these features is quite high in terms of mechanical equivalence banding, see **(Table 3.1)**, because their robust profile enables them to resist the stretching phenomena that occurs more prominently in higher aspect ratio UHAR features.

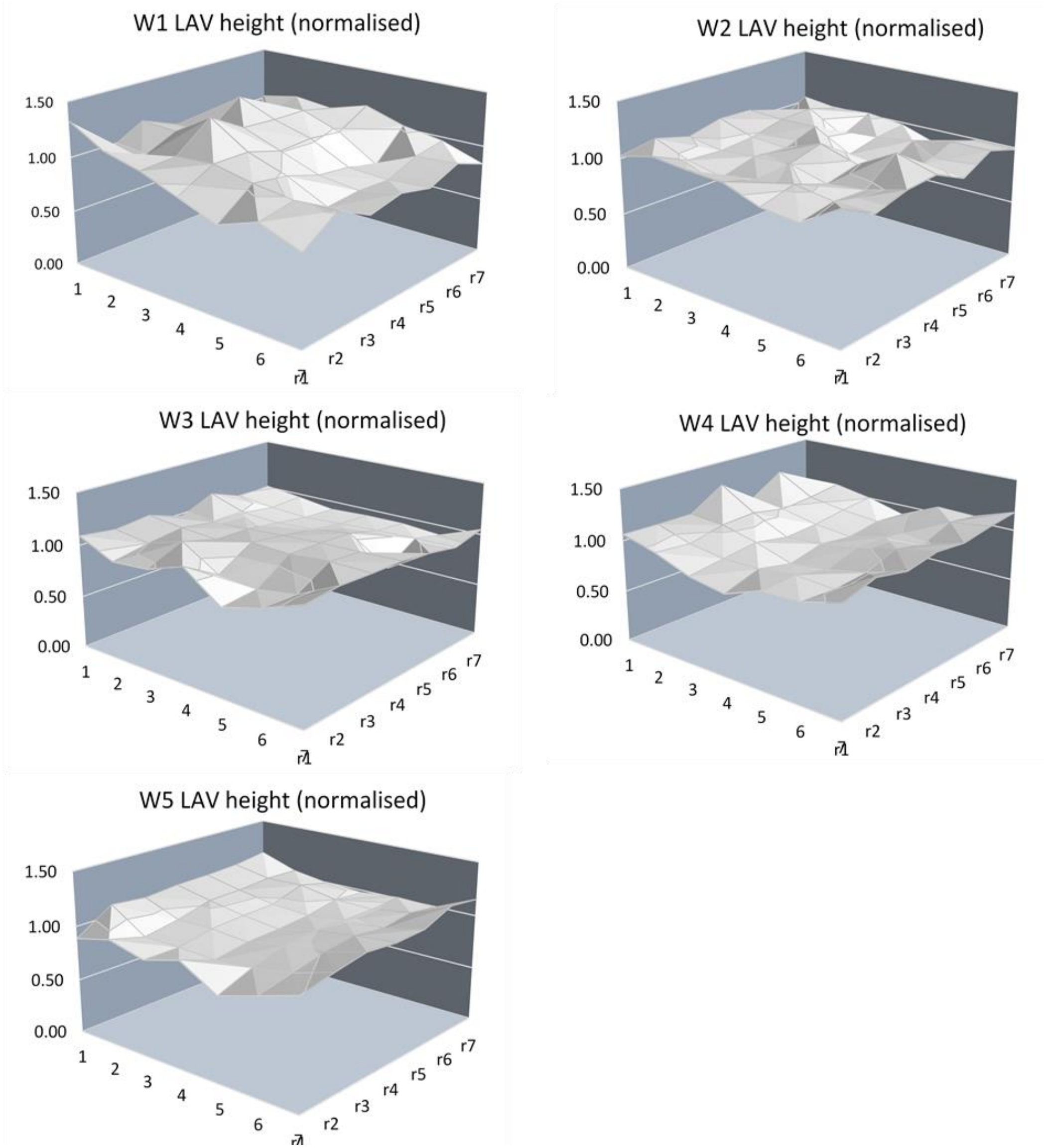

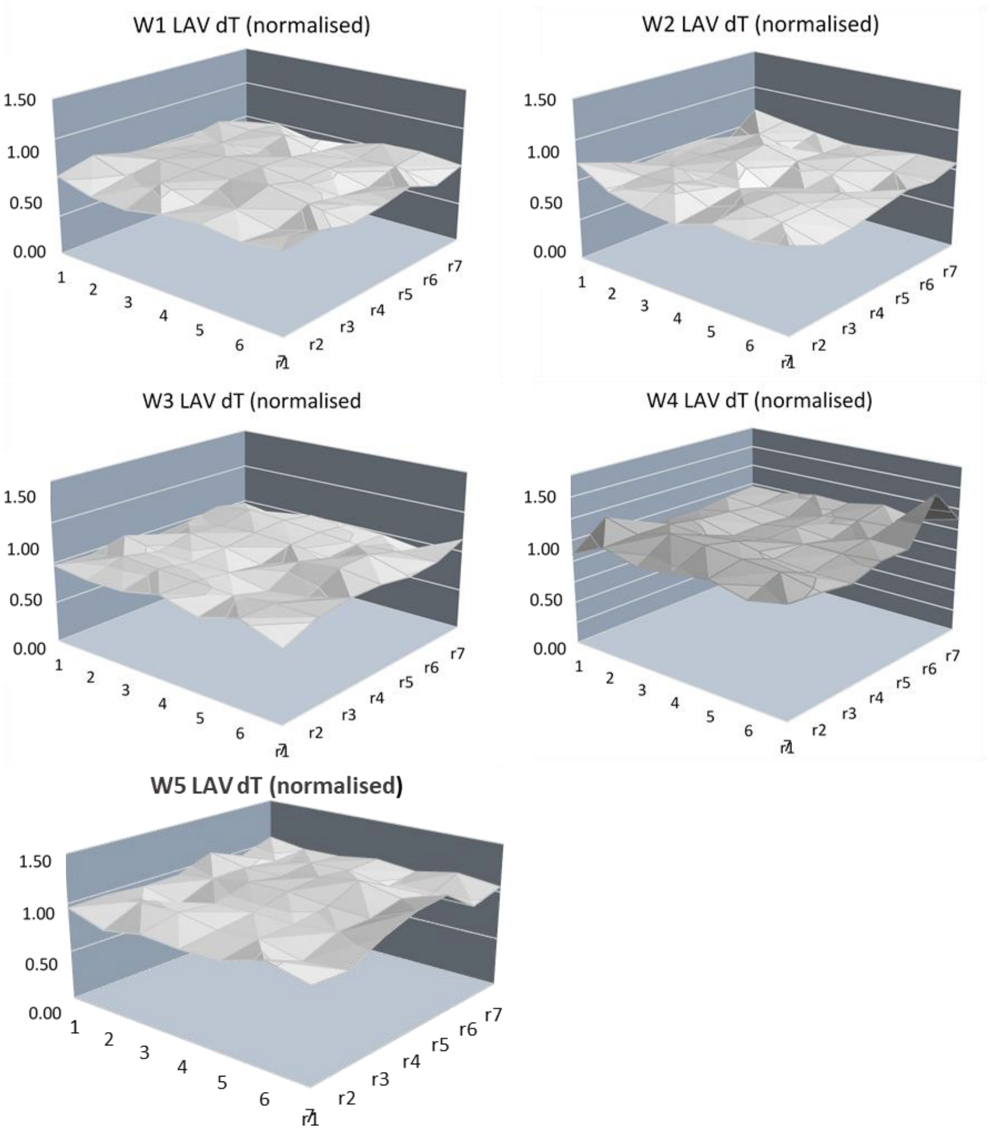

Figure 3.19 - Multi-mechanical UHAR slide; array fluctuations in pillar height. Localised area variations in pillar tip diameter over the 7 x 7 mm array area, discretised into 1mm^2 sub-areas. The height measurements (z-axis) are normalised to the average tip diameter of the entire array for each pattern. The overall changes in pillar height contribute to the upper and lower bounds of the error in the spring constant, and therefore the end effective array mechanics.

Figure 3.20 - Multi-mechanical UHAR slide; array fluctuations in pillar tip diameter. Localised area variations in pillar height over the 7 x 7 mm array area, discretised into 1mm2 sub-areas. The height measurements (z-axis) are normalised to the average height of the entire array for each pattern. The overall changes in pillar height contribute to the upper and lower bounds of the error in the spring constant, and therefore the end effective array mechanics.

Analysis of area variation of both pillar height and tip diameter demonstrate the continuous nature of the arrays, with no imaged sections dropping out due to unsuccessful replication **(Appendix B.4).** These analyses also demonstrate the highest average fluctuation across an array is 13%, which is a remarkable improvement for these kinds of features compared to the UHAR square samples which had an average overall feature change across an area this large of +/- 50% at the same replica number.

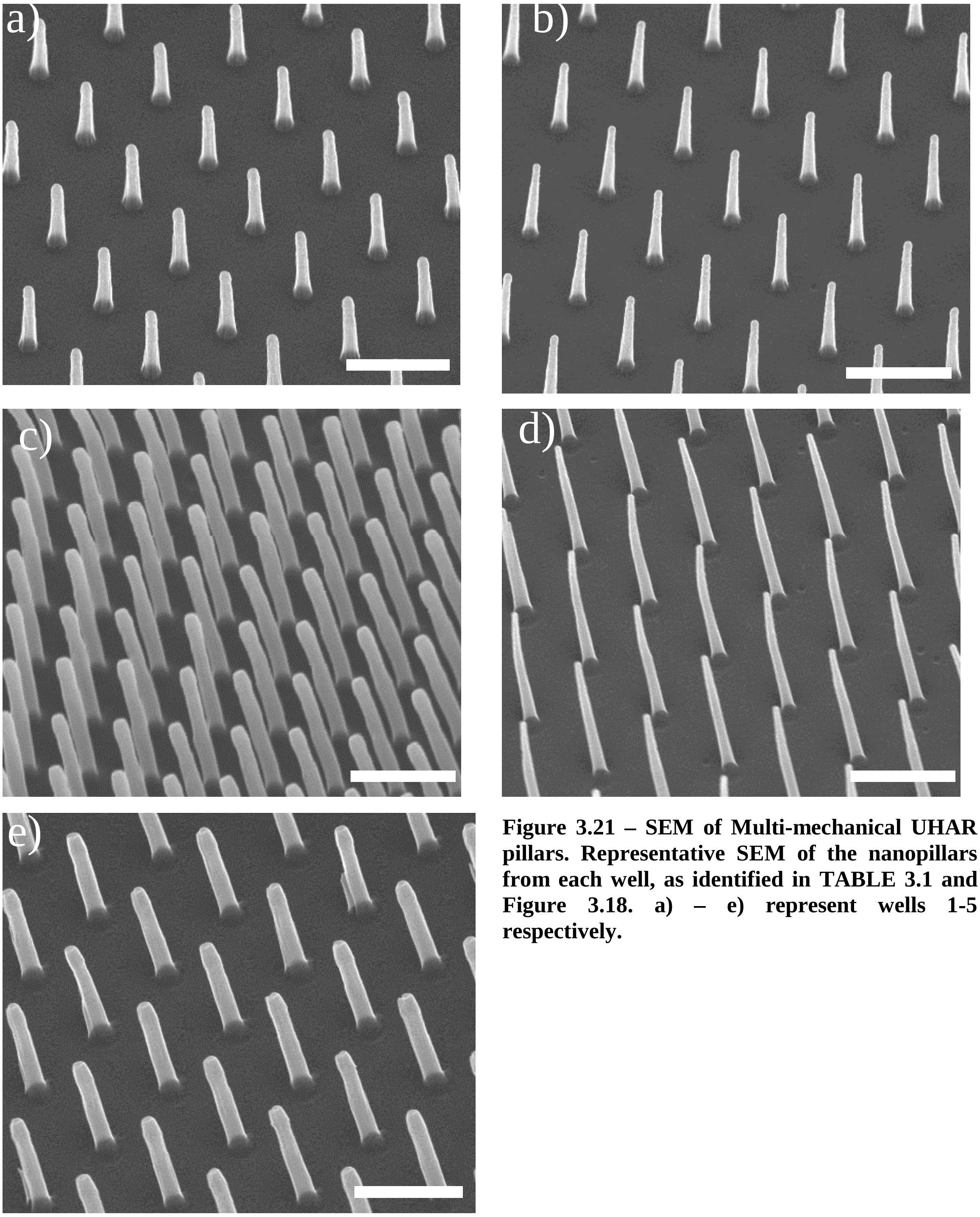

Figure 3.21 – SEM of Multi-mechanical UHAR pillars. Representative SEM of the nanopillars from each well, as identified in TABLE 3.1 and Figure 3.18. a) – e) represent wells 1-5 respectively.

As the tip diameter is the dominant parameter in the calculation of a spring constant, it is encouraging to observe strict conservation of dimensions within wells for the entire array (**Figure 3.19**). What is of particular note here is that the largest fluctuations occur at the edges of an array. This is most likely due to the etching of the quartz pillars, with edge pillars forming a slightly different profile and tip diameter than those in the centre. Pillar areas are deliberately oversized to ensure that deformed pillars are excluded from the well, and to give tolerance to the alignment of multi-well and UHAR slide.

It is important that pillar profiles are also conserved across replication cycles. Area variations indicate that the key pillar dimensions are mostly conserved within each pillar pattern. Therefore, limiting the analysis to the centre of the pattern the average profile for nanopillars can be extracted for replicas 30, 60, 90 and 110, and compared (**Figure 3.22**).

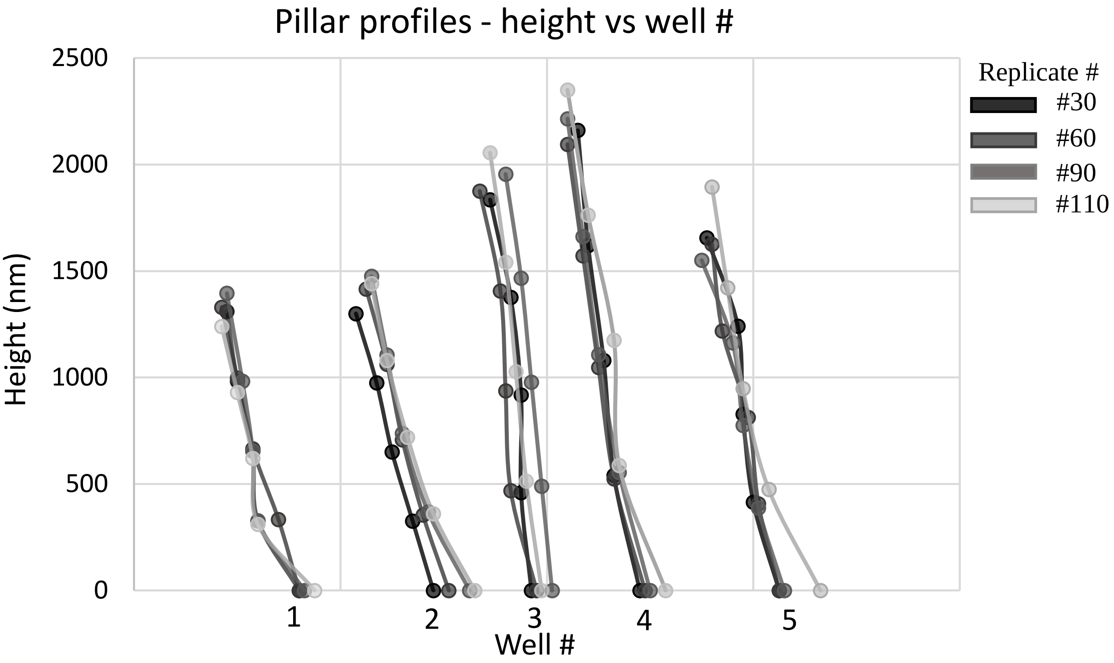

Figure 3.22 - Sample-to-Sample variations in pillar profiles for multi-mechanical UHAR slides across 110 replicas. These graphs represent the pillar profiles extracted from the 5-point measurement system employed in chapter 5 for spring constant calculation, with replicas 30 – 110 in dark – light grey respectively. Well # 1- 5 indicate the well imaged. The profiles are extracted using diameter measurements at five key points, the tip, middle and base of the pillar, and the mid-points between these.

Of interest here is the slight variance in base diameter for each pillar, as this becomes larger with stretching. This indicates that the stretching pulls not only the pillar in the mould, but also has a force on the surrounding polycarbonate. **(Figure 3.23)** demonstrates relatively consistent pillar shapes over the measured cycles, showing that the pillars are consistent over 110 cycles, a marked improvement from where these fabrications started with the small-tool, which for pillars of this narrow diameter and high aspect ratio had a replication cycle limit of 40.

What is also promising is the consistency of mechanical properties of pillars across replication cycles, remaining almost the same and definitely within error. This indicates the stretching is proportionally uniform across the five patterns, as any drastic change in diameter or height of the pillars would cause these to fluctuate with higher magnitude.

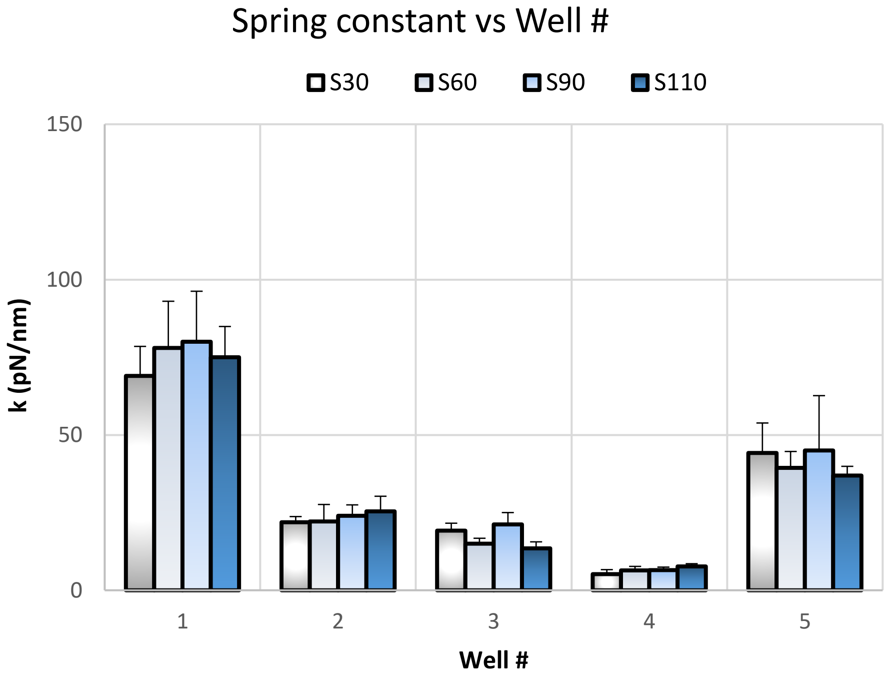

Figure 3.23 - Bar chart demonstrating the change in spring constant for each well of the multi-mechanical UHAR slide samples over 110 replicas. Bar chart of spring constant vs well#, from replicas 30-110. The analysis over multiple replication cycles shows remarkable consistency of pillar mechanical properties compared to the small tool equivalent, with almost all the larger changes being accounted for by standard deviation from measurements.

Looking at the wells individually, an average and a standard deviation for the profile and the pillar spring constant can be examined. By comparing the standard deviation of the spring constant to the maximum and minimum spring constants for each well, the applicability of the average value can be verified to see if it is appropriate for quotation across multiple replicas in the same batch.

Comparing these ranges to those established in the literature, samples can be bracketed into batches that have consistent mechanical properties across each UHAR array. At 110 replication cycles the point of failure has not been reached, indicating that a single inlay could produce samples in the hundreds. Analysing the variation of the mean values of the spring constants across an array, and the mean value of the array across replication cycles, the overall mechanical properties of sample batches can be established.

As the mechanical properties of individual arrays are almost impossible to empirically measure due to their nanoscale feature sizes, methods like FEA and quality analysis, must be used so that pillar arrays that are to be mass-produced like this can have values for comparison to the literature. There is potential for adapting certain AFM based methods in the literature[75, 76] for determining individual pillar mechanics, however these are needlessly difficult and time consuming.

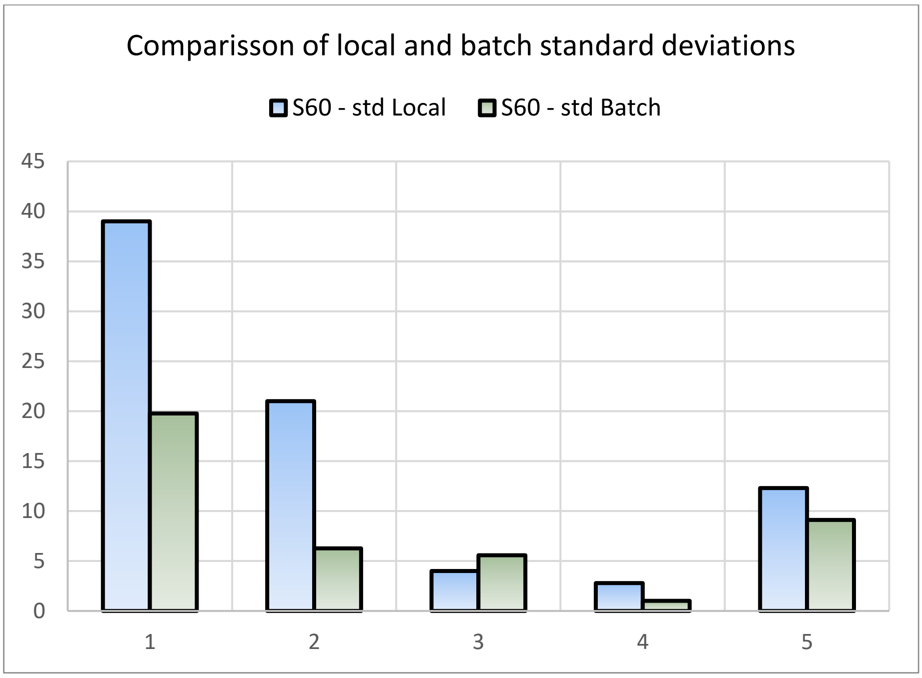

Figure 3.24 - Comparison of the change in spring constant of pillars in the array – local variations vs batch variations. This graph compares the standard deviation between pillars of the same array, and over the 110 parts measured of the multi-mechanical UHAR slide samples, in blue and green respectively. The results demonstrate that for the majority of pillars, the variations from part to part are smaller than those present across the entire array.

(Figure 3.24) is a comparison of the standard deviation in spring constant across the arrays of shot #60, and the standard deviation of variations of the other spring constants from that of shot #60 for each pillar array. By arranging the changes in calculated values like this, it can be seen that defining the error in Ē of the array by variations that occur across the array is more representative than across replication cycles.

Importantly though, it demonstrates that there is relatively little change across the production of the 110 samples. This means that for at least 110 samples a consistent set of spring constants, and therefore effective array moduli, can be explicitly defined. This is proof that ultra-soft nanopillar arrays, with equivalent Young’s moduli in the range of sub 20kPa, can be produced at large areas on a large scale for high throughput biology experimentation. **(Figure 3.25)** is an illustration of the measured Ē.

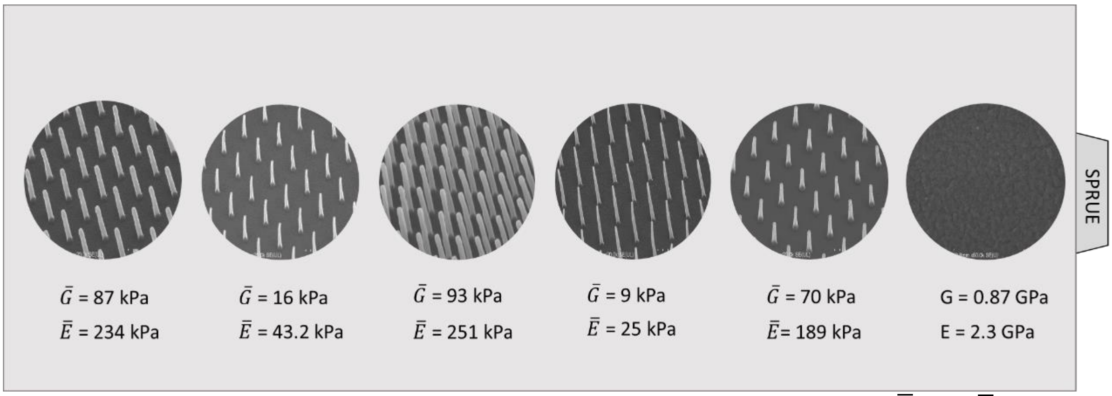

Figure 3.25 - Multi-mechanical UHAR slides: finalised sample map including $\bar{G}$ and $\bar{E}$. Finalised sample map, including calculated values of $\bar{G}$ and $\bar{E}$, of the multi-mechanical UHAR slide samples, including the values of the control well.

3.4 The effect of Ultrasonic Welding on UHAR pillar arrays

The final test for these devices was to determine the effect that ultrasonic welding had on the UHAR nanopillars. As the weld is from a polycarbonate slide to a polystyrene well plate, some care must be taken in ensuring that the non-chemical weld seem is airtight, and that the nanopillars are not damaged significantly in the process of welding. **(Figure 3.26)** illustrates the effects of the welding process on the pillar arrays.

Overall, damage to the nanopillar arrays due to ultrasonic welding is minimal inside the wells. An area exists within the vicinity of the weld seam where pillars suffer damage, however this is highly localised and will therefore not impact performance. Interesting points to note are: **(Figure 3.5-a** and **c)** these demonstrate the behaviour of nanopillars within the first 0.5mm of the vicinity of the weld seam. There is a stark contrast where the weld seam has covered and not covered the nanopillars. Pillars under / around the weld seem are crushed or collapsed. **(Figure 3.5-d** and **e)** are areas where the weld seem has torn out areas of the polycarbonate slide upon separation. The nanopillars at the edge of the weld seam in these marks are still remarkably intact, and this trenching defect demonstrates that the polystyrene has penetrated into the softened polycarbonate. The integrity of the polycarbonate-polystyrene was established using a simple leak test. The weld failure rate for these wells was around 5% **(Appendix B.5)**. Overall, these welds can be improved by tuning the various welding parameters, particularly the welding energy, the holding time for the weld to form, and the weld seam design itself. However for a high quality weld to be guaranteed across the plate, the slide and plate materials should ideally be the same, and the bowing should be eliminated from slide fabrication.

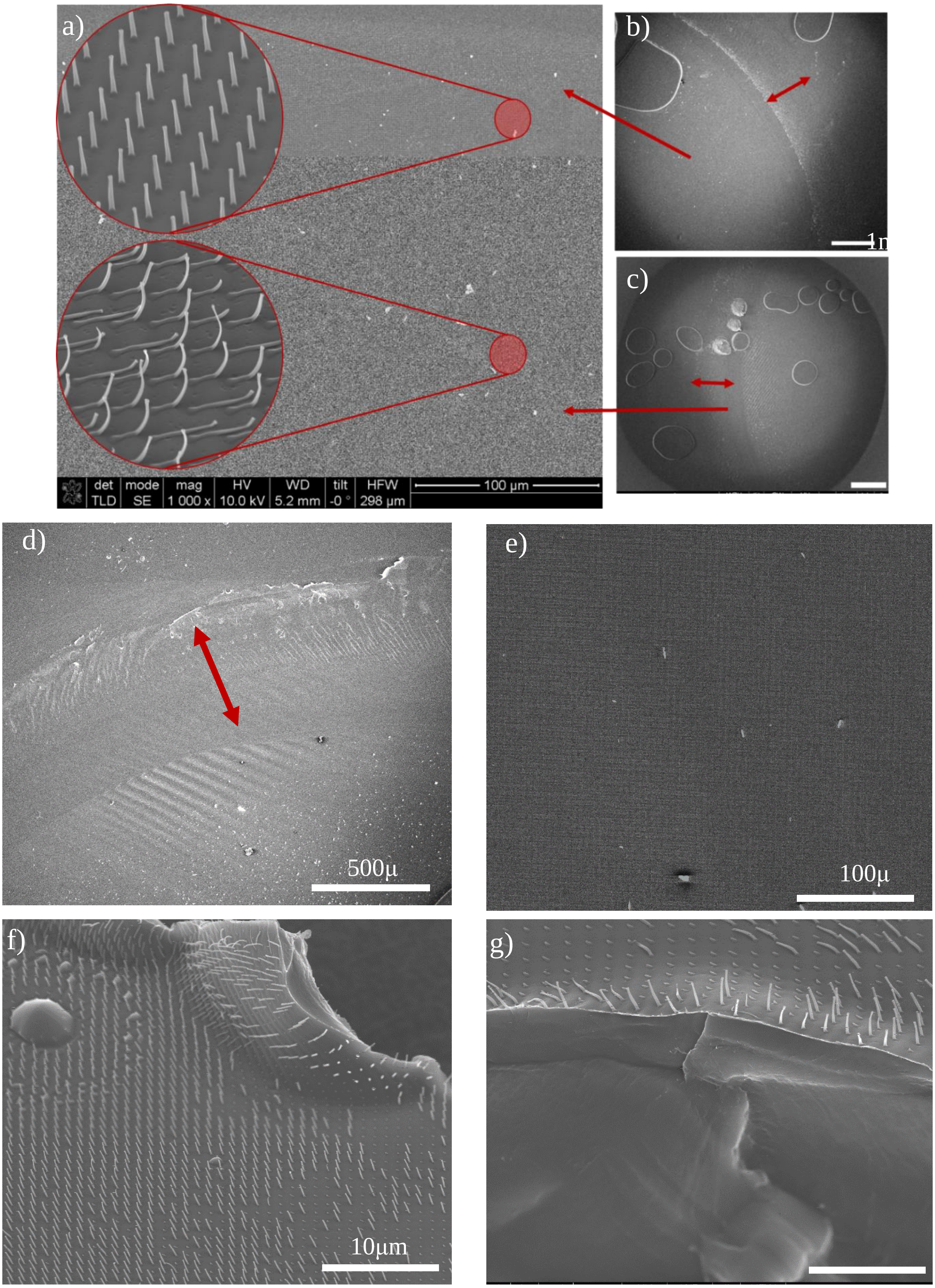

Figure 3.26 - Effects of ultrasonic welding on UHAR nanopillar arrays. SEM of the pillars in direct proximity (less than 1mm to) the weld seem b) and within the well c). Image d) another SEM of the weld seem. c) depicts a central area where the pillars are broadly undamaged, and f) and g) are areas where the weld seem has been "torn out" – causing defects.

3.5 Conclusions

The criteria for UHAR nanopillar arrays (defined in **section 3.1** were designed to break down the task of creating this combined technology into clear goals. This chapter dedicated itself to the understanding and fulfilment of these criteria.

1. *Samples must have a stable replication accuracy across pillar arrays*

Three metrics of consistent replication were defined and optimised: replication accuracy, replication success and replication equivalence. Replication success was quantified across the UHAR square parts, and the area of quality replication They were used to identify the area of quality replication, which were then linked to the distribution of thermal stress and mechanical demoulding force across the tool. By fabricating the nanopillar arrays in these quality replication areas, replication accuracy and equivalence is ensured, thus meeting criteria 1.

2. *Samples must have a predictable part to part tolerance*

By measuring initial values of the replicated nanopillars, and noting their position geographically on the sample, the batch ranges of the samples can be established based on established stretching relationships. This chapter has outlined the relationship between part geography and pillar stretching, as well as replication success. By combining these with thermal modelling, the areas of quality replication can be predicted for any inlay material, tooling design or thermoplastic used.

3. *UHAR pillar arrays must be able to contain different array designs with individual mechanical or geometrical properties*

Three generations of devices have been fabricated. One UHAR square to rapidly trial cell response to a pillar arrangement to determine the viability of large scale experiments on them. The multi-height UHAR slide samples fabricated nanofeatures that were robust enough to minimally deform at the edges of the samples, and the multi-mechanical UHAR slide samples created five distinct pillar profiles that each have a unique spring constant, one array falling within the bounds of a potentially myogenic array. Going forward, replication quality can be improved through two approaches. One is to improve the model of a pillar spring constant for conical pillars in order to accurately predict a pillar spring constant, as tackled in **Chapter 4.0** The other is to improve the fabrication of nanopillars with an aim to improve replication accuracy, which is explored in **Chapter 5.0**.

4.0 Analysis of pillar sidewall morphology: an amended spring constant

Chapter 3.0 outlined the approaches taken to fabricating multiwell integrated, large area UHAR nanopillar arrays with continuous mechanical properties and part-to-part tolerance in the range of 10’s of nanometres. This assessment relies on individual nanopillar spring constants being representative of the pillar features.

The majority of the literature that concerns itself with using pillar-based substrates to investigate cell-substrate based interactions use exclusively Euler-Bernoulli beam theory. The calculation is straightforward and relies only on easily attainable measurements of the substrate stiffness, pillar tip diameter, and pillar height. However, this simplicity rests on a number of assumptions that serve to simplify pillar deflection mechanics.

A pillar is generalised as an ideal cylinder. It is imperative for the use of the Euler-Bernoulli equation for the deflection response of such a beam that the cross section of this beam remains constant. The pillar is fixed at its base, and free at the opposite end, and all shear deformations are assumed to be negligible compared to the deformations induced by pillar bending. When these assumptions are subjected to scrutiny this straightforward calculation can become quite complex.

This thesis has already made reference to the different amended spring constant equations used to calculate the pillar spring constants for nanopillars. Thousands of individual pillars have been analysed during the course of this investigation, and in the course of such assessment it became apparent that the pillars being fabricated were not ideal cylinders.

As this body of work has concerned itself greatly with the replication accuracy of the techniques used to fabricate the polycarbonate nanopillar arrays, it would be careless to neglect the potential effect that this change in pillar profile may have on the pillar spring constants, whilst quoting with great enthusiasm the boundaries of the certainty to which the pillar mechanics can be estimated.

Looking to the literature, these assumptions have been explored mainly from the point of view of amending the Euler-Bernoulli equation to account for variations in pillar tip deflection tracking, as this relies heavily on referencing the tip of the pillar to its base during deflection.

These approaches include factoring in a pillar-base displacement factor due to substrate shear[77], an examination of deflection limitations[78], the effect of the application of torque along pillar elements[79], the addition of a base-tilt caused by strain of the bulk around the pillar base[80], and the inclusion of shear deformations in determining the deflection mechanics[71, 78].

This last addition is known as Timoshenko’s beam theory, and it adds shear terms to the Euler-Bernoulli derived equation. These shear strains begin to become more important at lower aspect ratios, where bending strain begins to lose dominance in the bending mechanics.

All of these consistently assert that neglecting to take these effects into consideration at aspect ratios below 10:1 result in an overestimation of individual pillar spring constants by up to 40%. This is important, because most of the pillars of interest have aspect ratios of height:tip diameter of over 10:1, however this changes if aspect ratio is taken from the largest width feature – the base diameter. It is therefore important to determine the exact point at which the Euler-Bernoulli assumptions break down in terms of aspect ratio, and deviation from the ideal cylinder.

Out of the literature on these devices being used for cell-based experiments, two of note took care to examine the profile of the pillars they are using, i.e. challenge the assumption of an ideal cylinder, and the effect this will have on the results of the experiment – namely the pillar spring constants. These investigations, however, lack the derivation of a generalised formula in the form of an amendment to the Euler-Bernoulli derived equation of a spring constant, something that will be of great use to future projects that deal with beams that have non-linear tapers. This effect is important to characterise, as it is independent of aspect ratio, and therefore the introduction shear strains into the deflection mechanism.

This chapter aims at addressing two main questions:

1. At what point in aspect ratio does the Euler-Bernoulli spring constant calculation, hence termed k_{EB}, fail to accurately represent an ideal cylindrical pillar?

2. Can a generalised formula be derived to represent the effect of non-linear taper on the spring constant of such a pillar?

Finite element analysis was again used as the experimental foundation of this chapter **(Methods 2.8).** In each section of this chapter, the results of the analytical calculation will be challenged by the results of the computed numerical analysis from COMSOL models.

4.1 Evaluating Euler-Bernoulli beam theory – core assumptions

It is important to address the underlying assumptions of Euler-Bernoulli beam theory when using it so extensively in a body of work. By understanding the boundary conditions that underpin the simplification of what is quite a complicated problem, it can lead to insights into the application and future development of a technology.

This section will address the first question posed in the chapter introduction – at what aspect ratio does the Euler-Bernoulli beam equation fail to represent the actual pillar spring constant accurately?

It will start by revising the basics of beam theory in order to establish the facets of this rather extensive field that are important to the argument being presented. It will then move on to analyse the differences between calculated k_{EB} and FEA results of a cylinder under ideal Euler-Bernoulli conditions, and the FEA results of a cylinder attached to a compressible bulk of the same material as the pillar. These results will be tested for variability in aspect ratio, and for robustness across material properties, such as Young's modulus. Lastly the introduction of a linear taper, categorised by sidewall angle of the pillar, is added to determine its effect on these results. Between these investigations, the applicability of the cantilever case of Euler-Bernoulli beam theory can be given boundary conditions.

4.1.1 Basics of Euler-Bernoulli beam theory

Beam theory is important for this body of work, as it is the foundation upon which pillar tracking, and therefore cell-substrate force magnitude calculation, and the concept of fabricating soft surfaces out of hard materials are built upon. Accurate depictions of pillar mechanics in response to applied forces are therefore essential to the formation of a robust theory of any investigated phenomena.

There are three important material properties that need to be considered when addressing beam theory, these are the Young's modulus, the shear modulus and Poisson's ratio.

E – the Young's modulus

$$E = \frac{\sigma}{\varepsilon} = \frac{uniaxial\ stress}{strain}$$ **Equation 4.1**

measures the *stiffness* of a material. i.e. how much a body of such material will resist a change in length when under lengthwise tension or compression. In biology it is often the metric of how rigid a material is when talking about the cell-substrate interaction.

G – the shear modulus

$$G = \frac{\tau_{xy}}{\gamma_{xy}} = \frac{shear\ stress}{shear\ strain}$$ **Equation 4.2**

measures the *rigidity* of a material. i.e. the degree to which a body of said material will deform in response to shearing stresses, a measure of response of non-axial strain. For isotropic materials, rearranging **Equation 1.3**;

$$E = 2 * G * (1 + \nu)$$ **Equation 4.3**

ν – the Poisson's ratio

$$\nu = -\frac{d\varepsilon_{trans}}{d\varepsilon_{axial}} = -\frac{transverse\ strain}{uniaxial\ strain}$$ **Equation 4.4**

For isotropic materials, $-1 \leq \nu \leq 0.5$ due to the condition that E must be positive. A perfectly *incompressible* material would have Poisson's ratio of 0.5. The polycarbonate used, Makrolon®, has a Poisson's ratio of 0.37**[81]**. PDMS has a Poisson's ratio approaching 0.5**[82]**, however to avoid the mistaken calculation of an infinite modulus as it is not a perfectly incompressible material, it is approximated to 0.4999.

Between these material properties, and the dimensions of the feature in question, beam theory can be used to describe the bending mechanics of said feature, i.e. predict the deflection under a given load. The basic idea is that a pillar can be idealised as a 3-dimensional beam with a 2-dimensional cross section under a point load – a cantilever. There are many cases of the theory of linear elasticity, but by far the most prevalent in engineering is the Euler-Bernoulli beam theory. It provides a means of calculating the deflection characteristics of beams under specific loading conditions, assuming that the strain due to bending is much greater than any strain due to internal stress of the pillar. This scenario is depicted in **(Figure 4.1)**.

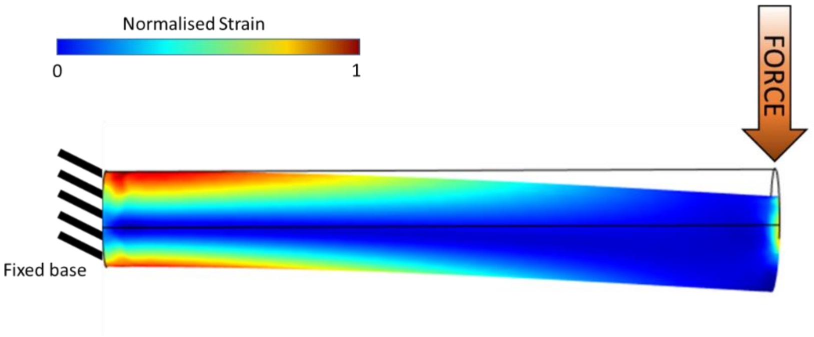

Figure 4.1 - FEA representation of a cantilever under an applied load. An applied force at the cantilever tip, with the standard Euler-Bernoulli assumptions of a fixed base and free end results in the illustrated bending mechanics.

The static equation is as follows:

$$\frac{d^2}{dx^2}\left[EI\frac{d^2w(x)}{dx^2}\right] = f$$ **Equation 4.5**

Where E is the Young's modulus, I is the second moment of area of a circular cross section, ($I = \frac{\pi}{4}r^4$), where r is the radius, w(x) is a function describing the deflection of the beam from its neutral axis at point x along the length of the beam, and f is a distributed load, i.e. a force per unit area. E and I are held constant in this equation; else they would need to be included in the derivative.

Using the special case of a cantilever beam, boundary conditions can be placed on the system in order to simplify the calculation. The beam is considered to be entirely fixed at one end, and entirely free at the other.

There are no torsional effects considered along the beam, due to the assumption that any deformation will be mainly due to deflection, and such strains will be minimal by comparison. The bending moments, shear forces and deflections of the beam will be linearly distributed along the length of the beam, with the shear force constant along the length, and the bending moment maximum at the base, and zero at the tip, where the deflection is largest. The spring constant is calculated from Hooke's law:

$$F = -k * \delta$$ **Equation 4.6**

Where F is the applied load, or force, k is the spring constant and δ is the change in dimension as a result of the force. As Hooke's law typically applies to a spring, δ typically is measured as the change in length, and the –ve sign implicates the force is restorative.

For a cantilever under a load, δ is taken to be the maximum deflection, in this case the deflection of the pillar tip. In this case, **Equation 4.6** becomes:

$$w_{max} = \frac{PL^3}{3EI}$$ **Equation 4.7**

Where P is a unit force, a point load. Rearranging for Hooke's law:

$$k_{EB} = \frac{3EI}{L^3}$$ **Equation 4.8**

where L is the length of the beam. This will hold for all: $\varepsilon_{bend} \gg \varepsilon_{shear}$ This will be termed the *shear criterion*.

4.1.2 Free base model

The first test is to determine the differences that exist between the Euler-Bernoulli calculations and finite element models where the base assumptions are challenged. To do this, an array of pillars with different aspect-ratios was created in COMSOL. These pillars were trialled in two cases, one where the base was fixed, and another where the pillar base was connected in union with a block of polycarbonate material deemed to be large enough with respect to the pillars under modelling to prevent any constriction of results, whilst minimising the time needed to model. This block was fixed in place to prevent any displacement of the base during experimentation.

Initial k_{EB} calculations were compared with cylinders modelled with a fixed base, and little to no difference was found between them, which is promising, as agreement between a model and a well-tested theory is always reassuring.

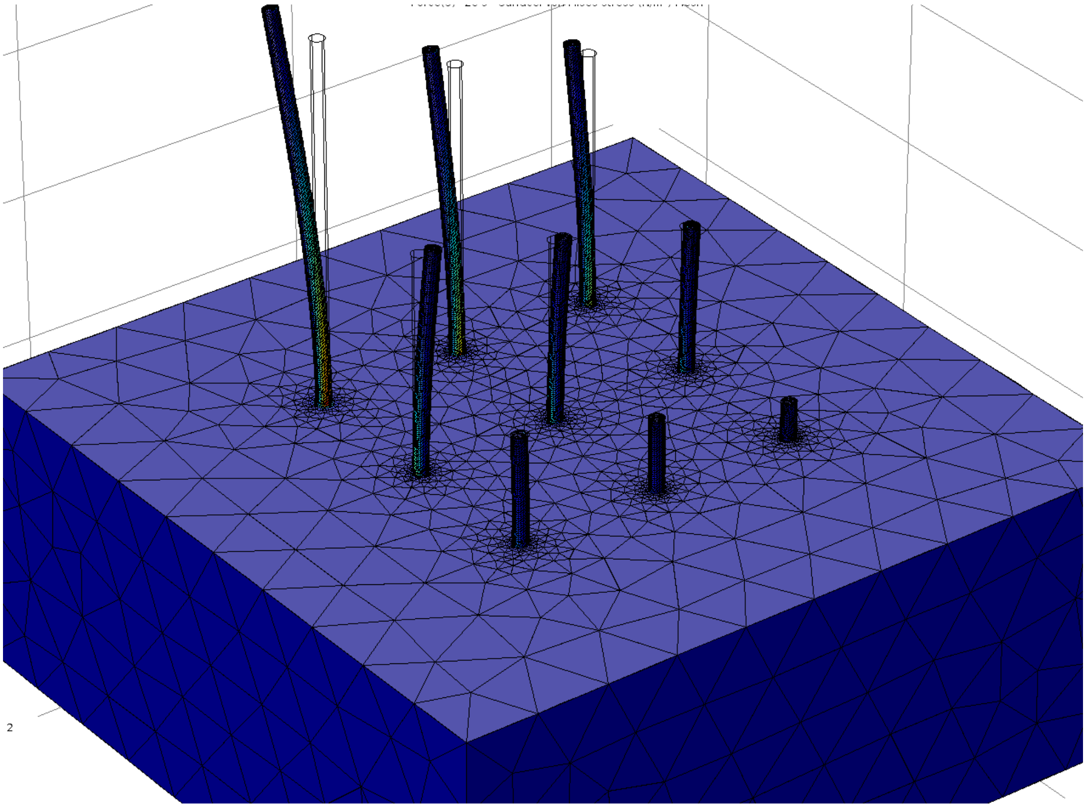

Figure 4.2 - FEA model used to determine the deflection under force of pillars of different aspect ratios. Here, aspect ratios are 25, 20, 17.5, 15, 12.5, 10, 7.5, 5 and 2.5 from left to right, top to bottom.

The Euler-Bernoulli calculations for cylindrical pillars of uniform cross section, diameter 100 nm, and heights ranging from 250 nm to 4000 nm were compared to COMSOL FEA simulation results of the same pillars. COMSOL determines the overall deflection of the pillar tips from their original position as a force is applied. By dividing the applied force by the displacement of the pillar tip, the spring constant of the model can be derived.

Firstly, a margin of error for the calculation must be established. From the literature, as in **chapter 3.0**, bulk PDMS is often quoted as having a standard error of around 20%[35], with a more extensive review of the literature giving a figure closer to 17% **Table 1.1**. For the purposes of these nanoscale features, however, an error in calculation of 10% would place any spring constant calculation within the same error range as the fabrication errors measured earlier, and still be small enough so as to keep arrays with stiffness of interest within the established boundaries of known cell response, see **Figure 3.7**. This would also place it in the higher range of pillar mechanical prediction accuracy than most of the literature.

The results, shown in **(Figure 4.3)**, show that even at high aspect ratios, the Euler-Bernoulli beam equation does not calculate to within 100% accuracy the pillar spring constant.

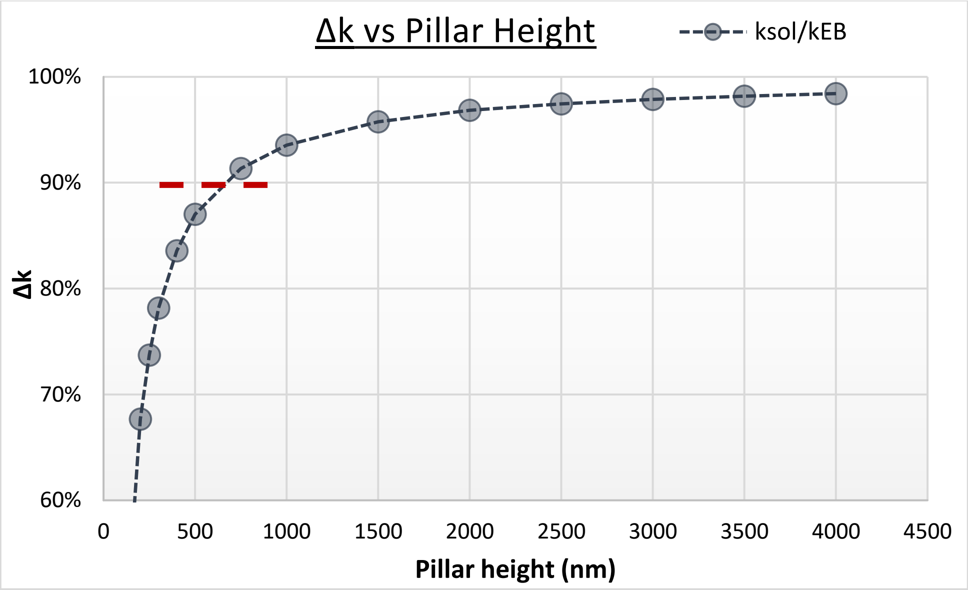

Figure 4.3 - graph of Δk vs pillar height, or aspect ratio, generated by dividing the simulated pillar spring constant (k_{sol}) by the calculated spring constant k_{EB}. Pillar diameter 100nm.

Looking at the figure, the 10% mark for error appears to occur at the shoulder of this graph, highlighted in red, at a value of an aspect ratio of 6.5:1, h:d. Anything above this can be reasonably represented using the Euler-Bernoulli equation. Anything above 20:1 begins to approach the value generated using the Euler-Bernoulli equation.

The shoulder represents the critical point at which the Euler-Bernoulli equation rapidly begins to over-estimate the stiffness of the pillar under force. This is surprisingly sharp and accelerates as the aspect ratio approaches zero.

This critical point is at an aspect ratio of 6:1, which is in contrast to the literature, which often quotes 10:1 as being the critical point of k_{EB} accuracy when comparing experimental or FEA results to calculations[77, 78, 80].

A number of reasons could be the cause. Primarily, the beam could be undergoing internal shear near the base of the pillar regardless of aspect ratio[80]. Another explanation could be that internal shear along the pillar axis is too great to be considered within the shear criterion. This implies that Timoshenko beam theory should be used at all times when considering cantilever beams made of materials with Poisson's ratio less than 0.5.

Lastly, it could be that the scale is not being taken into account in the finite element model. Any sub-nanoscale movements of the pillars would be considered infinitesimal. Taking this into account, any variance below 0.1nm will be excluded from the dataset and spring constant calculations. These are sub-angstrom, and nonsensical. However, this is not really an issue when comparing models, as the physics here scales with size. Regardless, at these high aspect ratios, the difference of 2% in the calculated vs simulated spring constants is negligible, counting for, at most, 0.1 pN/nm, which falls well within any measure of error that can be applied to such fabricated features.

Only when the spring constants begin to enter the 10's of pN/nm can these differences begin to be thought of as significant, and this only increases the stiffer the relative pillar becomes. As this happens, the calculations begin to magnify the pillar stiffness with increasing magnitude. Looking at the potential reasons for this diversion, in more detail, the two possible hypothesis that arise are:

- Either the pillar warps at the base, indicative of a bending moment that reaches a maxima somewhere *below* the pillar base, or
- The pillar is undergoing a measure of shear deformation along its neutral axis that the standard model is ignoring.

Investigations into this using FEA indicate that the answer is both.

4.1.3 Accounting for base-substrate interactions with FEA

One – fixing the base does not allow for base-substrate interactions to be measured.

Bending moment is considered maximum at the base, if this is not the case, then deflection is either not maximum at the pillar's free end, or there is some shear deformation of the pillar around the point at which it meets the substrate. COMSOL FEA allows for clear visualisation of this. Using a 2D approximation, the deflection magnitude can be visualised within each element. The deformation gradient can also be measured. These both clearly demonstrate that at the pillar base, regardless of aspect ratio, there is a reaction into the polycarbonate bulk that is *not* accounted for by this case Euler-Bernoulli beam theory alone.

(Figure 4.4) demonstrates a 2-D cross section of a model of one of the lower aspect ratio pillars – the 5:1 pillar. The finite elements in the free-base model can visibly be seen to be displacing at the base.

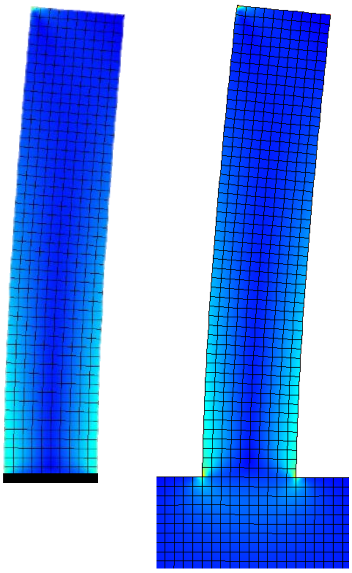

Figure 4.4 - FEA model used to determine pillar-base deformations. Finite element model results for stress at each element of fixed-base and free-base models to demonstrate the introduction of strain and rotation at the base in the model.

When comparing the fixed-base model to the free-base, it can be seen that by applying the fixed-base condition, the stress is restricted to the end of the pillar, whereas in reality it penetrates into the bulk, likely causing base-buckling. When measuring the deformation gradient of all z-axis (height) elements in the direction of displacement (here in the y-axis), this becomes even more apparent, see **(Figure 4.5)**.

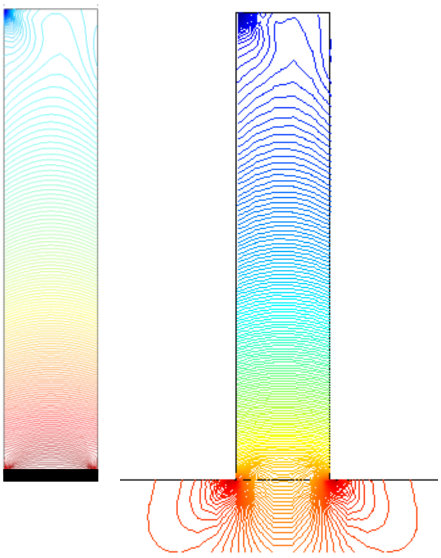

Figure 4.5 - FEA model results outlining deformation gradients along a fixed base and free base pillar. Finite element model results for deformation gradient along the pillar length, and into the material bulk.

A shear force is therefore applied around the pillar-substrate ‘joint’ – whilst there is no physical joint here, it is helpful to define this point in the structure as such to differentiate the ideal pillar from the bulk substrate.

The boundary conditions of the equation must then be revisited for these lower aspect-ratio pillars, or as is often the trend in the literature, a case-by-case amendment to the k_{EB} equation can be fabricated[77-80]. Here, one of two methods could be used. One is to follow the literature examples and attempt to account for torsion of the pillar base, or base-tilting. The other is to use linear regression analysis to determine the function w(h), displacement at height, in order to determine the point below the pillar at which a new *virtual base* can be established, a novel approach to determining this change.

As deflection will be non-zero at h = 0 of the pillar, i.e. at the substrate surface, by creating a new pillar of height $h + \Delta$, a new spring constant can be established. These deflection curves are material and aspect ratio based, however generally follow the same trend. However, due to these shear changes being so minimal at aspect ratios of interest, this was not deemed necessary to carry out. The method for doing this, however, should short pillar deformations become more interesting to study, would be simple.

4.1.4 Accounting for shear deformations along the pillar length

Two – the model fails to account for torsional forces and shear deformations.

The basic assumption of the Euler-Bernoulli beam theory, across all cases, has been termed in this text the shear criterion. A good method of demonstrating how a bending beam might fail to meet this criterion is using the following diagram, demonstrating a beam bending under Euler-Bernoulli assumptions, and then under those of *Timoshenko's beam theory*[83].

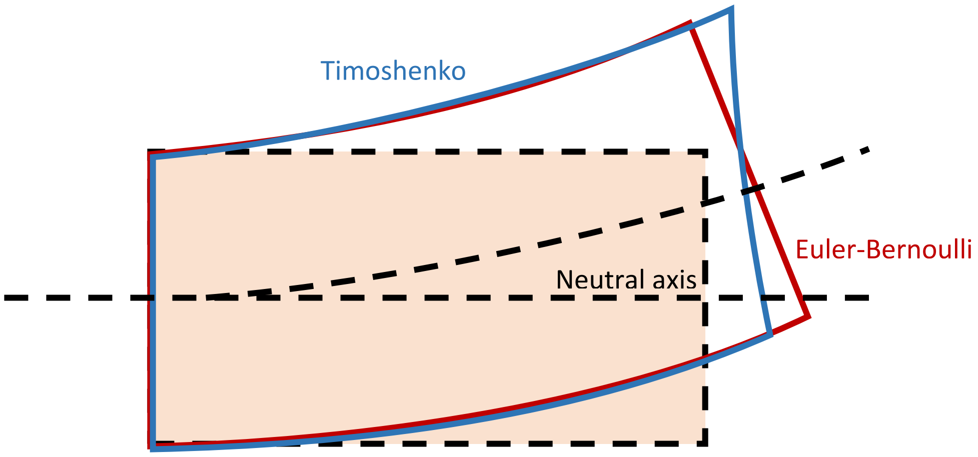

Figure 4.6 – Timoshenko bending vs Euler-Bernoulli bending. Diagram of the cross section of a bending beam, with Euler-Bernoulli assumptions (red) and using Timoshenko-beam theory (blue), including possible shear deformations.

Timoshenko's beam theory accounts for shear defamations by introducing a second term to the beam equation. This extended equation collapses to that of the Euler-Bernoulli beam if the following term approaches 1.

$$L/\kappa GA$$

Equation 4.9

Where κ is the Timoshenko shear coefficient. This appears to happen, even slightly, at higher aspect ratios, and by looking at what terms are dominant for the diameter:height ratio, where aspect ratio decreases, the shear term becomes the dominant factor in divergence from Euler-Bernoulli theory.

These shear deformations account for the discrepancy between the Euler-Bernoulli calculation and the FEA model. The pillar tip will deflect *more* when these strains are accounted for, causing the deflection to be larger, and therefore the spring constant to be lower. The degree to which shear deformation accounts for this change in deflection magnitude can be compared to the induction of non-zero deflection at the pillar base. Overall, the shear deformations dwarf these base deflections, which typically are less than 0.1 nm, or roughly 1% that of the pillar top.

Including the Timoshenko amendment into the Euler-Bernoulli equation is, therefore, only necessary when the aspect ratio is less that 6.5:1. Ideally, the fabricated pillars should be of aspect ratio 10:1 in order to have high certainty that the calculated values of k_{EB} are accurate, therefore it depends on the end-function of the technology, and how sensitive the experiment can be to discrepancies in this value.

With the threshold of tolerance set at an aspect ratio of 6.5:1, the study was expanded to varying the material properties of the substrate. It stands to reason that if base-compressibility was an important factor in the induction of higher levels of tip deflection, that by changing this value in the model, holding Poisson's ratio constant, then the divergence from k_{EB} should increase. The data did not confirm this.

Interestingly, the difference between these two values was found to be negligible, despite changing E from 100GPa to 1kPa, the variance remained almost constant. Looking further into the Timoshenko equation for the special case under consideration, **Equation 4.10**, the reason for this can be deducted, much in the same manner as previously alluded to.

$$w(x) = \frac{P(l-x)}{\kappa AG} - \frac{Px}{2EI}\left(L^2 - \frac{x^2}{3}\right) + \frac{PL^3}{3EI}$$ **Equation 4.10**

Examining this for the case x=0, i.e. w(x) is max., the shear term of the equation reduces to L/κAG and the Euler-Bernoulli term. That means that the change in spring constant at lower aspect ratios is dependent on the Timoshenko shear coefficient, the cross section area and the shear modulus.

4.1.5 Examining the effect of a taper on Euler-Bernoulli assumptions

The value $A/_L$ is the dominant relationship in the shear term, similar to the $I/_{L^3}$ relationship in the Euler-Bernoulli term, explaining the relative invariance to changes in Young's modulus in the simulation, as for *both* the shear and bending terms of the equation, the relationship of diameter to height is given a larger weight, $r^2/_L$ and $r^4/_{L^3}$ respectively.

Sidewall angle, or beam taper, however, plays an important role in the applicability of the Euler-Bernoulli formula.

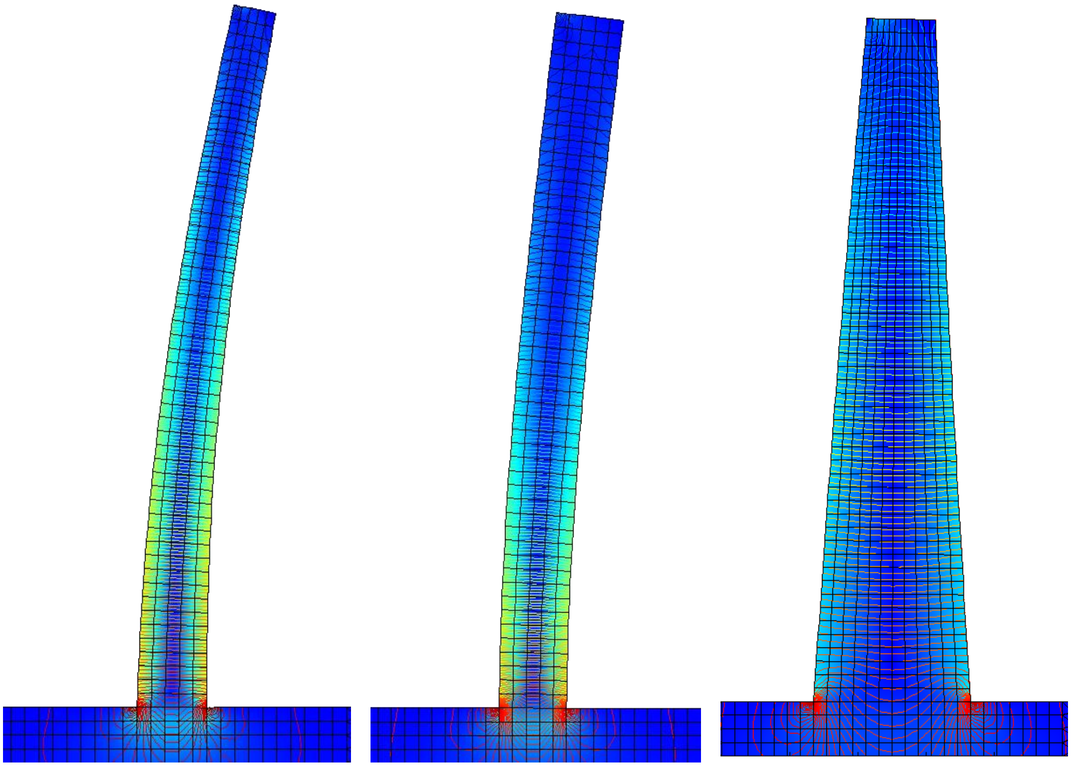

Figure 4.7 - FEA example comparison of tapered beams. A taper to a narrower tip than the cylindrical model, a cylindrical model, and a taper that decreases towards the width of the cylindrical model left to right.

As will be explained in more detail in the next section, there exists an amendment to the equation derived for a conically tapered beam of linear d(h) relationship. This was used to calculate the spring constants of the test cases.

Increasing this taper, or decreasing the d_T/d_B ratio, can be thought of as *artificially lowering* the aspect ratio of the beam in question **(Figure 4.7).** There exists a larger bulk of the pillar at the base, and this will undergo more shearing strain than a cylindrical beam might.

Looking at the data, in which multiple tip to base diameter (d_T/d_B) ratios and pillar heights were trialled. (**Figure 4.8**) outlines the results of the change in spring constant between calculated and modelled spring constants of pillars with changing aspect ratio, but constant diameter ratio. In order to be able to draw a comparison to a cylindrical model, aspect ratio was used as the x-axis.

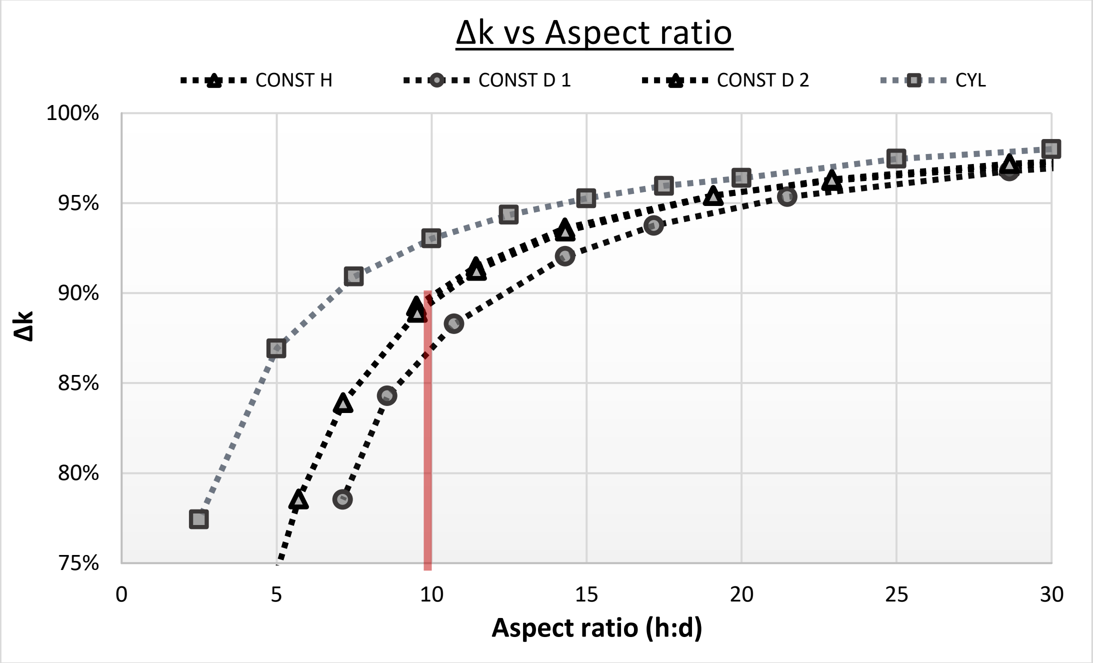

Figure 4.8 - Graph of the change aspect ratio has on tapered beams. Graph of ksol / kEB for four sets of data – cylindrical pillars, (CYL) constant diameter datasets 1 and 2, CONST D 1 and CONST D 2 respectively, and one constant height dataset, CONST H. The red bar marks where the smalletst tapered non-linear pillar models cross the 10% threshold.

From this graph, it can be noted that the shoulder of these curves collapse towards a more linear relationship, though it never reaches such. This is interesting, as it demonstrates the nonlinear interaction between taper and aspect ratio. For two different d_T/d_B the same aspect ratio when measured from the pillar tip will produce different Δk relationships, however they all converge around the same point at 10% error.

The values inevitably converge on the cylindrical relationship at higher aspect ratios, those of 20:1 or larger, but what can be seen is that the introduction of any taper will change the point at which an analytical calculation can be used appropriately. This is unsurprising as the pillar area will reach parity with an ideal cylinder at some sidewall angle:height relationship.

What is arguably most interesting about figure **4,8** is the jump that exists between a cylindrical pillar of changing aspect ratio, and those with a changing sidewall angle/aspect ratio relationship. A future line of investigation, if warranted, would be to develop a relationship based on the change in area/volume of a pillar and its cylindrical counterpart. This would allow for more direct comparisons to be made. Also of note is the parity between the constant height, and the constant diameter ratio 2 relationships. This implies a sidewall angle–aspect ratio relationship that could be derived, should it be deemed necessary.

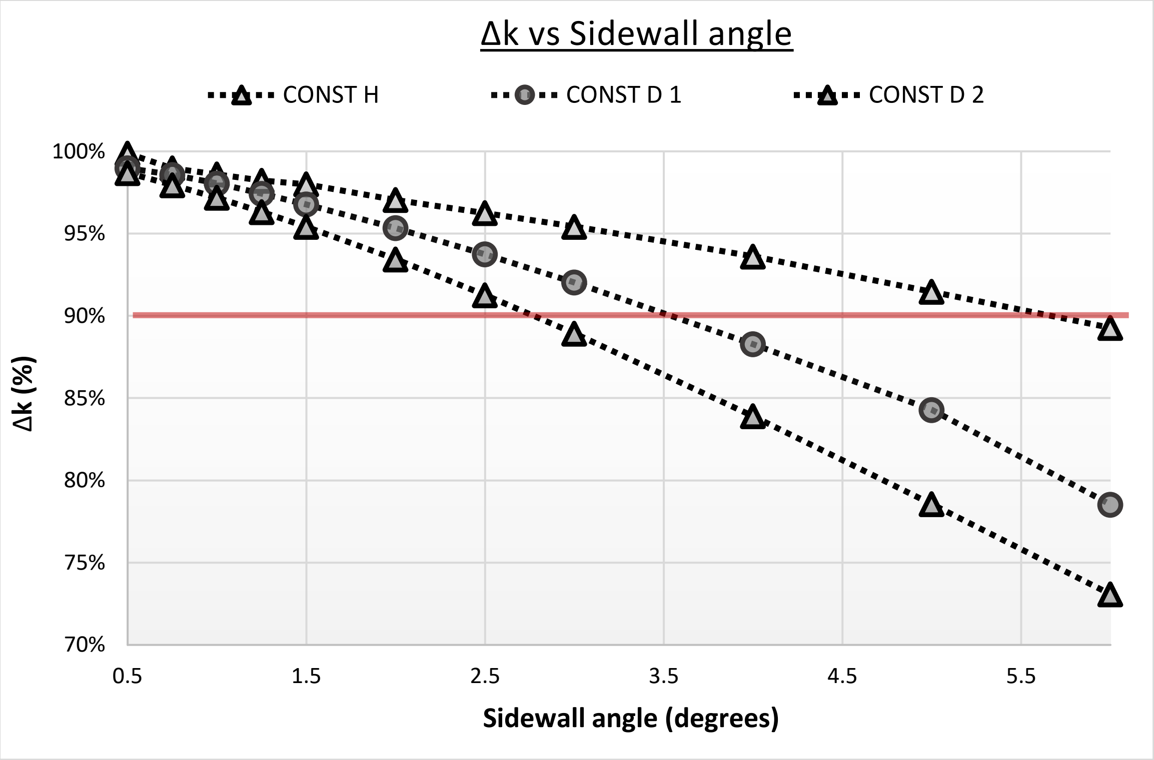

Figure 4.9 – Graph of the change sidewall angle has on tapered beams. Graph of ksol / kEB for three sets of data; constant diameter datasets 1 and 2, CONST D 1 and CONST D 2 respectively, and one constant height dataset, CONST H. The red bar marks where models cross the 10% threshold.

Looking at figure **number**, it can be seen that at a Δk value of 10%, the first dataset to cross this threshold is at 3°. All trialled interpolations between these representative datasets lie above this lower limit. A stricter limit of significant divergence, it can be argued, should apply to around a 5% change, where the gradient of these curves begin to accelerate, however for pillars with anything more than a 5nm, 1 pixel error, which equates to around a 5% change in diameter for the most commonly used pillars in this thesis, 100nm diameter tip, the change introduced due to measurement error is large enough to negate this. In summary, the data demonstrate that at sidewall angles of 3° or larger, a pillar must have an aspect ratio of 10:1 or higher in order to be considered similar enough to the modelled counterpart to warrant the use of the Euler-Bernoulli spring constant equation. For pillars with a sidewall angle of less than this, the values begin to collapse towards the cylindrical model.

The sidewall angle impact on the applicability of the Euler-Bernoulli approximation, that includes the taper amendment, therefore results in the *sidewall criterion* – namely:

$$if \left\{\begin{matrix} \angle_{SW} < 3° \\ \& \\ AR > 6.5:1 \end{matrix}\right\} then\ k_{EB} \approx k_{SOL}$$

$$if \left\{\begin{matrix} \angle_{SW} > 3° \\ \& \\ AR > 10:1 \end{matrix}\right\} then\ k_{EB} \approx k_{SOL}$$

Where $\angle_{SW}$ is the pillar sidewall angle, AR is the aspect ratio, k_{EB} is the spring constant calculated from the Euler-Bernoulli equation, and k_{SOL} is the spring constant calculated from the FEA model, where accuracy to the solution is determined by a hard error limit of 10%.

It is also important to note here that the amendment to include the taper in the Euler-Bernoulli equation does not fully account for the differences invoked by such a taper when comparing the results to pillars with a free-base.

This is important. It demonstrates that at more dramatic tapers, that is tapers with larger gradients, the shear forces begin to become non-negligible. Above sidewall angles of 3°, the aspect ratio is significantly, artificially lowered so as to need the Timoshenko shear relationship to be taken into account. To conclude this investigation, then, some points are to be noted.

For a cylindrical beam, the Euler-Bernoulli formula is applicable at aspect ratios above 6.5:1, d:h, with a critical aspect ratio of 6:1 where the shear criterion begins to break down. For aspect ratios above 10:1, the formula approaches unity with the model values, in agreement with literature. The reasons for this are twofold:

1. The fixed base assumption is, technically, invalid at all aspect ratios, with an exponential relationship with a maxima approaching 99% agreement.

This is because the bending is non-zero at the pillar base – i.e. there is a bending moment maxima that penetrates into the substrate bulk. This can be calculated, however at relevant aspect ratios to the work it can be excluded due to the small values of the pillar spring constants used.

2. The Euler-Bernoulli formula excludes torsional forces and internal pillar shear deformations.

This again is only relevant for shorter pillars, and using Timoshenko beam theory, along with an artificial pillar aspect ratio constant established by the bending curve, can account for the exaggeration of pillar stiffness. Looking at the additional term in the Timoshenko cantilever case, it can be seen that aspect ratio is still the dominant factor.

Turning our attention to the effect of changing material properties, specifically E, this assertion is backed up by the very minimal change in Δk values. The important factor for this body of work, and arguably the literature on the whole, is sidewall angle. No replicated pillar is going to be 100% cylindrical, and even a 5% difference between tip and base diameters can cause an increase in pillar spring constant by 15%. This artificial lowering of aspect ratio changes the aspect ratio minimum for EB to be applicable, and is described by the sidewall criterion.

Overall, for pillars fabricated in this body of work, Euler-Bernoulli approximations are appropriate measures, or predictions, of nanopillar spring constants, and therefore array equivalent rigidities. However care must be given when utilising the standard formula. This chapter section gives criteria that must be met in order to use the standard spring constant equation, in relation to aspect ratio of fabricated devices and any taper present in the profile, measured by the ratio: ${d_T}/{d_B}$ – a statement that as of the time of writing does not appear anywhere in the literature.

4.2 Deriving the general formula for a non-linear taper

As stated before, the pillars fabricated via injection moulding are not cylindrical. **(Figure 4.10)** demonstrates some of the measured pillar profiles from injection moulding that had significant variance from those that could be considered within enough of a margin of error for the cylindrical model to be appropriate.

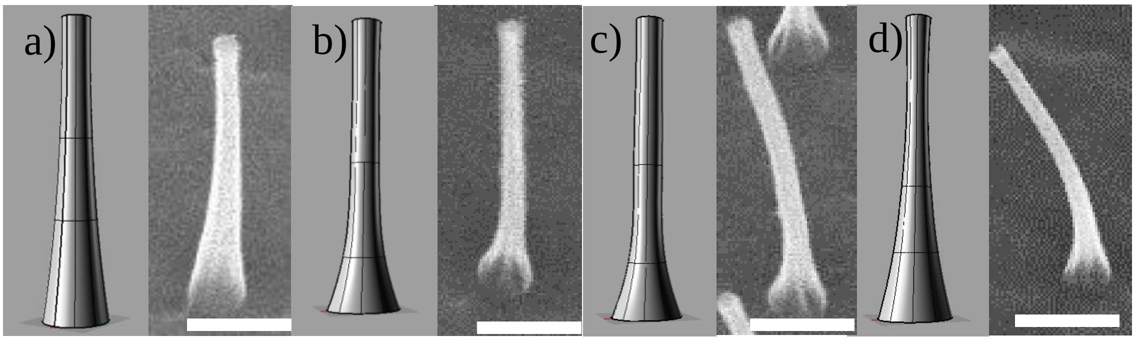

Figure 4.10 - Examples of stretched pillars with non-linear tapers. Rendering and SEM of nanopillars taken from measurements along the height. Scale bar 250nm.

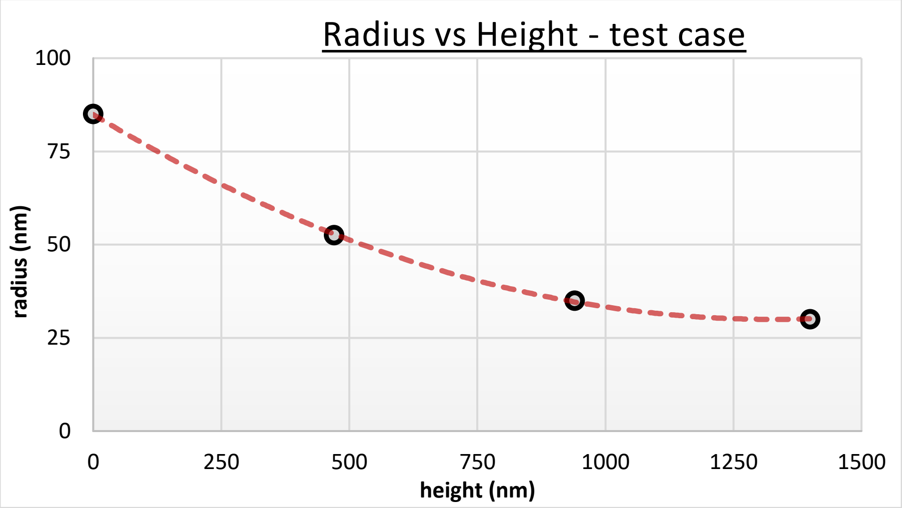

Figure 4.11 - Example of the r(h) relationship of a stretched UHAR nanopillar. An example of a typical r(h) relationship of a stretched pillar, deviating from the linear profile into a polynomic one.

For larger sidewall angles of the pillar master, the replicated pillars have a linear profile. The derivation of the spring constant of such a pillar, following the Euler-Bernoulli formula, is well described in the literature**[84]**. The important assumption violated by having a height dependent diameter is that of a continuous cross section, therefore the factor I, the second moment of area, changes along the beam – it is no longer constant.

Looking to the linear case as described in the literature, the Euler-Bernoulli formula can be rearranged in terms of the bending moment, and uses a first order Bézier curve to describe the function d(h) which is normalised to the length of the beam, L, such that:

$$\xi = \frac{h}{L}$$ **Equation 4.11**

Where h represents some distance along the beam, and L is the absolute length of the beam. The function d(h) now becomes d(ξ), and is represented by:

$$d(\xi) = d_T[1 + \xi(\gamma - 1)]$$ **Equation 4.12**

Where $\gamma = {}^{d_B}/_{d_T}$ - the relationship between base and tip diameter.

Thus:

$$I(\xi) = I'[1 + \xi(\gamma - 1)]$$ **Equation 4.13**

Where I' is the second moment of area of the cross section at d_T. There also exists the formulation of w(h) with respect to the concept of virtual work, such that w(h) becomes:

$$w(h) = \frac{PL^3}{EI'} \int_0^1 \frac{\xi^2}{[1 + \xi(\gamma - 1)]^4} \, d\xi \qquad \textbf{Equation 4.14}$$

And after integrating with respect to ξ ;

$$w(h) = \frac{PL^3}{3EI'} * \frac{1}{\gamma^3} \qquad \textbf{Equation 4.15}$$

And

$$k_{con} = k_{dT} * \gamma^3 \qquad \textbf{Equation 4.16}$$

By replicating this process and using a quadratic polynomial for the d(h) relationship, or a second order Bézier curve for the d(ξ) relationship, a generalised formula that describes the deflection behaviour of a pillar with a non-linear taper can be derived with more straightforward calculation. The simplest method of doing this would be to use the virtual work formulation and a Bézier d(ξ) relationship, however there is an issue with this.

4.2.1 Background on Bézier curves

An aside on Bézier curves: these curves operate by defining a series of points in a global co-ordinate system, called *control points*, and then linearly interpolating a series of tangents that lie on points on a virtual curve to create a polynomic curve in said co-ordinate system.

For a linear curve, i.e. a straight line, **Equation 4.17** is a simplified version of the standard expression of a first order Bézier curve, which can be written as follows:

$$d(\xi) = P_0 + \xi(P_1 - P_0) \qquad \textbf{Equation 4.17}$$

Where P_0 and P_1 are the end points of the curve, expressed in x and y co-ordinates for the purposes of plotting the curve. In this case, P_0 and P_1, the ends of the curve are simply d_B and d_T. Linearly interpolating between these points gives a straight line of standard formula y = mx + c.

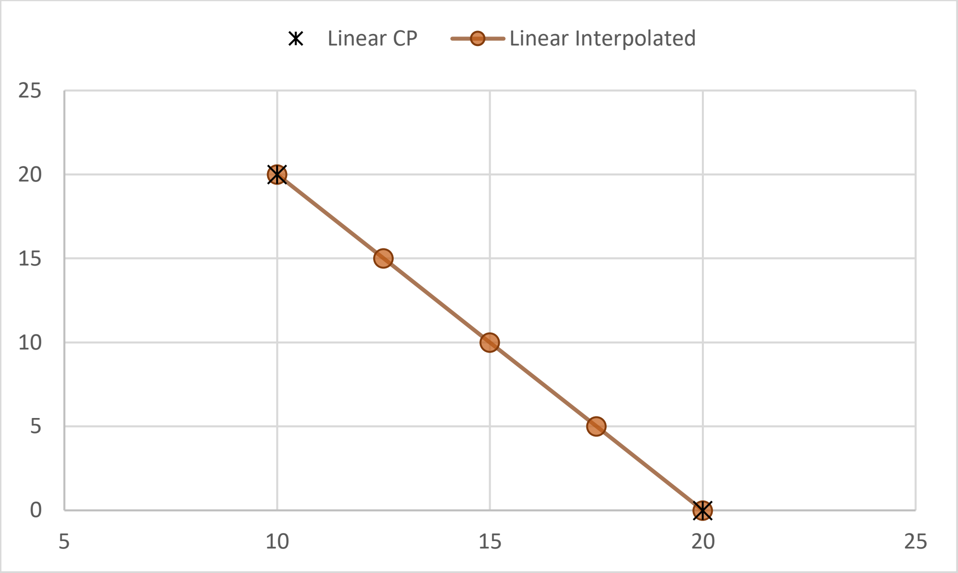

Figure 4.12 - Example of a first order (linear) Bézier curve with control points

When moving to a second order curve, an additional control point is needed to describe the curve formed, such that there are three control points: $P_{0,}$ P_1 and P_2, where P_0 and P_2 are d_B and d_T, following the formula:

$$d(\xi) = (1-\xi)^2 P_0 + 2\xi(1-\xi)P_1 + \xi^2 P_2 \qquad \textbf{Equation 4.18}$$

This control point, P_1, determines the point at which the curve begins to take place, and is *not* necessarily a point on the curve itself. Therefore, it is not as simple as taking, say, three readings – tip, mid and base diameter – and applying a quadratic polynomial of formula $ax^2 + bx + c$.

A Bézier curve must be fitted to the measured d(h) profile, and the value of P_1 determined for accurate calculation of the function d(ξ) and integration into the general formula for a non-linear taper.

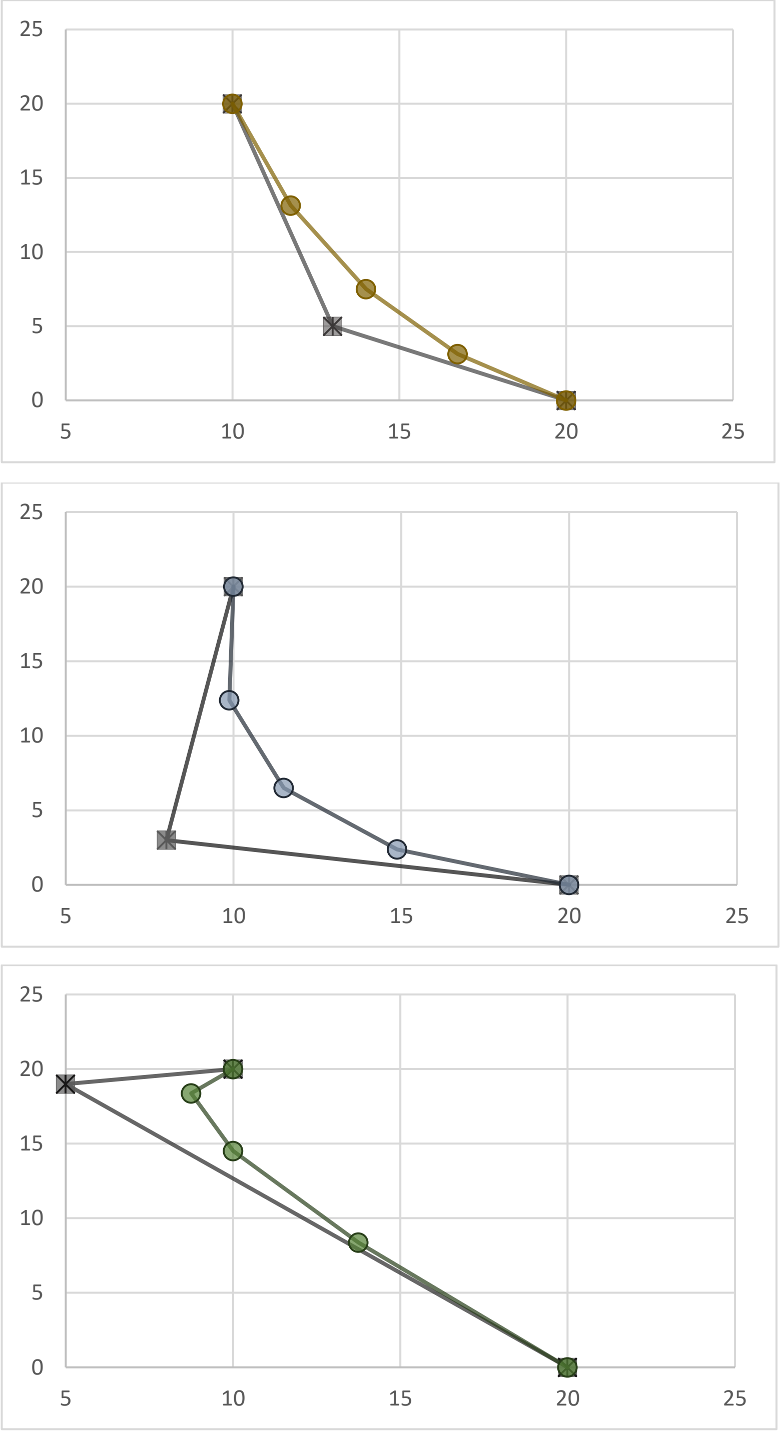

Control points:

$P_0 = (10,20)$

$P_1 = (13,5)$

$P_2 = (20,0)$

Control points:

$P_0 = (10,20)$

$P_1 = (8,3)$

$P_2 = (20,0)$

Control points:

$P_0 = (10,20)$

$P_1 = (5,19)$

$P_2 = (20,0)$

Figure 4.13 – Examples of Bézier curves obtained by simply varying the mid-cotnrol point P1.

In fact, Bézier curves are used in most computer graphics design programs to fabricated curved surfaces as it lowers the amount of lengthy calculation necessary to fabricate such results.

This is also true for use of COMSOL FEA software, and so was a necessary step for modelling any d(h) relationship. Therefore, establishing a P_1 value would be necessary whether a quadratic, or Bézier relationship was to be used.

To find P_1, a script was written in Matlab to cycle through a number of possible P_1 values and compare the calculated d(ξ) relationship with the measured d(h). The closest approximate d(ξ)'s P_1 value was then used for both calculation of the general formula, and for modelling in COMSOL. With this Matlab script in place, the operation of which has been explained in the methods section, second order Bézeier curve d(h) relationships could be derived and used for both modelling, and the generalised formula. Whilst this is not ideal, it is a simple enough task to derive the Bézier formula for a curve, so it still should be useful outside of this body of work.

4.2.2 Applying the Bézier relationship to the Euler-Bernoulli case

The mathematics, at first, seems relatively straightforward. The d(ξ) formula is simply inserted into the second area moment equation, and, as per the literature example, I(h) becomes:

$$I(\xi) = I'[\,(1-\xi)^2 P_0 + 2\xi(1-\xi)P_1 + \xi^2 P_2] \qquad \textbf{Equation 4.19}$$

This is then substituted into **Equation 4.14**:

$$w(h) = \frac{PL^3}{EI'}\int_0^1 \frac{\xi^2}{[\,(1-\xi)^2 P_0 + 2\xi(1-\xi)P_1 + \xi^2 P_2]^4}\,d\xi \qquad \textbf{Equation 4.20}$$

Now the maths becomes difficult. Integration of this formula appears pretty straight forward, however integrating what is, essentially, a quadratic polynomial raised to the *negative* fourth power is lengthy and difficult, both things that work against a productive thesis. m

The answer, then, is to somehow bring all of the relevant ξ-dependent terms into the numerator so that a straightforward integration can be carried out. The way to do this is to use a Maclaurin series expansion. This is a Taylor series expansion of a function around 0 and is used to approximate a function f(x) in discrete parts, similar to the way Simpson's rule approximates the integral of the function f(x). The use of a Bézier polynomial simplifies the form of each f(0) term, making the derivation easier, with the added bonus of already being in a format suitable for use in COMSOL modelling.

$$d(h) \approx f(x) = f(0) + f'(0)x + \frac{f''(0)}{2!}x^2 + \frac{f'''(0)}{3!}x^3 + \cdots + \frac{f^{(n)}(0)}{n!}x^n \qquad \textbf{Equation 4.21}$$

The function f(x) here being $f(x) = [d(\xi)]^{-4}$.

Doing so yields the equation:

$$f(\xi) = \frac{1}{{P_0}^4} + \frac{8(P_0 - P_1)}{{P_0}^5}\xi - \frac{4[2(P_0 - P_1) + 2(P_2 - P_1)]}{2{P_0}^5}\xi^2 + \frac{80(P_0 - P_1)^2}{2{P_0}^6}\xi^2$$ **Equation 4.22**

This can be substituted into **Equation 4.20** and integrated between the ξ values of 0 and 1. Doing so results in the following equation:

$$w(h) = \frac{PL^3}{3EI'} * \left[\frac{1}{{P_0}^4} + \frac{\left(3(P_0 - P_1) + 2(P_2 - P_1)\right)}{5{P_0}^5} + \frac{8(P_0 - P_1)}{{P_0}^6}\right]$$ **Equation 4.23**

Let the latter part of this equation then be termed Δ_{Bz} and rearrange for the spring constant, such that:

$$k_{Bz} = k_{dT} * \frac{1}{\Delta_{Bz}}$$ **Equation 4.24**

Thereby arriving at a general formula that takes the place of an amendment to the Euler-Bernoulli equation for a pillar spring constant. Due to the use of a Maclaurin expansion to arrive at this general formula, there will be a baseline error in the calculation of the k_{Bz} value. The maximum this will be can be estimated by comparing the functions d(h) and f(x). Doing this arrives at a maximum error of roughly 12%, however as will be shown in subsequent investigations of the accuracy of this general formula, this threshold is never reached, most likely due to the integration of the function f(x).

4.3 Testing the general formula, k_{Bz}, against FEA

With the equation for k_{Bz} established, it can now be tested against the results of FEA. Three rounds of testing were performed; two to establish the limitations in which this equation is applicable, and a final third test on the d(h) relationships of the multi-mechanical UHAR slide fabricated nanopillars, which encompass a variety of injection moulded nanopillar morphologies.

It is already known that, due to the use of the Maclaurin expansion, there can be up to a 12% variance between the function integrated, d(ξ) and the expanded function f(ξ). Therefore, any discrepancy beyond this can be attributed solely to violations of the Euler-Bernoulli assumptions, and these should be evident upon investigation of the model. The first case to test was that of a static base-diameter and changing profile d(h).

4.3.1 Static base diameter case

Looking at the SEM examples from **Chapter 3**, which exhibits the largest degree of stretching examples, and from earlier on, a particular case of stretching relative to the diameter base exists, **(Figure 4.10)**, case 2. With reference to **(Figure 3.6)** this can also be evidenced by a single pillar deforming in profile over time. Due to the nature of stretching of features during injection moulding, the stretched profile always deforms relative to a diameter base that remains relatively consistent – hence this test case being called the *static* d_B *case*. Therefore, the first goal is to have the equation satisfy this type of curvature. Four examples of a pillar profile evolving in this manner were investigated, and k_{Bz} calculated and compared to the results of the COMSOL model under Euler-Bernoulli assumptions (**Figure 4.14** and **Figure 4.15**).

From the model, it appears that the calculation consistently overestimates the spring constant by around 3-5% (in real terms this is at most 1pN/nm) until at the last pillar sidewall morphology, the model and the calculation converge, most likely due to minimal variance of the profile from an ideal cylinder, with the largest artificial shortening of aspect ratio being consigned to the base, where highest magnitude of bending moment is concentrated. This does not significantly affect the shift seen when using a free-base model. In fact, these Bezier curve sidewalls, as well as their conical counterparts, demonstrate a higher consistency with the Euler-Bernoulli approach than their cylindrical counterparts, probably due to the distribution of shear along the pillar sidewall.

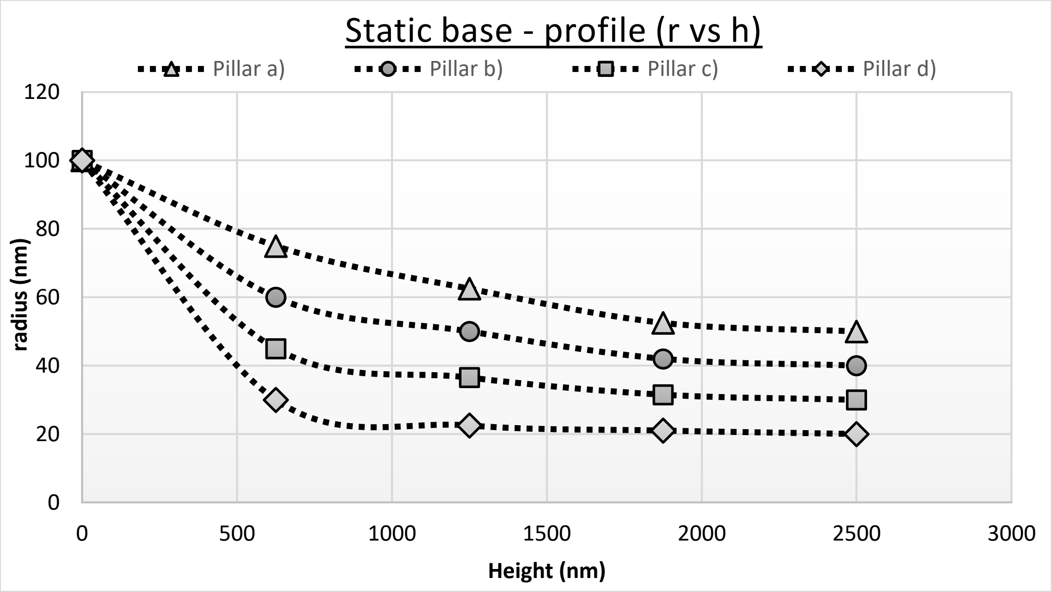

Figure 4.14 - Graph of four case pillar profiles, illustrating changes in stretching. A graph of the four case pillar profiles r(h) from Figure 4.10, with each example pillar a)-d), denoted by a triangle, circle, square and rectangle respectively.

Figure 4.15 - Bar graph demonstrating the difference between the model and calculated spring constants. Illustrates the relationship between the derived general formula and the FEA model results.

The reason for this consistent overestimation could be attributed to the use of the Maclaurin expansion. It would be expected that, if the f(x) were more accurate, this discrepancy would approach zero. It would appear, then, at first instance the approximation is close enough to the FEA model case to be considered appropriate. However, it is prudent to determine the limitations of this with respect to the assumptions of the Euler-Bernoulli model.

To do this, a series of profiles were calculated with different Bézier polynomials to test different $d_T : d_M : d_B$ relationships, and explore the effect that the slope of the curve in between these pillar dimensions has on the veracity of the equation. Taking case examples, different curve types were trialled to determine the point at which the Bezier curve amendment significantly fails to estimate the pillar spring constant.

4.3.2 Testing the limitations of pillar curvature: concave and convex profiles

The metric by which the pillar profiles are assessed is by calculating the gradient of the tangent to the curve at the mid-points between the tip and mid, and the mid and base diameters. These values, termed GDMT and GDMB (gradient at diameter (mid-tip) and gradient at diameter (mid-base)) represent the degree of curvature at these points. The tangent to a Bezier curve of second order is simply the first derivative of the d(t) relationship. By plotting both the sidewall profiles, and the discrepancy between calculated and modelled spring constant under Euler-Bernoulli boundary conditions, the relationship between profile and applicability of this equation can be determined. **(Figure 4.16)** illustrates a selection of the profiles trialled.

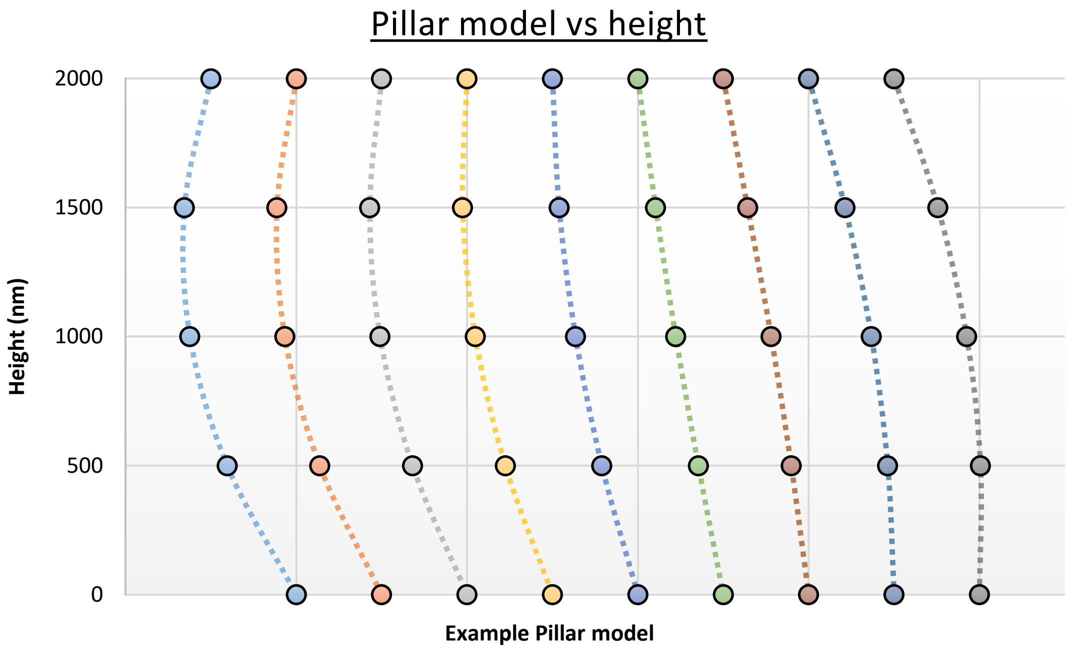

Figure 4.16 - d(h) relationships representing various Bézier curves. These are example d(h) relationships of the curves that were trialled to determine the upper and lower limits of the applicability off the equation, moving from concave to convex, left to right each relationship represents a potential pillar sidewall morphology. What is important here is the transition from concave to convex

The pillar profiles move from dm < dt to dm > dt, concave to convex, passing through an approximately linear relationship of dt:dm:db. The results of the k_{Bz}/k_{SOL} are plotted vs the pillar model number and demonstrate agreement in a somewhat narrow range.

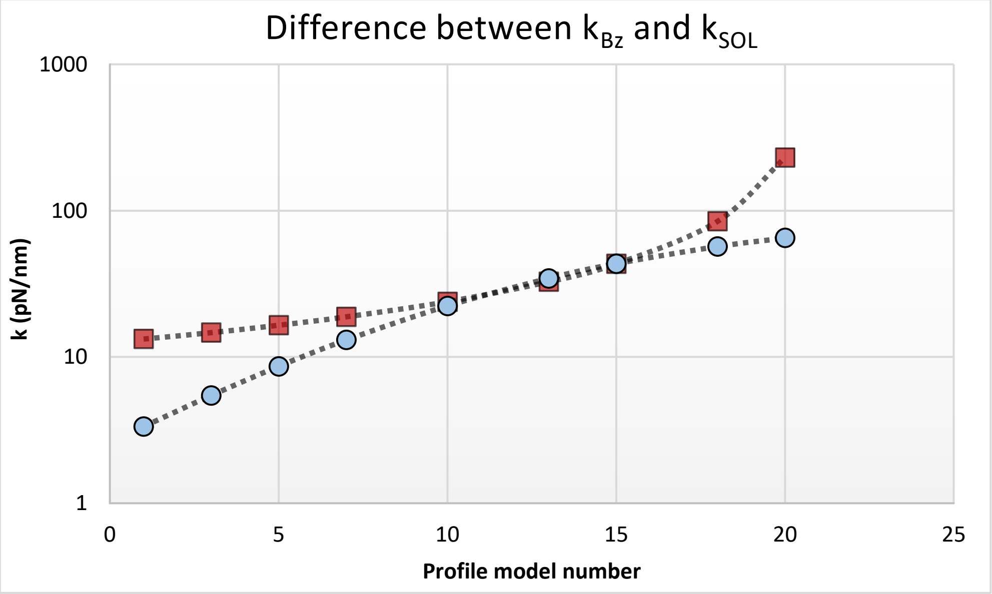

Figure 4.17 - Graph of k_{Bz} and k_{SOL} vs the pillar model number. 20 different Bézier curves were investigated, ranging from very concave to very convex – see Methods – figure 2.5.3 for examples of these, and the results of the calculated spring constant (red square) compared to their FEA modelled counterpart (red square).

The distribution is also skewed. In cases where d_M begins to overtake d_B, the accuracy of the calculation starts to decrease more rapidly than where d_M is less than d_T.

Overall, an error of less than 10% is desirable, this often conforms with fabrication and measurement error ranges, and falls within the range of values that account for a correction of the natural over-estimation in the value of k produced by an Euler-Bernoulli calculation. This places the GMDT range at between -1.5 and -0.5.

The investigation was set up to only allow for two areas of deviation, in the accuracy of the derived equation to the actual phenomena, and in the assumptions inherent to the Euler-Bernoulli theory. Firstly, the bending moment assumptions must be taken into account. These stipulate that they are largest at the pillar base, and minimal at the top. This implies that shear stress is highest at the base, allowing deflection to be largest at the top, and is factored into the Euler-Bernoulli formula.

Looking at the COMSOL simulations of the d_T>d_M cases, this is not true. The stress is highest somewhere between d_B and d_M, indicating that the Euler-Bernoulli boundary conditions are not applicable to this case.

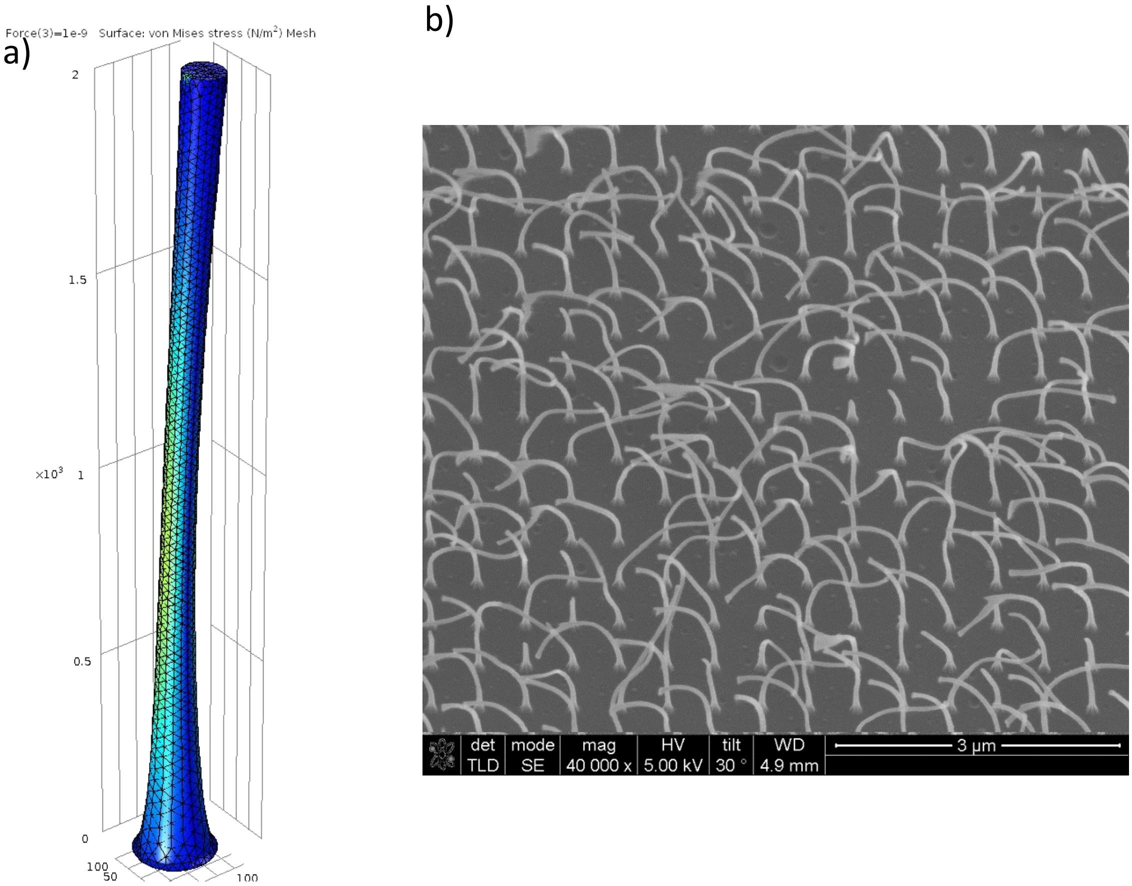

Figure 4.18 - Illustration of the type of pillars prone to collapse that fall outside the limits set on k_{Bz}. a) FEA model of a pillar with $d_T > d_M$, and b) SEM of pillars of similar dimension with compromised structural integrity.

A pillar such as this may be important to study at some point, however, as of the writing of this thesis, almost all pillars that have been fabricated with this morphology are not able to retain structural integrity during or after the demoulding process, and tend to collapse or fail to replicate entirely, such as in figure **(Figure 4.18-b)**.

Profiles in the accepted range encompass all measured pillars of interest and can be quantified by the following criteria.

- $d_T < d_M < d_B$, and
- $-1.5 < d/d\xi\ [d(\xi)]$ at $\xi = 0.75 < -0.5$.

This investigation serves to set hard limits on the taper for this particular case of stretched nanopillars. Within these ranges, and for higher aspect ratio pillars, this range becomes more flexible, such as the examples in the following **(Figure 4.19)**.

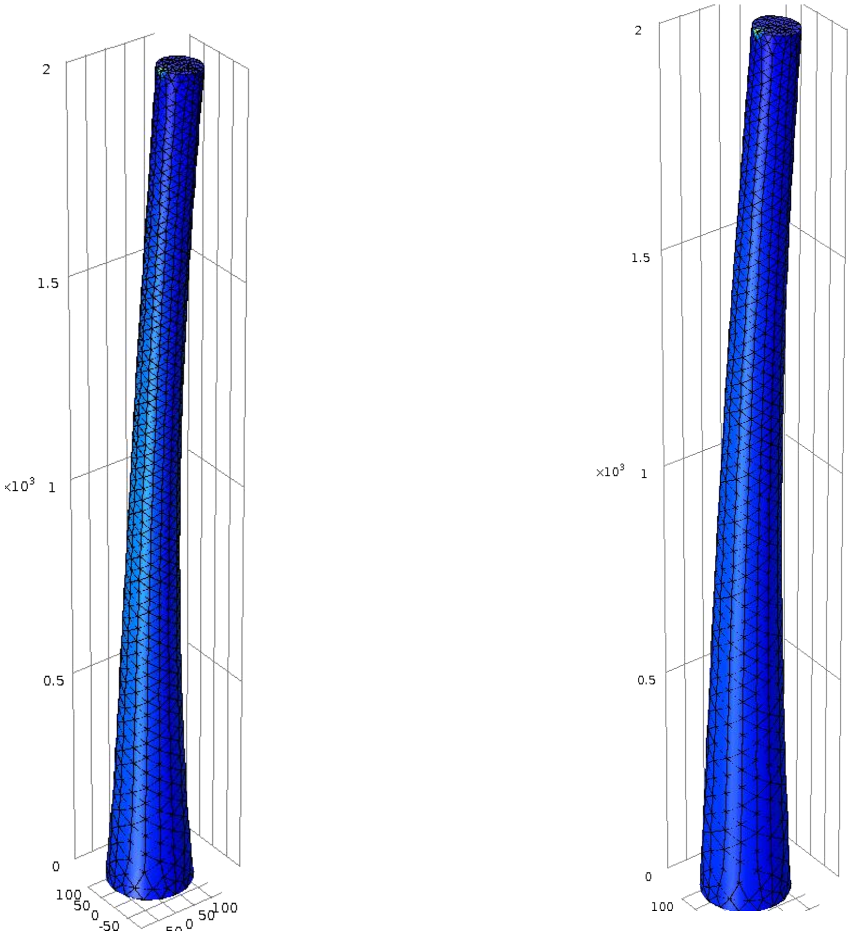

Figure 4.19 - Examples of pillars that fit within the defined Bézier limits. The pillar on the left has a slightly concave profile, tapering inwards towards the centre. This closely matches the type of profile a stretched but structurally intact pillar will have – note the high strain at the centre of the pillar. The pillar on the right approaches a more linear d(h) relationship. The differences, though apparently slight, can cause large variations in the calculated spring constants, with the difference between these two pillars varying by factor 10x..

Finally, with the diameter and gradient of curvature limitations set, the formula can be tested against actually fabricated and analysed pillars that are of relevance to cell biology, with sufficiently variable d(h) relationships, namely pillars from the multi-mechanical UHAR slide.

4.3.3 Testing k_{Bz} against fabricated UHAR nanopillars

These pillars each have different degrees of curvature and stretching, as well as aspect ratios and tip diameters. By comparing the FEA case to the calculated values, the veracity of this approach for all future HAR pillar fabrications can be tested.

Overall – agreement is well within the stated 10% goal, with a maximum variance of 0.06 between the calculated and modelled spring constant values. This variance likely comes down to the use of a Maclaurin approximation in determining the effect of the d(h) relationship on the Euler-Bernoulli equation, as well as potentially some differences between the modelled pillar profile and the calculated one using the Matlab script.

The change between the linear sidewall angle approach, and the calculated values here ranges between 1 and 8 pN/nm, which can affect the calculated value of effective shear modulus of an array by as much as 40kPa. These seemingly small gains in accuracy in determining the pillar spring constant can therefore translate into much larger gains in accuracy when determining the effective array mechanics, highlighting the highly sensitive nature of this approach to substrate fabrication for cell-substrate interaction control.

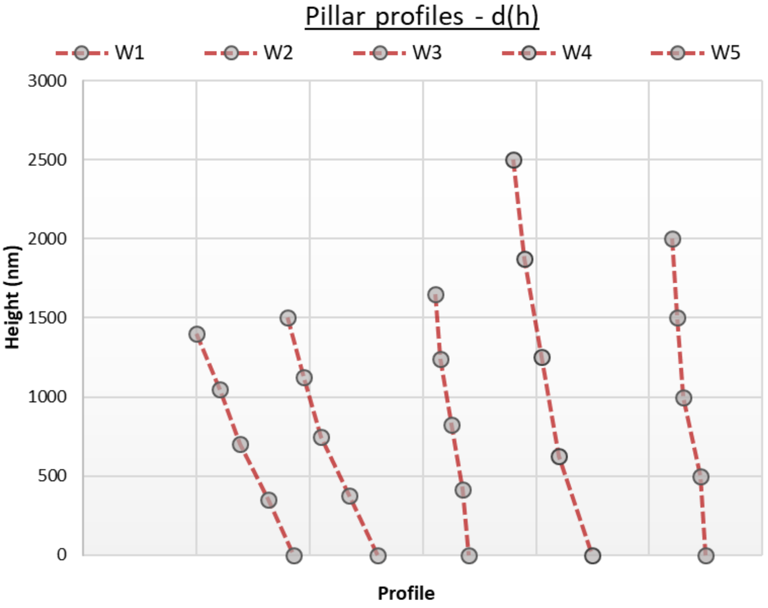

Figure 4.20 - Example pillar profiles, d(h) for the multi-mechanical UHAR slide pillars. W1 – W5, left to right.

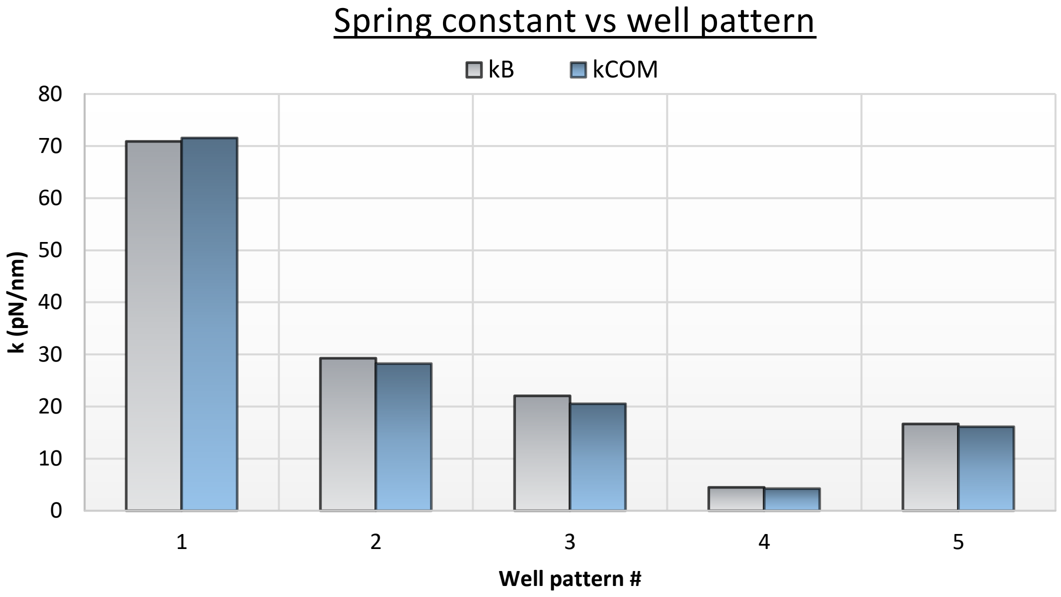

Figure 4.21 - kBz vs kSOL for the multi-mechanical UHAR slide pillars.

For the cases of slide-part fabricated nanopillar arrays for experimental use, the spring constant equation derived and demonstrated here is accurate enough as to be considered highly representative of the pillar deflection mechanics. So far, the case presented here has been highly specific to the kinds of pillar profiles resultant of the high-throughput, rapid injection moulding process. Most other forms of micro- and nano-scale pillar replication technologies use a soft lithography process. The variance in this process is often poorly categorised between parts, but the literature suggests that this variance is low due to the low-throughput nature of this technique. With less replicates being fabricated, overall from a single master, the time available for the kind of process variance that induces these changes in pillar morphology is limited.

Due to the larger feature sizes of these devices, they are far less sensitive to minute changes in the processing conditions. A change of 5 nm in the diameter of an injection moulded nanopillar is far more impactful to the end pillar mechanics than the same change on a 5 micrometre diameter pillar. The question arises, then, if such changes in sidewall morphology will be truly influential on pillars fabricated using soft lithography, typically made from a variety of PDMS-based materials. The answer depends entirely on the morphology of the pillar. The nature of the amendments to the Euler-Bernoulli equation infer that even at the largest (a linear conical profile), the relationship reduces to a dimensionless constant that relies mainly on d_B/d_T. As this is the case, and with the data that show that changing the material properties of the pillar substrate has little effect on the efficacy of the Euler-Bernoulli formula.

If a quoted pillar has used the cylindrical formula and has a d_B/d_T ratio anywhere outside of 1.05, then the spring constant can be variable by minimum 15%.

This translates across inferences of cellular forces, array stiffness, even pillar mechanical property effects on cell behaviour. The main issue that can be foreseen with this is in the inadvertent fabrication of slightly different pillar substrates, that end up having erroneously attributed spring constants – this will affect the results of replication studies. The most significant development for this technology will be a thorough study that compares the effectiveness of gels to equivalent pillar substrates, and what, if any, different effects seeding on a nanotopography will have relative to a flat surface. Cell sensitivity may be low enough to these degrees of changes in mechanical environment to allow for equivalence to be drawn unilaterally across different topographies and pillar morphplogies. Overall, it is important that awareness be brought to the often overlooked assumption that these results are founded on the assumption that any fabricated pillar will act as an ideal, Euler-Bernoulli cantilever would.

4.4 Conclusions

This chapter set out to create a general formula for calculating the pillar spring constants of pillars with non-linear tapers. This is an important thing to be able to do with a degree of accuracy and without using finite element analysis. This both saves time in the analysis process, allowing QA to be fully automated, and allows for a deeper understanding of the effect that changes from the Euler-Bernoulli spring constant has on bending mechanics.

Presented in this chapter is a generalised formula that accurately predicts the spring constants of fabricated nanopillars to within a maximum error of 6%, depending on the aspect ratio of the pillar device fabricated. This error comes from the basic assumptions that are required to use the Euler-Bernoulli approach. In real terms this is typically less than 1pN/nm when dealing with injection moulded UHAR nanopillars. When compared to the error present in calculating the dimensions of the nanopillars, this error in calculation is negligible.

It is easily incorporated into the presented Matlab code for determining pillar dimensions from an SEM, and included in a loop that can be used to determine if the standard Euler-Bernoulli spring constant, a linear taper amended spring constant, or a non-linear taper amended spring constant should be used.

This chapter has also outlined the key criteria that must be satisfied in order to use Euler-Bernoulli beam theory, a useful tool for determining the veracity of this equation in a wider context. From initial analysis, it was apparent that a *shear criteria* is necessary to be upheld.

This criteria is strongly linked to the aspect ratio and sidewall angle. This gives the first criteria as:

$$for \begin{Bmatrix} \angle_{SW} < 3° \\ \& \\ AR > 6.5:1 \end{Bmatrix} - \; k_{EB} \; \approx \; k_{SOL}$$

$$for \begin{Bmatrix} \angle_{SW} > 3° \\ \& \\ AR > 20:1 \end{Bmatrix} - \; k_{EB} \; \approx \; k_{SOL}$$

Secondly, if the taper is non-linear in its d(h) relationship, then there exists a limitation on the applicability of this case of the Euler-Bernoulli formula, such that:

$$for \, \{\mathrm{dT} \; < \; \mathrm{dM} \; < \; \mathrm{dB}\}$$

$$and$$

$$\left\{-1.5 \; < \frac{\mathrm{d}}{\mathrm{d}\xi}[\mathrm{d}(\xi)] \; (\mathrm{at} \; \xi = \; 0.75 \;) < \; -0.5\right\}$$

$$k_{Bz} \; \approx \; k_{SOL}$$

Combined, these limitations allow for the use of a general formula for non-linear tapered cantilever beams in the Euler-Bernoulli special case, a novel addition to the literature. Taking this further would require the inclusion of Timoshenko beam theory for shorter aspect ratio pillars and, depending on the application, some of the pillar-base position considerations from the literature that are required for accurate pillar tracking.

5.0 ICP deep silica etch optimisation: towards better replication accuracy

Whilst **Chapter 3.0** dealt with the limitations of using hybrid polymer inlays to fabricate UHAR nanopillars over larger areas, using injection moulding. That chapter identified the contribution that pillar sidewall angle has on replication accuracy of nanopillars. It also demonstrated the limitations of conventional RIE when trying to etch quartz pillars above an aspect ratio of 10:1. These pillars tend to degrade in replication accuracy across replication cycles faster than their more robust counterparts.

This is compounded by the fact that the current reactive ion etching (RIE) methods have reached their limits. The hard-mask thickness for higher aspect ratios is too difficult to deposit with adequate morphology, and unreliable mask-erosion rates exist in the process. Adding to this the fact that the etched features are subject to large variability over time in the RIE 80+ machine, and the relatively low etch rate of 30nm/min. The variability of the etched features, and the high mask erosion rates change with feature width, causing an unpredictable change from initial design across multiple pillar diameters. This, as demonstrated already, causes a drastic change in the expected pillar spring constants. Therefore, there exists scope for the generation of a new etch process that takes into account three additional key variables not included in the optimised RIE etching process. These are:

- Sidewall angle
- Mask erosion
- Uniformity across tip diameters

Following these aims the process should result in a fully tuneable, accurate, high-yield and rapid process of fabricating mechanically equivalent pillars-in-arrays and pillar-arrays.

The best option for achieving this is to use **I**nductively **C**oupled **P**lasma reactive ion etching, or **ICP** RIE. ICP etching typically has very high etch rates, exceeding 300nm/min, and is a highly directional form of etching. This is achieved by inductively coupling the plasma to the substrate by applying a bias across the chamber. This technique allows the plasma energy, controlled by the source power, to be separated from the incident ion energy. This is also what gives ICP etching its highly directional nature.

The ICP etching tool used in this work was an SPTS Omega® Synapse™, referred to often simply as the SPTS tool or Synapse etcher. For brevity this thesis will refer to it as the SPTS tool. The schematic for this is shown in **(Figure 5.1)**.

Key points of this particular tool are:

1. Gas inlet at top of chamber, increasing the distance from the substrate for better decoupling of plasma energy and ‘etching energy’.
2. Chamber walls are heated, reducing the energy lost by radiation to the chamber, and the quantity of by-product build-up on the chamber walls. The multi-pole magnetic bucket also encourages higher plasma density away from the chamber walls. (Higher plasma density increases both etch rate and reduces the operation pressures achievable. The lower pressure capability will increase the MFP (mean-free path), which again increases anisotropy by reducing lateral etching).
3. Wafer clamped electrostatically, allowing for helium back-cooling to more easily maintain a desirable substrate temperature.

All of these points increase the viability of the ICP process for etching directionally sensitive nanoscale features, especially with the need for high control over sidewall angle of such features, which will be *highly* dependent on the directionality of the etching process.

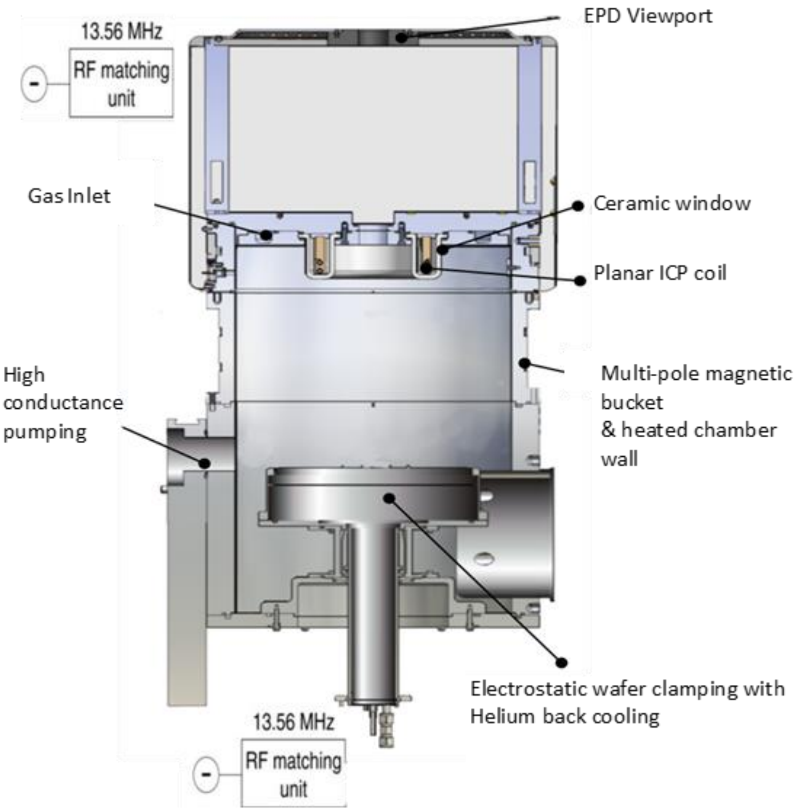

Figure 5.1 - Schematic of the SPTS synapse etch tool. Indicating the main points of interest that relate to the etching quality expected. Image from SPTS.

ICP etching is incredibly fast compared to its RIE counterpart, especially of strongly bonded substrates such as silica. The established etch rate for the RIE process is 30nm/min, sometimes reaching as low as 16nm/min or as high as 40nm/min. ICP etching of quarts using the SPTS tool has typical etch rates of 300–500nm/min, an increase on the average RIE etch rate by more than a factor of 10. This promises a reduction in etch times, for example for 1 micron features, from 33 mins to less than 3. Not only will ICP etching allow for highly directional etches, but they will also be very fast. Therefore, the aims of this process are clear. As well as achieving high levels of control over nanopillar properties, such as tip diameter and sidewall angle, the etch rate of the ICP process should be in the 300–500nm/min regime. In order to do this, the levels of lateral mask erosion should be minimised by the process, and therefore the ratio of the mask diameter to the tip diameter maintained as close to 1:1 as possible.

An understanding of the relationship between process variable and the different mechanisms present during plasma etching is essential to arrive at any reliable conclusions about an optimised process. Etching mechanisms fall into two modes of etching: physical and chemical. These modes interact differently with the process parameters, such as gas flow rate, pressure, or source power, and are not entirely independent of one another. The most important factor to consider are the etch gases being used.

Typically, a fluorine-based gas is used to remove the silicon, SF_6, CF_4, C_4F_8, CHF_3, with the sulphur/carbon used to remove oxygen. Whilst this gas mixture is primarily aimed at creating SiFx gases, which are volatile at low pressures and thus easily removed from the substrate surface, they also generate non-volatile fluorocarbon materials that reside on the substrate. These insulate areas of the quartz from etching, and whilst this is useful for protecting sidewalls from lateral etching, it can be a hindrance to both directionality and etch rate. O_2 or an inert gas are introduced to chemically react with or simply physically sputter this resistive layer. This adds another parameter to be mindful of when tuning etch process variables.

As the materials allowed into this shared etched tool are limited, the Ni mask must be changed to aluminium. The introduction of an aluminium mask also adds another condition, namely that the selectivity of the mask should be maximised. As this process is ultimately designed to reach aspect ratios of 20:1 and above, the less mask needed the lower the mask aspect ratio, and therefore the more circular the mask will be.

5.1 Designing the optimisation experiment - groundwork

As well as discussing the merits of ICP etching, it would also be useful to discuss briefly the trends that are typically present in plasma etching physics and chemistry that were used to inform the decisions made in the course of this investigation.

There are several variables that can be used to control the etching process; source power, platen power, pressure, gas composition, gas flow rate, substrate temperature, mask material, mask thickness, substrate material, chamber temperature, helium back cooling flow, position on carrier wafer, carrier wafer material and masking, and even the relative geometry of the nanofeatures to name a handful can have an influence on the end result.

This parameter space is large, and needs to be narrowed, as using a standard monothetic analysis would result in far too many experiments to be performed. In order to do this, an extensive literature review was conducted to look at the key parameters that ICP etching experiments, particularly those using dielectric substrates, identified as having the dominant impact on certain quality characteristics of the etch process.

5.1.1 Review of the literature

In total, more than 30 papers were identified that dealt with fast ICP etching of dielectric or silicon-based substrates[85-117]. Each investigation differed in its final aims, and therefore came to a different conclusion about the dominant process parameter on their results, which tended to be etch rate and surface roughness.None of the investigations were concerned with etching free-standing features, or features on the sub-micron scale. The focus was either on gratings, pits or waveguides, all in the micro-millimetre scale. With the advent of plasmonics and metamaterials, as well as the surge in new NIL techniques and applications, the influence of process parameters on standalone features will be both beneficial to the current body of research, and fill a gap in the literature for use by the wider research community.

As each etch tool differs in key parameters, such as chamber configuration, gas inlet control systems, wafer clamping mechanisms and, in two cases, the method of inductively coupling the plasma, the results of the literature review can be considered general. This also means that any results obtained using the SPTS synapse tool are highly specific. However, in the context of the literature, the general trends that are discovered will be discussed, and these will apply to the process as a whole regardless of tool. The key parameters, or dominant parameters, were highlighted from each publication, and the following table compiled the five most cited process variables and the number of times cited as the, or one of the, dominant variables.

Process parameter	No. times counted
Gas Flow Rates	20
Gas Composition	20
Source Power	16
Pressure	14
Platen Power	11
Substrate Temp.	4
DC Bias	6

Table 5.1 - Table of key ICP parameters from the literature. A table of process parameters and the number of times they appeared as a significant control factor in the literature, indicating the key parameters for ICP etching in general.

Table 5.1 indicates that the four most occurring dominant process parameters, and their primary effects on etch metrics, are:

- Individual gas flow rates/ overall flow rate - these were used interchangeably in the literature.
- Gas composition - chemical mechanism of etching, including sidewall angle due to formation/removal of fluorocarbon layers.
- Source power –ion energy, plasma density, and etch rate
- Chamber pressure – mean free path, and anisotropy of etch features.

Immediately, this goes against intuition. As the platen power will have the most control over the incident ion energy and directionality, it should be expected that this will be the dominant parameter. Substrate temperature is also very low on this list, only being cited four times as a dominant parameter. In fact, it is only in these four publications that temperature is investigated at all. This is odd because of the influence observed in RIE of substrate temperature effecting etch profile and etch rate (**Section 3.3.2**). This significantly lowers the number of variables. As substrate material and mask material are inherent to later process steps or equipment restrictions, namely fabrication of inlays for injection moulding, these can be ignored.

Carrier wafer material could be varied, introducing perhaps an aluminium-oxide layer onto the silicon wafer. This approach would take time and optimisation of a process, as well as incurring expense in pre-purchasing such wafers, and so were also disregarded. The top four occurrences in the table, therefore, were chosen as the experimental variables for the investigation.

Due to the gas constraints in the JWNC and the existence of a standard deep quartz etch for microtrenches and sub-millimetre scale gratings, the gas composition was kept as two chemicals, C_4F_8 and O_2. This is also useful, as C_4F_8 has been known to facilitate high selectivity to photoresist based masks, which would be an avenue for further optimisation of this process.

The relative makeup of these gases was chosen to be varied. In order to preserve the independence of these variables, the overall flow rate remained the same, whilst the relative composition of these two gases changed by altering their individual flow rates. By holding the overall flow rate constant and varying the flow rates of the two individual gasses in the mixture, the gas composition ratio could be amended whilst maintaining a consistent level of throughput of gasses through the machine. This is important as flow rates of the individual gasses determine the gas density, an imperative parameter for plasma striking. The next variable to take the place of flow rate was the platen power.

One of the main methods of establishing robustness in a process in fabrication engineering, process engineering in particular, is the Taguchi Method for design of experiments. As the process for etching these high aspect ratio features needs to be as immune as possible to the slight variations that can occur in the fabrication process, from the bonding of the quartz to the carrier wafer to the actual plasma etching itself. As the etch rate is so high, and the overall etch time therefore so small, any slight variation in these processes will be amplified as they take up a larger percentage of the overall process time.

5.1.2 Experimental design – Taguchi Method

Originally developed for improving the quality of manufactured goods, the Taguchi Method challenges the conventional method of quantifying the success of a process by assessing the loss of quality from a target value. It does this by establishing signal-to-noise ratios (S/N) to evaluate the closeness of a quality characteristic of a product to its target value. By assessing these, the optimum level settings of the various factors that control process outcomes (the control factors) can be established.

The Taguchi method is essentially a method of experimental design that has a particular focus on the robustness of the end process. The main strength of this approach is in its ability to combine several control factor settings into single experiments, lowering the overall number of experiments needed. The Taguchi method has since been expanded into many other realms of process design, most notably for this body of work, the optimisation of dry-etch recipes, a select few results of which are shown in **(Figure 5.2)**.

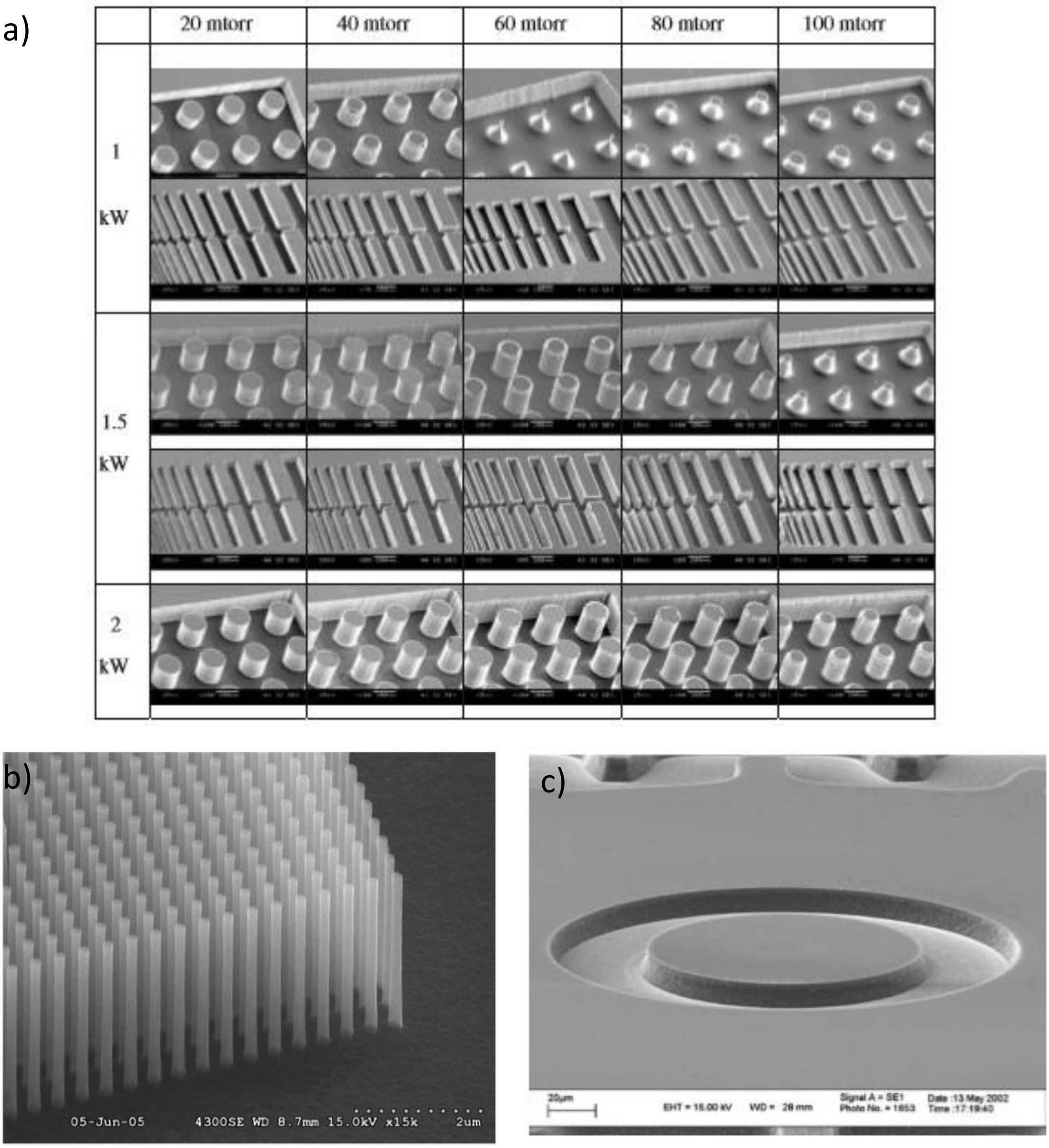

Figure 5.2 – Examples from the literature of Taguchi optimised plasma etch processes. Etched features in a) and b) silicon of low and high aspect ratio pillars[118], and in c) SU-8 photoresist that have been optimised using Taguchi design[119]. Images replicated with permission from the copyright holder.

In order to ascertain what the relevant control factor levels should be, an initial test was carried out using an existing recipe on the SPTS etch tool, and will be referred to as the *standard microtrench recipe*. The effect of these control factors on the following quality characteristics of etched quarts nanopillars, will form the foundation of determining the optimum etch recipe:

- etch rate; *ER*
- sidewall angle; *SWA*
- change of pillar tip diameter from initial mask diameter; *Δdt*
- rate of mask erosion; *MER*

For this, a so-called L9 array was selected. This orthogonal array contains 4 control variables, each with 3 level settings, making a total of 9 experiments. This array was chosen because of its coherence with findings from the literature, as well as the relatively low number of experiments it requires due to the time constraints involved in a PhD investigation.

	Control variables				**Response characteristic**			
Exp#	*Source Power (W)*	*Platen Power (W)*	*Pressure (mTorr)*	C_4F_8:O_2	*Etch Rate (nm/min)*	*SWA (°)*	*Δdt (nm)*	*MER (%)*
1	1	1	1	1	A_1	B_1	C_1	D_1
2	1	2	2	2	A_2	B_2	C_2	D_2
3	1	3	3	3	A_3	B_3	C_3	D_3
4	2	1	2	3	A_4	B_4	C_4	D_4
5	2	2	3	1	A_5	B_5	C_5	D_5
6	2	3	1	2	A_6	B_6	C_6	D_6
7	3	1	3	2	A_7	B_7	C_7	D_7
8	3	2	1	3	A_8	B_8	C_8	D_8
9	3	3	2	1	A_9	B_9	C_9	D_9

Table 5.2 - Example of an L9 Taguchi array. Indicating the response quality characteristics, control variables and the order of their combination.

Each response characteristic has nine values, defined here by the letters A, B, C and D, each corresponding to a particular combination of level settings. The analysis of the data itself contains four parts. Firstly, the *mean-of-means*. In this analysis, in each instance where a control factor level setting is used, for example Platen Power level setting 1, the mean is taken of each response characteristic value. For brevity, let us focus on etch rate at the moment – values A_n. The platen power level setting 1 appears three times, in rows 1, 4 and 7. That means that the etch rate assigned to the use of platen power setting 1 is the mean of A_1, A_4 and A_7. This is repeated for all three level settings, and the results are graphed demonstrating the effect that changing the platen power in this range will have on the etch rate.

Secondly, the *signal-to-noise* ratio is calculated and graphed in a similar manner. In this experiment, two S/N were used. *Smaller-is-better* – this S/N looks for the level settings that *minimise* the response. For example, it is desirable that Δdt is as small as possible to yield a process that maintains the designed mask diameter, for this a smaller-is-better S/N is used. It is described by **(Equation 5.1)**. *Larger-is-better* is nominally the opposite, it looks for the level settings that *maximise* the response. For example, etch rate should be as high as possible in this process. It is described by **(Equation 5.2**).

$$S/N = -10\,log_{10}(SUM(Y^2)/n)$$ **Equation 5.1**

$$S/N = -10\,log_{10}(SUM(1/Y^2)/n)$$ **Equation 5.2**

Where Y = responses for the given factor level combination, and n = the number of responses in the factor level combination. These analyses, the mean-of-means and the S/Ns, allow for the control factors to be ranked in order of impact on the process. The mean values for the means and S/N are taken for each data point, and the maximum variance between the different responses calculated. The larger this maximum variance, the more dominant the parameter will be.

Using analysis of variance, or ANOVA, can indicate whether the response characteristic is sensitive to changes in the control factor. ANOVA also lends statistical weight to the experimental results. The total % contribution to the overall result can be measured, and the null hypothesis tested. By comparing the p-value of any given result to the standard accepted value for confidence, the veracity of the observed relationships can be obtained.

The optimum process will therefore consist of the factor level settings that give the desired response change, maximised or minimised, and the ANOVA will determine which control factor is the most important in establishing this effect, which is important when deciding between conflicting level settings. From this, and lastly, a linear-regression analysis is performed using the chosen optimal level settings, if they do not already appear together in the L9 array, and a prediction will be made about the value of each response characteristic.

This is tested against step a confirmation experiment, where any changes from the prediction indicate a level of noise still residual in the process. The rest of this chapter will then outline the findings of the Taguchi experiment, and its subsequent confirmation experiment.

5.2 Establishing initial control factor levels

This section will deal exclusively with determining the initial control factor levels that the L9 array will be based on. As will be demonstrated, the microtrench recipe was not suitable for etching of nanoscale standalone features **(Figure 5.3).** There also existed the possibility for trialling a different adhesive between the quartz substrates and the silicon carrier wafer, namely SANTOVAC® oil, a polyphenyl ether (PPE) oil. This oil is a preferable adhesive over alternative thermally conductive pastes due to its ability to form very thin bonding layers, and its solubility in water.

Interestingly, no significant difference was found to exist between these two approaches, despite PPE being an insulating material **(Appendix C.2).** The choice of adhesive is paramount to maintaining consistent thermal contact between the quartz substrate and the carrier wafer. The standard microtrench recipe has the following parameter settings, outlined in **Table 5.3**.

Process parameter	Setting
Source Power	1200 W
Platen Power	250-300W (ramping)
Pressure	6mTorr
Gas Composition	C_4F_8 / O_2
Gas flow rates	80sccm / 25sccm
Substrate Temp.	40°C

Table 5.3 - Table of control factor settings for the standard microtrench recipe.

The etch rate was recorded at roughly 500nm/minute for quartz with an Al mask. An initial etch test was performed on initial patterns of nanofeatures of different diameters across three pitches, 1, 2 and 5µm.**(Figure 5.3)**.

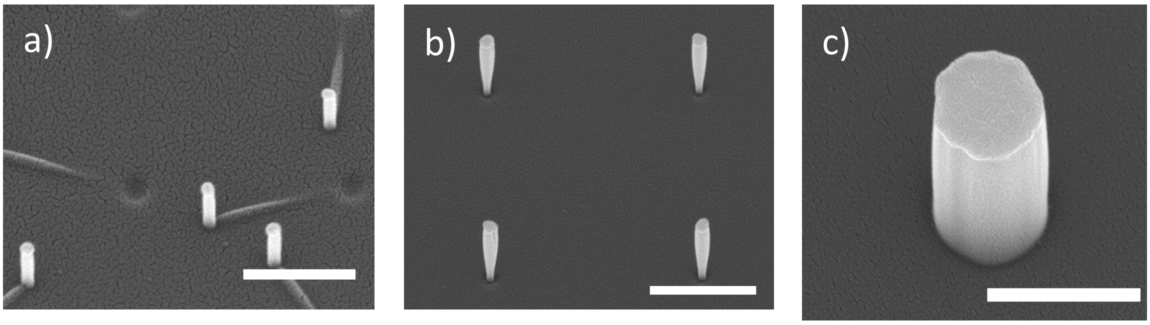

Figure 5.3 - Initial results of etching nanoscale pillars using ICP RIE. a) 1µm pitch, 100nm diameter mask pillars. b) 2µm pitch, 200nm diameter mask pillars. c) 5µm pitch, 500nm diameter mask pillars.

Of immediate interest, with respect to use of the established microtrench recipe, is the formation of nanofeatures through two distinct etching 'phases' depending on the feature pitch. This can be seen when looking at SEM images in **(Figure 5.3-a/b/c)**. For the 2µm and 5µm pitch features, the etch process proceeds as normal, with standing features being etched in the same location as their respective mask dots – this is termed the *primary etching phase*. However, the 1µm pitch features have etched, collapsed, and new features have been etched in the location of the mask after feature-collapse, illustrated by the indentation from the undercut primary feature is visibly present in the image. This is termed the *secondary etch phase*.

The secondary etch features are thin, around 40nm wide on average, and arrayed randomly due to the nature of the collapse from etch undercutting, causing narrowing of the feature base. This creates a randomised array of pillars that is pitch-dependent, as will be highlighted later in this section. A randomised array like this could be useful for control arrays where pitch is randomised by either computer program during e-beam lithography, or for more ordered arrays.

This raises the interesting observation that aspect ratio could play a part in the success of etched features using ICP etching. Temperature of the substrate, and therefore of the features being etched, has been demonstrated both in the literature and in work using RIE processes, to play an important role in etch dynamics. As the aspect ratio of these features decreases, their etch profiles become less undercut. This could be due to a difference in temperature through the pillar as it is etched, with a temperature build-up at the base contributing to an increase in etch rate.

As substrate temperature is expected to play a part in this trend of undercutting in features, two options of exerting a level of control over these are explored. The first is to use a cyclical, often called a pulsed, etch, where the active etching plasma, in this case the C_4F_8 and O_2 mixture is replaced by a gas that is not expected to interact with the substrate. This was, ultimately, the route taken and will be presented in **Subsection 5.2.1**.

Secondly, the substrate temperature can be controlled to reach sub-zero temperatures. This is commonly referred to as cryogenic etching. Both avenues are explored, and the relationship between cycle time, which infers the temperature the substrate is allowed to reach, the direct substrate temperature to the etch rate of features, the pillar tip and base diameters, the sidewall angle of etched pillars, and the overall change in pillar tip diameter from the designed mask diameter. These results can be found in **Appendix C.2.** These two attempts at controlling the substrate temperature could be factored into the further Taguchi experiment, however that design requires all control factors of a process to be *independent* variables. Platen power, gas composition, pressure, these all effect the substrate temperature directly. Therefore, these two attempts to mitigate the observed heating effect on pillar etching are trialled separately, so that the independent effects of source power, platen power, pressure and gas composition ratios can be determined for future reference of etching of quartz nanofeatures. In this way, the results become far more generally applicable.

5.2.1 Cyclical etch – Helium "cooling" cycles

There are numerous examples of cyclical etch processes being used in the literature, often divided into two categories. One is the BOSCH process, a well-known and widely used process of cyclical etch and passivation steps, typically in silicon etching, where a plasma conducive to etching is used to etch a set amount of the exposed silicon substrate, and then the plasma is purged and switched to a fluorocarbon-based gas plasma to facilitate the deposition of passivation layers. In doing so, a cycle is established of etch-passivation-etch in which already etched areas of the sample are protected from any further directional etching. It is commonly used to fabricate very high aspect ratio features, however has the issue of "scalloping" of sidewalls, causing etched surfaces that are very unsuitable to imprinting steps. A similar approach could be attempted without the passivation step, as the use of C_4F_8 as a mixed-gas process already facilitates the continuous deposition/removal of passivation layers. In doing so, an "inert gas", i.e. one that is not expected to play an active role in the etching process, can be purged into the chamber to "cool" the substrate, also allowing for a relaxation phase in the etch chemistry and a reduction in the so-called dwell time of reactants on the substrate surface, which should both aid in the reduction of isotropic etching.

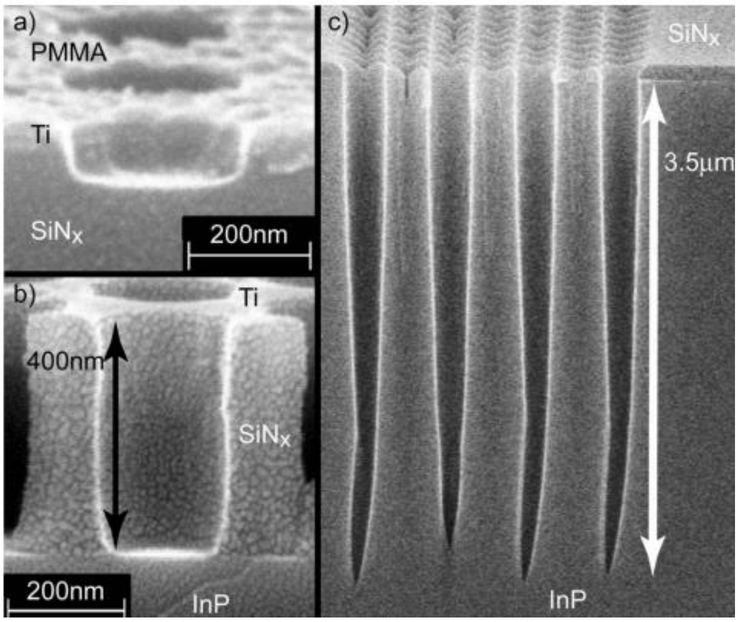

Figure 5.4 - Examples from the literature of a cyclical etch process used to etch deep trenches into SiNx and InP[120]. Images replicated with permission from the copyright holder.

This has been done in literature, using a cyclical etch / purge technique using nitrogen. As nitrogen was unavailable for this tool, another similarly low vapour-pressure gas, helium, was chosen as it was deemed the best alternative at hand.

These approaches have been reported to particularly benefit the preservation of mask material, especially of photoresist masks, mentioned earlier as a potential avenue for improvement of the process.

It is important to understand the relationship between the cycle-time and the different etch characteristics of the nanopillars. As the Taguchi process should demonstrate the relationships between the source power, platen power, pressure and gas composition, which will be of interest to the wider community, it will be important to know how to alter the final recipe should it fail to meet spec. This can be done by understanding the direct effect of cycle time. It is also important to establish in the first instance what cycle time, if any, will be worth using.

To that end, three cycle times were chosen, keeping the overall etch time consistent:

1. 8 x 15 second cycles
2. 6 x 20 second cycles
3. 4 x 30 second cycles

with each cycle alternating between C_4F_8/O_2 and He. The same pattern has been used for all these ICP etch experiments, namely four pitches and two sets of gratings, each with five distinct diameters. The remainder of this chapter outlines these results. As there was little change in all but etch rate of the 500nm diameter+ data, this will be left out of analysis.

(Figure 5.5) illustrates the results of the 1µm pitch data experiments. Little difference was found in the trends between these and the other two pitch arrays examined, which be found in the appendices for reference (**Appendix C**).

The effect of cycle time on each quality characteristic of the pillars, etch depth, tip diameter, base diameter, sidewall angle and change in tip diameter from designed mask diameter, the trend appears to be relatively consistent. The etch rate steadily increases across all diameters with cycle time, as does the amount by which the tip diameter changes from the initial mask design, an indication of undercutting in the etch and mask erosion.

Interestingly, even though there is a maximum of the tip and base diameters at 20 second cycle times, the sidewall angle appears to decrease in an almost parabolic fashion to almost 90° features, particularly at larger diameters.

This indicates that above a 30 second cycle time any improvements in sidewall angle will be miminal until the pillars collapse as seen in the standard microtrench recipe. Lastly, with regards to sidewall angle and etch depth, the two trends appear to be inverse of eachother.

Whilst this is non-optimal, it will make generalisations of the product pillars depending on the etch parameters easier.

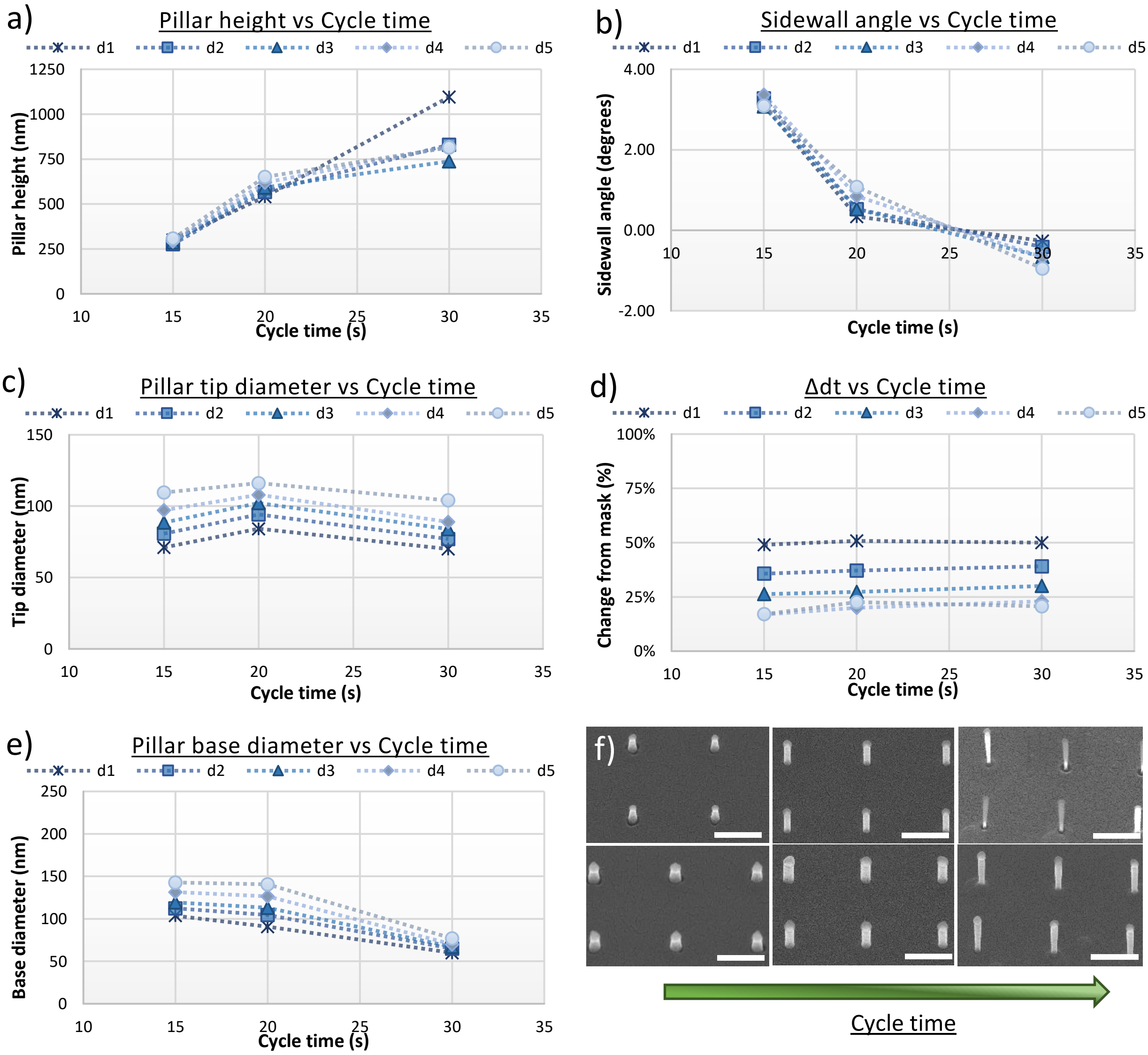

Figure 5.5 – Results of the helium cooling cycle approach to deep silica etching. a) – e) **graphs depicting the trends in pillar etch depth, tip and base diameters, sidewall angle and the change in tip diameter from the designed mask diameter for** 1µm **pitch samples.** f) **are example SEM of the nanopillars etched using 15s, 20s and 30s cycle times from left to right, scale bar 0.5µm.**

The reason behind the inflection point in the diameter measurements is most likely related to a combination of the rate of deposition/removal of inert fluorocarbon layers, the temperature that the substrate can reach during the available etch time and the available time for isotropic etching chemistry to begin to dominate the anisotropic ICP facet of the process, however it is unclear why a 20 second cycle time would yield better conditions for mask preservation during etch than its 15 second counterpart.

The change between mask diameter and final pillar tip diameter appears to be consistent across all cycle times. This implies that the change observed here is also strongly pitch related. If similar trends are observed in the substrate-temperature experiment, then it can be concluded that this effect is independent of temperature.

It would also seem that the smaller the initial mask diameter, the more linear the response from each etch characteristic that is measured. This enforces the observation that variations in feature size, even by as little as 10nm, will influence the end results of fabrication, and again is an argument for why the final etch recipe needs to be robust across a range of diameters, as well as pitches.

To summarise:

- The etch rate increases with longer cycle times, although is still lower than a continuous etch.
- Change from designed mask diameter is a linear trend, and appears to be closely related to feature-to-feature spacing.
- Increasing the mask diameter overall increases every response, except the rate of mask erosion and mask undercutting.
- Cyclical etching does not produce the conical etched features that non-cyclical etching does. This makes it a good starting point for recipe optimisation.
- The inflection maxima at the 20 second cycle time is likely related to the rate of inert fluorocarbon deposition on the mask vs the rate of mask etching and quartz etching.
- *All features* are formed in the primary etching phase, a distinct improvement from the microtrench recipe.

Observing the trends in the data, any improvements in etch rate by increasing the cycle time will be met with a deterioration in sidewall angle, however slight, and an increased change in diameter tip from the initial design. An argument can be made for reducing the cycle time to 25 seconds, reducing the overall height of the etched pillars and preserving the mask better, however for the purposes of optimisation the 30 second cycle time is good enough to start with. Amendments can be made to an optimised recipe based on these insights, and the 40°C, 30s He cooling cycle was chosen as the initial recipe.

5.3 L9 matrix experiment

Selecting the 30s cooling cycle as a base recipe, with the standard microtrench recipe settings for source power, platen power, temperature, pressure and gas flow rate and composition, the next task was to select the relevant level settings. These are shown in **Table 5.4.**

Level	Source power	Platen power	Pressure	O_2 %
1	1000 W	250 W (MT)	6 mTorr (MT)	5.56 %
2	1400 W (MT)	375 W	8 mTorr	18.75 %
3	1800 W	500 W	10 mTorr	35.71 % (MT)

Table 5.4 - Level settings for each of the four control factors based on the selected microtrench recipe.

The O_2% of the gas composition (5.56, 18.75 and 35.71 %, equating to a C_4F_8 : O_2 ratio of 90:5, 80:15 and 70:25 sccm respectively) are controlled by the relative flow rates of each gas. The total flow rate, 95sccm, was held constant to lower any residual noise from this factor. Note that in the standard microtrench recipe the a C_4F_8 : O_2 ratio of 80:25sccm does not appear here. It is important for Taguchi analysis to have normally distributed data to analyse, this is best achieved by having linear changes in the control variables. Due to constraints caused by maintaining adequate plasma density, this was best achieved using the outlined gas ratios. The level settings of the microtrench recipe are indicated in **Table 5.4** with (MT).

The other variations were chosen based on observations from the literature, and a basic understanding of the effects each control factor is likely to have on the response. Entering these level settings into the orthogonal array matrix as shown in **Table 5.5** gives the total L9 experiment: 9 experiments, each with four response quality characteristics to be measured. These are measured each for five diameters, over four pitches.

This gives a total of 20 datasets, however for brevity only the 0.5µm pitch data will be presented for discussion as these features presented the most full and convincing dataset, the other results are summarised and placed in **Appendix C.3** – L9 results for 1 and 2µm pitch pillar arrays**.** The 5µm pitch pillars, and the etched grating features were used as references for missing data-points where etched features were not able to be measured.

	Control variables				Response characteristic			
EXP #	*Source Power (W)*	*Platen Power (W)*	*Pressure (mTorr)*	C_4F_8:O_2	*Etch Rate (nm/min)*	*SWA (°)*	*Δdt (nm)*	*MER (%)*
1	1000	250	6	90:5	A_1	B_1	C_1	D_1
2	1000	375	8	80:15	A_2	B_2	C_2	D_2
3	1000	500	10	70:25	A_3	B_3	C_3	D_3
4	1400	250	8	70:25	A_4	B_4	C_4	D_4
5	1400	375	10	90:5	A_5	B_5	C_5	D_5
6	1400	500	6	80:15	A_6	B_6	C_6	D_6
7	1800	250	10	80:15	A_7	B_7	C_7	D_7
8	1800	375	6	70:25	A_8	B_8	C_8	D_8
9	1800	500	8	90:5	A_9	B_9	C_9	D_9

Table 5.5 - L9 orthogonal array with level settings for the control factors filled. Following these, 9 experiments were conducted using these different combinations of level settings.

The data will be presented with one diameter response examined in detail, as well as the variance across diameters.

5.3.1 – L9 Taguchi - results

(Figure 5.6) shows example SEM images of the 100nm diameter dataset. Of note is the extreme variance between all of the different pillar dimensions depending on the level settings of the control factors of the etch. Laying out the SEM images in this manner also makes obvious two trends in the data that will be backed up by analysis. First, increasing the source power uniformly and visibly *decreases* the etch rate. This is surprising, as conventional thinking would posit that increasing plasma energy should increase the etch rate. Secondly, and unsurprisingly, the increasing platen power increases the etch rate. However, the increasing platen power does not continue to increase anisotropy of the etch.

These are interesting discoveries in the etch mechanics, and are repeated over all pitch datasets (**Appendix C.3**C.3 – L9 results for 1 and 2µm pitch pillar arrays**, image C.3.5)**. The interplay between different control factors appears to be strong, and will be decoupled in the analysis, yet it would appear that there is interplay between source and platen power that is imperative in determining the result of the etch. From a preliminary analysis of these SEM, it can be deduced that an important feature of ICP RIE is the difference in magnitude between source and platen power.

0.5 micron pitch, 100 nm mask – L9 array

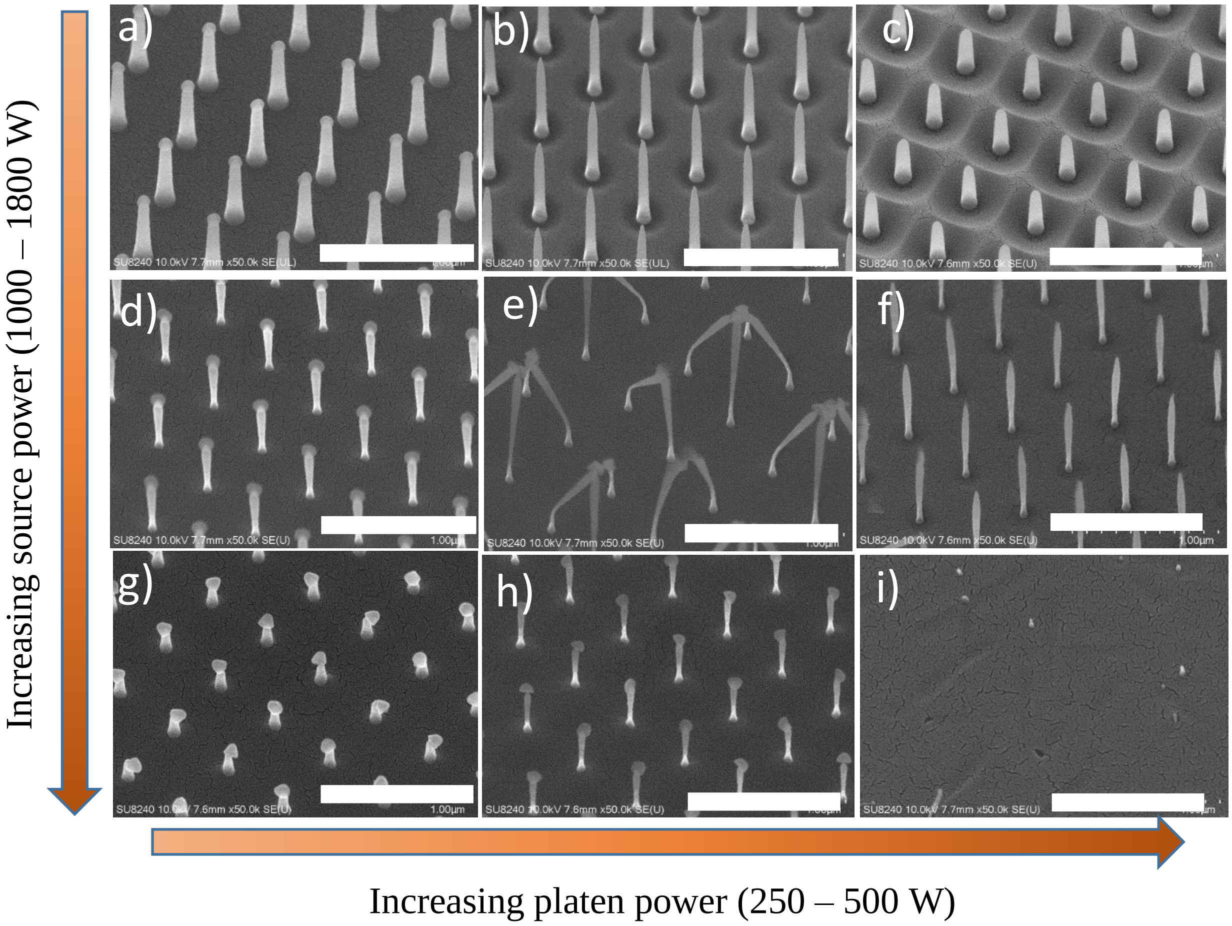

Figure 5.6 - SEM results of the L9 matrix experiment for the 0.5µm pitch, 100nm diameter mask pillars. a) – i) are experiments 1 – 9 respectively. Scale bar 1µm.

Of particular interest is **(Figure 5.6-c).** There is a peculiar trenching occurring at the base of these pillars, the square nature of which implies some sort of overlap between a radially motivated phenomena. This looks like an exaggerated effect of the base trenching present upon closer inspection of **(Figure 5.6-b),** and is most likely caused by an increased etch rate of the substrate surface after the entire mask has been etched. Aside from being an interesting morphology, potentially revealing more about the relationship between mask selectivity and etch mechanics, it seems to be an advancing trend regardless of other changes in the pressure and gas ratio. An array like this could have some novel application.

By using spider diagrams, the end pillar results can be overlaid onto the original design specifications, and the quantified differences observed.

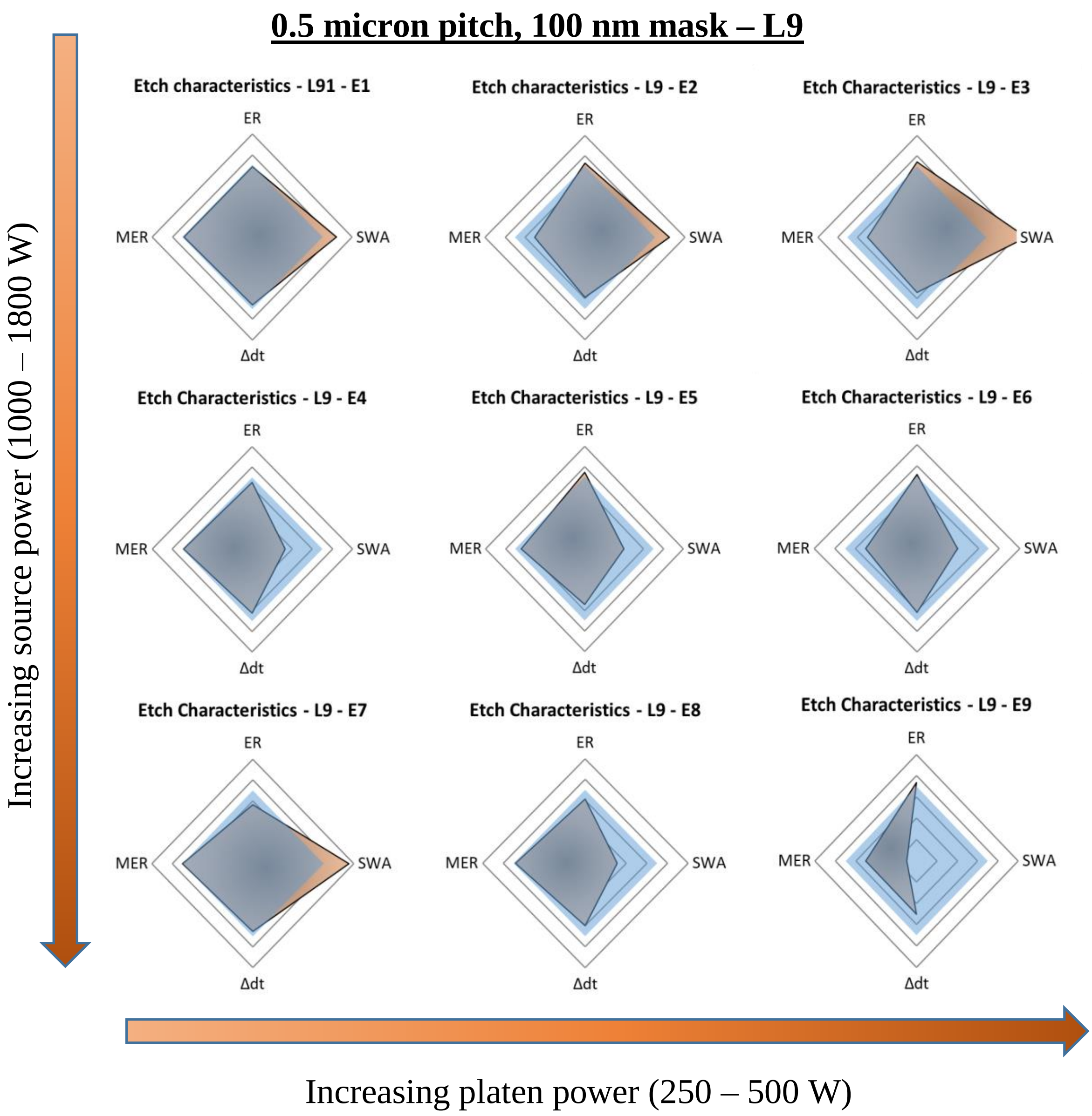

Figure 5.7 – Normalised results of the L9 matrix experiment for the 0.5µm pitch, 100nm diameter mask pillars. marked E1-E9 for experiments 1-9 respectively. The blue area indicates the ideal parameters, and the orange areas indicate the measured results.

The four main quality criteria here are etch rate, sidewall angle, Δdt and mask erosion. An ideal etch would have an etch rate of 500 nm/minute, 0° sidewall angle, 0nm change from mask diameter, and a 0% level of mask erosion. As the latter three are somewhat unlikely, these were amended to 1° sidewall angle, 10% change in pillar diameter tip and 5% mask erosion. Normalising the response data in these four categories then to the aims of the etch process, spider graphs were plotted for each experiment, and these are shown in **(Figure 5.7).**

From **(Figure 5.7)** it becomes immediately obvious which etch results are closest matched to the target parameters, and which are not. All of experiments **E4-6** fail to meet the sidewall angle target, and there is a grouping of four experiments, **E5, 6, 8** and **9** that remain bounded below the target conditions. Experiment **E7** preserves mask integrity quite well, however it has an insufficient etch rate and a very high sidewall angle.

Experiments **E1-3** may suffer from increasingly degenerative mask erosion rates, yet this is compensated for by matching or exceeding the etch rate, and have the closest sidewall angles to the target 1°.

As there are multiple factors changing between each experiment, in order for the previous assertions to become sound the source and platen powers must be the dominant control factors in all aforementioned response characteristics. This is gleaned from an analysis of the mean-of-means and the signal-to-noise ratios. The S/N graphs for etch rate, sidewall angle, Δdt and mask-erosion are shown in figures **5.8-5.11**, with the S/N response tables added in each, tables **5.6-5.9.**

Looking at the rankings in the response table, the platen power is the most dominant control factor in establishing etch rate, followed very closely by the source power. In fact it is only a variance of 0.02dB. This backs up the earlier observation from the SEM and spider graph analysis that these two control factors are indeed having a large effect on the height of the final etched pillars.

The variability induced in the process caused by the pitch has been alluded to, in which the variation caused due to changing aspect ratio in the nanopillar arrays has been accounted for, and presented in more detail in the appendices (**Appendix C.3).** The following discussion will focus on the findings for 1 diameter size, outlining the responses in the four main quality characteristics. Namely etch rate, sidewall angle, change in tip diameter and magnitude of lateral mask erosion.

5.3.1 Etch rate response

As the S/N used was *larger-is-better*, the larger a response value, the higher the S/N ratio is. Therefore the control factor level setting that is highest in the S/N in the graph is the optimum setting. In this case that would be:

- Source power of **1000W**
- Platen power of **500W**
- Pressure of **8mTorr**
- C_4F_8:O_2 ratio of **90:5**

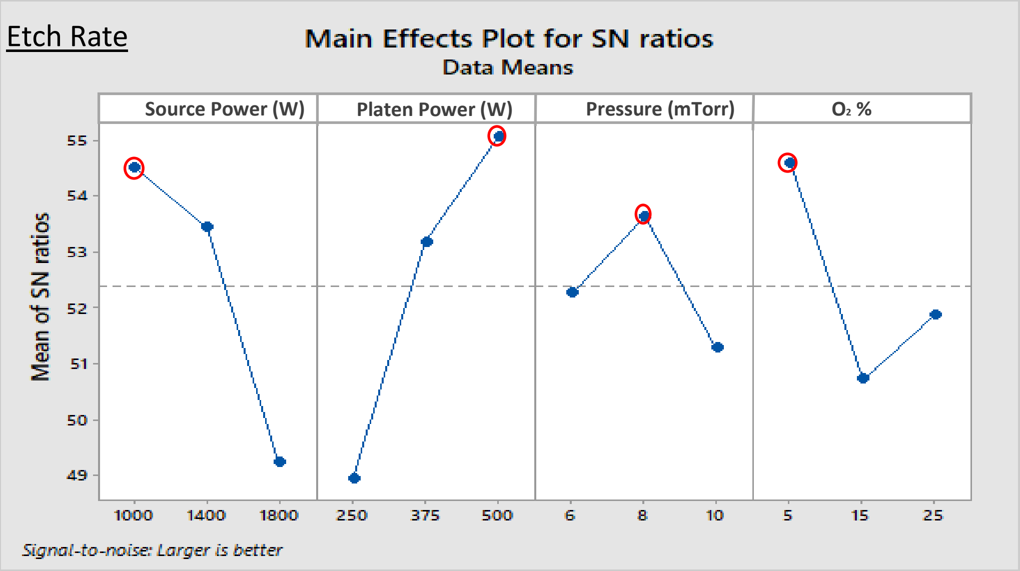

Figure 5.8 - Graph of S/N for the etch rate of pillars for the matrix experiment. Outlined in red circles are the optimum level settings.

Response Table for S/N				
Larger is better				
Level	**Source Power**	**Platen Power**	**Pressure**	**O_2%**
-	(W)	(W)	(mTorr)	(%)
1	54.61	49.42	52.26	54.27
2	53.55	52.94	53.69	51.05
3	49.12	54.92	51.33	51.96
Delta	5.48	5.5	2.37	3.22
Rank	**2**	**1**	**4**	**3**

Table 5.6 - The response table for S/N for the etch rate. Dominant parameters are ranked in the table.

An interesting trend in the O_2 % influence on the etch rate is revealed. It is counter-intuitive that a low O_2 concentration in the plasma leads to higher etch rate. The lower amounts of oxygen should mean that there is less etching of fluorocarbon passivation material deposited during the etch, leading to a lower etch rate as the surface begins to build up greater passivation. This could be a result of saturation in the plasma after a point, where the O_2 concentration simply reduces the available C_mF_n species available for etching. As the O_2 concentration is somewhat lower in the rankings however, it could just be that in this process, the platen and source powers are simply so much more dominant in the etching mechanism that they override any normal effect that this control factor usually would have.

Looking at the response data for the sidewall angle, again the dominance of source and platen power can be seen. It would appear that a lower etch rate is conducive to a lower sidewall angle. From this, it can be inferred that the directionality of the etch depends heavily on both the plasma species available for etching of quartz, and the source-platen combination. These are best controlled by the three control factors – source power, platen power and the gas composition.

5.3.2 Sidewall angle response

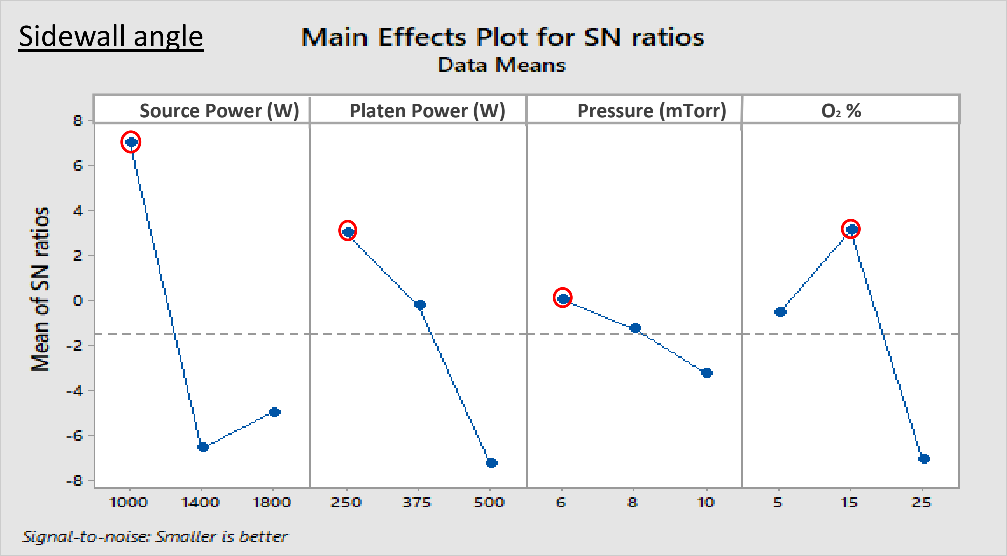

Figure 5.9 - Graph of S/N for the sidewall angle of pillars for the matrix experiment. Outlined in red circles are the optimum level settings.

Response Table for S/N				
Smaller is better				
Level	**Source Power**	**Platen Power**	**Pressure**	**O_2%**
-	(W)	(W)	(mTorr)	
1	7.04	2.98	0.02	-0.56
2	-6.56	-0.23	-1.27	3.13
3	-4.97	-7.24	-3.25	-7.06
Delta	13.59	10.21	3.28	10.19
Rank	**1**	**2**	**4**	**3**

Table 5.7 - Response table for the S/N for the sidewall angle. Dominant parameters are ranked in the table.

From the graphs and data in **(Figure 5.9)** and **(Table 5.7)**, the optimum level settings for maintaining a sidewall angle close to 1° are:

- Source power of **1000W**
- Platen power of **250W**
- Pressure of **6mTorr**
- C_4F_8:O_2 ratio of **80:15**
-

with source power being the most dominant control factor, followed closely by platen power and oxygen concentration. This is where the results of this optimisation experiment begin to become tricky. As each response characteristic was analysed, conflicting optimum settings began to arise. This meant that, at some point, trade-offs need to be made as to what the final recipe settings would be.

Again it can be seen in the trends from the graphs that platen power increase does not equate to more isotropic etching. The inflection point still exists in the oxygen concentration data, implying that removal of fluorocarbon passivation material is not the only purpose that this control factor serves to influence. Source power saturates in its influence on sidewall angle at some point between 1000W and 1400W. This hints again that it is the magnitude of the difference between the two power settings that really influences the directionality of the etch, and the energy of the reactions that take place at the substrate surface.

5.3.3 Tip diameter response

Next are the results for the Δdt, the change in pillar tip diameter from the initial mask design. It should be noted again that this is distinct from the amount of lateral mask erosion. Change in the final pillar tip diameter can arise from more sources than just mask preservation issues, such as field distortion, mask faceting and uneven temperature distribution throughout the pillar itself. It is, therefore, another metric that will allow inference about the uniformity of the plasma interaction with the substrate surface.

Immediately there is a shift in the dominant control factors, with the source power falling to 4th position. Platen power takes precedence as the control factor in the change in pillar tip diameter. The next important control factor is the chamber pressure. 6mTorr is marked as the optimum pressure for preserving diameter from the mask, with the response falling and then rising again with the move to 10mTorr.

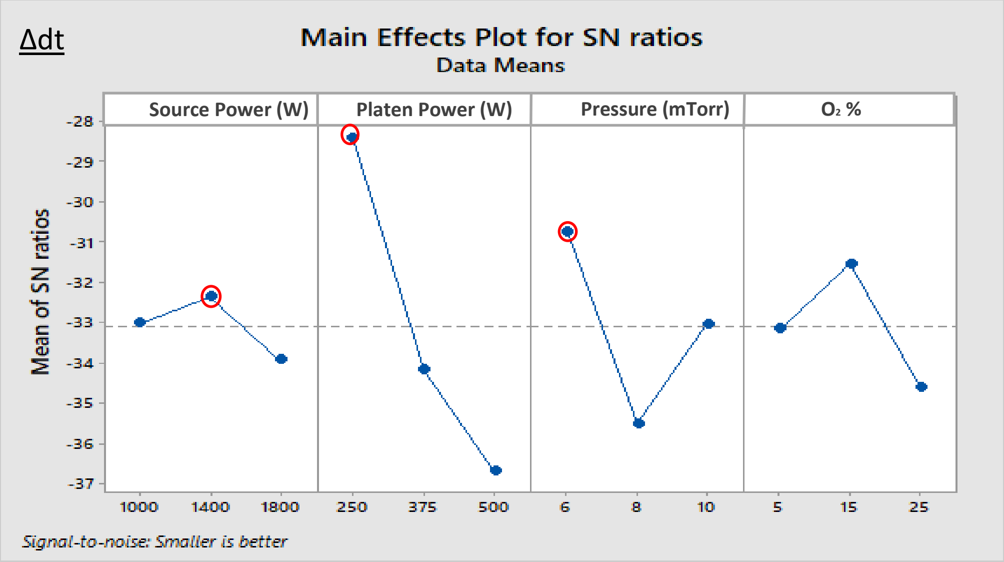

Figure 5.10 - Graph of S/N for the Δdt of pillars for the matrix experiment. Outlined in red circles are the optimum level settings.

Response Table for S/N				
Smaller is better				
Level	**Source Power**	**Platen Power**	**Pressure**	**O_2%**
-	(W)	(W)	(mTorr)	
1	-33.02	-28.41	-30.74	-33.15
2	-32.36	-34.19	-35.52	-31.54
3	-33.92	-36.7	-33.04	-34.6
Delta	1.56	8.29	4.78	3.07
Rank	**4**	**1**	**2**	**3**

Table 5.8 - Response table for the S/N for the Δdt. Dominant parameters are ranked in the table.

It is likely that the platen power and the pressure effect both the ion energy at impact, the directionality of this impact and the mean-free path of the reactants at the surface. It has already been hypothesised that this was the main factor in the difference seen between response of nanopillar formation at different pitches. Field distortion may also play a role in this, increasing faceting, however with the relatively minimal role that source power appears to play in this response characteristic, this seems unlikely.

The 3rd most influential control factor is the gas composition. It has a maxima in the response at a ratio of 80:15sccm. This mimics the trend in the sidewall angle, which is unsurprising as the directionality of the etch here will be larger, thus preventing faceting or mask undercutting.

This could be a result of the levels of O_2 in the plasma reaching an equilibrium where passivation material is removed at sufficient rate to maintain good directionality in the etch, before reaching a stage where the fluorocarbon layers being deposited are removed too fast. Thus facilitating isotropic etching of the pillar sidewalls.

Overall, the optimum process conditions for maintaining pillar tip diameter relative to the designed mask diameter are:

- Source power of **1400W**
- Platen power of **250W**
- Pressure of **6mTorr**
- C_4F_8:O_2 ratio of **80:15**

5.3.4 Lateral mask erosion response

The trends in the lateral erosion of the metal hard mask are important. They will inform the conclusions about the link between the control factors and the mechanism behind the changes in sidewall angle and reduction in pillar tip diameter. If the change in pillar tip diameter is matched by the change in lateral mask erosion rate, then any changes observed are due to the degradation of the metal mask. However, if they are not, then one of the aforementioned effects must be in play; mean-free path of reactants, field distortion or mask undercutting.

These trends, when compared the aggregate data and the other pitch data **(see Section 5.3.5** and **Appendix C.3)** begin to coalesce into a concise set, and from this and optimum recipe can be selected. With reference to **(Figure 5.11)**, the platen power and pressure settings are dominant. This is in line with the Δdt setting, although the platen power much more so than pressure. This implies that etch directionality is a critical factor in lateral mask erosion, which in turn will affect the isotropy of the etch. However, the existence of pressure as a critical factor, closely followed by source power being separated by only 0.2dB, implies that a different phenomenon is taking place than with the Δdt dataset.

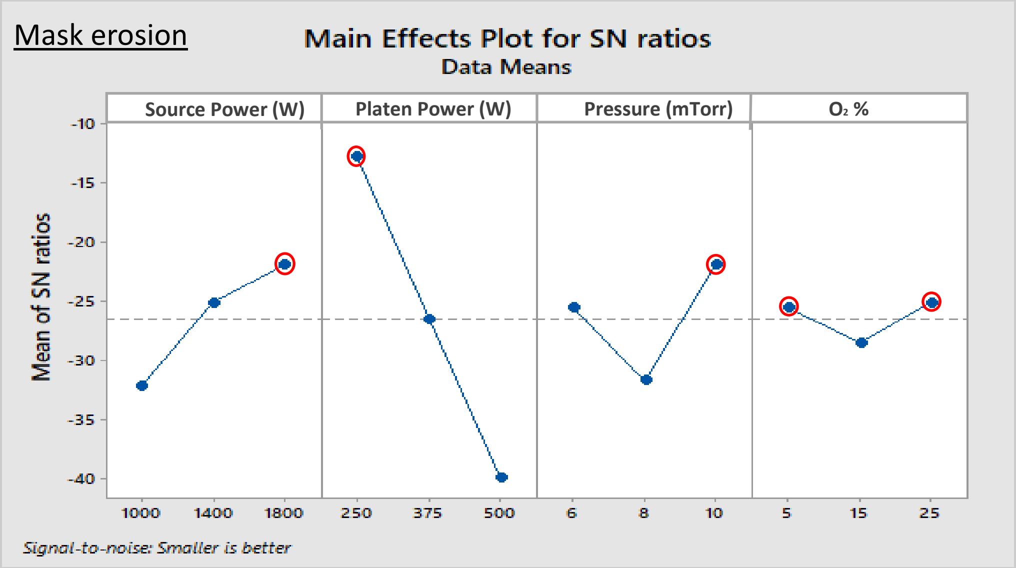

Figure 5.11 - Graph of S/N for the lateral mask erosion of pillars for the matrix experiment. Outlined in red circles are the optimum level settings.

Response Table for S/N				
Smaller is better				
Level	**Source Power**	**Platen Power**	**Pressure**	**O_2%**
-	(W)	(W)	(mTorr)	
1	-32.21	-12.83	-25.63	-24.99
2	-24.54	-25.93	-31.77	-28.59
3	-22.01	-40	-21.36	-25.19
Delta	10.21	27.17	10.41	3.6
Rank	**3**	**1**	**2**	**4**

Table 5.9 - ***Response table for the S/N for the lateral mask erosion*****. Dominant parameters are ranked in the table.**

Looking at the raw data, a change in pillar tip diameter was not always incidental to a change in mask erosion rate. This, along with the exaggerated dependence on the platen control factor, and the diminished and inverted pressure relationship, implies that the instances of dramatic undercutting of the pillars are not due to mask erosion.

The 10mTorr pressure appears to be most conducive to preservation of the aluminium mask, which coincides with conventional knowledge on the effect of pressure on mask selectivity. Pressure typically controls the mean-free path of the plasma, thus controlling the collision rate at the surface and in the plasma itself. Higher pressures reduce collisions, and this any sputtering effect on the metal mask will be reduced.

This is another important insight into the process, as it provides further evidence for the chemical nature of the isotropic etching that is causing the Δdt of the pillar tips and sidewall angle changes. This helps to build a clearer picture about the reactions taking place at the surface of the substrate to fabricate these structures, which in turn will allow any process optimisation to be pre-empted, saving time and improving efficiency.

Overall, the optimum level settings for preserving the metal mask, and thus increasing selectivity, are:

- Source power of **1800W**
- Platen power of **250W**
- Pressure of **10mTorr**
- C_4F_8:O_2 ratio of **90:5** *or* **70:25** (although due to the small factor impact any setting would be equally as good in this range).

5.3.5 Aggregate diameter analysis

These results and insights can be compared to the data collated for the full spread of diameters in the experiment, which will also indicate the levels of variance induced by this noise factor. Any divergences from the initial diameter dataset will be noted and expanded upon.

Firstly, the etch rate response across all diameters at 0.5µm pitch only varies slightly from the 100nm diameter analysis. The Platen response becomes more linear, and stronger, essentially re-enforcing all of the inferences collected from the data.

The sidewall angle response is also very similar, with the pressure increasing in relevance across all diameters. Source power still remains the dominant control factor in determining sidewall angle, however interestingly the other three responses appear to become more congruent. The optimum platen setting changes in this regime to 375W.

This could be due to the lower aspect ratio, i.e. higher diameter features etching more uniformly, see **(Figure 5.13)** for a comparison of the different diameter responses, and this will influence the data.

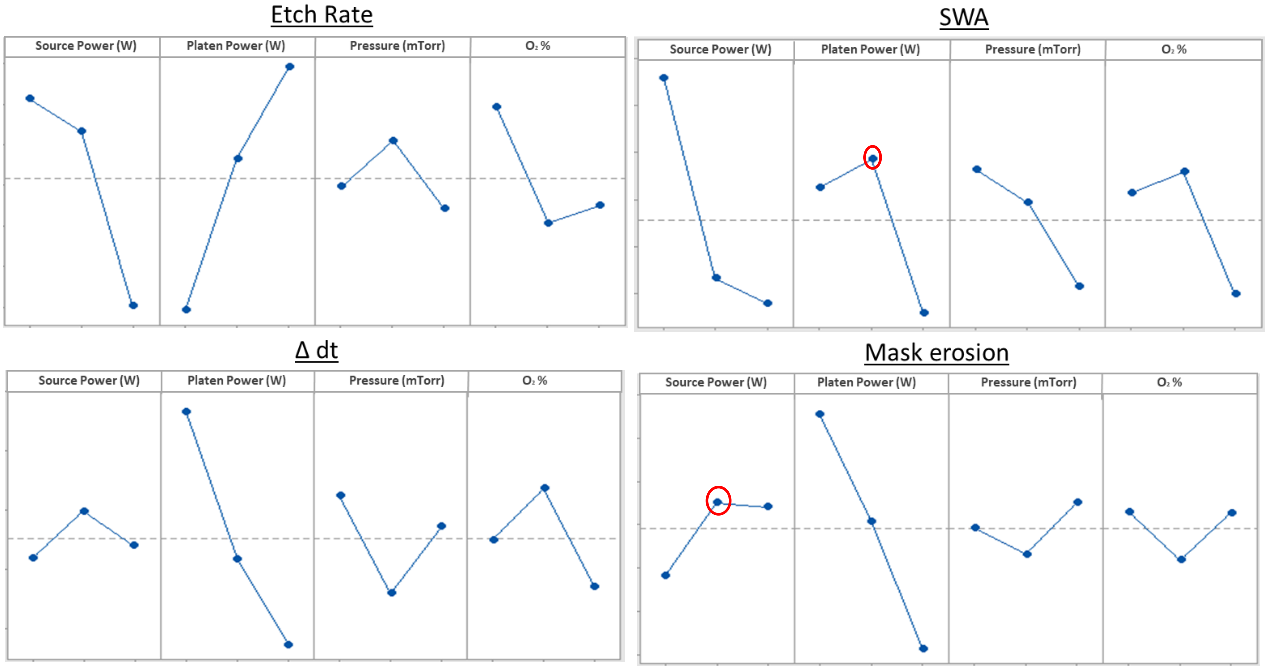

Figure 5.12 - S/N responses of the full diameter dataset. These will be more representative of the variances included in the process.

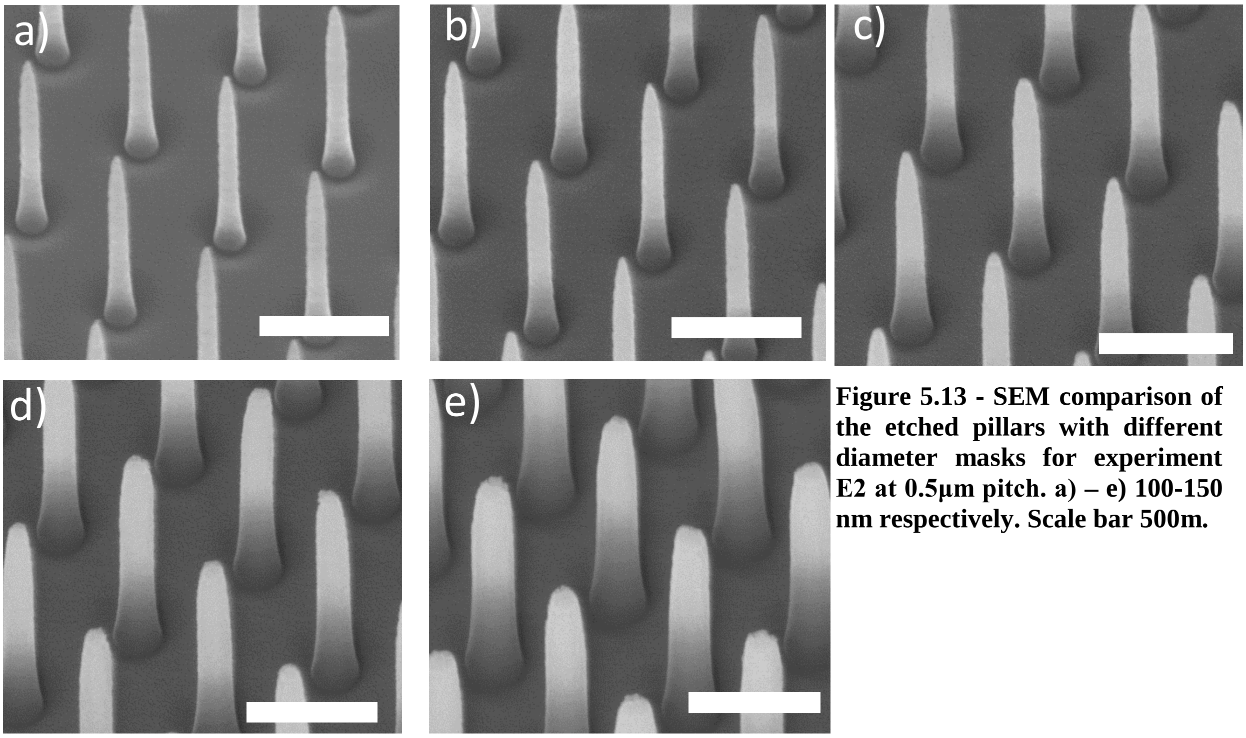

Figure 5.13 - SEM comparison of the etched pillars with different diameter masks for experiment E2 at 0.5µm pitch. a) – e) 100-150 nm respectively. Scale bar 500m.

The change in pillar tip diameter from the mask, as well as the mask erosion, match very closely their 100nm diameter pillar counterparts, with very little change in the optimum parameters save for the source power changing from 1800W optimum to 1400W optimum, marginally. Overall, the two datasets would appear to be in agreement, especially for the optimum level settings and the dominant control factors for each of the etch responses.

There is some variance between each diameter for every level setting. This can best be gauged by plotting the standard deviation of the mean-of-means for each level setting, for each control factor, across all five diameters, as shown in **(Figure 5.14)**.

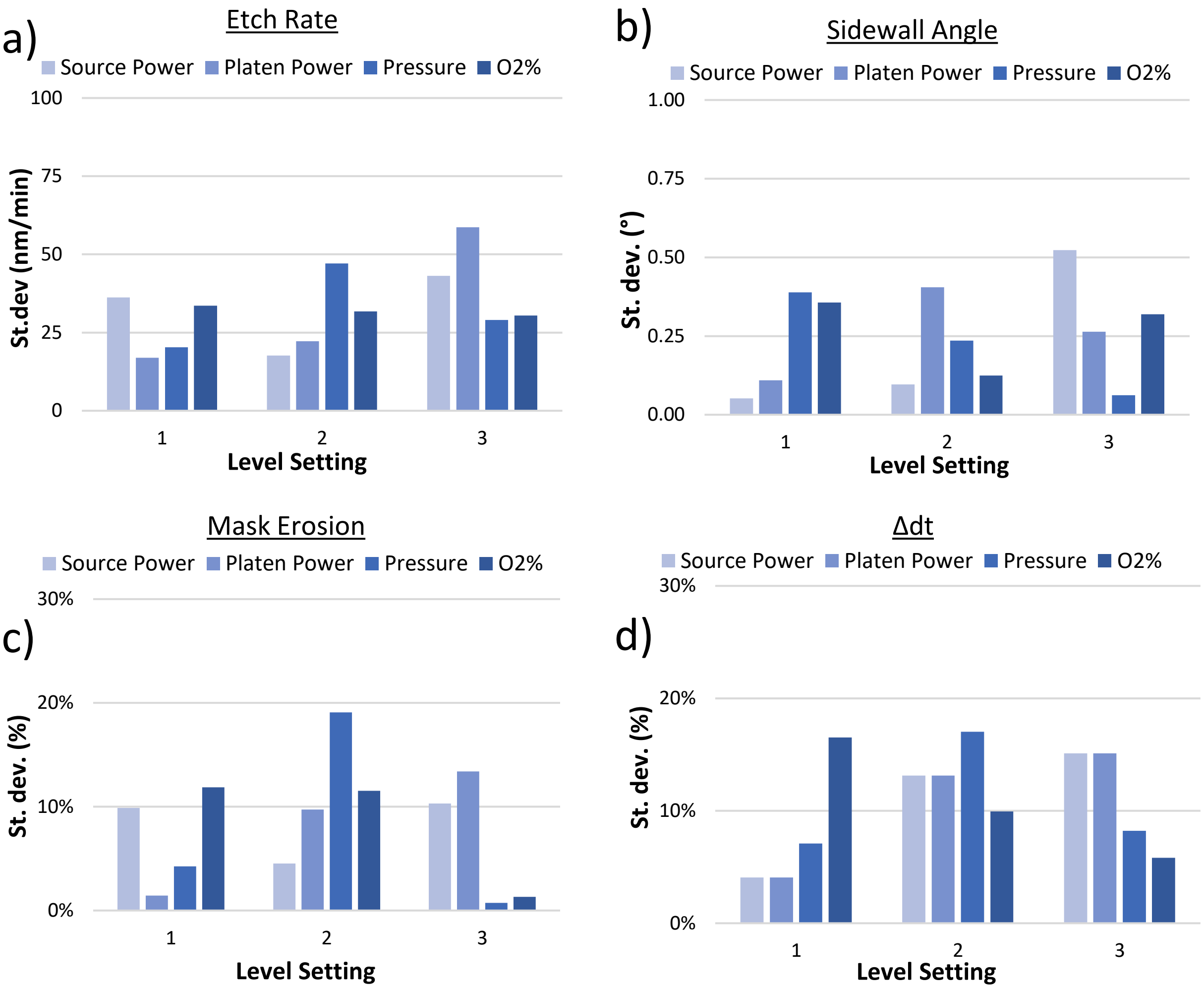

Figure 5.14 - Bar charts demonstrating the standard deviation present across all 5 diameter pillars for each level setting. Data is grouped by etch response characteristic for 0.5µm pitch arrays.

There are some important points to note about the standard deviation between the means of all the diameter datasets for each level setting, of each control factor.

Decreasing the source power decreases the relative isotropy of etched features, shown in **(Figure 5.14-b)**, as well as the variance in overall sidewall angle. The variance of etch rate and mask erosion has a minimum at 1400W source power, so there is a trade-off to be made here for this pitch dataset. The variance between sidewall angles decreases with increasing platen power. This is unsurprising, especially considering that most etched features were severely over-etched at the 500W platen power.

The variance between diameters however is minimal at 250W source power, as is the relative amount of lateral mask erosion, and the etch rate. The data seem to be in agreement here that 250W platen power makes the most robust process for etching 0.5µm pitch pillars using this process.

The trend in variance for the oxygen concentration level settings does not appear to follow any set trend. This is most likely due to the varied role that this control factor plays in all of the different response characteristics, and so the parameters of minimal variance will need to be selected based on the rankings of the Taguchi analysis, as well as a prioritising of the most important etch characteristics.

Increasing pressure also appears to uniformly decrease the variance between diameters. An interesting insight into this control factor given that higher pressures should result in more chemical-based, isotropic etching.

Contextualising this with the trends from the other datasets, **(Appendix C.3)**, some slight variations do occur between pitches in the optimum level settings, and in some of the responses. However, this can be weighted across the entire pitch range investigated, as will be discussed in the next sub-section, to decisively select the best level settings.

5.4 Determining the optimum level settings across all pitches

So far, each individual pitch has its own set of optimum level settings for maximising etch rate, whilst minimising sidewall angle and pillar tip diameter deviation from a target value, and preserving the Al etch mask. These are laid out in tandem in **Table 5.10.**

		Etch rate				**Sidewall angle**				**Δdt**				**Mask erosion**			
		SP	*PP*	*Pr*	*O_2*	*SP*	*PP*	*Pr*	*O_2*	*SP*	*PP*	*Pr*	*O_2*	*SP*	*PP*	*Pr*	*O_2*
0.5µ	*Opt*	1	3	2	1	1	1	2	2	2	1	1	2	3	1	3	3
	Rank	**2**	**1**	**4**	**3**	**1**	**2**	**4**	**3**	**4**	**1**	**2**	**3**	**3**	**1**	**2**	**4**
1µm	*Opt*	1	3	2	1	1	1	3	2	2	1	1	1	3	1	3	2
	Rank	**2**	**1**	**4**	**3**	**1**	**3**	**4**	**2**	**4**	**1**	**3**	**2**	**3**	**1**	**2**	**4**
2µm	*Opt*	1	3	2	1	1	1	2	1	3	1	1	2	3	1	3	3
	Rank	**2**	**1**	**4**	**3**	**2**	**1**	**3**	**4**	**2**	**1**	**3**	**4**	**3**	**1**	**2**	**4**

Table 5.10 – optimum level settings and their rankings for each HAR pitch.

The optimum level settings, despite the variations observed in the actual etching of the nanopillar features, are surprisingly corroborative. The plate power (the most commonly ranked 1st in impact on the process) has the same optimum level setting for every metric. As does the pressure in all but one case – the sidewall angle for the 1µm pitch arrays.

There have been a variety of incidents of conflicting optimums in level settings, mostly grouped by etch rate and sidewall angle vs tip diameter and mask preservation. What tends to maintain a high etch rate and a more anisotropic pillar sidewall also tends to erode the metal mask at a faster rate. It is therefore important to rank the etch characteristics in order of importance.

First in this ranking is arguably the sidewall angle. It has already been demonstrated that this nanopillar dimension not only dominates the mechanical properties of individual nanopillars, but also their replication accuracy. The dominant factors for controlling sidewall angle are source power, platen power and O_2%, the optimum level settings of which are **1000W**, **250W**, and **80:15** ratio respectively.

Secondarily will be tip diameter conservation. This is also an important facet of the process to ensure robust results from, and precise control over. The rankings for this process outcome are slightly more varied than for the sidewall angle, however platen power is consistently the most dominant control factor, followed by pressure and then O_2%. These have optimum level settings of **250W**, **6mTorr** and **80:15** respectively.

Thirdly would be the etch rate. It is important that a high etch rate be maintained. These level settings consistently had the same rankings and order, with platen power, source power and O_2% the top three dominant factors. These have optimum level settings of **1000W**, **500W** and **90:5** respectively.

Turning attention to mask erosion, the rankings and level settings of which were almost as unanimous as those for the etch rate. The top three were platen power, pressure and source power, with optimum level settings of **250W**, **10mTorr** and **1800W** respectively.

This makes selecting the optimised recipe slightly conflicted, however by ranking the etch characteristics like this it allows for a tertiary order of importance and rank to be imposed onto the results. Deference was given first to the ranking of the response characteristic, then to the rank of the control factor within that, then to the level setting.

This leaves a recipe of:

- Source power = **1000W**
- Platen power = **250W**
- Pressure = **6mTorr**
- Gas ratio = **80:15**

This can now be trialled with a confirmation etch, and the veracity checked against the following predictions from the linear regression analysis performed in Minitab, outlined in **Section 5.5**, which were carried out using the data for each pitch, and using the above optimum level settings. It can also be compared to the experiment **E1**, as three of the four level settings remain constant, and the effect of changing the gas composition ratio directly compared to the confirmation etch result.

5.5 Confirmation etch results

Using these, optimum process settings, the following predictions were made about the expected response of etch rate, sidewall angle, Δdt and mask erosion rate.

For the 0.5µm pitch data, the predicted outcomes were an etch rate of *430nm/minute*, a sidewall angle of *1.4°*, and a *5%* change in pillar tip diameter, with a *5%* reduction in mask diameter due to lateral etching.

For the 1µm pitch data, the predicted outcomes were an etch rate of *425nm/minute*, a sidewall angle of *1.47°*, and a *20%* change in pillar tip diameter, with a *5%* reduction in mask diameter due to lateral etching.

For the 2µm pitch data, the predicted outcomes were an etch rate of *440nm/minute*, a sidewall angle of *1.3°*, and a *25%* change in pillar tip diameter, with a *5%* reduction in mask diameter due to lateral etching. Mean results for all diameter pillars are depicted in **Table 5.11** and contrasted with their predicted counterparts.

	Etch rate (nm/min)		***Sidewall angle (°)***		***Δdt (%)***		***Mask erosion (%)***	
	predicted	*measured*	*predicted*	*measured*	*predicted*	*measured*	*predicted*	*measured*
0.5µm	430	488 ± 18	1.40	1.56 ± 0.25	5	3 ± 3	5	3 ± 2.5
1µm	425	480 ± 19	1.47	1.56 ± 0.1	20	2 ± 4	5	1 ± 7
2µm	440	459 ± 40	1.30	1.59 ± 0.2	25	5 ± 7	5	3 ± 5

Table 5.11– Predicted vs measured response characteristics for the confirmation experiment. ± standard deviation.

The confirmation etch appears to exceed the linear projections in all cases except the sidewall angle, where it is only slightly higher than predicted by on average 0.15°, which can be considered to be well within the measurement errors identified earlier in this work, and can therefore be categorised as successful.

Taking these results in pitch category, the 0.5μm pitch results differ from their predicted values by 1.13x, 1.14x, 0.6x and 0.6x for the response characteristics respectively. The similarity between the magnitude of the delta between the etch rate and sidewall angle, as well as between the mask erosion and pillar tip diameter change it can be concluded that these increases in response are all concurrent with one another. The increased mask preservation has led to a lower variation of the pillar tip diameter from the design specification, and this has been offset only slightly by the increase in etch rate, most likely due to the preservation of sidewalls contributing to the anisotropy of the features. Together these increase the sidewall angle from its prediction by 14%. **(Figure 5.15)** demonstrates the improvements that the Taguchi experiment has made from the initial He cool cycle recipe.

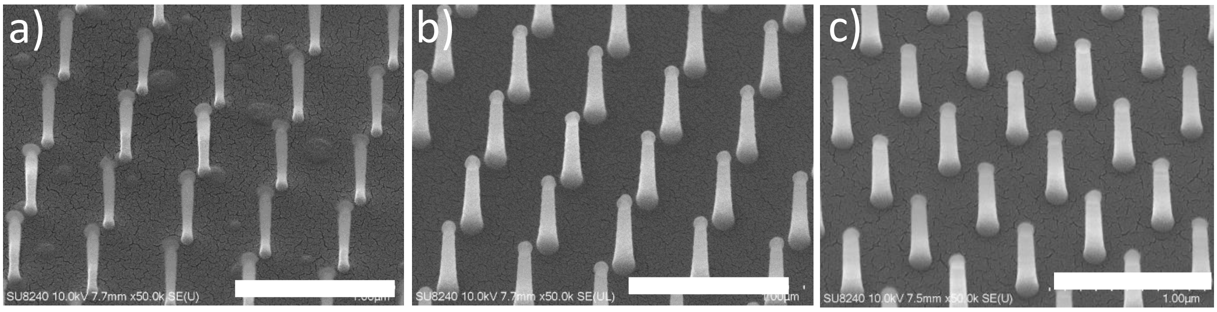

Figure 5.15 - Progression of the etched nanofeatures using fine tuning of the He cooling cycles (0.5μm pitch). SEM of the 0.5μm pitch pillars for 100nm diameter mask, with a) the 40°C, 30 second He cycle recipe, b) experiment E1 and c) the confirmation etch. SU8200, 15kV beam, 30º tilt, scale bar 1μm.

The SEM qualitatively demonstrate the remarkable improvement in etched pillar response from the base cyclical recipe alone. Between the **E1** and confirmation etch experiments can be seen the more isotropic response of the sidewall, with similar base diameters but a pillar tip diameter that closely matches the mask diameter, in some places remaining on the 100nm diameter target. This last improvement has come directly from the increase in O_2% in the gas composition, a level setting tied directly to improved sidewall angle and pillar tip diameter conservation.

The 1μm pitch pillars respond even better than their linear projections. The etch rate is improved by roughly the same amount as the 0.5μm pitch projections, factor 1.13x. The sidewall angle is consistent this time, the etch responding robustly across this increase in pitch. The vast improvements are demonstrated in the Δdt data, with the undercut levels at 2% which come in at 0.2x the predicted data, and 1% mask erosion rates.

Again this improvement between **E1**, which had a sidewall angle in excess of 2.5°, comes from changing the gas composition. **Figure 5.16** qualitatively demonstrates this.

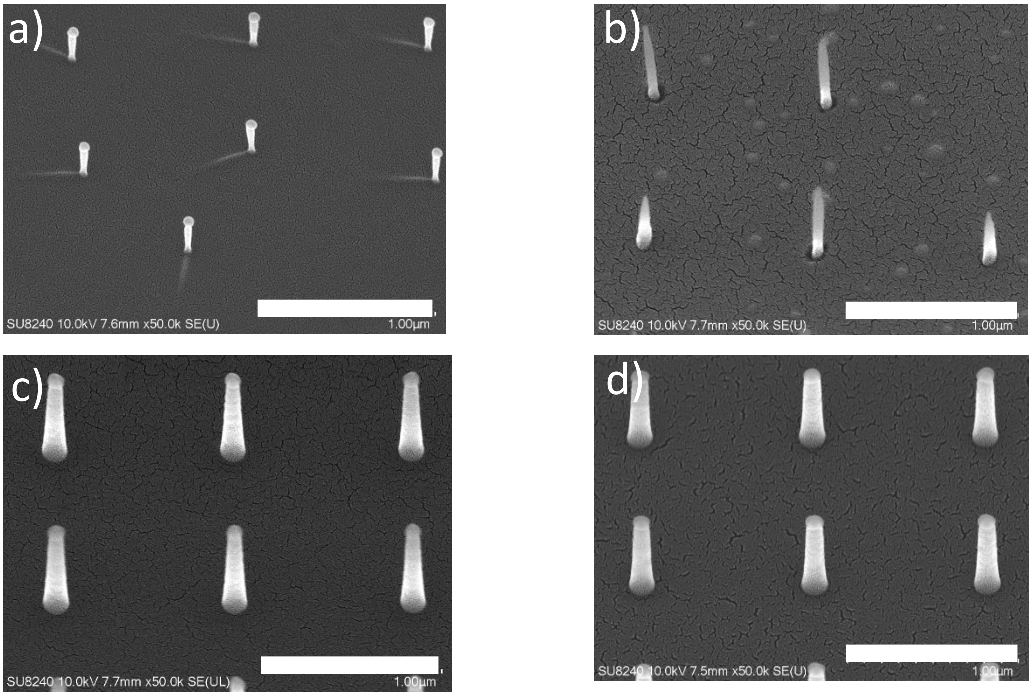

Figure 5.16 - SEM progression of the 1µm pitch pillars from the standard microtrench recipe to the optimised He cooling cycle. SEM of the 1µm pitch pillars for 100nm diameter mask, with a) the standard microtrench recipe b) the 40°C, 30 second He cycle recipe, c) experiment E1 and d) the confirmation etch for this pitch. SU8200, 15kV beam, 30° tilt . Scale bar 1µm.

When comparing the SEM qualitatively, with which the standard microtrench recipe can now be included, the improvements are much more dramatic. The increase in etch isotropy from the standard recipe, to the initial cooling cycle and then to the **E1** and confirmation etch show consistent improvement in pillar tip diameter preservation, sidewall angle and mask selectivity.

Interestingly, these are only accompanied by a relatively slight decrease in etch rate, around 20-30 nm/minute or so, coincidentally the etch rate of the 80+ RIE process. The reason for the improved pillar robustness between **E1** and the confirmation etch remains the same – preservation of mask and consistency of pillar tip diameter to spec.

The 2µm pitch pillars respond just as well as the lower pitch arrays. The etch rate is slightly lower, however is more consistent to the predicted value, only differing by 1.04x. the sidewall angle has a 1.17x increase from the prediction, and is the largest out of the three pitches however only by 0.03 of a degree, well within any measurement error.

The Δdt is 0.17x the predicted value, and the lateral mask erosion 0.3x. This again follows the same trend in sidewall angle increase by mask preservation. Qualitatively the results are less dramatic than the 1µm pitch counterpart array, see **(Figure 5.17)** however the improvements still speak for themselves, particularly with regards to how consistent the etched features are over diameter and pitch.

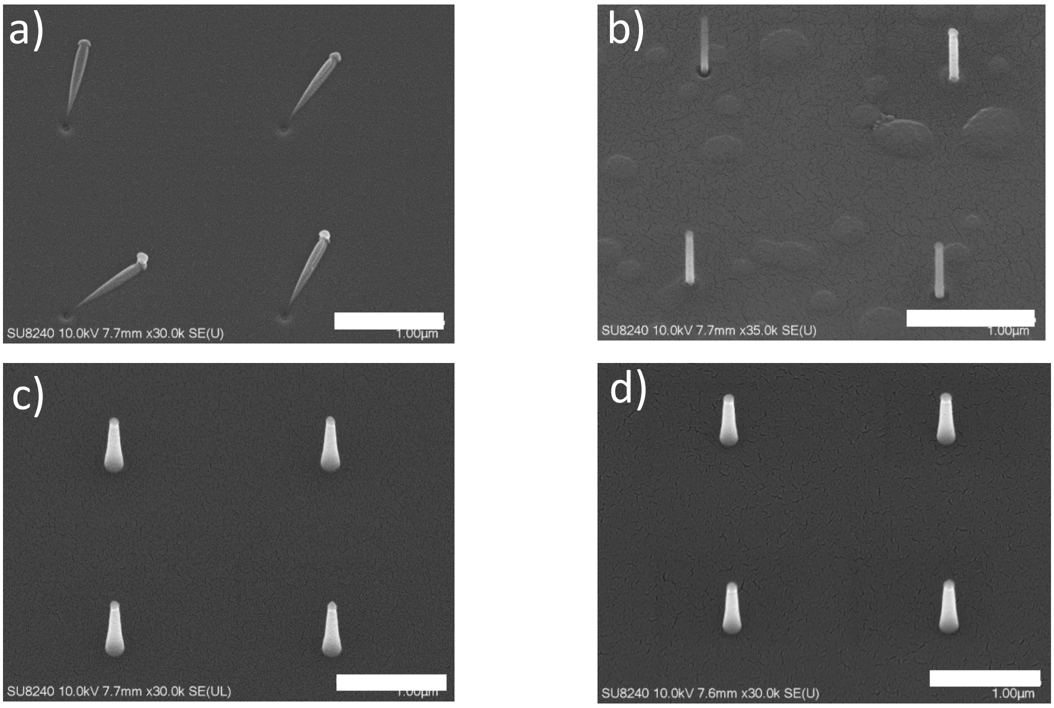

Figure 5.17 - SEM progression of the 2µm pitch pillars from the standard microtrench recipe to the optimised He cooling cycle. SEM of the 2µm pitch pillars for 100nm diameter mask, with a) the standard microtrench recipe b) the 40°C, 30 second He cycle recipe, c) experiment E1 and d) the confirmation etch for this pitch. Scale bar 1µm.

The 2µm pitch pillars appear to be closer matched between **E1** and the confirmation etch, however the pillar tip diameter is increased, following the same inferred process as before, and the base has quantitatively shrunk, forming a more uniform feature. Whilst the image for the initial helium cooling cycle recipe are free standing and fully formed, they are much different from the 1 and 0.5µm pitch features. The difference across all of these pillars ranging from profile morphology, sidewall angle, etch rate and mask undercutting.

Overall, the Taguchi optimisation experiment can be said to be a success. Whilst profile angles of 1° were not achieved, the lower limit of anisotropy has been set at roughly 1.5°. The Taguchi analysis has offered insight into the effects that the four main control factors in the ICP etch process, namely source power, platen power, chamber pressure and gas composition ratio, and these can be used to tune the sidewall angle whilst maintaining the very low levels of mask erosion and undercutting that lead to a change of the pillar tip diameter from the designed mask features.

The etch rate has been maintained at a consistent level, and now the response characteristics for the etched features are consistent across diameter and pitch, two previously identified design features that dramatically affect the pillar dimensions after etching.

The optimised process has proven robust across all design parameters, tuneable to within 100s of nm/minute, with sub-degree sidewall angle control at the nanoscale. These high aspect ratio features are now ready to be pushed beyond the current fabrication limitations, into larger heights and wider high aspect ratio features.

5.6 Conclusions

The ICP RIE process was selected because of its proven ability to etch deep, highly anisotropic features into a variety of materials, in this case the interest was in etching quartz. With etch rates in excess of 500nm a minute, they far outstrip the conventional reactive ion etching approach.

The aim was to have a recipe that could etch arrays of nanopillars over multiple diameters and pillar-to-pillar distances with minimal variance in the etch rate, sidewall angle and change in pillar tip diameters. This was quantified as being an etch rate approaching the 500nm/minute mark, a sidewall angle approximate to 1°, almost perfect anisotropy, and a reduction of pillar tip diameter from the designed mask by a maximum of 10-15%. This has been achieved, and in areas exceeded. An etch recipe with 450nm/ minute uniform etch rata across pitch and diameter has been demonstrated.

The sidewall angle, whilst not at the 1° mark, is close enough to the target value as to be considered successfully achieved, and the change in pillar tip diameter exceeds the 10-15% intended value by quite some margin, falling within the measurement error in SEM-based intensity measurements. The effect of adhesion material, substrate temperature and helium cooling cycle approaches were investigated to improve etch response, and the effects of changing these over a series of incremental values measured and analysed. The control factors, identified from the literature, and their effects on the identified response characteristics have been identified and discussed.

These two facets of the exploration of this process will allow for any future work carried out using the SPTS synapse etch tool to be pre-emptively hypothesised and will allow for a streamlined process to optimisation. These responses will also be of interest to the scientific community at large, especially with the advent of some new biomedical and optoelectronic based technologies.

6.0 Conclusions

This thesis set out to create an experimental platform to fulfil a niche that existed in the field of cell mechanics. It did this taking high throughput manufacturing of ultra-high aspect ratio nanopillar arrays using injection moulding, and combining it with standardised microscope slide sized part designs and the multiwell format. Five key aims were established in order to facilitate these, namely that:

1) Pillar arrays must be replicated over sufficiently large surface area to cover a standard 96-well size, and with a consistent morphology over shots so as to be considered mechanically equivalent.

2) Fabrication of microscope slide sized parts with arrays of distinct nanopillars.

3) Combination with a 24-well plate.

4) Establish what effect, if any, the stretching of nanopillars will have on pillar bending mechanics.

5) Develop the nanofabrication process to increase pillar aspect ratio and improve replication accuracy.

Chapter 3.0 concerned itself with aims 1-3 by setting out three criteria and seeking to fulfil those, namely that samples must have stable replication accuracy, predictable part-to-part tolerance and be able to contain different array designs with individual mechanical properties. By defining three metrics of consistent replication, accuracy, success and equivalence, and linking those to distribution of thermal stress in a cooling areas of quality replication could be identified and even predicted. It was found that these are influenced by the design of the ejection mechanism of the tool. Satisfying these three criteria fulfils aim 1 of this thesis. The fabrication of three generations of UHAR devices that were mechanically consistent over 60 – 200+ replication cycles, and integrating two of these with a 24 well plate using ultrasonic welding, aims 2 and 3 were fulfilled.

During the course of the fabrication of UHAR arrays over many replication cycles, the individual nanopillars were measured to stretch and deform. It was posited that this could have an impact on the use of Euler-Bernoulli beam theory, which would inevitably affect the estimation of bulk array mechanical properties.

This also opened an inquiry into the literature as to the general understanding that exists of the underlying assumptions of the Euler-Bernoulli case of a fixed based cantilever when applied to the case of fabricated pillar arrays. A gap in the literature was identified, whereby a concise outline of the restrictions that exist on using this simplified case was lacking.

Chapter 4.0 used FEA to test different stress-strain responses of pillars under different base conditions, fixed and free, across a spectrum of aspect ratios. It identified definitively that for a cylindrical pillar an aspect ratio of 6.5:1 and above is strictly required. This was termed the shear criteria. Taking this one step further, an aspect ratio dependent amendment was found (again using FEA) to exist, that any pillars with sidewall angles of above 3° would fall outside acceptable accuracy of an Euler-Bernoulli case unless the aspect ratio was above 20:1.

These criteria, however, were not sufficient to account for the changes in morphology of the pillar, and only applied to features with straight sidewalls. For ease of calculation, a further amendment to the Euler-Bernoulli equation for the spring constant was required to account for non-linear tapers along the pillar profile. This was tested and verified with multiple FEA modelling experiments and hard limits set on the degree of curvature that can be present in the pillar in order for the amendment to be accurate. By making more accurate models of the fabricated nanopillar arrays, a more realistic estimation of spring constant and therefore cell response can be given, thus satisfying aim 4.

Finally, with clear evidence that sidewall angle is important to replication accuracy, **Chapter 5.0** took the opportunity to develop a new protocol for ICP etching for higher aspect ratio quartz nanopillars. To this end, a Taguchi L9 experiment was conducted to optimise rapid etching of quartz nanopillars with precision control over etch depth, sidewall angle and mask protection. This resulted in a rapid, cyclical etching process with 0.5° sidewall angle control, and an etch rate of over 400nm/min, a result that trumps any found in the literature.

6.1 Application to cell-based experiments

The device presented in section **3.3.3** were used in published work**[70]** to determine the effect that pillar arrays of different $\bar{E}$ would have on MC3T3 pre-osteoblast cells grown over 24 hours, and draw comparison to the literature on their responses. There are three key things to note about the biological results of these experiments that prove the veracity of this approach to using nanopillar arrays to act as a mechanical surface.

The first is that each of the five pillar arrays elicit a different response from the cells as they mature (**Figure 6.1**).

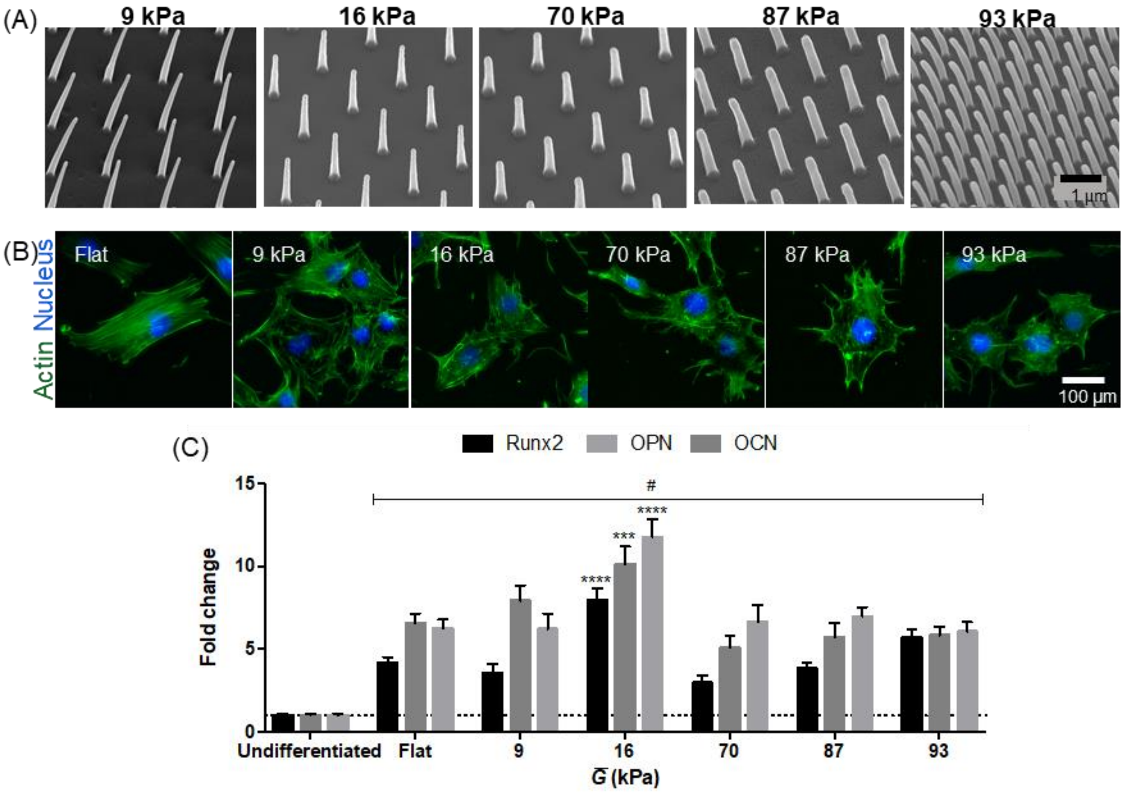

Figure 6.1 – Results of the MC3T3 culture on the multimechanical pillars presented in chapter 3 as presented in the published work[70]. (A) are SEM of the nanopillar arrays. Immunostaining images (B) illustrate the actin (green) and nucleus (blue) of each cell. Visually, these demonstrate the different morphologies that each cell culture exhibits on individual pillar arrays. (C) are the results presented in the published work of the qPCR analysis for three different osteogenic markers.

This result is very promising, as it illustrates that there is no cross talk between different cell cultures in separated wells. It also highlights that different pillar structures after welding remain intact, and that any damage does not negatively affect cell morbidity. Lastly, the successful cultivation of cells on pillar arrays confirm that steps taken to prevent pillar collapse are successful.

The second point to note about these results concerns the array with $\bar{G}$ of 16kPa. This array falls within the range of the native bone microenvironment of pre-osteoblast cells, 8-17kPa**[1]**. MC3T3 cells on this pillar array exhibit increased expression of osteogenic markers when compared to the flat control surface. This indicates strongly that pillar arrays fabricated using this optimised design method can mimic effectively a specific mechanical environment.

Lastly, fluorescence staining images of the cells on the pillar arrays demonstrate that there are focal adhesion sites on the pillar arrays, demonstrating that the cells are indeed interacting with the nanopillars, rather than simply deforming around them or settling above them (**Figure 6.2**), with the measured pitch of the illuminated pillars equalling 1μm.

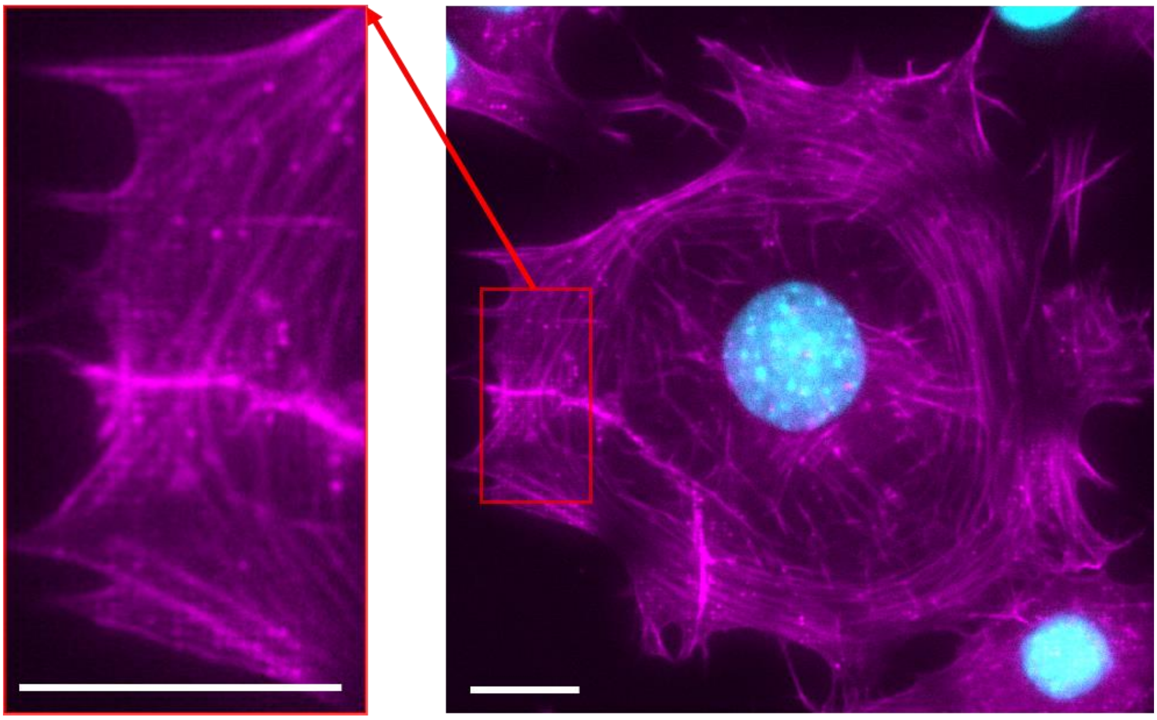

Figure 6.2 – Fluorescent microscopy image of an MC3T3 cell on a nanopillar array, with the actin coloured purple and the nucleus coloured blue. Image taken by Dr Marie Cutiongco of Glasgow University. What is important to note here is the appearance of the highly ordered actin clusters that illustrate the cell's interaction with the nanopillar array. Scale bar 30µm.

This final point is non-trivial and makes for an impressive demonstration of the hypothesis presented regarding equivalent shear moduli, as these cells respond as if they are on a continuous surface[53].

6.2 Summary

To conclude, this body of work presents the injection moulded UHAR nanopillar arrays in a multiwell format that is familiar to biologists and easy to integrate into existing experimental protocol. It has created a unique predictive tool using FEA of thermal stress to streamline part design, and developed a roadmap to establishing quickly the batch tolerances of the process. An amendment to the Euler-Bernoulli spring constant was developed for pillars with non-linear profile tapers, and an optimised process has been presented for rapid ICP etching of delicate quartz nanofeatures.

These improvements to the fabrication process allow for a design to device process that allows for rapid production and development of a platform for cell engineering. These devices have been tested against the standard mechanical platform, hydrogels, and have proved to be of equivalent efficacy whilst having the additional benefit of highly tuneable nanofeature dimensions, promising to allow for further avenues of probing cell-nanotopography interactions.

7.0 Appendices

Appendix A – Additional methods data

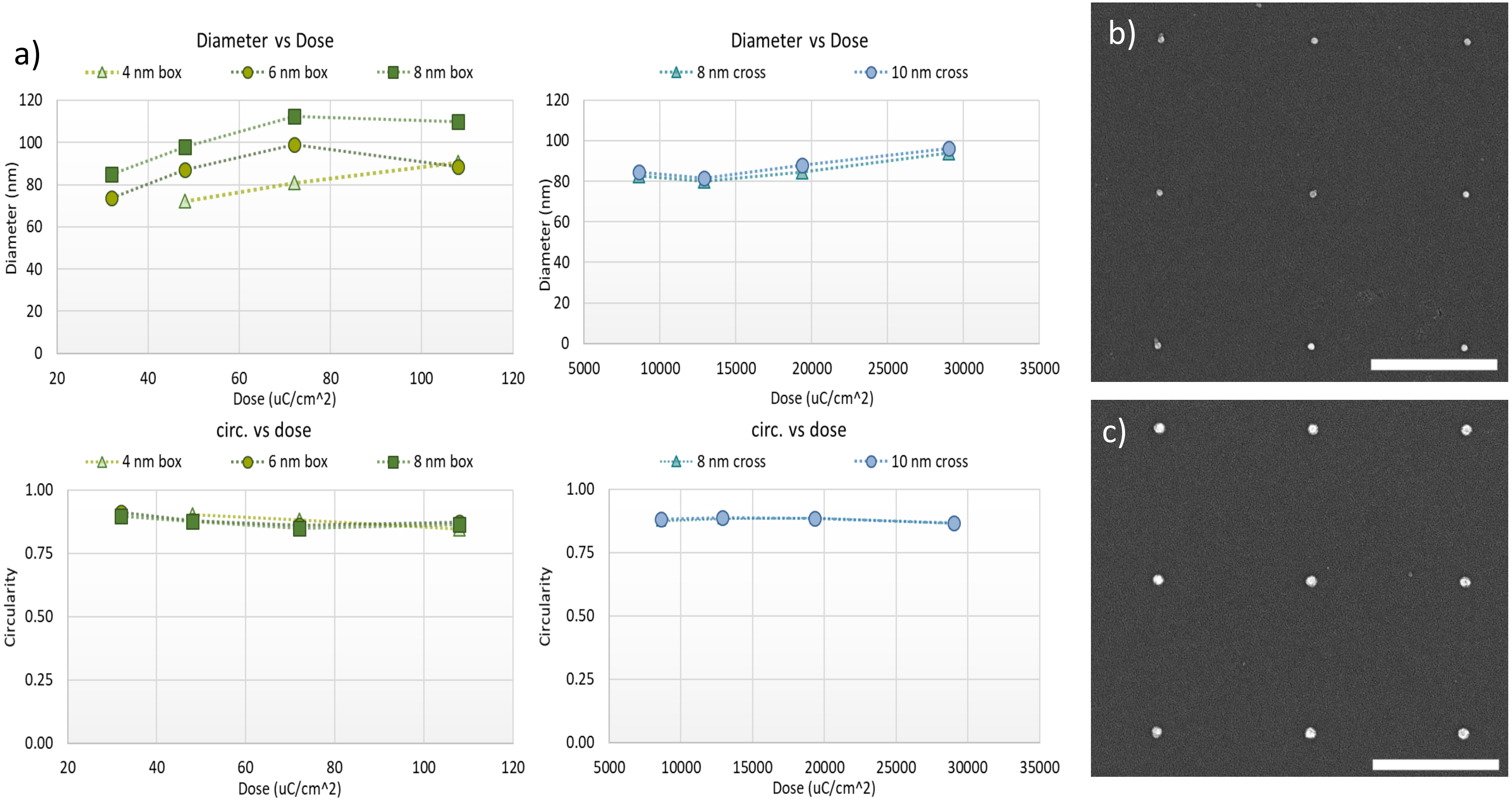

Figure A.1 – Results of the circularity test for smaller nanodot resolution. a) Graphs of diameter vs dose and circularity vs dose comparing the cross and box multipixel methods. b) and c) are examples of smaller circular dots made possible by using asterisks, with b) allowing 1 micron pitch dots as small as 30nm. Scale bar 1µm

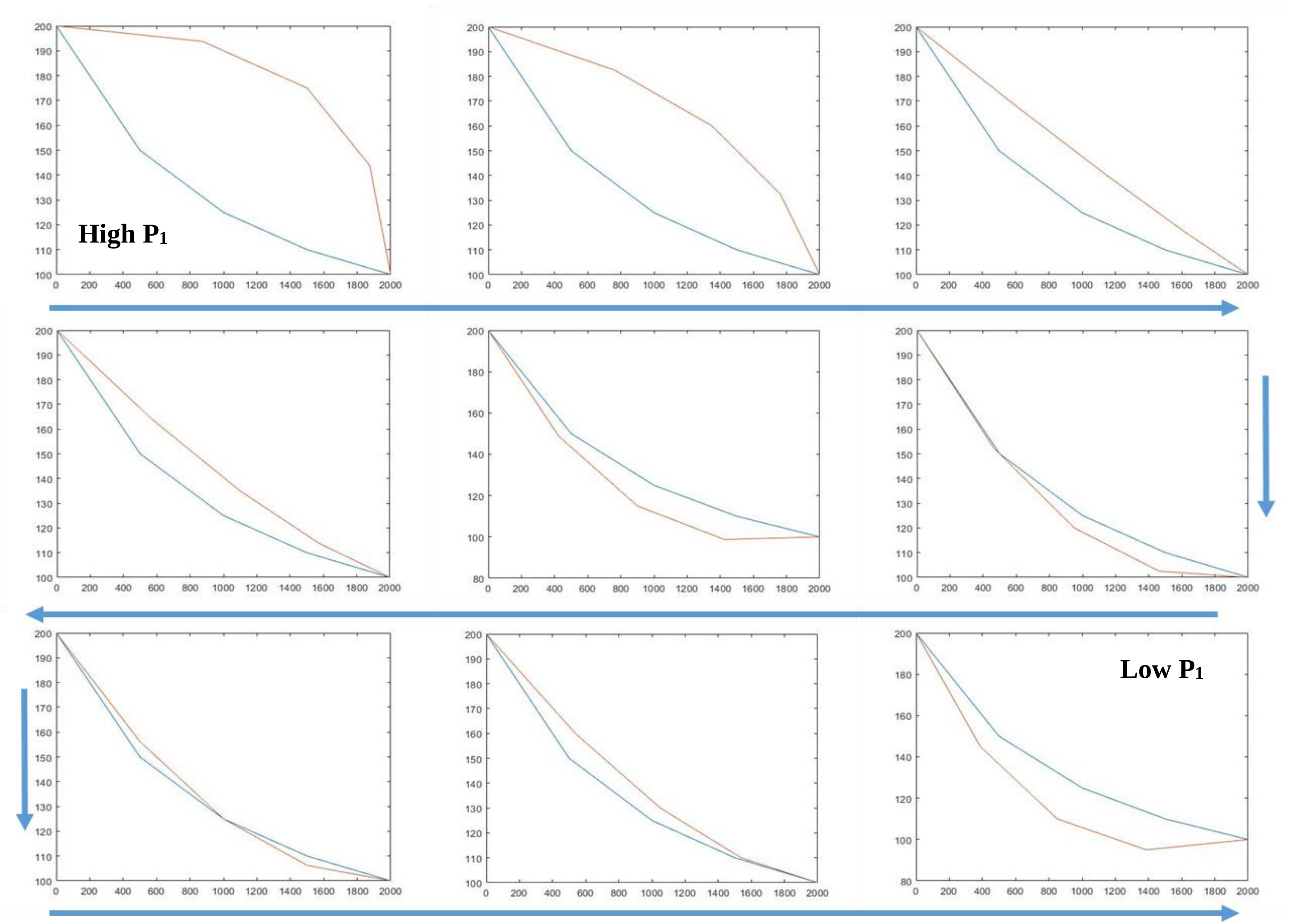

Figure A.2 – Illustration of the Bézier curve fitting process.

Examples of Bézier curves (red) fitted to the profile distribution (blue), with the curve inverting as the value of P1 moves from large to small, indicated by the direction of the blue arrows. Pillar diameter on the y-axis, height shown on the x.

Appendix B – Additional information of Upscaling UHAR pillar arrays

B.1 - Defining quality replication

In order to determine the quality and adequate replication success threshold, the equivalent Young’s modulus of the pillar array as a marker for the point at which failed pillar replication begins to alter the mechanical properties of the array.

As the arrays are fabricated with a 1µm pitch, assuming 100% successful replication this will yield a Young’s modulus with a fill factor proportional to that pitch. Skipping alternative rows and columns of nanopillars in the array will begin to decrease the moduli, with a minimum at 50% of total pillar replication – which is essentially an array with double the pitch, 2µm.

Here, small areas where replication begins to decrease will have a higher pitch. This allows the calculation of a delta, as the percentage of missing pillars can be subtracted from the percentage of fabricated pillars, and a change in the equivalent moduli calculated.

$$E_T = \%_{replicated} * E_1 + \%_{skipped} * E_2 \qquad \textbf{Equation B.1}$$

Where E_T is the total Young’s moduli of the array, E_1 and E_2 are the Young’s moduli of a 1 and 2µm pitch respectively. Using this method, a total pillar replication success rate of 50% is the baseline and can be considered a value of 0% successful replication – i.e. the mechanical properties at this point definitively fall outside the threshold for fabrication success. This results in table **B.1**:

What must also be taken into consideration is the relative surface area that a cell is expected to cover as a ratio of the measured area of the nanopillar array. To do this a hypothetical, idealised surface area of a fibroblast is used, which according to a research of the literature equates to 890 μm^2. This exceeds our measurement area by 10%. As the average cell can be expected to cover an additional area, it allows for some tolerance to the established thresholds that is taken to be +/- 10% replication success. This sets a final threshold of 68% pillar replication for the adequate replication threshold and 78% for the quality replication threshold.

Total	Replicated	Failed	$\bar{E}_1$	$\bar{E}_2$	$\bar{E}_{total}$	% decrease
100.00%	100.00%	0.00%	8.65	2.16	8.65	0.00%
95.00%	90.00%	10.00%	8.65	2.16	8.00	8.11%
90.00%	80.00%	20.00%	8.65	2.16	7.35	17.65%
85.00%	70.00%	30.00%	8.65	2.16	6.71	29.03%
80.00%	60.00%	40.00%	8.65	2.16	6.06	42.86%
75.00%	50.00%	50.00%	8.65	2.16	5.41	60.00%
70.00%	40.00%	60.00%	8.65	2.16	4.76	81.82%
65.00%	30.00%	70.00%	8.65	2.16	4.11	110.53%
60.00%	20.00%	80.00%	8.65	2.16	3.46	150.00%
55.00%	10.00%	90.00%	8.65	2.16	2.81	207.69%
50.00%	0.00%	100.00%	8.65	2.16	2.16	300.00%

Table B.1 – table of pillar replication success rates as determined by $\bar{E}$. pillar replication success rates and their equivalent effect on the young’s modulus of the array, with the adequacy and good thresholds highlighted as 90 % and 80% respectively, or more accurately 88% and 78%. E is given in pn/nm.

B.2 – Insights from 2-D FEA of cooling through the polycarbonate parts

Outlined here are the results from the 2-D model that formed the basis of some of the inferences about the nature of thermal stress, and therefore residual stress, in the injection moulded parts. **Figure B.1 - a)** depicts an unusual trend where at 1.75ms (highlighted by the grey box) the middle of the part beings to cool more rapidly than the part in contact with the inlay. This will add another dimension of thermal stress to the part that contributes to the bowing effect from part warpage.

From **Figure B.1 -b)** it can be seen that the polycarbonate-steel and polycarbonate-inlay-steel corner begin to cool at the same rate at around 0.3s, and the polycarbonate-inlay / polycarbonate-steel interfaces are consistently higher / lower respectively. This indicates that despite recipe optimisation the cooling rates are still quite different across the part, causing the increased part warpage observed. Lastly, from **c)** it can be observed that the polymer inlay acts as a heat-sink, causing the tool to cool from the back inwards, with particularly sharp thermal gradients at the part corners. Combined with the insight into the cooling rates through the centre of the part, this explains the bowing effect along the part face, despite attempts to correct this through recipe optimisation.

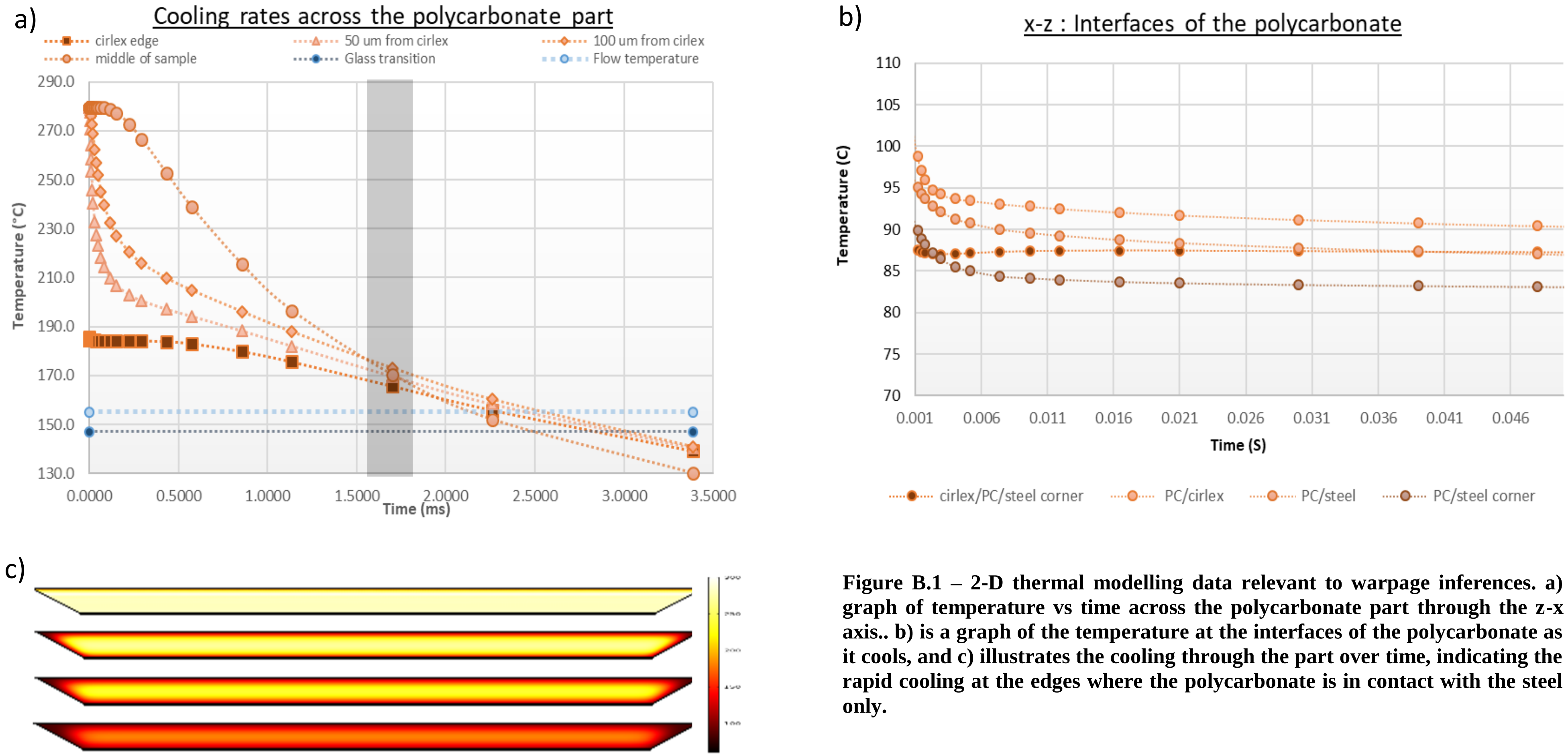

Figure B.1 – 2-D thermal modelling data relevant to warpage inferences. a) graph of temperature vs time across the polycarbonate part through the z-x axis.. b) is a graph of the temperature at the interfaces of the polycarbonate as it cools, and c) illustrates the cooling through the part over time, indicating the rapid cooling at the edges where the polycarbonate is in contact with the steel only.

B.3 – UHAR slide replication accuracy at sample edges

Changes across the UHAR slide for the multi-height pillar samples are documented for all pillar heights. Presented here is a summary of these results, focusing on the height changes across the 1µm pillars, as these demonstrate the most dramatic results.

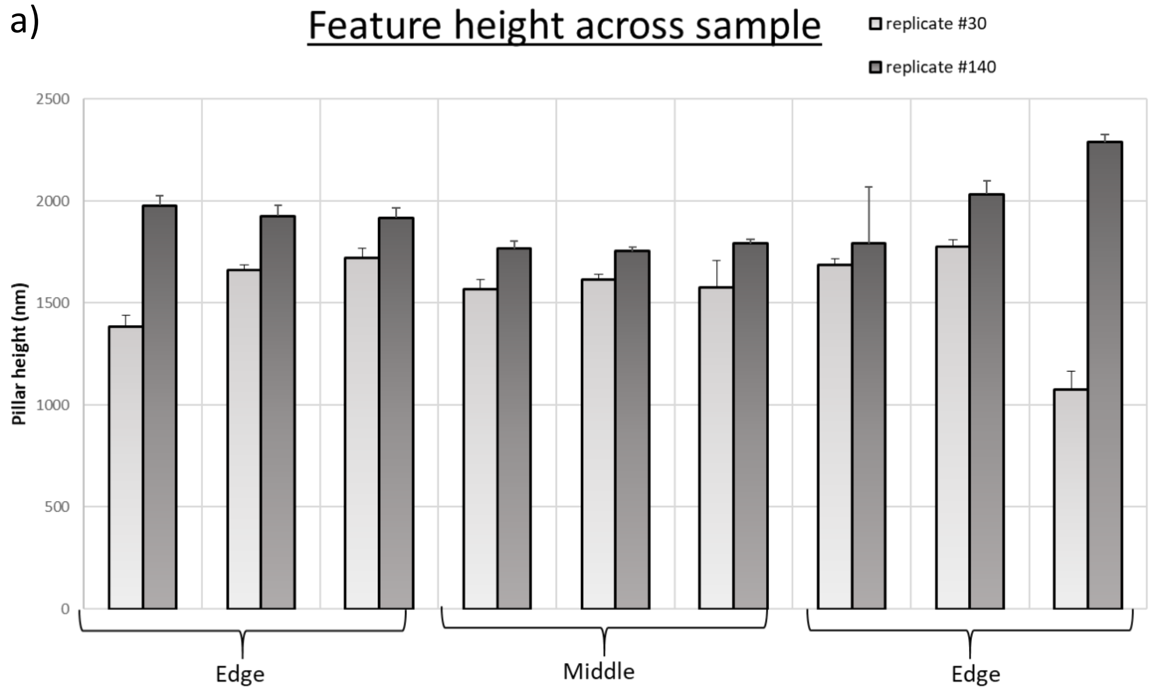

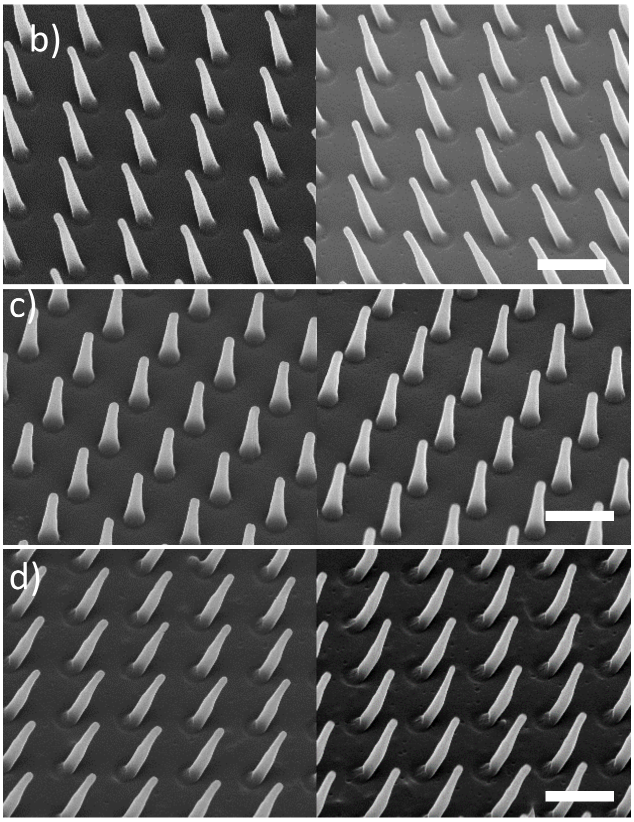

Edge – 1µm tall replicated features at shots 30 and 140. Note the exaggerated stretching over the interim 110 shots and the direction of stretching towards the edge of the sample, away from the middle.

Middle – 1µm tall replicated features at shots 30 and 140. Note the uniformity in the pillar structures, even over so many shots, and the verticality of the features.

Edge –1µm tall replicated features at shots 30 and 140. Note the exaggerated stretching over the interim 110 shots and the direction of stretching towards the edge of the sample, away from the middle.

Figure B.2 – Edge replication accuracy for multi-height UHAR slides. Examples of the pillars deforming differently along the edge arrays of the sample, outside the area of quality replication predicted by thermal modelling. Scale bar 1µm.

B.4 – Multi-mechanical slide tip diameter and height variations

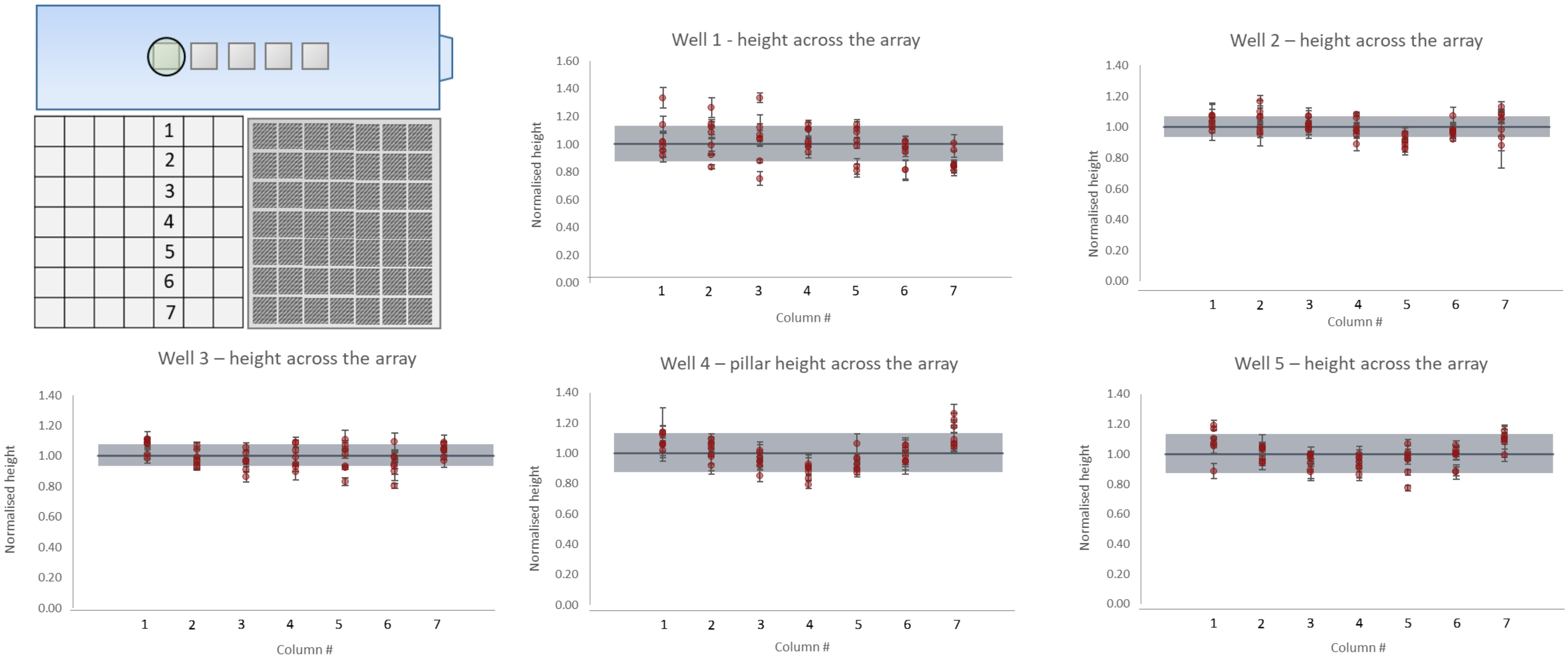

Figure B.3 - An alternative visualisation of the data to the 3-D area maps of pillar height across multi-mechanical UHAR slide arrays. These are alternative representations of the 3-D area maps of pillar height variations across individual pillar arrays. The standard deviation is included, as well as the normalised (blue line) and the tolerance (grey band). Column number indicates the position in the array of the discretised surface area measured. For example, column 3 has 7 data points, corresponding to each discretised measurement area in that column.

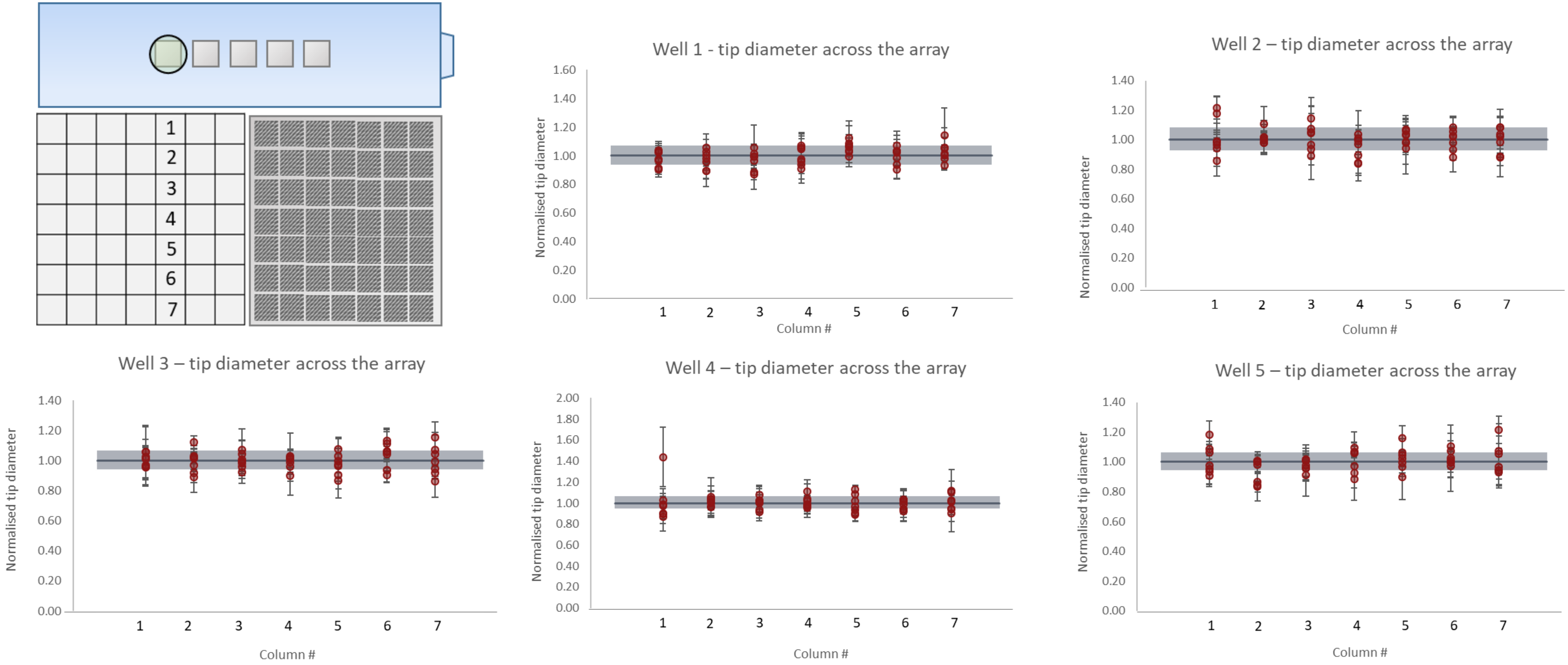

Well 1 - tip diameter across the array

Well 2 – tip diameter across the array

Well 3 – tip diameter across the array

Well 4 – tip diameter across the array

Well 5 – tip diameter across the array

Figure B.4 - An alternative visualisation of the data to the 3-D area maps of pillar tip diameter across multi-mechanical UHAR slide arrays. These are alternative representations of the 3-D area maps of pillar tip diameter variations across individual pillar arrays. The standard deviation is included, as well as the normalised (blue line) and the tolerance (grey band). Column number indicates the position in the array of the discretised surface area measured. For example, column 3 has 7 data points, corresponding to each discretised measurement area in that column.

B.5 – Testing well integrity of polycarbonate-polystyrene welds

In order to test if the weld seems were entirely hermetic, a leakage experiment was conducted. As has been stated before isolation between individual wells is essential to the accuracy of reporting proper results of biology techniques such as qPCR by preventing cross-talk between different cell samples.

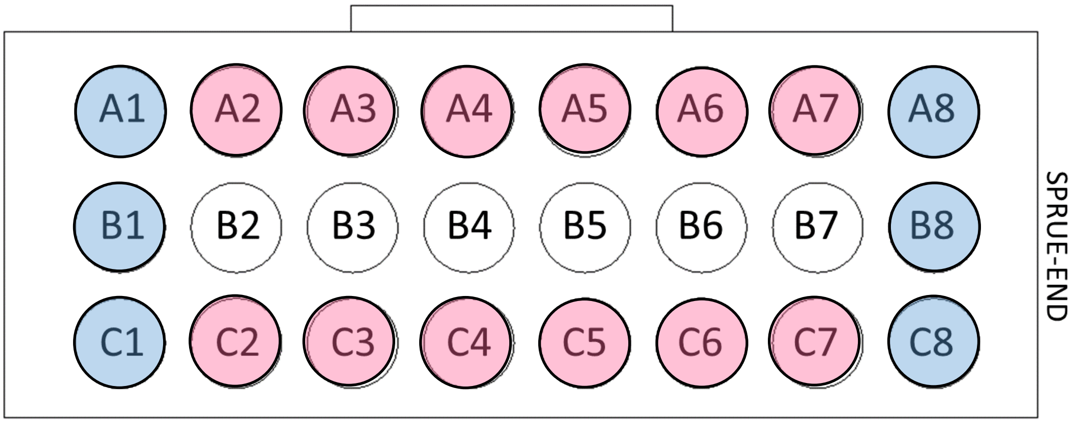

Figure B.5 – Multiwell leakage experiment. This figure demonstrates the results of the multiwell leakage experiment designed to test the integrity of the polycarbonate-polystyrene welds. Blue indicates the welds failed initial dye tests, whilst pink indicates a failure in the secondary round of incubation tests. Failure is determined by leakage of media.

The first round involved placing dye in each well and allowing it to sit, agitating the well plate, and finally subjecting the well plate to high stresses to see whether the weld integrity holds. Wells where the weld seem was compromised would leak at the various stages of the stress test, and indicate under which experimental conditions they would be viable. As the dye was a dark blue colour, and clearly visible when leaked from the wells, this was easy to tell.

In the next series of tests, each well was filled with cell media, which has a pinkish-colouration that stains the clear slides when allowed to dry, and placed inside an incubator at ambient cell culture temperature, around 30°C, in high humidity. They were left for three days and checked at the end of this time, chosen as it is the longest that the cell media will be allowed to sit in each well. Media can evaporate during this time period, however a lid is usually placed onto the well plate samples to minimise this.

The outer wells, rows A and C indicated in pink in **Figure B.5** , were found to be universally susceptible to leakage into the surrounding slide. Rates of fluid dissipation here were high, indicating soft leakage from sub-mm scale pores as no substantial staining was found in the surrounding polycarbonate slide. This will be due to similar reasons to columns 1 and 8. These wells had a failure rate of 1 in 10.

The central wells had minimal fluid dissipation, row B, wells 2-7. This was most likely due to small amounts of evaporation in the incubator. The failure rate of the welds in these wells was less than 5%, i.e. for every 20 wells tested, 1 would fail.

By keeping the experimentation and pattern generation localised to this location in the multiwell plate, the chances of leakage are minimised, and can be accounted for by increasing the number of experiments using these devices, and monitoring media volume of the wells. If a well appears to be leaking media to a significant amount, it can be discounted from any experimental results. This does not invalidate the other wells. If they do not leak, they are not being leaked into.

Appendix C – Additional data for optimisation of ICP deep silica etch

C.1 – Polyphenyl ether adhesive for good thermal contact

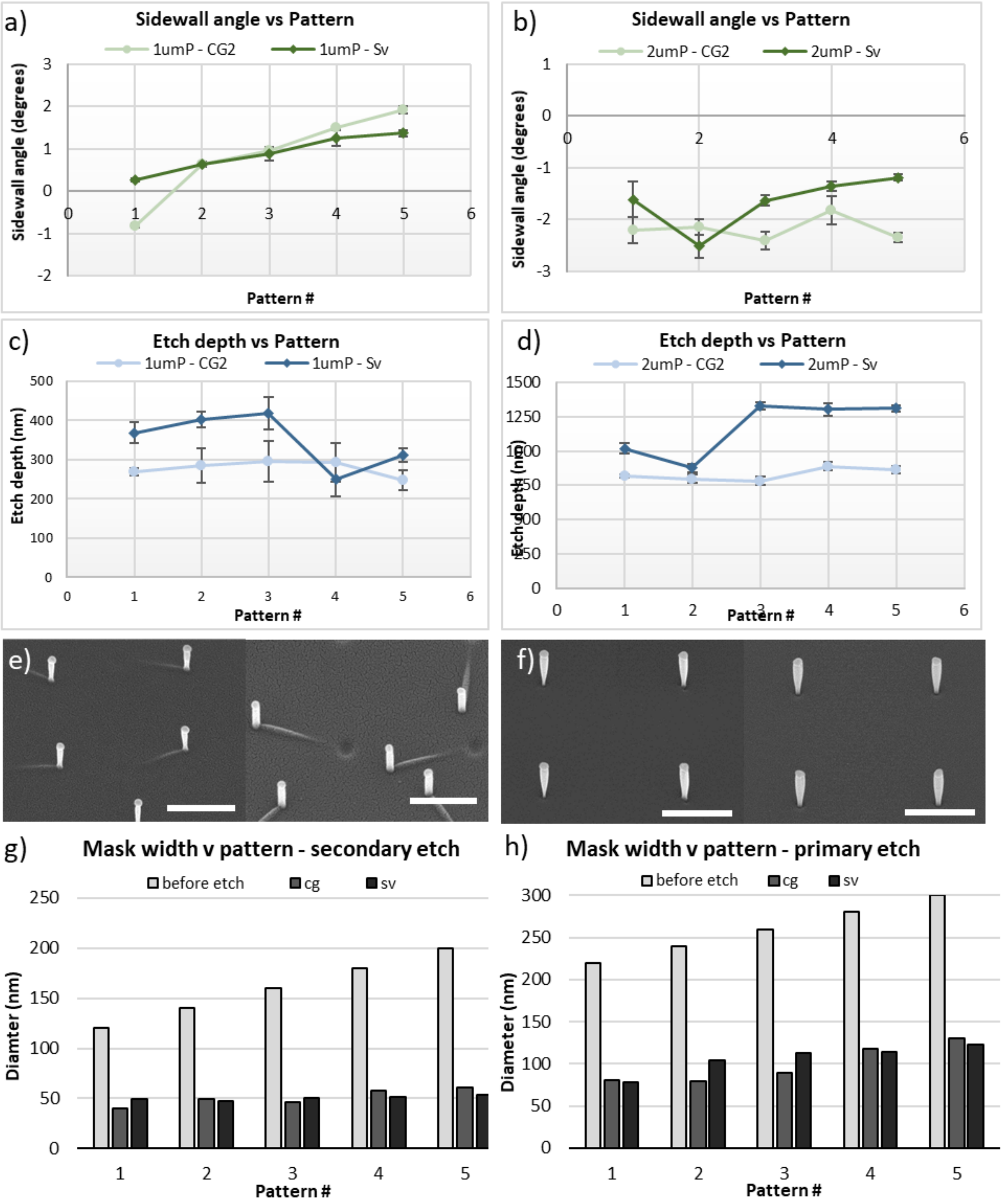

Figure C.1 – Results of the adhesion material tests. a) and b) are the measured sidewall angle of formed nanofeatures for the 1 and 2µm etched features, whilst c) and d) depict the changing etch rate. e) are SEM of the secondary etched, 1µm pitch pillars, and f) are SEM of the primary etched 2µm pitch pillars (scale bar 1µm). g) and h) depict the change from initial hard mask of the nanopillar tip diameter. Pattern number 1 – 5 indicate increasing diameter nanopillar arrays in 20nm increments.

As stated in the chapter, an investigation was carried out to determine the effect of changing from a thermally adhesive paste (COOLGREASE^{TM}) to a polyphenyl ether oil, abbreviated to CG and Sv respectively.

Presented here are the results of this investigation. The important points to note about these results are the limited differences between the performance in sidewall angle and etch depth between the two adhesive materials.

C.2 – Low temperature etching results

The low temperature etch recipes proved fruitful in lowering the amount of pillar tip shrinkage, and interestingly did not affect greatly the etch rate. The sidewall angles typically remained high, however, and the 15°C etch remained close enough to the 30s He cooling cycle that the extra processing time in low temperature etches could be eliminated by selecting the cyclical approach demonstrated in the chapter proper.

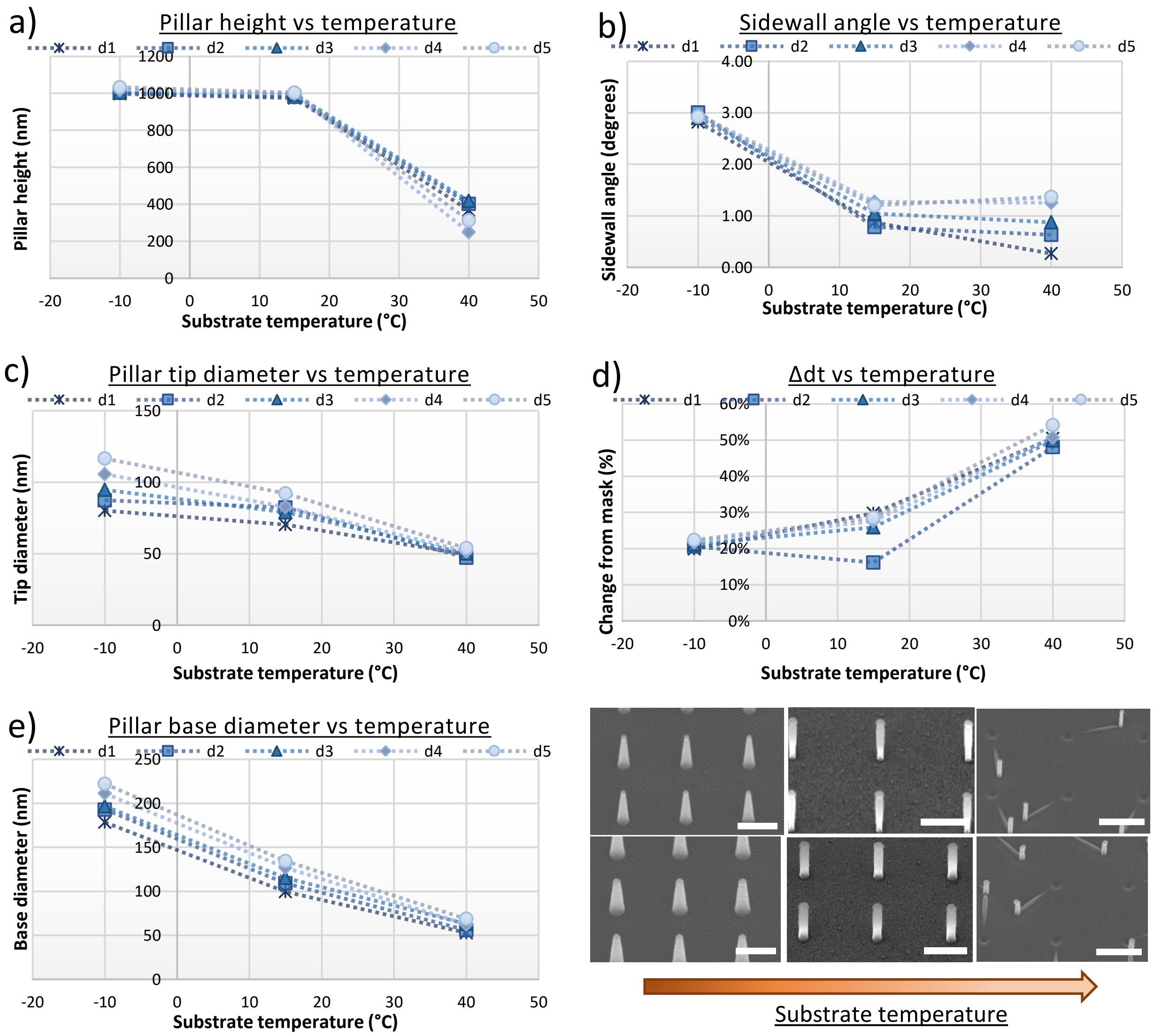

Figure C.2 – Results of the low temperature etch investigation a) – e) graphs depicting the trends in pillar etch depth, tip and base diameters, sidewall angle and the change in tip diameter from the designed mask diameter for 1µm pitch samples. f) are example SEM of the nanopillars etched using -10, 15 and 40°C recipes from left to right, scale bar 0.5µm.

C.3 – L9 results for 1 and 2μm pitch pillar arrays

1 micron pitch, 100 nm mask – L9 array

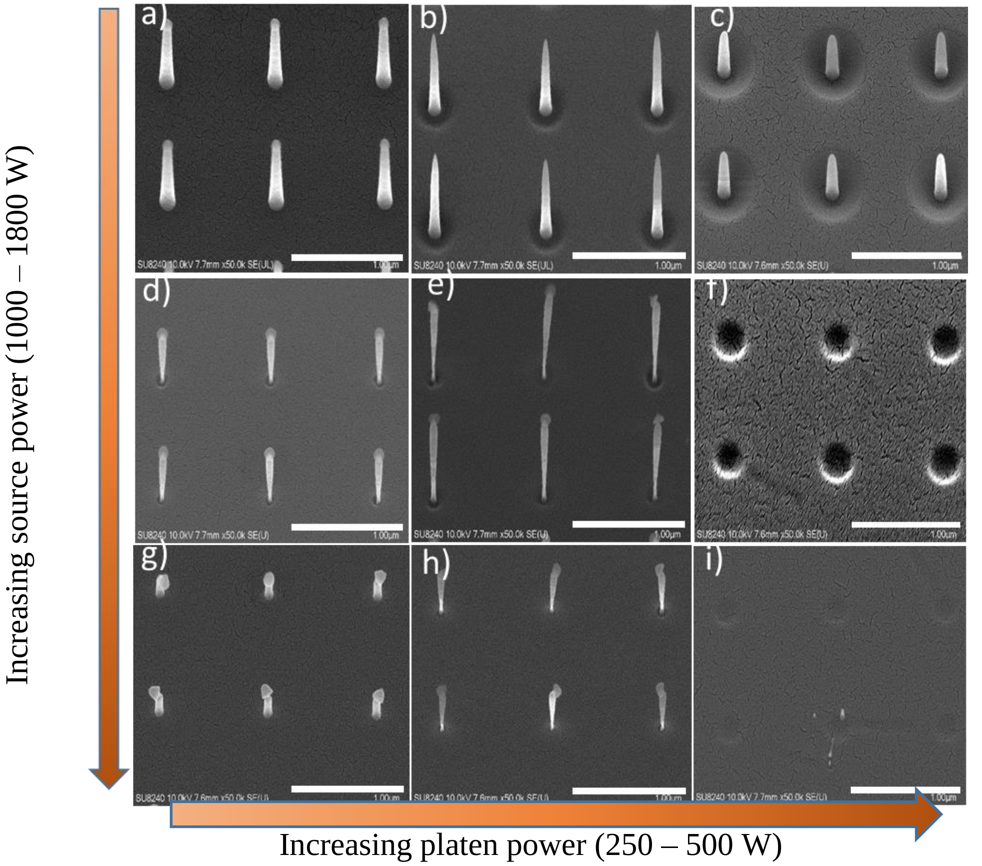

Figure C.3 – SEM results of the L9 matrix experiment for the 1μm pitch, 100nm diameter mask pillars. a) – i) are experiments 1 – 9 respectively. Scale bar 1μm.

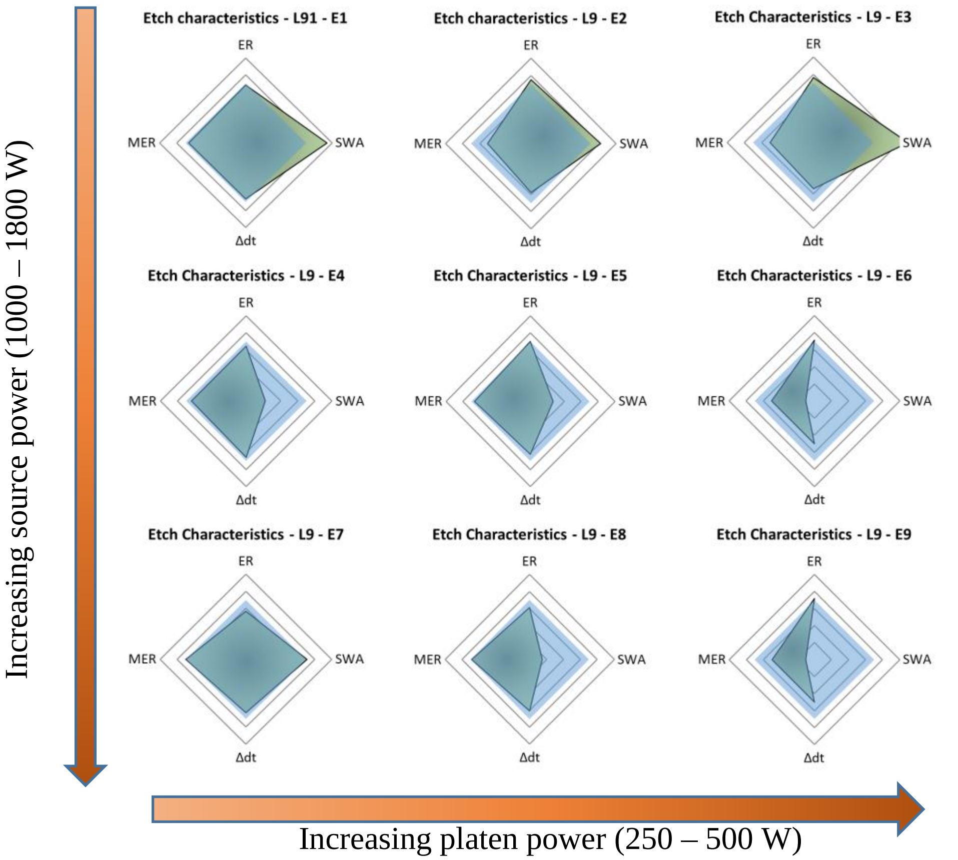

Figure C.4 – normalised results of the L9 matrix experiment for the 1μm pitch, 100nm diameter mask pillars. marked E1-E9 for experiments 1-9 respectively.

2 micron pitch, 100 nm mask – L9 array

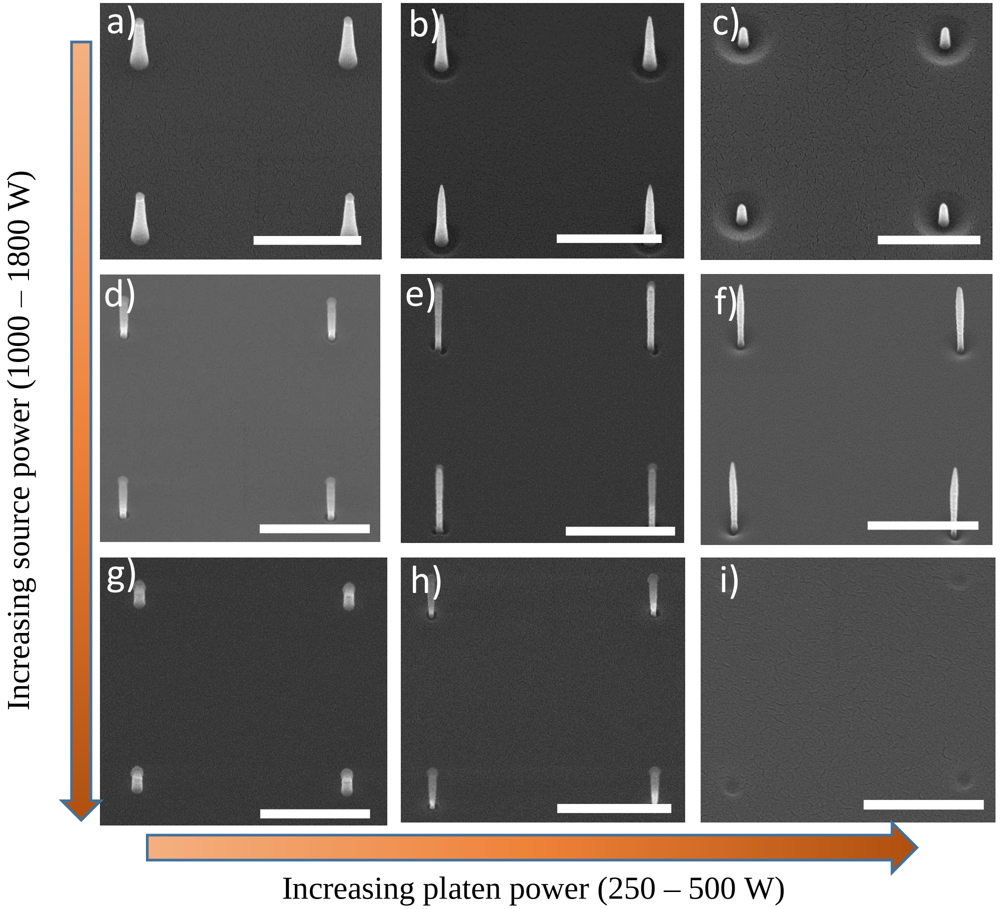

Figure C.5 – SEM results of the L9 matrix experiment for the 2µm pitch, 100nm diameter mask pillars. a) – i) are experiments 1 – 9 respectively. Scale bar 1µm.

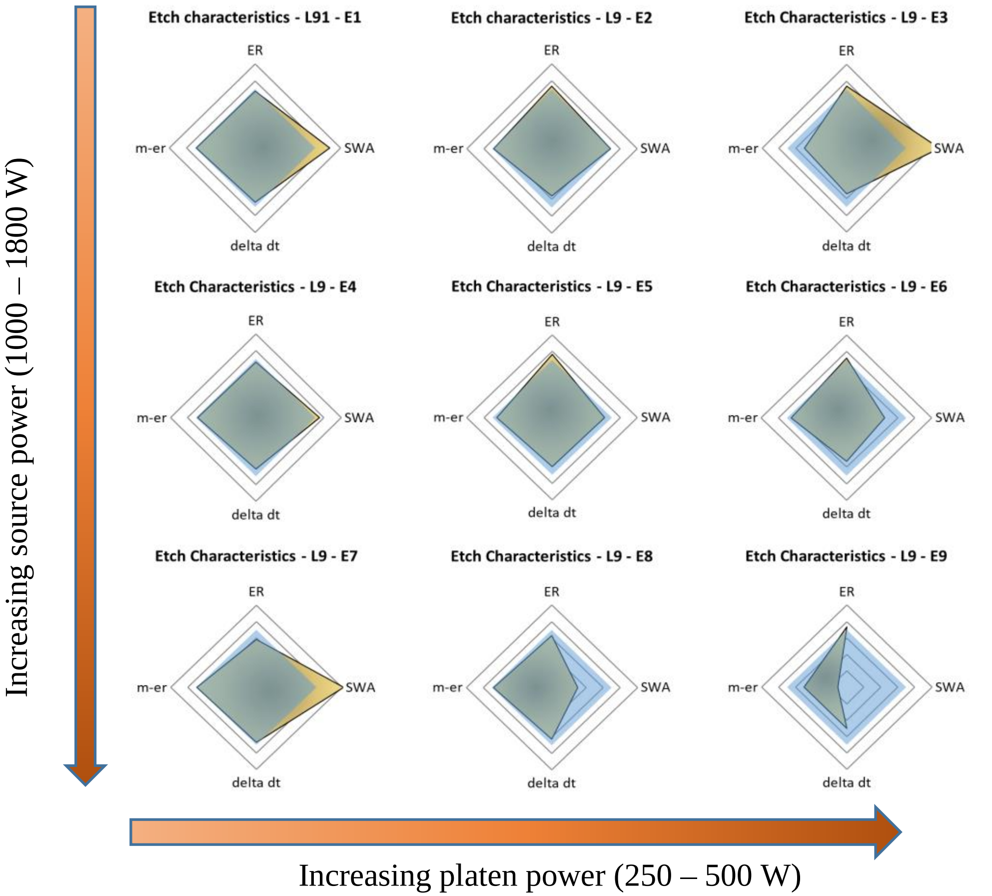

Figure C.6 – normalised results of the L9 matrix experiment for the 2µm pitch, 100nm diameter mask pillars. marked E1-E9 for experiments 1-9 respectively.

Figure C.7 – S/N responses of the full diameter dataset (1µm pitch).

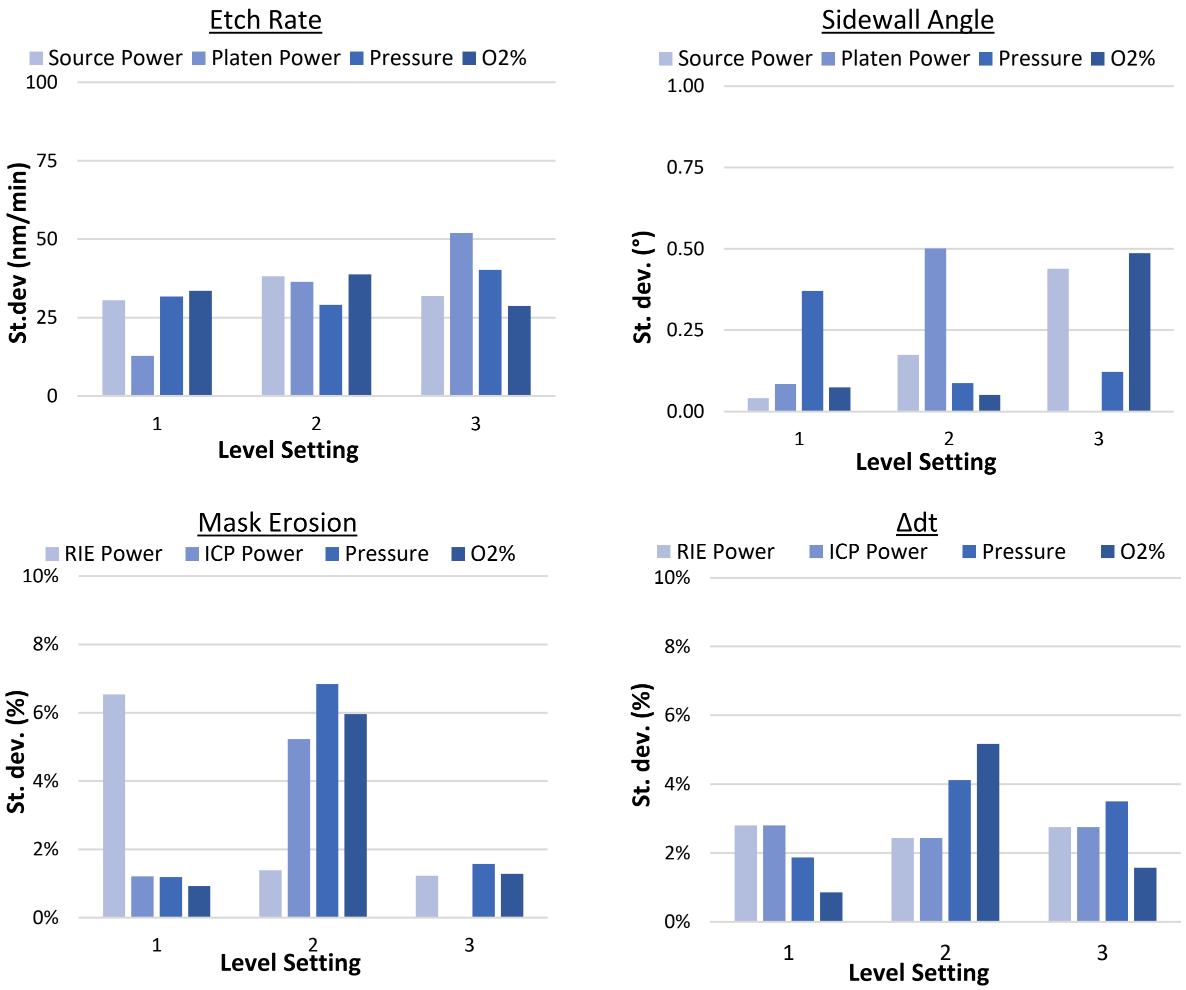

Figure C.8 – Bar charts demonstrating the standard deviation present across all 5 diameter pillars (1µm pitch) for each level setting, grouped by etch response characteristic for 1µm pitch arrays.

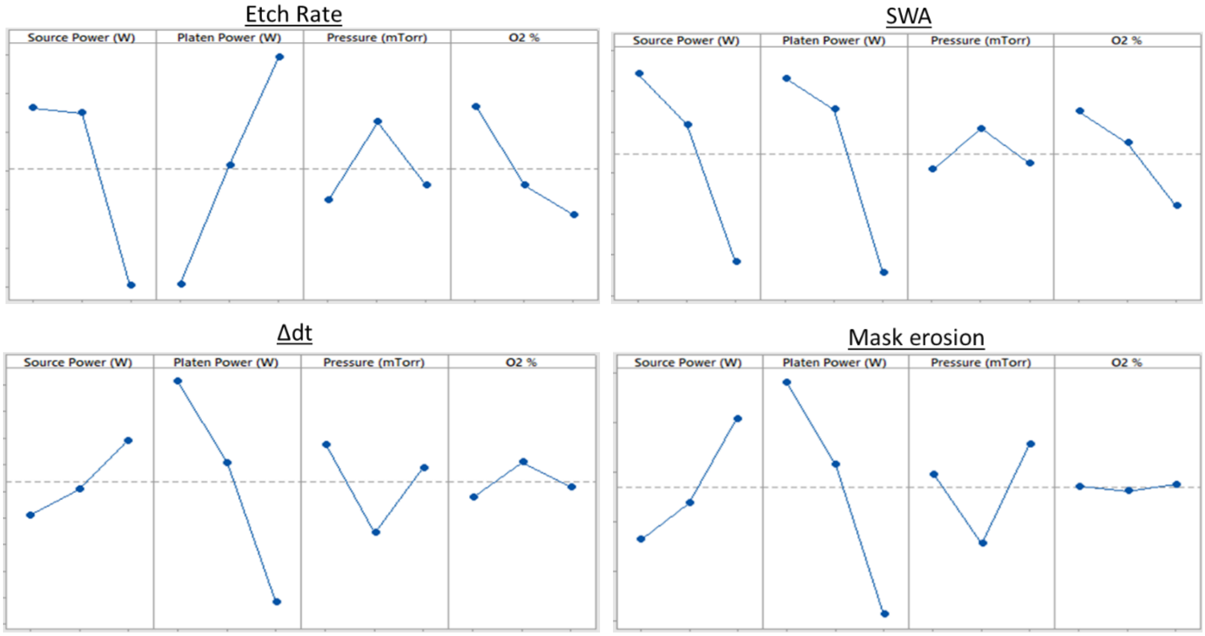

Figure C.9 – S/N responses of the full diameter dataset (2µm pitch).

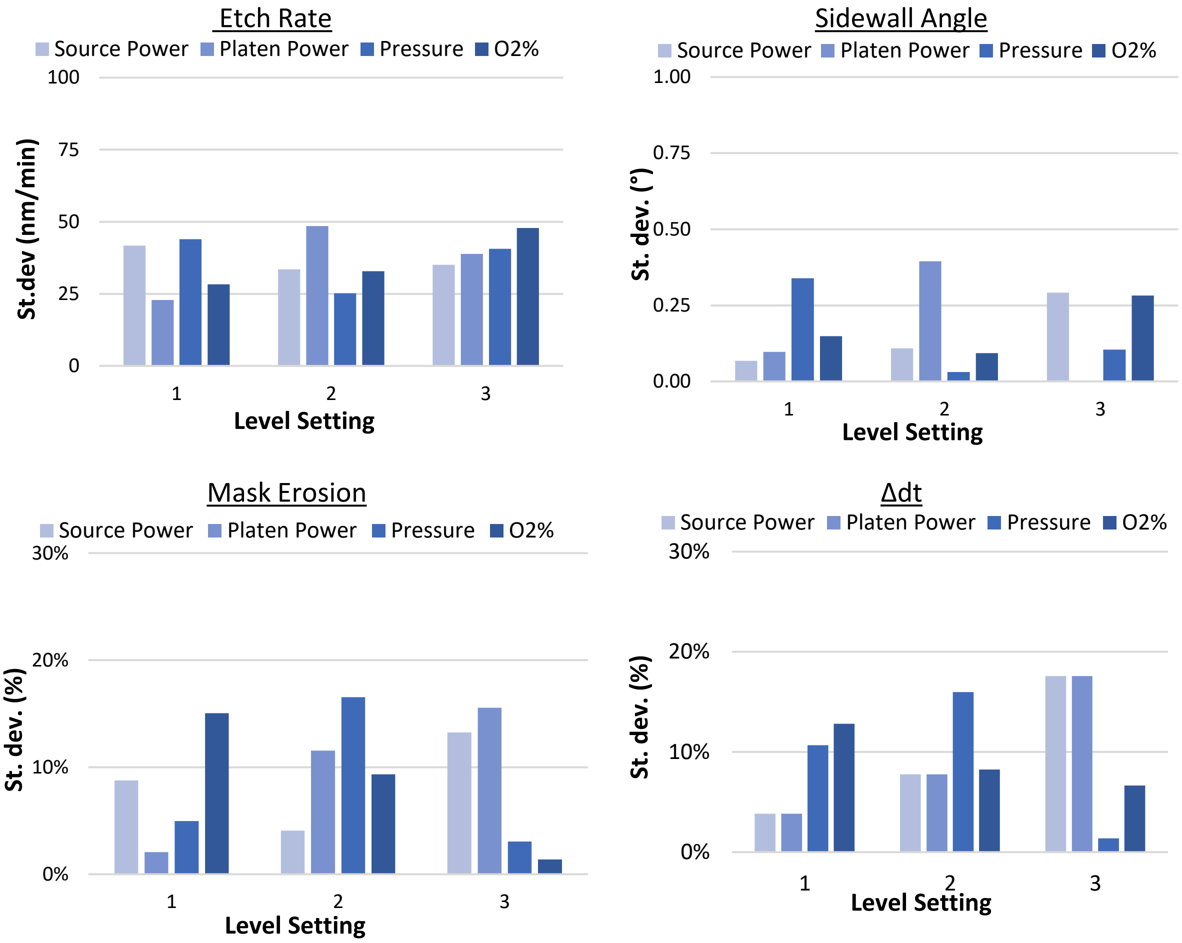

Figure C.10 – Bar charts demonstrating the standard deviation present across all 5 diameter pillars (2µm pitch) for each level setting, grouped by etch response characteristic for 2µm pitch arrays.

8.0 References

1. Engler AJ, Sen S, Sweeney HL, et al. Matrix elasticity directs stem cell lineage specification. *Cell* 2006; 126: 677-689. DOI: 10.1016/j.cell.2006.06.044.
2. Grade S and Goetz M. Neuronal replacement therapy: previous achievements and challenges ahead. *Npj Regenerative Medicine* 2017; 2. DOI: 10.1038/s41536-017-0033-0.
3. Jorgensen JT, Norregaard K, Tian P, et al. Single Particle and PET-based Platform for Identifying Optimal Plasmonic Nano-Heaters for Photothermal Cancer Therapy. *Scientific Reports* 2016; 6. DOI: 10.1038/srep30076.
4. Lukianova-Hleb EY, Ren X, Sawant RR, et al. On-demand intracellular amplification of chemoradiation with cancer-specific plasmonic nanobubbles. *Nature Medicine* 2014; 20: 778-784. DOI: 10.1038/nm.3484.
5. Harifi T and Montazer M. Application of nanotechnology in sports clothing and flooring for enhanced sport activities, performance, efficiency and comfort: a review. *Journal of Industrial Textiles* 2017; 46: 1147-1169. DOI: 10.1177/1528083715601512.
6. Gehrke I, Geiser A and Somborn-Schulz A. Innovations in nanotechnology for water treatment. *Nanotechnology Science and Applications* 2015; 8: 1-17. DOI: 10.2147/nsa.S43773.
7. Curtis A and Wilkinson C. Topographical control of cells. *Biomaterials* 1997; 18: 1573-1583. DOI: 10.1016/s0142-9612(97)00144-0.
8. Bucaro MA, Vasquez Y, Hatton BD, et al. Fine-Tuning the Degree of Stem Cell Polarization and Alignment on Ordered Arrays of High-Aspect-Ratio Nanopillars. *Acs Nano* 2012; 6: 6222-6230. DOI: 10.1021/nn301654e.
9. Kim JH, Park BG, Kim S-K, et al. Nanotopographical regulation of pancreatic islet-like cluster formation from human pluripotent stem cells using a gradient-pattern chip. *Acta Biomaterialia* 2019; 95: 337-347. DOI: 10.1016/j.actbio.2018.12.011.
10. Yang K, Jung H, Lee H-R, et al. Multiscale, Hierarchically Patterned Topography for Directing Human Neural Stem Cells into Functional Neurons. *Acs Nano* 2014; 8: 7809-7822. DOI: 10.1021/nn501182f.
11. Yim EKF, Pang SW and Leong KW. Synthetic nanostructures inducing differentiation of human mesenchymal stem cells into neuronal lineage. *Experimental Cell Research* 2007; 313: 1820-1829. DOI: 10.1016/j.yexcr.2007.02.031.
12. Dalby MJ, Gadegaard N, Tare R, et al. The control of human mesenchymal cell differentiation using nanoscale symmetry and disorder. *Nature Materials* 2007; 6: 997-1003. DOI: 10.1038/nmat2013.
13. McBeath R, Pirone DM, Nelson CM, et al. Cell shape, cytoskeletal tension, and RhoA regulate stem cell lineage commitment. *Developmental Cell* 2004; 6: 483-495. DOI: 10.1016/s1534-5807(04)00075-9.
14. Zhao W, Hanson L, Lou H-Y, et al. Nanoscale manipulation of membrane curvature for probing endocytosis in live cells. *Nature Nanotechnology* 2017; 12: 750-+. DOI: 10.1038/nnano.2017.98.
15. Teixeira AI, Abrams GA, Bertics PJ, et al. Epithelial contact guidance on well-defined micro- and nanostructured substrates. *Journal of Cell Science* 2003; 116: 1881-1892. DOI: 10.1242/jcs.00383.
16. Discher DE, Janmey P and Wang YL. Tissue cells feel and respond to the stiffness of their substrate. *Science* 2005; 310: 1139-1143. DOI: 10.1126/science.1116995.
17. Pelham RJ and Wang YL. Cell locomotion and focal adhesions are regulated by substrate flexibility. *Proceedings of the National Academy of Sciences of the United States of America* 1997; 94: 13661-13665. DOI: 10.1073/pnas.94.25.13661.

18. Yang B, Wolfenson H, Chung VY, et al. Stopping transformed cancer cell growth by rigidity sensing. *Nature Materials* 2020; 19: 239-+. DOI: 10.1038/s41563-019-0507-0.

19. Chin L, Xia Y, Discher DE, et al. Mechanotransduction in cancer. *Current Opinion in Chemical Engineering* 2016; 11: 77-84. DOI: 10.1016/j.coche.2016.01.011.

20. Rath N, Munro J, Cutiongco MF, et al. Rho Kinase Inhibition by AT13148 Blocks Pancreatic Ductal Adenocarcinoma Invasion and Tumor Growth. *Cancer Research* 2018; 78: 3321-3336. DOI: 10.1158/0008-5472.Can-17-1339.

21. Juin A, Spence HJ, Martin KJ, et al. N-WASP Control of LPAR1 Trafficking Establishes Response to Self-Generated LPA Gradients to Promote Pancreatic Cancer Cell Metastasis. *Developmental Cell* 2019; 51: 431-+. DOI: 10.1016/j.devcel.2019.09.018.

22. Yeung T, Georges PC, Flanagan LA, et al. Effects of substrate stiffness on cell morphology, cytoskeletal structure, and adhesion. *Cell Motility and the Cytoskeleton* 2005; 60: 24-34. DOI: 10.1002/cm.20041.

23. Zuk PA, Zhu M, Mizuno H, et al. Multilineage cells from human adipose tissue: Implications for cell-based therapies. *Tissue Engineering* 2001; 7: 211-228. DOI: 10.1089/107632701300062859.

24. Dickinson LE, Rand DR, Tsao J, et al. Endothelial cell responses to micropillar substrates of varying dimensions and stiffness. *Journal of Biomedical Materials Research Part A* 2012; 100A: 1457-1466. DOI: 10.1002/jbm.a.34059.

25. Murphy WL, McDevitt TC and Engler AJ. Materials as stem cell regulators. *Nature Materials* 2014; 13: 547-557. DOI: 10.1038/nmat3937.

26. Swift J, Ivanovska IL, Buxboim A, et al. Nuclear Lamin-A Scales with Tissue Stiffness and Enhances Matrix-Directed Differentiation. *Science* 2013; 341. DOI: 10.1126/science.1240104.

27. Trappmann B, Gautrot JE, Connelly JT, et al. Extracellular-matrix tethering regulates stem-cell fate. *Nature Materials* 2012; 11: 642-649. DOI: 10.1038/nmat3339.

28. Engler AJ, Griffin MA, Sen S, et al. Myotubes differentiate optimally on substrates with tissue-like stiffness: pathological implications for soft or stiff microenvironments. *Journal of Cell Biology* 2004; 166: 877-887. DOI: 10.1083/jcb.200405004.

29. Charrier EE, Pogoda K, Wells RG, et al. Control of cell morphology and differentiation by substrates with independently tunable elasticity and viscous dissipation. *Nature Communications* 2018; 9. DOI: 10.1038/s41467-018-02906-9.

30. Ye K, Wang X, Cao L, et al. Matrix Stiffness and Nanoscale Spatial Organization of Cell-Adhesive Ligands Direct Stem Cell Fate. *Nano Letters* 2015; 15: 4720-4729. DOI: 10.1021/acs.nanolett.5b01619.

31. Gilbert PM, Havenstrite KL, Magnusson KEG, et al. Substrate Elasticity Regulates Skeletal Muscle Stem Cell Self-Renewal in Culture. *Science* 2010; 329: 1078-1081. DOI: 10.1126/science.1191035.

32. Nam J, Johnson J, Lannutti JJ, et al. Modulation of embryonic mesenchymal progenitor cell differentiation via control over pure mechanical modulus in electrospun nanofibers. *Acta Biomaterialia* 2011; 7: 1516-1524. DOI: 10.1016/j.actbio.2010.11.022.

33. Pagliari S, Forte G, Ebara M, et al. Substrate stiffness modulates phenotype and gene expression in neonatal cardiomyocytes in vitro. *Journal of Tissue Engineering and Regenerative Medicine* 2012; 6: 239-239.

34. Huth S, Sindt S and Selhuber-Unkel C. Automated analysis of soft hydrogel microindentation: Impact of various indentation parameters on the measurement of Young's modulus. *Plos One* 2019; 14. DOI: 10.1371/journal.pone.0220281.

35. Tse JR and Engler AJ. Preparation of hydrogel substrates with tunable mechanical properties. *Current protocols in cell biology* 2010; Chapter 10: Unit 10.16-Unit 10.16. DOI: 10.1002/0471143030.cb1016s47.

36. Cavo M, Fato M, Penuela L, et al. Microenvironment complexity and matrix stiffness regulate breast cancer cell activity in a 3D in vitro model. *Scientific Reports* 2016; 6. DOI: 10.1038/srep35367.

37. Tan JL, Tien J, Pirone DM, et al. Cells lying on a bed of microneedles: An approach to isolate mechanical force. *Proceedings of the National Academy of Sciences of the United States of America* 2003; 100: 1484-1489. DOI: 10.1073/pnas.0235407100.

38. Fu J, Wang Y-K, Yang MT, et al. Mechanical regulation of cell function with geometrically modulated elastomeric substrates. *Nature Methods* 2010; 7: 733-U795. DOI: 10.1038/nmeth.1487.

39. Ghassemi S, Biais N, Maniura K, et al. Fabrication of elastomer pillar arrays with modulated stiffness for cellular force measurements. *Journal of Vacuum Science & Technology B* 2008; 26: 2549-2553. DOI: 10.1116/1.3013424.

40. Ghassemi S, Meacci G, Liu S, et al. Cells test substrate rigidity by local contractions on submicrometer pillars. *Proceedings of the National Academy of Sciences of the United States of America* 2012; 109: 5328-5333. DOI: 10.1073/pnas.1119886109.

41. Xia YN and Whitesides GM. Soft lithography. *Angewandte Chemie-International Edition* 1998; 37: 550-575. DOI: 10.1002/(sici)1521-3773(19980316)37:5<550::Aid-anie550>3.3.Co;2-7.

42. Chandra D and Yang S. Stability of High-Aspect-Ratio Micropillar Arrays against Adhesive and Capillary Forces. *Accounts Chem Res* 2010; 43: 1080-1091. Review. DOI: 10.1021/ar100001a.

43. Liu HZ, Lei B, Jiang WT, et al. Ultrasound-assisted recovery of free-standing high-aspect-ratio micropillars. *RSC Adv* 2016; 6: 16640-16644. Article. DOI: 10.1039/c5ra26898b.

44. Gadegaard N, Mosler S and Larsen NB. Biomimetic polymer nanostructures by injection molding. *Macromolecular Materials and Engineering* 2003; 288: 76-83. DOI: 10.1002/mame.200290037.

45. Christiansen AB, Clausen JS, Mortensen NA, et al. Injection moulding antireflective nanostructures. *Microelectronic Engineering* 2014; 121: 47-50. DOI: 10.1016/j.mee.2014.03.027.

46. Nagato K, Hamaguchi T and Nakao M. Injection compression molding of high-aspect-ratio nanostructures. *Journal of Vacuum Science & Technology B* 2011; 29. DOI: 10.1116/1.3662405.

47. Muntada-López O, Pina-Estany J, Colominas C, et al. Replication of nanoscale surface gratings via injection molding. *Micro and Nano Engineering* 2019; 3: 37-42. DOI: olga.

48. Pranov H, Rasmussen HK, Larsen NB, et al. On the injection molding of nanostructured polymer surfaces. *Polymer Engineering and Science* 2006; 46: 160-171. DOI: 10.1002/pen.20459.

49. L. Xie LS, and B. Jiang. *Modelling and Simulation for Micro Injection*

Molding Process. 2002.

50. Stormonth-Darling JM and Gadegaard N. Injection Moulding Difficult Nanopatterns with Hybrid Polymer Inlays. *Macromolecular Materials and Engineering* 2012; 297: 1075-1080. DOI: 10.1002/mame.201100397.

51. Stormonth-Darling JM, Pedersen RH, How C, et al. Injection moulding of ultra high aspect ratio nanostructures using coated polymer tooling. *Journal of Micromechanics and Microengineering* 2014; 24. DOI: 10.1088/0960-1317/24/7/075019.

52. Reynolds PM, Pedersen RH, Stormonth-Darling J, et al. Label-Free Segmentation of Co-cultured Cells on a Nanotopographical Gradient. *Nano Letters* 2013; 13: 570-576. DOI: 10.1021/nl304097p.

53. Rasmussen CH, Reynolds PM, Petersen DR, et al. Enhanced Differentiation of Human Embryonic Stem Cells Toward Definitive Endoderm on Ultrahigh Aspect Ratio Nanopillars. *Advanced Functional Materials* 2016; 26: 815-823. DOI: 10.1002/adfm.201504204.

54. Elbourne A, Chapman J, Gelmi A, et al. Bacterial-nanostructure interactions: The role of cell elasticity and adhesion forces. *Journal of Colloid and Interface Science* 2019; 546: 192-210. DOI: 10.1016/j.jcis.2019.03.050.

55. Wu S, Zuber F, Maniura-Weber K, et al. Nanostructured surface topographies have an effect on bactericidal activity. *Journal of Nanobiotechnology* 2018; 16. DOI: 10.1186/s12951-018-0347-0.

56. Buch-Manson N, Bonde S, Bolinsson J, et al. Towards a Better Prediction of Cell Settling on Nanostructure ArraysSimple Means to Complicated Ends. *Advanced Functional Materials* 2015; 25: 3246-3255. DOI: 10.1002/adfm.201500399.

57. Buch-Manson N, Spangenberg A, Gomez LPC, et al. Rapid Prototyping of Polymeric Nanopillars by 3D Direct Laser Writing for Controlling Cell Behavior. *Scientific Reports* 2017; 7. DOI: 10.1038/s41598-017-09208-y.

58. Hulshof FFB, Zhao Y, Vasilevich A, et al. NanoTopoChip: High-throughput nanotopographical cell instruction. *Acta Biomaterialia* 2017; 62: 188-198. DOI: 10.1016/j.actbio.2017.08.023.

59. Unadkat HV, Hulsman M, Cornelissen K, et al. An algorithm-based topographical biomaterials library to instruct cell fate. *Proceedings of the National Academy of Sciences of the United States of America* 2011; 108: 16565-16570. DOI: 10.1073/pnas.1109861108.

60. Moe AAK, Suryana M, Marcy G, et al. Microarray with Micro- and Nano-topographies Enables Identification of the Optimal Topography for Directing the Differentiation of Primary Murine Neural Progenitor Cells. *Small* 2012; 8: 3050-3061. DOI: 10.1002/smll.201200490.

61. Joergensen NL, Le DQS, Andersen OZ, et al. Topography-Guided Proliferation: Distinct Surface Microtopography Increases Proliferation of Chondrocytes In Vitro. *Tissue Engineering Part A* 2015; 21: 2757-2765. DOI: 10.1089/ten.tea.2014.0697.

62. Hu J, Gondarenko AA, Dang AP, et al. High-Throughput Mechanobiology Screening Platform Using Micro- and Nanotopography. *Nano Letters* 2016; 16: 2198-2204. DOI: 10.1021/acs.nanolett.5b04364.

63. Mih JD, Sharif AS, Liu F, et al. A Multiwell Platform for Studying Stiffness-Dependent Cell Biology. *Plos One* 2011; 6. DOI: 10.1371/journal.pone.0019929.

64. Xie C, Hanson L, Xie W, et al. Noninvasive Neuron Pinning with Nanopillar Arrays. *Nano Letters* 2010; 10: 4020-4024. DOI: 10.1021/nl101950x.

65. Hanson L, Zhao W, Lou H-Y, et al. Vertical nanopillars for in situ probing of nuclear mechanics in adherent cells. *Nature Nanotechnology* 2015; 10: 554-U592. DOI: 10.1038/nnano.2015.88.

66. Shiu J-Y, Aires L, Lin Z, et al. Nanopillar force measurements reveal actin-cap-mediated YAP mechanotransduction. *Nature Cell Biology* 2018; 20: 262-+. DOI: 10.1038/s41556-017-0030-y.

67. Wang S, Wan Y and Liu Y. Effects of nanopillar array diameter and spacing on cancer cell capture and cell behaviors. *Nanoscale* 2014; 6: 12482-12489. DOI: 10.1039/c4nr02854f.

68. Kim D-H, Kim P, Song I, et al. Guided three-dimensional growth of functional cardiomyocytes on polyethylene glycol nanostructures. *Langmuir* 2006; 22: 5419-5426. DOI: 10.1021/la060283u.

69. Pedersen RH, Xu Q, Stormonth-Darling JM, et al. Strategies for High Quality Injection Moulding of Polymer Nanopillars. *Macromolecular Materials and Engineering* 2015; 300: 172-180. DOI: 10.1002/mame.201400134.

70. Huethorst E, Cutiongco MF, Campbell FA, et al. Customizable, engineered substrates for rapid screening of cellular cues. *Biofabrication* 2020; 12: 025009-025009. DOI: 10.1088/1758-5090/ab5d3f.

71. Lemmon CA, Sniadecki NJ, Ruiz SA, et al. Shear force at the cell-matrix interface: enhanced analysis for microfabricated post array detectors. *Mechanics & chemistry of biosystems : MCB* 2005; 2: 1-16.

72. Engler AJ, Carag-Krieger C, Johnson CP, et al. Embryonic cardiomyocytes beat best on a matrix with heart-like elasticity: scar-like rigidity inhibits beating. *Journal of Cell Science* 2008; 121: 3794-3802. DOI: 10.1242/jcs.029678.

73. Minoura K, Yamada M, Mizoguchi T, et al. Antibacterial effects of the artificial surface of nanoimprinted moth-eye film. *Plos One* 2017; 12. DOI: 10.1371/journal.pone.0185366.

74. Paivanranta B, Saastamoinen T and Kuittinen M. A wide-angle antireflection surface for the visible spectrum. *Nanotechnology* 2009; 20. DOI: 10.1088/0957-4484/20/37/375301.

75. Jarzabek DM, Kaufmann AN, Schift H, et al. Elastic modulus and fracture strength evaluation on the nanoscale by scanning force microscope experiments. *Nanotechnology* 2014; 25. DOI: 10.1088/0957-4484/25/21/215701.

76. Vlassov S, Oras S, Antsov M, et al. ADHESION AND MECHANICAL PROPERTIES OF PDMS-BASED MATERIALS PROBED WITH AFM: A REVIEW. *Reviews on Advanced Materials Science* 2018; 56: 62-78. DOI: 10.1515/rams-2018-0038.

77. Schoen I. Substrate-mediated crosstalk between elastic pillars. *Applied Physics Letters* 2010; 97. DOI: 10.1063/1.3463040.

78. Xiang Y and LaVan DA. Analysis of soft cantilevers as force transducers. *Applied Physics Letters* 2007; 90. DOI: 10.1063/1.2716376.

79. Kajzar A, Cesa CM, Kirchgessner N, et al. Toward physiological conditions for cell analyses: Forces of heart muscle cells suspended between elastic micropillars. *Biophysical Journal* 2008; 94: 1854-1866. DOI: 10.1529/biophysj.107.115766.

80. Schoen I, Hu W, Klotzsch E, et al. Probing Cellular Traction Forces by Micropillar Arrays: Contribution of Substrate Warping to Pillar Deflection. *Nano Letters* 2010; 10: 1823-1830. DOI: 10.1021/nl100533c.

81. Covestro. Makrolon® OD2015, https://solutions.covestro.com/en/products/makrolon/makrolon-od2015_56979909-00001927?SelectedCountry=US (2018, 2018).

82. Johnston ID, McCluskey DK, Tan CKL, et al. Mechanical characterization of bulk Sylgard 184 for microfluidics and microengineering. *Journal of Micromechanics and Microengineering* 2014; 24. DOI: 10.1088/0960-1317/24/3/035017.

83. Hutchinson JR. Shear Coefficients for Timoshenko Beam Theory. *Journal of Applied Mechanics* 2000; 68: 87-92. DOI: 10.1115/1.1349417.

84. McCutcheon WJ. DEFLECTIONS AND STRESSES IN CIRCULAR TAPERED BEAMS AND POLES. *Civil Engineering for Practicing and Design Engineers* 1983; 2: 207-233.

85. Abe T and Esashi M. One-chip multichannel quartz crystal microbalance (QCM) fabricated by Deep RIE. *Sensors and Actuators a-Physical* 2000; 82: 139-143. DOI: 10.1016/s0924-4247(99)00330-1.

86. Ahamed MJ, Senkal D, Shkel AM, et al. Improvement of Side-wall Roughness in Deep Glass Etched MEMS Vibratory Sensors. *2014 1st Ieee International Symposium on Inertial Sensors and Systems*. 2014, pp.127-128.

87. Ahamed MJ, Senkal D, Trusov AA, et al. Study of High Aspect Ratio NLD Plasma Etching and Postprocessing of Fused Silica and Borosilicate. *Journal of Microelectromechanical Systems* 2015; 24: 790-800. DOI: 10.1109/jmems.2015.2442596.

88. Ashraf MW, Tayyaba S, Afzulpurkar N, et al. Optimization of Fabrication Process for MEMS based Microneedles Using ICP Etching Technology. In: Yuan L (ed) *Mems, Nano and Smart Systems, Pts 1-6*. 2012, pp.4611-+.

89. Bliznetsov V, Lin HM, Zhang YJ, et al. Deep SiO2 etching with Al and AlN masks for MEMS devices. *Journal of Micromechanics and Microengineering* 2015; 25. DOI: 10.1088/0960-1317/25/8/087002.

90. Ceriotti L, Weible K, de Rooij NF, et al. Rectangular channels for lab-on-a-chip applications. *Microelectronic Engineering* 2003; 67-8: 865-871. DOI: 10.1016/s0167-9317(03)00148-5.

91. Chen H and Fu C. An investigation into the characteristics of deep reactive ion etching of quartz using SU-8 as a mask. *Journal of Micromechanics and Microengineering* 2008; 18. DOI: 10.1088/0960-1317/18/10/105001.

92. Cheong HW, Lee WH, Kim JW, et al. A study on reactive ion etching lag of a high aspect ratio contact hole in a magnetized inductively coupled plasma. *Plasma Sources Science & Technology* 2014; 23. DOI: 10.1088/0963-0252/23/6/065051.

93. Chun I, Efremov A, Yeom GY, et al. A comparative study of CF4/O-2/Ar and C4F8/O-2/Ar plasmas for dry etching applications. *Thin Solid Films* 2015; 579: 136-143. DOI: 10.1016/j.tsf.2015.02.060.

94. Efremov A, Lee J and Kwon K-H. A comparative study of CF4, Cl-2 and HBr + Ar inductively coupled plasmas for dry etching applications. *Thin Solid Films* 2017; 629: 39-48. DOI: 10.1016/j.tsf.2017.03.035.

95. Garay AA, Hwang SM and Chung CW. Inductive couple plasma reactive ion etching characteristics of TiO2 thin films. *Thin Solid Films* 2015; 587: 20-27. DOI: 10.1016/j.tsf.2014.11.055.

96. Goyal A, Hood V and Tadigadapa S. High speed anisotropic etching of Pyrex((R)) for microsystems applications. *Journal of Non-Crystalline Solids* 2006; 352: 657-663. DOI: 10.1016/j.jnoncrysol.2005.11.063.

97. Huff M and Pedersen M. Electrical field-induced faceting of etched features using plasma etching of fused silica. *Journal of Applied Physics* 2017; 122. DOI: 10.1063/1.4991706.

98. Ichiki T, Sugiyama Y, Taura R, et al. Plasma applications for biochip technology. *Thin Solid Films* 2003; 435: 62-68. DOI: 10.1016/s0040-6090(03)00370-5.

99. Jensen S and Hansen O. Characterization of the microloading effect in deep reactive ion etching of silicon. In: Maher MA and Jakubczak JF (eds) *Micromachining and Microfabrication Process Technology Ix*. 2004, pp.111-118.

100. Kim D-P, Woo J-C, Baek K-H, et al. Dry etching of TiN in N-2/Cl-2/Ar adaptively coupled plasma. *Vacuum* 2011; 86: 380-385. DOI: 10.1016/j.vacuum.2011.08.002.

101. Kim J-H, Cho S-W, Park CJ, et al. Angular dependences of SiO2 etch rates at different bias voltages in CF4, C2F6, and C4F8 plasmas. *Thin Solid Films* 2017; 637: 43-48. DOI: 10.1016/j.tsf.2017.03.047.

102. Kwon K-H, Efremov A, Yun SJ, et al. Dry etching characteristics of Mo and Al2O3 films in O-2/Cl-2/Ar inductively coupled plasmas. *Thin Solid Films* 2014; 552: 105-110. DOI: 10.1016/j.tsf.2013.12.013.

103. Lallement L, Gosse C, Cardinaud C, et al. Etching studies of silica glasses in SF6/Ar inductively coupled plasmas: Implications for microfluidic devices fabrication. *Journal of Vacuum Science & Technology A* 2010; 28: 277-286. DOI: 10.1116/1.3298875.

104. Lin L, Jing X, Liu F, et al. Deep dry etching of fused silica using C4F8/Ar inductively coupled plasmas. *Journal of Materials Science-Materials in Electronics* 2017; 28: 480-486. DOI: 10.1007/s10854-016-5546-6.

105. Lin Y-H, Cheng Y-C, Chu N-N, et al. The study of compensative structure assisted convex and concave corner structures etching by Inductively Coupled Plasma-Reactive Ion Etch (ICP-RIE). *2015 Ieee 10th International Conference on Nano/Micro Engineered and Molecular Systems*. 2015, pp.491-493.

106. Min SR, Cho HN, Li YL, et al. Inductively coupled plasma reactive ion etching of titanium nitride thin films in a Cl-2/Ar plasma. *Journal of Industrial and Engineering Chemistry* 2008; 14: 297-302. DOI: 10.1016/j.jiec.2008.01.001.

107. Park JH, Lee NE, Lee J, et al. Deep dry etching of borosilicate glass using SF6 and SF6/Ar inductively coupled plasmas. *Microelectronic Engineering* 2005; 82: 119-128. DOI: 10.1016/j.mee.2005.07.006.

108. Pedersen M and Huff M. Plasma Etching of Deep High-Aspect Ratio Features Into Fused Silica. *Journal of Microelectromechanical Systems* 2017; 26: 448-455. DOI: 10.1109/jmems.2017.2661959.

109. Sun L, Jin H, Ye X, et al. Surface modification and etch process optimization of fused silica during reaction CHF3-Ar plasma etching. *Optik* 2016; 127: 206-211. DOI: 10.1016/j.ijleo.2015.10.046.

110. Tang Y-H, Lin Y-H, Chen P-L, et al. Comparison of optimised conditions for inductively coupled plasma-reactive ion etching of quartz substrates and its optical applications. *Micro & Nano Letters* 2014; 9: 395-398. DOI: 10.1049/mnl.2014.0093.

111. Thienot E, Domingo F, Cambril E, et al. Reactive ion etching of glass for biochip applications: Composition effects and surface damages. *Microelectronic Engineering* 2006; 83: 1155-1158. DOI: 10.1016/j.mee.2006.01.029.

112. Wang B and Li Y. Fabrication of fused-silica sub-micron gratings with high aspect ratio by transfer holographic resist masks with ICP dry etching. *Optoelectronics and Advanced Materials-Rapid Communications* 2010; 4: 1465-1468.

113. Wang SQ, Zhou CH, Ru HY, et al. Optimized condition for etching fused-silica phase gratings with inductively coupled plasma technology. *Applied Optics* 2005; 44: 4429-4434. DOI: 10.1364/ao.44.004429.

114. Wang Y, Lin Z, Zhang J, et al. Side-wall roughness in SOI rib waveguides fabricated by inductively coupled plasma reactive ion etching. *Applied Physics B-Lasers and Optics* 2004; 79: 879-881. DOI: 10.1007/s00340-004-1648-6.

115. Weigel C, Markweg E, Mueller L, et al. A monolithic micro-optical interferometer deep etched into fused silica. *Microelectronic Engineering* 2017; 174: 40-45. DOI: 10.1016/j.mee.2017.01.002.

116. Wu BQ. Quartz etch optimization. In: Tanabe H (ed) *Photomask and Next Generation Lithography Mask Technology Xi*. 2004, pp.94-105.

117. Zhang C, Hatipoglu G and Tadigadapa S. High-Speed Ultrasmooth Etching of Fused Silica Substrates in SF6, NF3, and H2O-Based Inductively Coupled Plasma Process. *Journal of Microelectromechanical Systems* 2015; 24: 922-930. DOI: 10.1109/jmems.2014.2359292.

118. Chen SC, Lin YC, Wu JC, et al. Parameter optimization for an ICP deep silicon etching system. *Microsystem Technologies-Micro-and Nanosystems-Information Storage and Processing Systems* 2007; 13: 465-474. DOI: 10.1007/s00542-006-0211-2.

119. Hong G, Holmes AS and Heaton ME. SU8 resist plasma etching and its optimisation. *Microsystem Technologies-Micro-and Nanosystems-Information Storage and Processing Systems* 2004; 10: 357-359. DOI: 10.1007/s00542-004-0413-4.

120. Wuest R, Strasser P, Robin F, et al. Fabrication of a hard mask for InP based photonic crystals: Increasing the plasma-etch selectivity of poly(methyl methacrylate) versus SiO2 and SiNx. *Journal of Vacuum Science & Technology B* 2005; 23: 3197-3201. DOI: 10.1116/1.2062567.